Εθνικό Μετσόβιο Πολυτεχνείο
Σχολή Πολιτικών Μηχανικών
Τομέας Γεωτεχνικής

National Technical University of Athens
School of Civil Engineering
Geotechnical Division

Διπλωματική Εργασία

Βασιλειάδης Μιχαήλ

Επιβλέποντες:

Καθηγητής Γ. Γκαζέτας

Επ. Καθ. Ι. Αναστασόπουλος

Υπόγειος Αγωγός Υποβαλλόμενος σε Κανονική και Ανάστροφη Διάρρηξη Τεκτονικού Ρήγματος

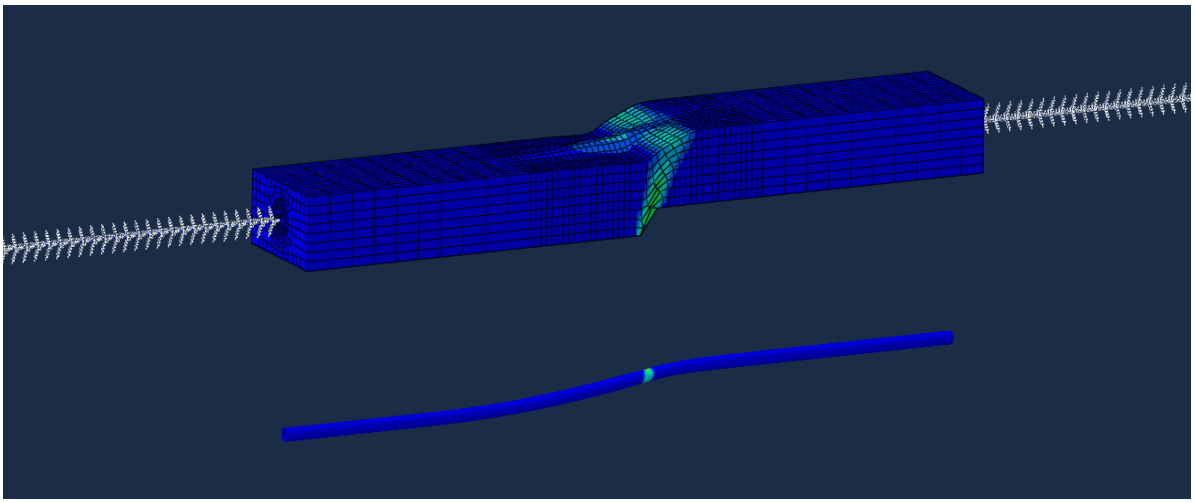

Buried Pipeline Subjected to Normal and Reverse Tectonic Fault Rupture

Diploma Thesis

Vasileiadis Michail

Supervised by:

Professor G. Gazetas

Ast. Prof. I. Anastasopoulos

Νοέμβριος 2012

Στους γονείς μου, Στέλιο και Ευδοξία

και στην αδερφή μου, Εύη

Ευχαριστίες

Κατά τη διάρκεια των σπουδών μου είχα την τιμή και την τύχη να βρεθώ δίπλα σε ανθρώπους ευφυείς, καταξιωμένους επιστήμονες και μηχανικούς μα πάνω απ' όλα προσωπικότητες που με τη διδασκαλία τους και τη στάση τους ξεχώρισαν στα μάτια μου και έγιναν πρότυπα.

Μια τέτοια προσωπικότητα είναι ο Καθηγητής κ. Γ. Γκαζέτας τον οποίο ευχαριστώ ιδιαίτερα που με τίμησε με την εμπιστοσύνη του και μου έδωσε την ευκαιρία να εκπονήσω αυτή τη διπλωματική υπό την επίβλεψη και καθοδήγησή του. Η αγάπη και ο ενθουσιασμός του για το μάθημα, την επιστήμη και τη δουλειά του είναι αξιοθαύμαστα και αδιαμφισβήτητα αποτέλεσαν έμπνευση για μένα.

Θερμές ευχαριστίες οφείλω, ακόμα, στον Επίκουρο Καθηγητή κ. Ι.Αναστασόπουλο καθώς υπήρξε δίπλα μου καθόλη τη διάρκεια εκπόνησης της διπλωματικής, πάντα φιλικός και πρόθυμος να με βοηθήσει με την πολύτιμη εμπειρία και τις γνώσεις του.

Επιπλέον, θα ήθελα να ευχαριστήσω όλα τα παιδιά που δουλέψαμε μαζί στο εργαστήριο εδαφομηχανικής, που με την παρέα τους έκαναν πραγματικά ευχάριστο το κλίμα κάτω από το οποίο δούλευα όλον αυτό τον καιρό. Ιδιαίτερα ευχαριστώ τον υποψήφιο διδάκτορα Α. Τσάτση που με βοήθησε ουσιαστικά με την εργασία μου.

Θέλω ακόμη να ευχαριστήσω τους φίλους μου και όλα τα άτομα που ήταν δίπλα μου και μοιραστήκαμε αυτά τα χρόνια.

Νιώθω, τέλος, απέραντη ευγνωμοσύνη απέναντι στην οικογένειά μου. Τους ευχαριστώ για την απλόχερη αγάπη που είχα κάθε λεπτό της ζωής μου, για τις αξίες και αρετές που μου μετέδωσαν και γιατί πάντα με συμβουλεύουν και στηρίζουν κάθε μου απόφαση.

Σύνοψη

Η παρούσα διπλωματική εργασία διερευνά την μηχανική συμπεριφορά υπογείου χαλύβδινου αγωγού, που χρησιμοποιείται στην μεταφορά πετρελαίου ή φυσικού αερίου, υποβαλλομένου σε κανονική ή ανάστροφη διάρρηξη τεκτονικού ρήγματος. Η διερεύνηση βασίζεται σε αριθμητική προσομοίωση με την μέθοδο των πεπερασμένων στοιχείων. Κύριος στόχος της εργασίας είναι η ανάπτυξη προσομοιώματος που να λαμβάνει υπόψη την ανελαστική συμπεριφορά τόσο του εδλαφους όσο και του αγωγού, καθώς και τις γραμμικές μή-γραμμικότητες, δίνοντας έμφαση στην ρεαλιστική προσομοίωση της διεπιφάνειας εδάφους-αγωγού με αποκόλληση και ολίσθηση. Αφετέρου, διερευνάται παραμετρικά η επιρροή των σημαντικότερων παραμέτρων του προβλήματος. Εξετάζονται διαφορετικές προσεγγίσεις ως προς τις συνοριακές συνθήκες στα άκρα του αγωγού, καταλήγοντας στη δημιουργία ενός υβριδικού «συνόρου» τύπου Winkler, το οποίο προσομοιώνει ικανοποιητικά την συνέχεια του αγωγού και του εδάφους. Το αναπτυχθέν προσομοίωμα εφαρμόζεται για την προσομοίωση κανονικού και ανάστροφου ρήγμτος. Τα αποτελέσματα παρουσιάζονται με βάση την «οριακή» μετατόπιση ρήγματος σε σχέση με τον λόγο της διαμέτρου προς το πάχος του αγωγού (D/t). Η αστοχία ορίζεται από κατάλληλα λειτουργικά κριτήρια για τον αγωγό τα οποία ελέγχονται καθ’ όλη τη διάρκεια των αναλύσεων. Οι παράμετροι που εξετάζονται, πέραν του λόγου D/t, είναι η επίδραση του πάχους της εδαφικής στρώσης, η σχέση τάσεων-παραμορφώσεων του χάλυβα του αγωγού και η εσωτερική πίεση λόγω του μεταφερόμενου ρευστού.

Synopsis

The present diploma thesis investigates the mechanical behavior of a buried steel pipeline, commonly used for oil and gas transportation, subjected to Dip-Slip tectonic fault rupture. The investigation is based on numerical simulation with the finite element code ABAQUS 2011. The main objective of this study is to develop a proper model that accounts for large displacements and strains, inelastic material behavior of the pipe and the soil, as well as proper contact and friction at the pipe-soil interface. Different approaches are examined concerning the pipe boundaries, finally leading to the development of a hybrid boundary capable of simulating the natural continuation of the pipe. The model is used to study the normal and reverse fault ruptures. The main results are presented in terms of “critical” fault displacement for different performance criteria, which are monitored throughout the analyses, with respect to the D/t ratio. Other parameters that are examined are the soil layer’s depth, the stress-strain relation of the pipe steel, and the internal pipe pressure.

TABLE OF CONTENTS

CHAPTER 1

CHAPTER 2

CHAPTER 3

CHAPTER 4

CHAPTER 5

CHAPTER 6

CHAPTER 7

CHAPTER 8

Chapter 1
Introduction and study motivation

1.1 Introduction

Buried pipelines are commonly used to support electric power distribution, telecommunications, and to transmit water, sewage, liquid and gas. Pipelines, also mentioned as lifelines, often cross tectonically active areas and may cross active faults capable of producing large earthquakes and large ground deformations. There are various examples of earthquakes that severely damaged buried pipelines such as the earthquakes of San Fernando 1971, Managua 1972, Haicheng 1975, Tang-shan 1976, Miyagiken-Oki 1978, Northridge 1994, Kobe 1995, Chi-Chi 1999, Kocaeli 1999 and the more recent ones, those of Chile 2010, Christchurch 2010-2011 and Japan 2011. Based on the observed damage mechanisms of buried pipelines, seismic effects can be either caused by transient strain and curvature in the ground due to traveling wave effects, or caused by permanent ground deformations such as fault deformation, landslide, and liquefaction-induced soil movements. Among them, the ground movements of active faults, even though relatively limited to small regions, can have the most severe effects on buried pipelines. There are few cases in which pipelines were damaged only by wave propagation (Mexico City 1985-Michoacan earthquake). Fault movement, though, is applied on the pipeline quasi-statically and might cause significant damage to the pipe regardless the seismic intensity.

1.2 Faults

Although this study focuses on faults that propagate through the upper soil layers, it is considered reasonable to present a brief theoretical background concerning faults and their association with the genesis mechanism of earthquakes. An active fault is a discontinuity between two portions of the earth crust along which relative movements can occur. The theory that is currently considered to be the most accurate for the description of this mechanism is the Elastic Rebound Theory. Because of friction and the rigidity of the rock, the rocks cannot glide or flow past each other. Rather, stress builds up in rocks and when it reaches a level that exceeds the rock's strength, the accumulated potential energy is dissipated by the release of strain, which is focused into a plane along which relative motion is accommodated, the fault. Strain is both accumulative and instantaneous depending on the rheology of the rock. The ductile lower crust and mantle accumulates deformation gradually via shearing, whereas the brittle upper crust reacts by fracture - instantaneous stress release - to cause motion along the fault. A fault in ductile rocks can also release instantaneously when the strain rate is too great. The energy released by instantaneous strain release causes earthquakes. There are two ways to simulate the fault's surface: the Asperities model, a model of inhomogeneous macroscopic roughness and the Barrier's model, where the surface is considered discontinuous with areas of variable shear strength.

Basic types of faults

The two sides of a fault are known as the *hanging wall* and *footwall*. By definition, the hanging wall occurs above the fault plane and the footwall occurs below the fault. Faults are distinguished on the basis of the movement of the footwall relative to the hanging wall.

Strike slip faults

Strike-slip are the faults that primarily exhibit horizontal movement **(Figure1.2.1)**. The fault surface is usually near vertical and the footwall moves either left or right or laterally with very little vertical motion.

Dip-slip faults

Dip slip faults are those in which vertical displacement primarily occurs. They are divided in to 2 categories: normal and reverse faults. Normal **(Figure1.2.2)** are the faults in which the hanging wall moves down relative to the foot wall due to tensional stress. The term "normal" does not have the sense of "common" and what is normal about them is that their movement tends to follow the gravitational pull on the fault blocks involved. A reverse fault **(Figure1.2.3)** is one in which the hanging wall moves up relative to the foot wall due to compression. If the hanging wall is pushed up and then over the foot wall at a low angle it is called a thrust fault.

Oblique-slip faults

A fault which has a component of dip-slip and a component of strike-slip is termed an oblique-slip fault **(Figure1.2.4)**. Nearly all faults have some component of both dip-slip and strike-slip, so defining a fault as oblique requires both dip and strike components to be measurable and significant. Finally, it has to be clarified that not all of the faults reach the surface. Whether the rupture will propagate up to the surface depends on various parameters such as the magnitude of bedrock movement, the depth of the soil layer, the fault's angle and the soil properties.

1.3 Pipelines

Overview

Oil and gas pipelines are usually made from steel of various strength and characteristics **(Table 1.1)** or from plastic (HDPE), with inner diameter typically from 4 to 48 inches (100 to 1200 mm). Another material that has been used is the glass-reinforced plastic (GRP) a composite material made of plastic reinforced by glass fibers. Most pipelines are typically buried at a depth of about 0.9 to 2.5m. The oil is kept in motion by pump stations along the pipeline sited at the originated station of the line and at 30 to 160 kilometer intervals along the length of the pipeline while the gas is kept in motion by compression stations sited at 70 to 500 kilometer intervals, depending on pipeline design, topography and capacity requirements. The usual flow speed is of about 1 to 6 meters per second for the oil and 20 to 60 m/s for the gas.

As a rule pipelines for all uses are laid in most cases underground. However in some cases it is necessary to cross a valley or a river on a pipeline bridge. Pipelines for petroleum running through permafrost areas often run overhead in order to avoid melting the frozen ground by hot petroleum which would result in sinking the pipeline in the ground. Laying the pipeline on the ground is also preferred sometimes in cases where the pipeline crosses a fault of important offset potential such as the Trans-Alaska oil pipeline **(Figure 1.3.1)**.

A brief comparison of buried to surface pipelines leads to the following observations:

- Buried pipelines
  - are more protected against temperature fluctuations and weather phenomena in general, as well as against accidents like crashes and terrorist attacks.
  - Have a small impact to the surrounding environment.

- Can extend for thousands of kilometers without interfering and causing problems to other infrastructure systems such as roads.
- Have the same, or even smaller, cost compared to the on ground pipelines, since the excavation cost is counterbalanced if not exceeded by the cost of the special footings needed for the surface pipelines.

➢ Surface pipelines

- Can be easily inspected
- Can accommodate, generally, bigger fault offsets

Pipelines can be categorized as:

Gathering pipelines

Group of smaller interconnected pipelines forming complex networks with the purpose of bringing crude oil or natural gas from several nearby wells to a treatment plant or processing facility.

Distribution pipelines

Composed of several interconnected pipelines with small diameters, used to take the products to the final consumer.

Transportation or transmission pipelines

Mainly long pipes with large diameters, moving products (oil, gas, refined products) between cities, countries and even continents. 'Transmission' pipelines are the main 'arteries' of the oil and gas business.

Construction Sequence

Before any other step of the construction, the construction corridor has to be cleared of brush, trees, large rocks and any other obstructions. Then, the trench in which the pipe will be laid is excavated **(Figure 1.3.2)**. Machine excavators are used for the excavation along with any necessary hand digging and general field labor activities. The pipeline parts are placed alongside the trench. Next step is the bending of the pipes. Since, the route of the trench is not a constant line the pipeline should get bended at certain points, in order to conform to the trench. Afterwards, the joints of the different parts are welded into bigger pipe parts. Although the pipe would arrive at the right-of-way with a corrosion-resistant coating, crews apply additional coating to the welded areas and repair any damage to the factory-applied coating to prevent corrosion. The pipe coating is a special material that prevents water from contacting the steel of the pipe and causing corrosion. When the welding and coating are complete, the pipe is suspended over the ditch by side-boom tractors, which are crawler tractors with a special hoisting frame attached to one side **(Figures 1.3.4, 1.3.5)**. Then, the pipeline is gradually lowered to the bottom of the ditch. In rocky soil or solid rock, it is sometimes necessary to put a bed of fine soil in the bottom of the ditch before lowering the pipeline. The fine fill material protects the pipe coating from damage. The final cuts on the pipe are made to connect the entire pipeline and coat the final tie-in welds **(Figure 1.3.6)**. The pipeline is then tested to prove its structural soundness and ability to fulfill its design function. The line is filled with water and then pressurized to check for leaks. Finally, the trench gets covered by the backfill and the surface gets cleaned up and restored if possible to its previous state.

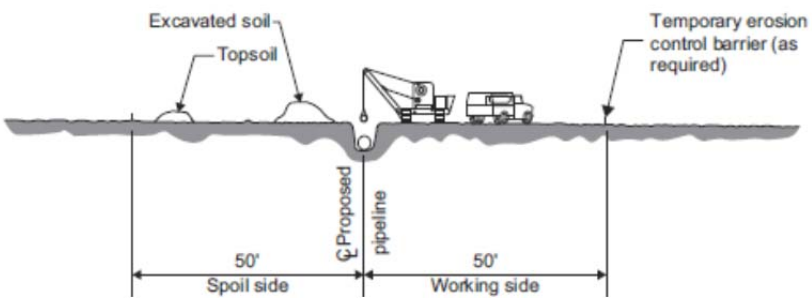

1.4 Literature Review

The problem of pipelines crossing active faults has been approached using analytical, numerical, as well as experimental methods. The initiators of the analytical studies were Newmark and Hall (1975) **(Figure 1.4.1)**. In their pioneer work they studied the ability of a continuous pipe to resist large displacements caused by strike-slip faults Focusing upon cases where the fault rupture provokes severe elongation of the pipeline, so as tension is the prevailing mode of deformation. In their model the pipe is assumed to be firmly attached to the surrounding soil at two anchor points located at distance L from fault trace. These anchor points correspond to elbows, thrust blocks, tie-ins and other features, which can develop substantial resistance to axial movement. The authors neglected the bending stiffness of the pipe as well as the lateral interactions at the pipe-soil interface. They discovered that the bearing capacity of a buried pipeline to fault movement depends on the soil conditions, pipe and fault characteristics and that minimizing the longitudinal resistance of the soil to the pipe motion maximizes the pipe resistance. They have also suggested that the pipe should be placed in a trench with shallow sloping sides so that it can accommodate itself to the transverse as well as the longitudinal components of the fault movement. Subsequently, Kennedy et al (1977) **(Figure 1.4.2)** extended Newmark and Hall's procedure to determine the pipe capacity to resist fault movement by taking uniform passive soil pressure and the large deflection theory into consideration. It is assumed that the pipeline is a flexible cable deformed into a single constant curve approaching asymptotically to the undistorted portion of the pipeline. In this model, only the axial tensile force at the point of inflection is used for equilibrium, no flexural resistance was considered. Therefore with the omission of the flexural rigidity of the pipe, this model cannot satisfy the equilibrium condition for a pipeline crossing a strike-slip fault or oblique-slip fault that will cause compression in the pipeline. Vougioukas and Carydis (1979) **(Figure 1.4.3)** proposed a model applicable both for strike-slip and for dip-slip faults, either normal or reverse, and calculated the ductility demands for the pipelines to resist large fault displacements. Wang and Yeh (1985) **(Figure 1.4.4)** proposed a localized large

deflection beam model to analyze pipeline behavior crossing the strike-slip fault. They modeled a large deflection pipe as a constant curvature curved segment and the remaining small deflection pipe as a semi-infinite beam on elastic foundation. This model includes the bending rigidity of the pipe, a shear force at the point of inflection of the curve pipe crossing the fault zone, and a boundary condition related to semi-infinite beam on elastic foundation at some distance away from the fault zone. Their methodology refers only to strike-slip faults and relies on partitioning of the pipeline into four distinct segments two in the high curvature zone on both sides of the fault trace, and another two outside this zone. This model yielded more realistic results provided that the appropriate parameters are chosen. Chiou et al. (1994) came to the conclusion that the curvature of the deformed pipe is unknown and can hardly be predicted in advance. Moreover, the constant curvature model overestimates the stiffness of the buried pipe and consequently underestimates its strain. Karamitros et al. (2006) **(Figure 1.4.5)**, trying to improve the models of Kennedy and Wang, proposed a more sophisticated analytical method for strike-slip faults, which they later extended to be applicable for normal faults as well (2011). They presented an analytical methodology, refining existing methodologies using a combination of beam-on-elastic-foundation and beam theory, and computed axial force, bending moment and maximum strain on the pipeline. They also compared their analytical predictions with results from a three-dimensional finite element model, which employed a relatively coarse shell element mesh for describing the pipe and nonlinear springs to simulate the soil. As in all the aforementioned studies, their analytical model does not take into account second order effects such as local buckling and sectional deformation and applies only under certain strain limits and only when the fault results in elongation of the pipe, thus, when tension and bending are the prevailing modes of deformation**.**

There is also a number of researchers that studied the problem using numerical models. The majority of them used the Finite Element Method and studied mostly the strike-slip case. Takada et al. (2001) studied elasto-plastic shell-mode buckling of a pipe subjected to normal and reverse fault movement using shell finite element

method. Based on analytical results and on Kennedy's work they proposed a simplified method for the maximum axial strain in steel pipes considering the deformation of the pipe cross-section **(Figure 1.4.6)**. O'Rourke and Liu (1997) developed a numerical model to analyze pipe response to fault offsets and compared their numerical results with the results from other analytical approaches. They concluded that Kennedy's analytical solution is the best available for pipe response to strike-slip faults primarily in tension. The seismic analysis of buried and unburied pipelines, under both transient and permanent ground movements have been examined by Arifin et al. (2010), using beam finite elements for the pipeline and nonlinear springs to model the effects of the surrounding soil. Odina and Tan (2009) investigated buried pipeline response under seismic fault displacement, using a beam-type finite element model with elastic-plastic springs for the soil effects. In a subsequent publication, Odina and Conder (2010), extended the work by examining the effects of Lüder's plateau of the stress-strain material curve on the pipeline response crossing active faults.

It is worth mentioning the work of Vazouras et al. (2010, 2012) on which we based our approach. They simulated a buried pipeline crossing a strike-slip fault using ABAQUS **(Figures 1.4.7, 1.4.8)**. They conducted various parametric studies regarding the type of soil, the fault angle and the diameter to thickness ratio of the pipe **(Figure 1.4.9)**. They also examined the effect of internal pipe pressure **(Figure 1.4.10)**. Although their model is limited to the upper 5m of the ground and does not take into consideration the actual fault propagation, it has the advantage that the soil is simulated by continuum brick elements and not by unconnected soil springs which have been the most common option by the other researchers. That has certain significant advantages as it will be described in the following chapter.

Significant experimental research has been conducted, under the NEESR project (Network for Earthquake Engineering Simulation) by Cornell University and Rensselaer Polytechnic Institute supervised by Professor T.D.O'Rourke (2008). The research, elaborated at the Cornell (CU) and Rensselaer (RPI) NEES equipment site,

utilizes the equipment for large-scale soil-structure interaction and centrifuge-scale split box testing. The equipment at Cornell consists of large-displacement servo-hydraulic actuators and ancillary hydraulic systems, soil-storage facilities and frame support system for large-scale lifeline soil-structure interaction, a variety of instrumentation, and data acquisition systems **(Figure 1.4.11)**. The RPI facilities use advanced split-box-centrifuge containers for simulation of lifeline systems. These containers are used in the upgraded RPI 150 g-ton centrifuge **(Figure 1.4.14)**. It is worth noticing that the large-scale ground rupture experiments involve the largest laboratory tests ever performed on pipeline response to ground deformation. The test not only demonstrates the ability of such pipelines to accommodate severe movement, but provides important data about strain concentrations, changes in shape, and soil-structure interaction Combined testing at CU and RPI provides information essential for design and construction in response to earthquakes, floods, landslides, large deformation induced by tunneling and deep excavations, and subsidence caused by severe dewatering or withdrawal of minerals and fluids during mining and oil production. The same large-scale equipment at Cornell has been used to test the behavior of a different construction method according to which the pipeline is placed in a segmental, reinforced concrete vault with special joints that can accommodate lateral offset and compressive deformation during fault rupture, thereby allowing for rotation and compression of the pipeline inside the vault at ball and slip joints, respectively **(Figure 1.4.16)**. Finally, Sim et al. (2011) (Imperial College of London and University of Tokyo) performed a series of shaking table tests modeling small diameter pipes crossing a vertical fault **(Figure 1.4.18)**. Their results indicated that the magnitude of bending moment is directly affected by the magnitude of fault displacement irrespective of any other factors. In particular, the intensity of shaking does not play a significant role in the magnitude of bending moment caused by fault action. In their experiments they also used tyre derived aggregate (TDA) backfill and proved that it is capable of reducing the bending moments incurred due to simultaneous faulting and shaking for maximum accelerations less than or equal to 0.5 g and vertical fault displacements less than the pipe diameter by up to 74%.

1.5 Motivation of the Study

Energy is one of the most important issues of modern world. For the time being and probably for lots of future decades, energy production will be based primarily on hydrocarbons. The transportation of energy is quite as vital as its very production and today, the most common way of transport for oil or natural gas are the pipeline networks. Every hour the world consumes millions of cubic meters of gas and oil and almost all of it moves through a pipeline.

Past and Present

The first recorded use of a pipe to transport a hydrocarbon was in China about 2,500 years ago. The Chinese used bamboo pipe to transmit natural gas from shallow wells: they burned it under pans to boil seawater to separate the salt, and make the water drinkable. Later records indicate that the Chinese used bamboo pipe, wrapped in wax, to light their capital, Peking, as early as 400 BC (Britannica). Today's oil and gas pipeline industry has its origins in the oil business. Oil had been drilled in Baku, Azerbaijan in 1848, and Poland in 1854, but the first major exploitation and commercialization started in 1859 in the USA. In the early 1860s, the oil was transported in wooden barrels on rivers by horse-drawn barges. Later, it was the railway that took the primary role in oil transportation. In 1865 a 152mm diameter gravity oil line was built in Pennsylvania, USA, transporting 7000 barrels/day. However, the real change in pipeline engineering was the building of long distance, large diameter pipelines: these were pioneered in the USA in the 1940s due to the energy demands of the Second World War.

Today, oil and gas provides most of the world with its energy. The fuels providing the world with its primary energy needs are:

Oil = 34%

Coal = 24%

Gas = 21%

Nuclear = 7%

Hydro = 2%

Other = 12%

The oil and gas business is big, and it is going to become bigger. The US Energy Information Administration's World Energy Outlook has predicted that fossil fuels will remain the primary sources of energy, meeting more than 90% of the increase in future energy demand. This expanding, secure industry is also highly profitable. Big oil companies have announced annual profits even of $US36 billion, the largest company profit ever accomplished. These profits are expected to continue in the foreseeable future, as the price of fuels continues to rise. The same augmenting trend is observed in pipeline construction market. The market size for oil and gas pipeline construction experienced tremendous growth and grew from $23billions in 2006 to over $45billions today. To support the growth in energy demand, pipeline infrastructure has grown by a factor of 100 in approximately 50 years. It has been estimated that world pipeline expansion could be up to 7% per year over the next 15 years. Internationally, 32,000km of new onshore pipelines are constructed each year corresponding to a $US28billion business. The total length of high pressure transmission pipelines around the world has been estimated at 3.500.000km **(Figures 1.5.2 - 1.5.6).**

Of those:

64% carry natural gas

19% carry petroleum products

17% carry crude oil

Pipelines are a very safe form of transporting energy, both for human and the environment. Relative reports demonstrated that pipelines are 40 times safer than rail tanks, and 100 times safer than road tanks for transporting energy. According to the USA Association of Oil Pipelines, oil pipeline spills amount to about 1 gallon per million barrel-miles. This is less than one teaspoon of oil spilled per thousand barrel-miles. Pipelines are, in general, the most economical way for gas and oil distribution. It is a long-term investment and probably the most energy efficient solution meaning that they consume less energy than the other options having at the same time higher capacity.

Pipeline systems are critical transportation infrastructures in most nations and essential to both standards of living and economies. The future for pipelines is both bright and challenging. They will continue to carry the bulk of our primary energy sources and is up to engineers to ensure they perform both safely and efficiently.

Performance in past earthquakes

The vulnerability of buried pipelines to seismic hazards has been demonstrated by the extensive damage observed during previous earthquakes **(Figures 1.5.7 -1.5.10).** Examples of documented pipeline damage, regardless its use and material, include: the 1905 San Francisco, 1933 Long Beach, 1952 Kern Country, 1964 Alaska,1964 Niigata, 1971 San Fernando, 1979 Imperial Valley,1987 Ecuador, 1989 Loma Prieta, 1990 Manjil Earthquake, 1991 Costa Rica, 1994 Northridge,1995 Kobe,1999 Chi-Chi, 1999Kocaeli, 2010 Chile, 2010-2011 Christchurch and 2011 Japan. Three

characteristic cases are those of Alaska, San Fernando and Ecuador. In 1964, the Anchorage, Alaska earthquake caused over 200 breaks in gas pipelines and 100 breaks in water distribution pipelines at Anchorage. Gas lines within fault zones were ruptured. Most of the pipeline damage was due to landslides and ground cracking. The 1971 San Fernando earthquake resulted in 1,400 breaks in various piping systems. The city of San Fernando temporally lost water, gas and sewage services. Most of the damage was caused due to liquefaction-induced lateral spreading. The 1987 Ecuador earthquake destroyed the trans-Ecuadorian pipeline, which represented the largest single pipeline loss in history. It cost over $850 million in lost sales and reconstruction.

The situation in Greece

Currently, in Greece, the major pipeline networks operating are the 300km Thessaloniki-Athens gas pipeline and the ITG (Interconnector Turkey-Greece) **(Figure 1.5.11)**. However, Greece is about to play a significant role for Europe's energy supply. There are 4 proposed plans for transporting gas from the Caspian and Middle East areas to Europe: TAP (Trans-Adriatic Pipeline), ITGI(Interconnector Turkey-Greece-Italy), Nabucco and SEEP(South East Europe Pipeline). In the first two of those scenarios Greece will play the role of the energy hub for Europe. TAP would run 800km from Komotini through Greece and Albania, to end near San Foca, Italy via a 110km offshore part. ITGI includes 600km onshore pipeline running all along the northern part of Greece and 200km offshore pipeline across the Ionian Sea. It also includes the connection of Bulgaria with Greece via the 170km IBG(Interconnector Greece-Bulgaria) pipeline **(Figure 1.5.13)**. It is obvious how important this is for Greece especially if we consider that, according to Energy Information Administration EIA ,Office of oil and gas 2008 Report, the cost per Km for the construction of a pipeline varies from 0.8 to over 3 million euros, with the part of the management and engineering corresponding to the 20-25% of the total cost. Looking at the tectonic map of Greece **(Figure 1.5.12)** it is easy to observe that

it is almost inevitable for the pipeline not to cross any fault zone along its way. It is quite interesting, as well, that the type of the great majority of faults of northern Greece is dip-slip, something that makes the investigation of this problem even more important and on time.

Scope of the study

As already mentioned, little analytical work has been done for a pipe crossing a normal or reverse fault. For a pipe subject to a normal fault, the pipe-soil system is no longer symmetric, and the transverse interaction force at the pipe-soil interface for downward movement of the pipeline is much larger than that for upward movement. Similarly, for a pipe subject to a reverse fault, it appears that no closed-form simplified analytical approach is currently available. The behavior in such cases is difficult to generalize, in part because there are two angles of intersection in addition to the aforementioned asymmetric nature of the soil resistance in the vertical plane. The international regulations for this kind of problem are thus limited. Apart from the relatively inadequate analytical research there are also few numerical models simulating dip-slip fault rupture. In addition, most of them substitute the soil with soil-springs attached to the pipe having as a result to neglect the interaction between the springs (as it would happen in the real soil) as well as the original fault propagation. Finally, none of the previous researchers has given a documented answer to the problem of boundary conditions at the edges of the pipe rather than assuming fixed conditions at the edges of the pipe. What is pioneering about our work is the model we used to simulate the problem, which is probably the most realistic model ever used for this kind of problems. We tried to overcome the aforementioned problems using a hybrid-beam model, in order to take into consideration the very large dimensions and affected area of the real problem. We also adopted and incorporated in the finite-element code, an elastoplastic Mohr-coulomb constitutive model with isotropic strain softening that has been proved capable of capturing the predominant mode of deformation caused by faults

compared with laboratory experiment results (Anastasopoulos2007). Apart from the significance that pipeline networks are going to have for Greece and the various problems of the previous models that we want to solve, it has been a great motivation for our study the fact that the very same problem will be examined in our laboratory. Using a split-box device the behavior of pipes under dip-slip faults is going to be examined, having, thus, the opportunity to investigate closely the actual mechanisms that occur and to compare analytical with experimental results.

To sum up, through our research we aim to:

- Propose of a proper model for the problem
- Investigate the mechanical behavior of the pipe and the effect of various parameters

Figures of Chapter 1

Basic Types of Faults

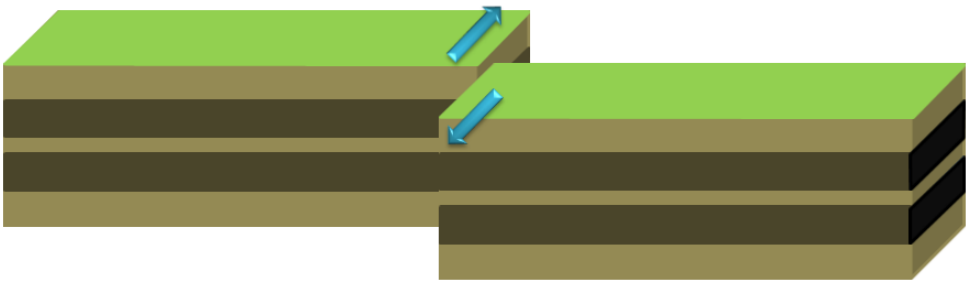

Figure 1.2.1. Strike Slip Fault.

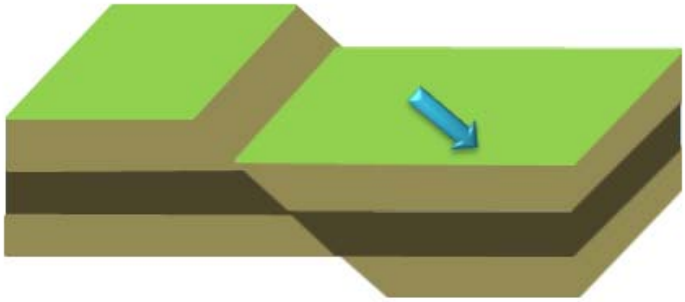

Figure 1.2.2. Normal Fault.

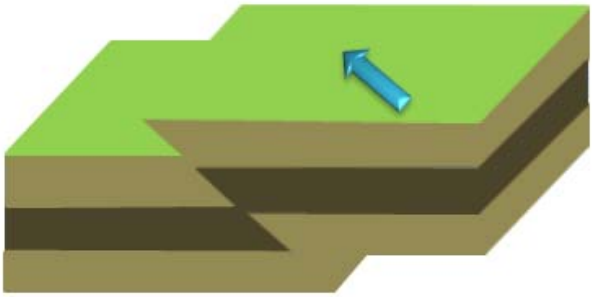

Figure 1.2.3. Reverse Fault.

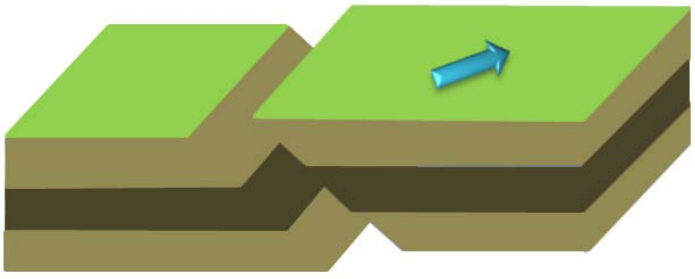

Figure 1.2.4. Oblique Fault.

Figure 1.2.5. The San Andreas Fault, a right-lateral strike-slip fault, that caused the massive 1906 San Francisco earthquake (www.SanAndreasFault.org).

Figure 1.2.6. The Denali Fault, Alaska (www.arcticgas.gov).

Figure 1.2.7 Normal fault at Tucki Mountain, Death Valley, California (www.geotripper.org).

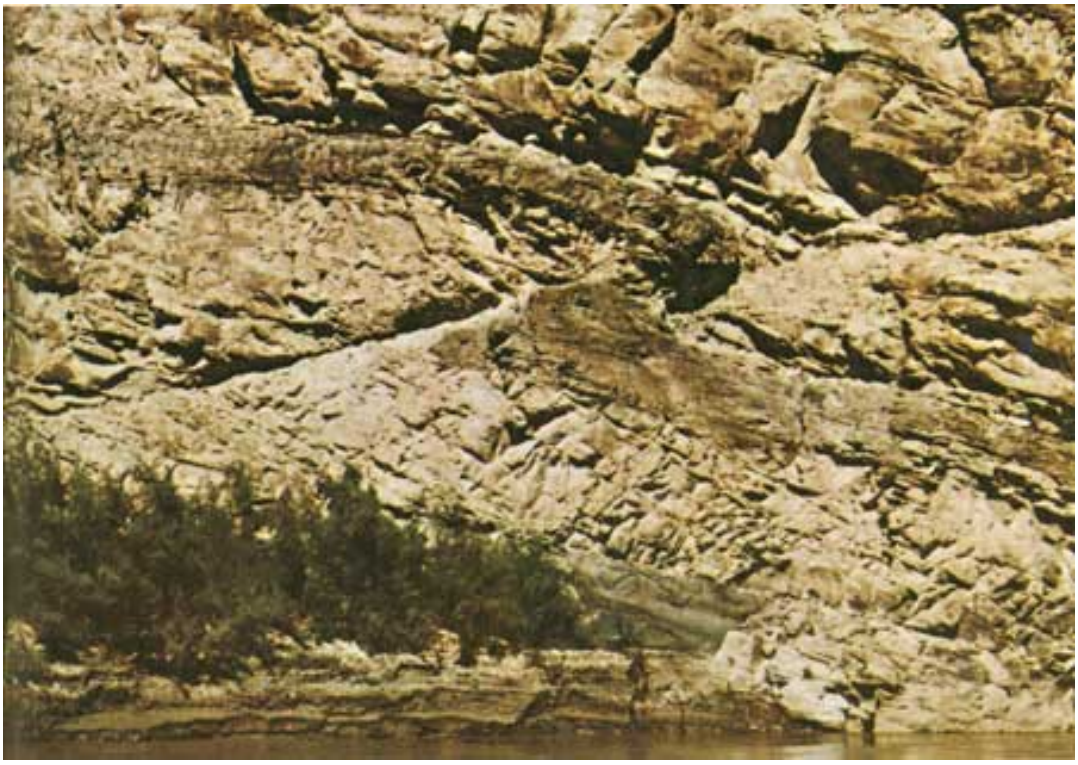

Figure 1.2.8. Reverse fault at Colorado (USGS gallery).

Table 1.1. Grades of steel pipes and their minimum strength.(American Petroleum Institute)

Grade	Yield Strength, Minimum		Ultimate Tensile Strength, Minimum	
	psi	MPa	psi	MPa
A25	25,000	(172)	45,000	(310)
A	30,000	(207)	48,000	(331)
B	35,000	(241)	60,000	(414)
X42	42,000	(290)	60,000	(414)
X46	46,000	(317)	63,000	(434)
X52	52,000	(359)	66,000	(455)
X56	56,000	(386)	71,000	(490)
X60	60,000	(414)	75,000	(517)
X65	65,000	(448)	77,000	(531)
X70	70,000	(483)	82,000	(565)

Figure 1.3.1. The trans-Alaska oil pipeline where it crosses the Denali Fault. The special footings allow the pipe to move 6m laterally and 1.5m vertically (Alaska Natural Gas Transportation Projects).

Figure 1.3.2. Excavation of the trench (www.constructionphotography.com).

Figure 1.3.3. Excavating pipe trench using trenching machine (Lincolnshire gas pipeline works, United Kingdom).

Figure 1.3.4. Laying down the gas pipeline that runs from Edmonton to Vancouver, Canada (Canadian Energy pipeline Association).

Figure 1.3.5. Pipe-laying process of the 370km Fujairah oil pipeline in the United Arab Emirates (www.pipelinesinternational.com).

Figure 1.3.6. Welding process. South Wales gas pipeline. UK's largest high-pressure gas pipeline (317 km) (www.nationalgrid.com).

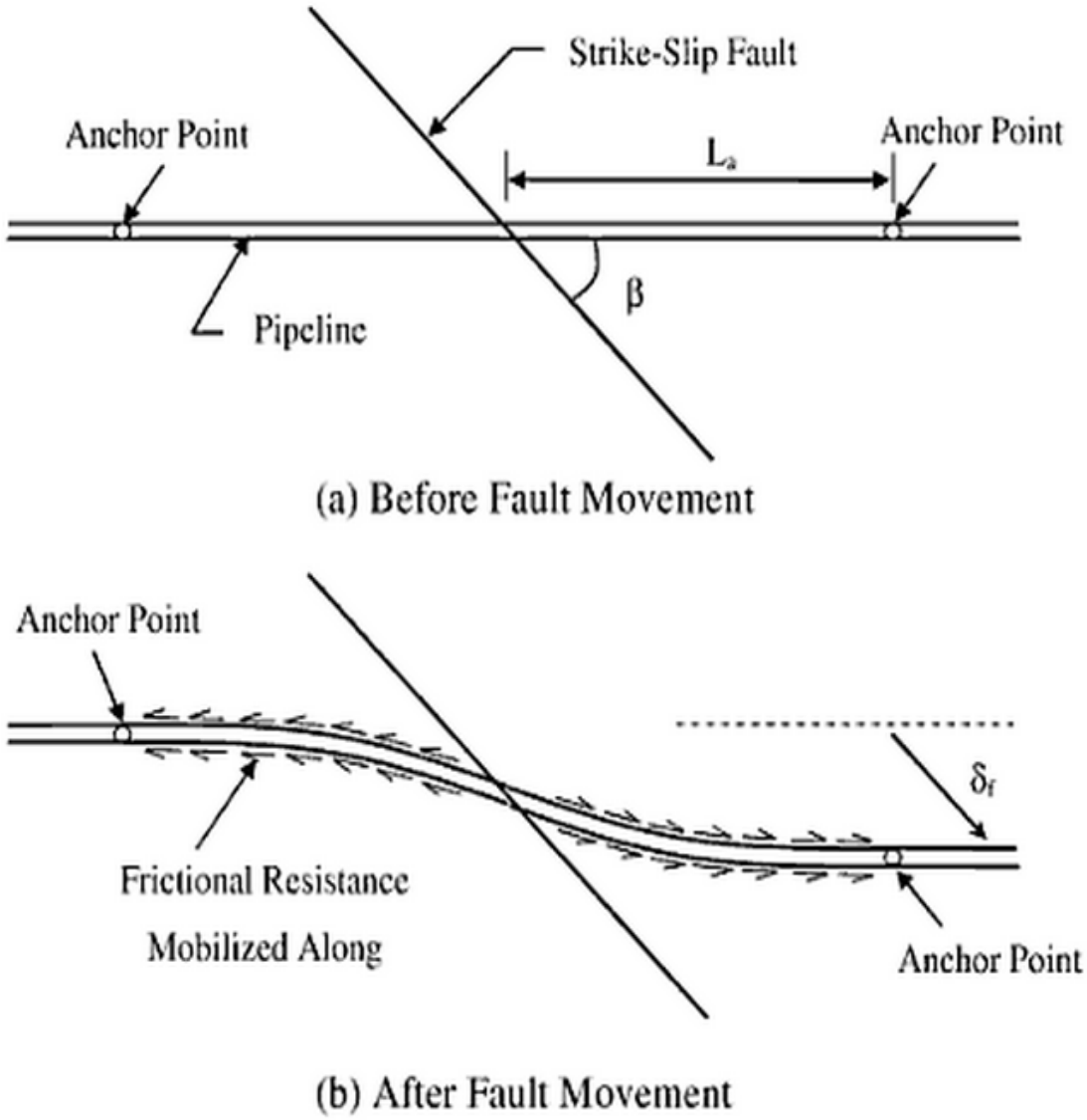

Figure 1.4.1. Newmark and Hall model (1975).

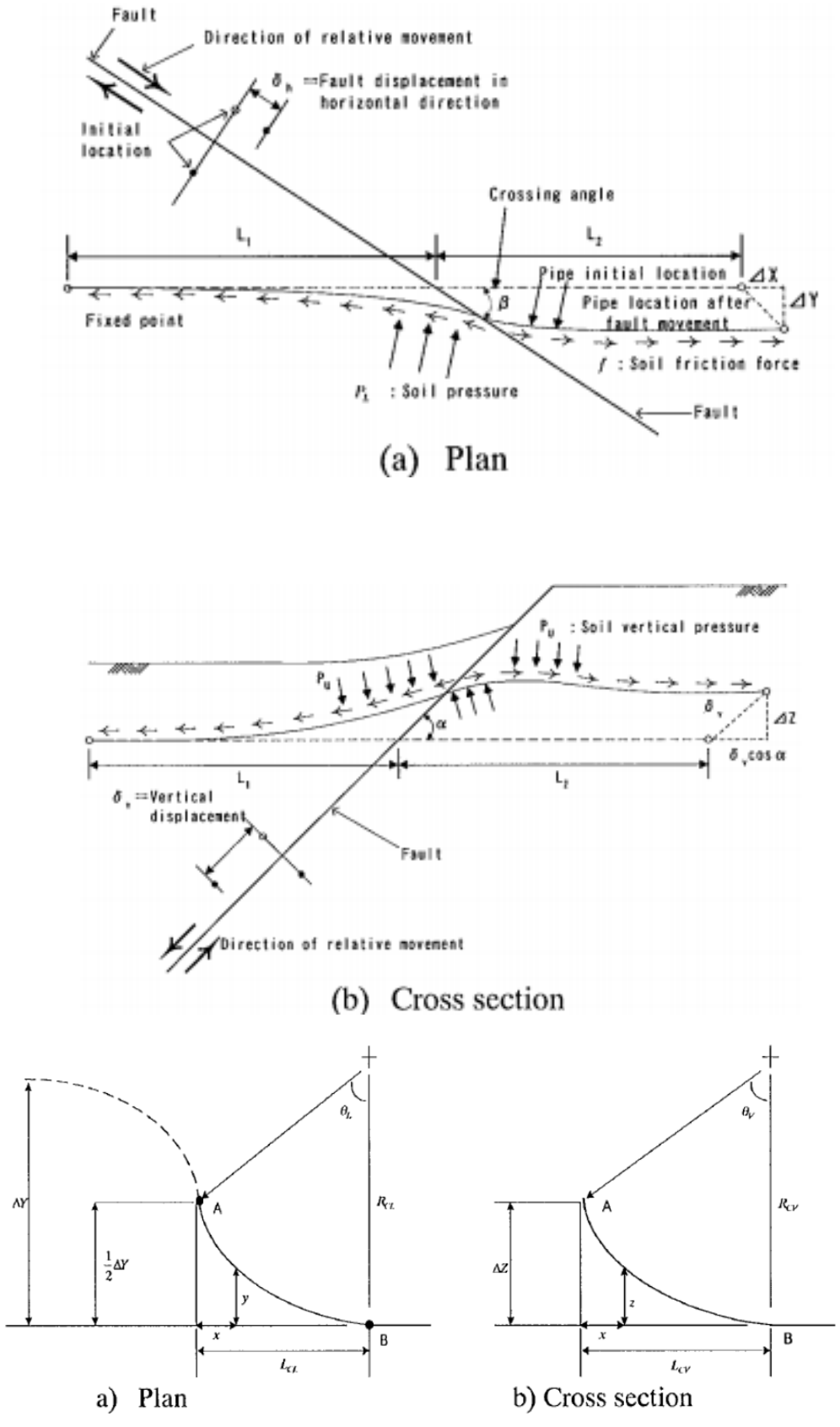

Pipe deformation near the fault, after Kennedy et al.

Figure 1.4.2. Kennedy's model (1977).

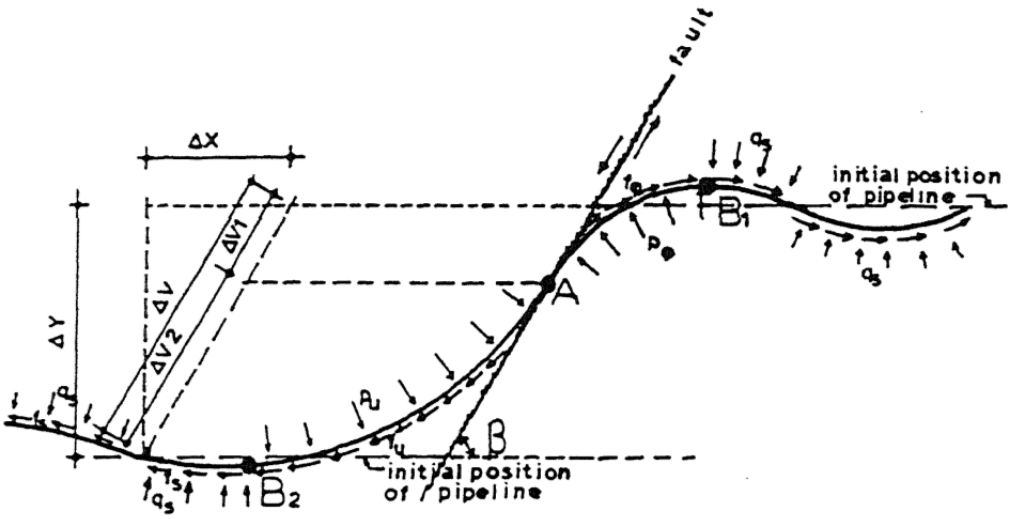

Model of pipeline subjected to vertical fault movement (side view).

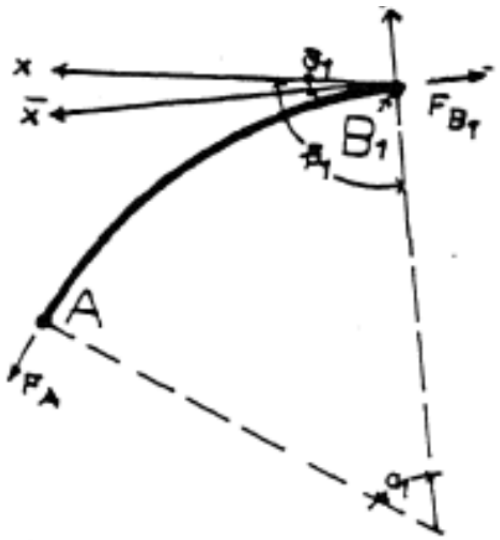

Detail of large deformation area of the model.

Figure 1.4.3. Vougioukas and Carydis model (1979).

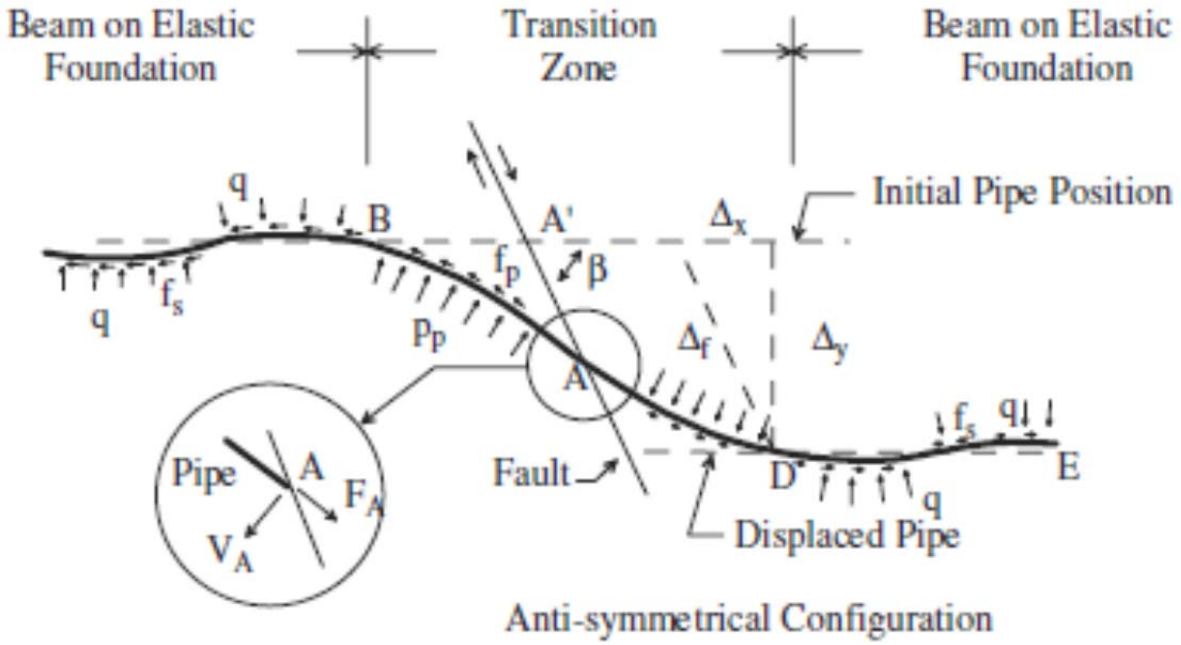

Figure 1.4.4. Pipeline analysis model proposed by Wang and Yeh (1985).

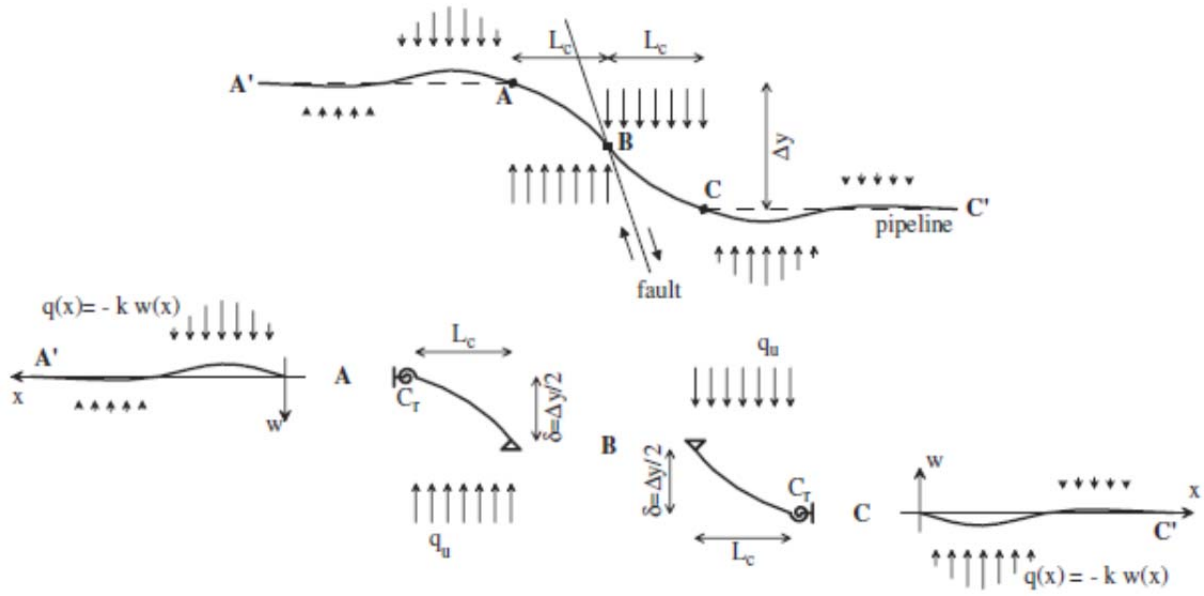

Figure 1.4.5. Partitioning of the pipeline into four segments. Wang and Yeh method on which Karamitros' approach was based.

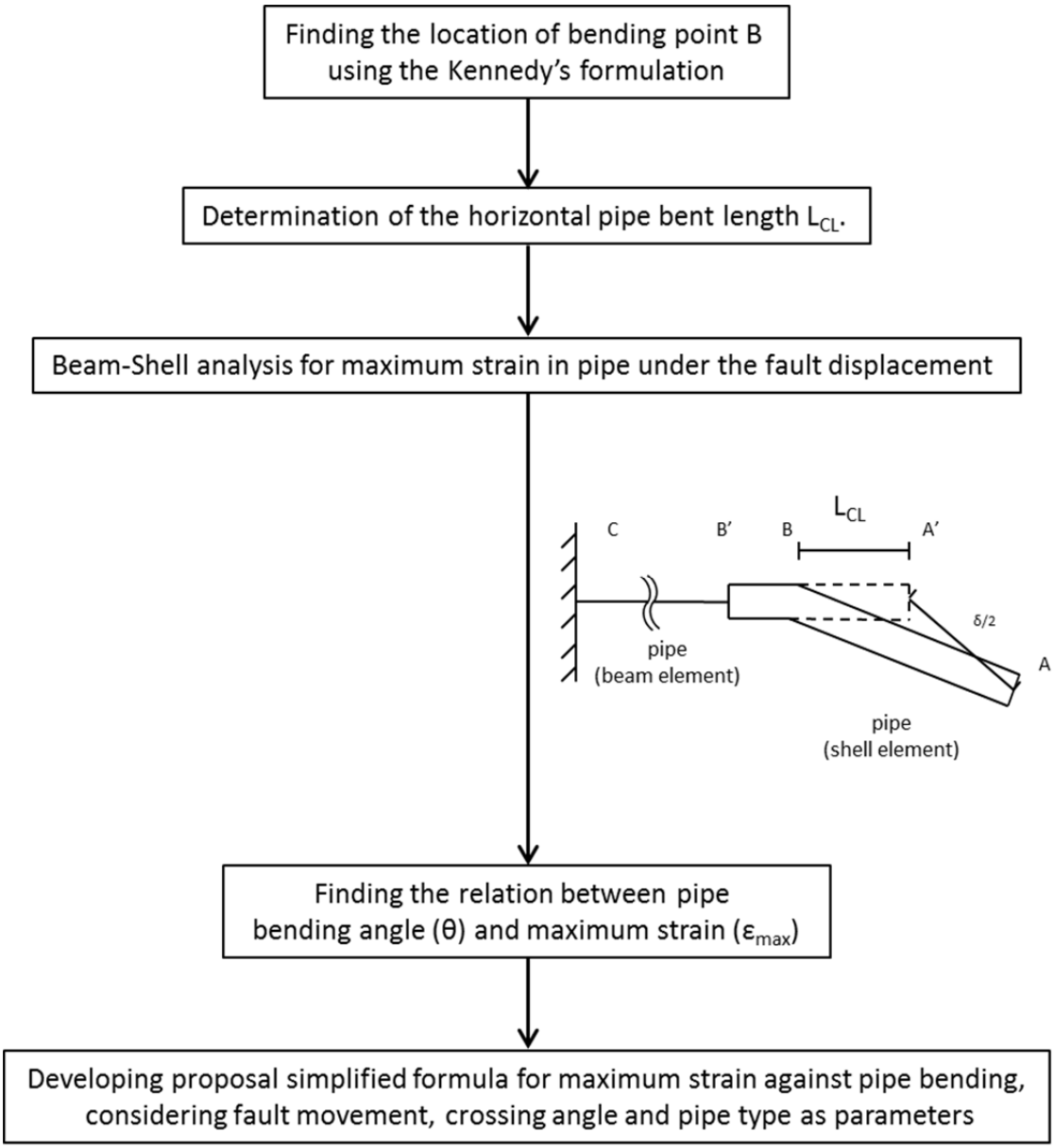

Figure 1.4.6. Flow of the simplified method proposed by Takada et al (2001).

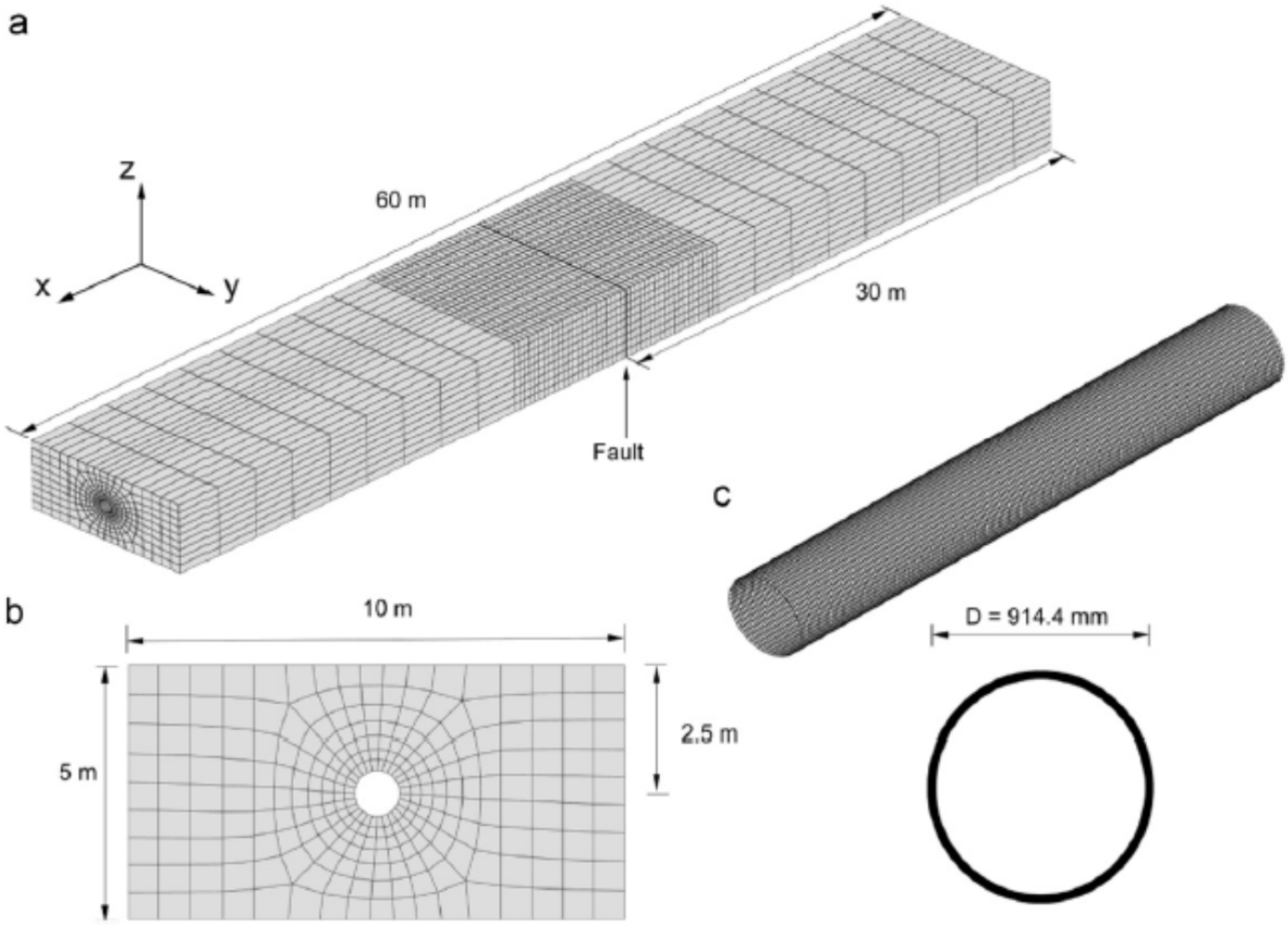

Figure 1.4.7. The FE model used by Vazouras et al.(2011): (a) soil formation with horizontal tectonic fault, (b) cross-section and (c) steel pipeline.

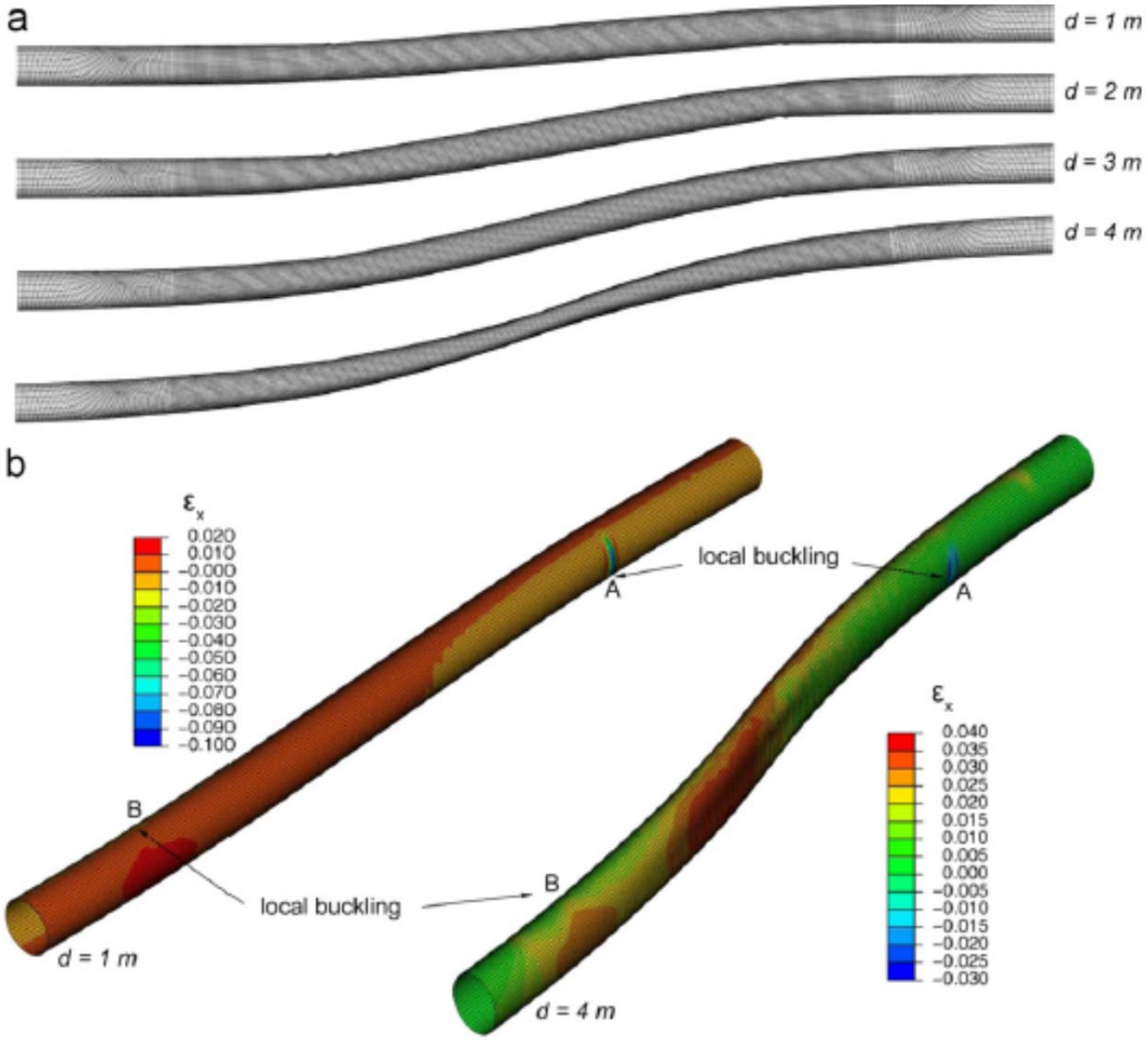

Figure 1.4.8. Results from Vazouras et al. model (2011). (a) Plan view of deformed shape of a pipeline for fault offset d=1-4m and (b) distribution of longitudinal normal strain for seismic fault displacement equal to 1 and 4m (X65pipe, D/t=72).

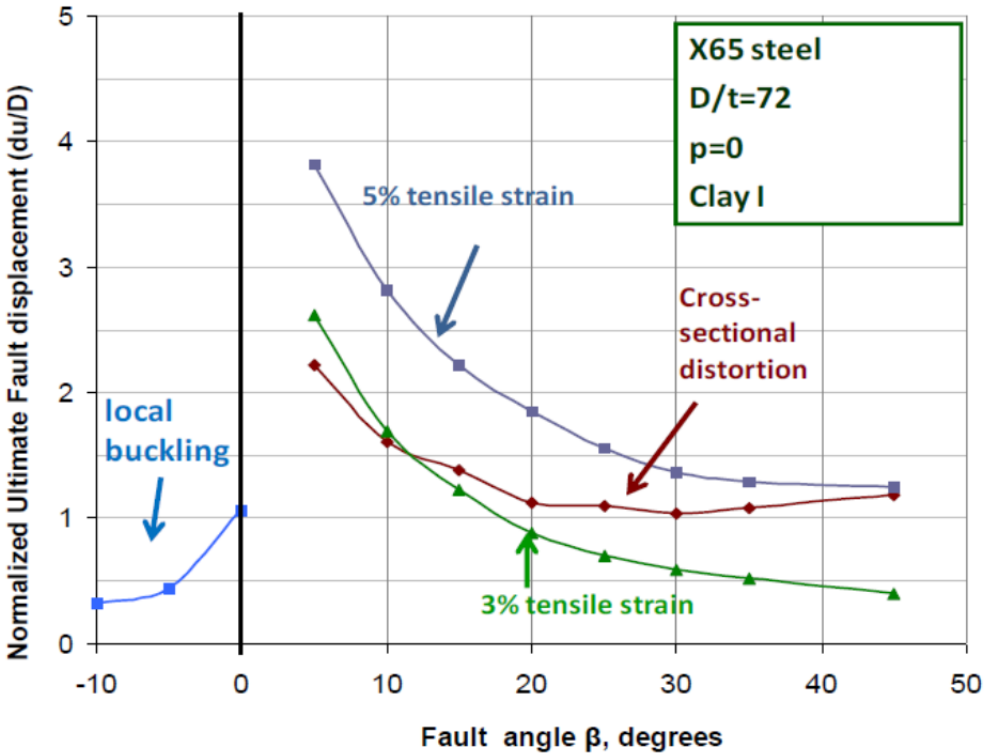

Figure 1.4.9. Normalized ultimate fault displacement for various performance limits at different angles of β (X65 pipe, Clay, D/t=72, zero pressure), Vazouras et al.

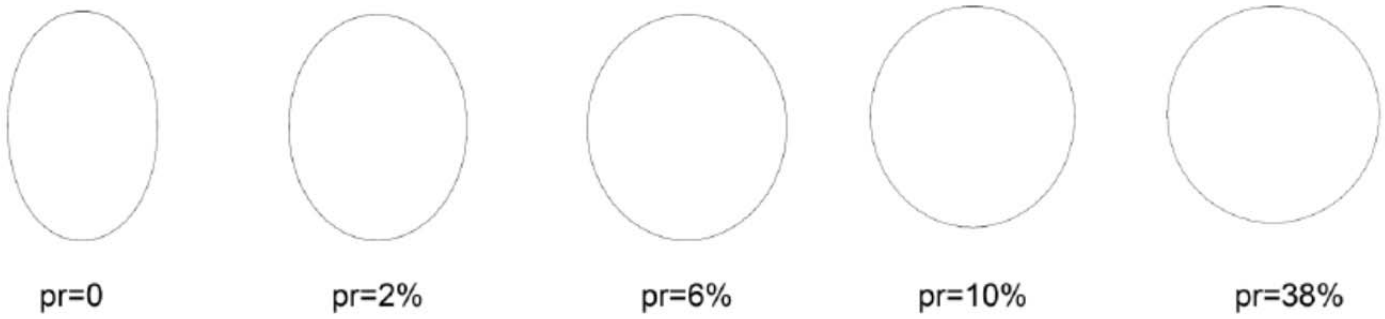

Figure 1.4.10. Effect of internal pressure on the evolution of cross-sectional deformation in pressurized pipelines for the same fault displacement d=1m (X65,Clay,D/t=96,β=35^{o}), Vazouras et al (2011).

Table 1.2. The Cornell and RPI test parameters.

Parameter[1]	Cornell NEES Site	RPI NEES Site
Diameter, D	100-600 mm	200-5000 mm
Diameter to Thickness Ratio, D/t	10-120	10-250
Depth of Burial	0.6-1.5 m	0.6-20 m
Maximum Length of Pipeline[2]	15 m	46 m
Pipeline Intersection Angle for Horizontal Deformation, α	+30° to 90° 90° to -30°	62° to 90° 90° to -62°
Normal Deformation Angle, β_N	30° to -90°	90°
Thrust Deformation Angle, β_T	$\leq 30°$	NA
Maximum Displacement	1.8 m	4.0 m
Maximum Rate of Displacement	0.1 m/s	0.9 m/s

1 refers to prototype or actual field scale
2 refers to actual test box dimensions; the effective pipeline length can be increased experimentally through the use of actuators in the Cornell facility and special springs in the Rensselaer split box

Table 1.3. The whole of the full scale, centrifuge and numerical NEES tests.

	Horizontal Deform. Angle, α					Vertical Deform. Angle, β					Oblique Deformation				
						Normal, β_N			Thrust, β_T		α/β_N			α/β_T	
Lifeline	30°	65°	90°	-30°	-65°	30°	60°	90°	30°	60°	65°/90°	90°/90°	-65°/90°	65°/30°	-65°/30°
Welded Steel D=150-400 mm D/t = 20-50	N	R N	R N	N	C R N	N	N	C R N	N	N	R N	C R N	R N	N	N
Welded Steel D=400-1500 mm D/t = 50-120	N	R N	R N	N	R N	N	N	R N	C N	N	R N	R N	R N	C N	N
Polyethylene D=150-400 mm D/t=10-20	N	R N	R N	N	C R N	N	N	R N	N	N	R N	R N	R N	N	N
Polyethylene D=400-1500mm D/t= 20-50	N	R N	R N	N	R N	N	N	R N	C N	N	R N	R N	R N	C N	N

* C - Full scale tests at the Cornell NEES site, R- Centrifuge tests at the RPI NEES site, N- Numerical simulation

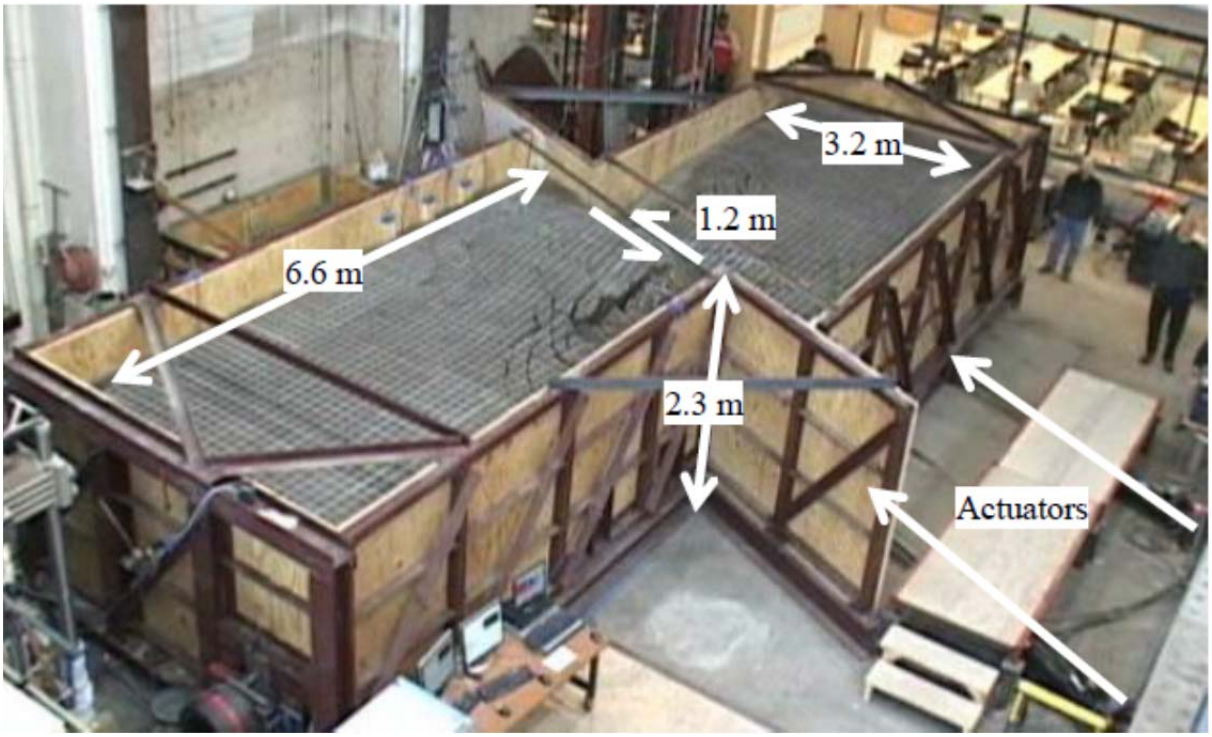

Figure 1.4.11. Cornell split-box test basin.

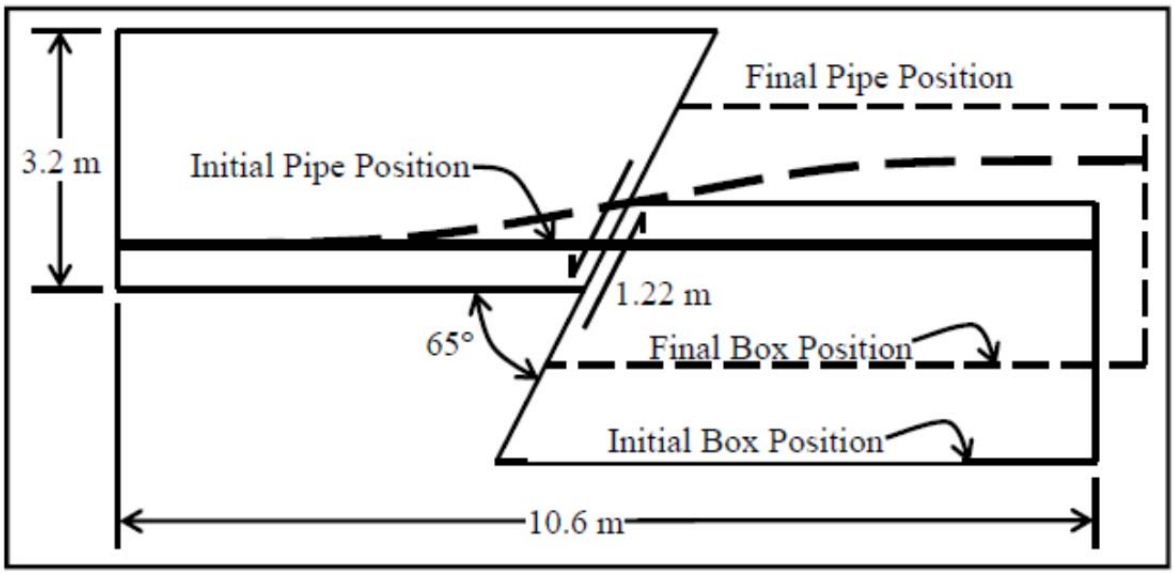

Figure 1.4.12. Plan View of Full Scale Pipeline Test.

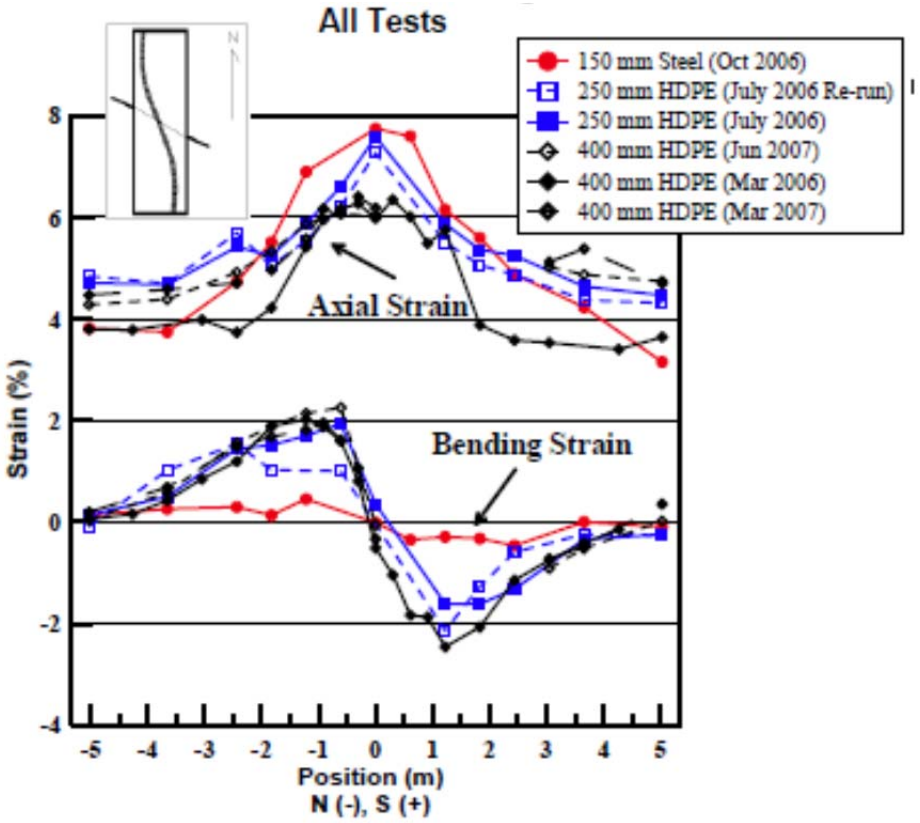

Figure 1.4.13. Measured Axial and Bending Strain for all full scale tests (NEESR Final Report 2008).

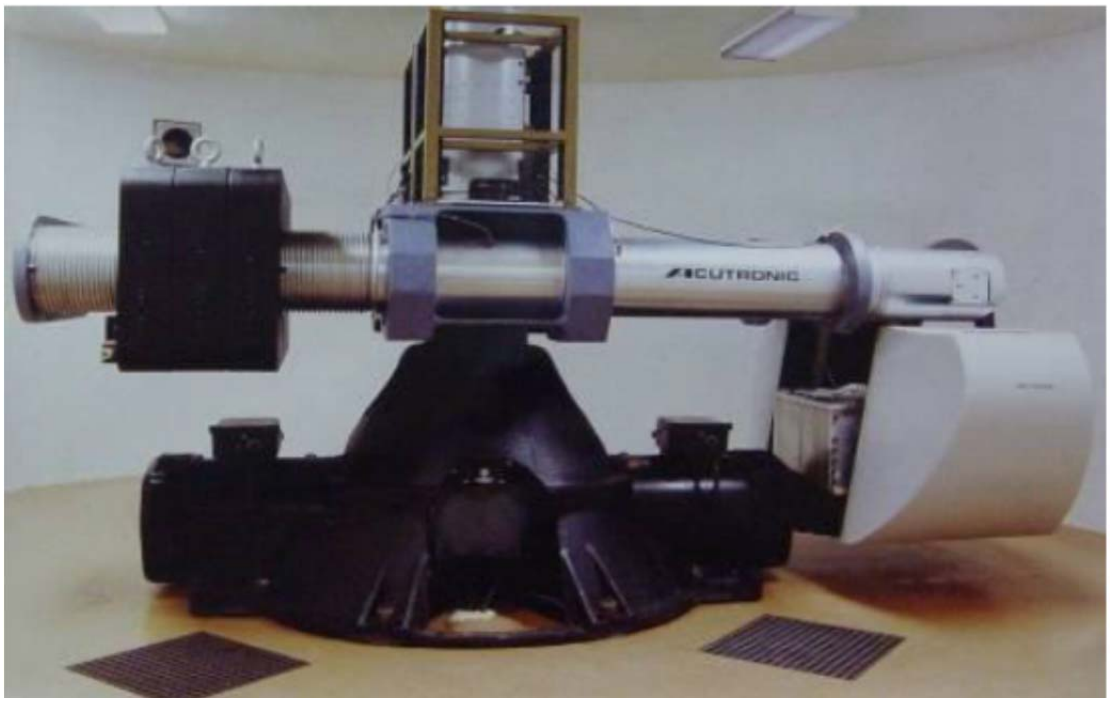

Figure 1.4.14. RPI 150g-Ton Centrifuge.

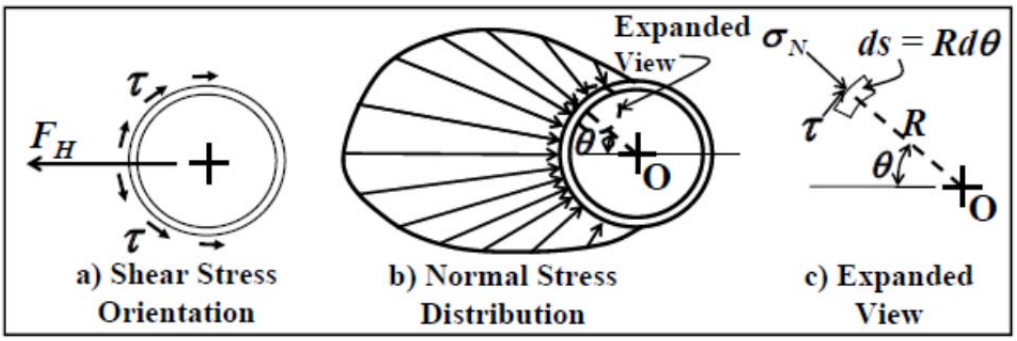

Figure 3.9. Soil-Pipe Interaction Showing Shear and Normal Stresses

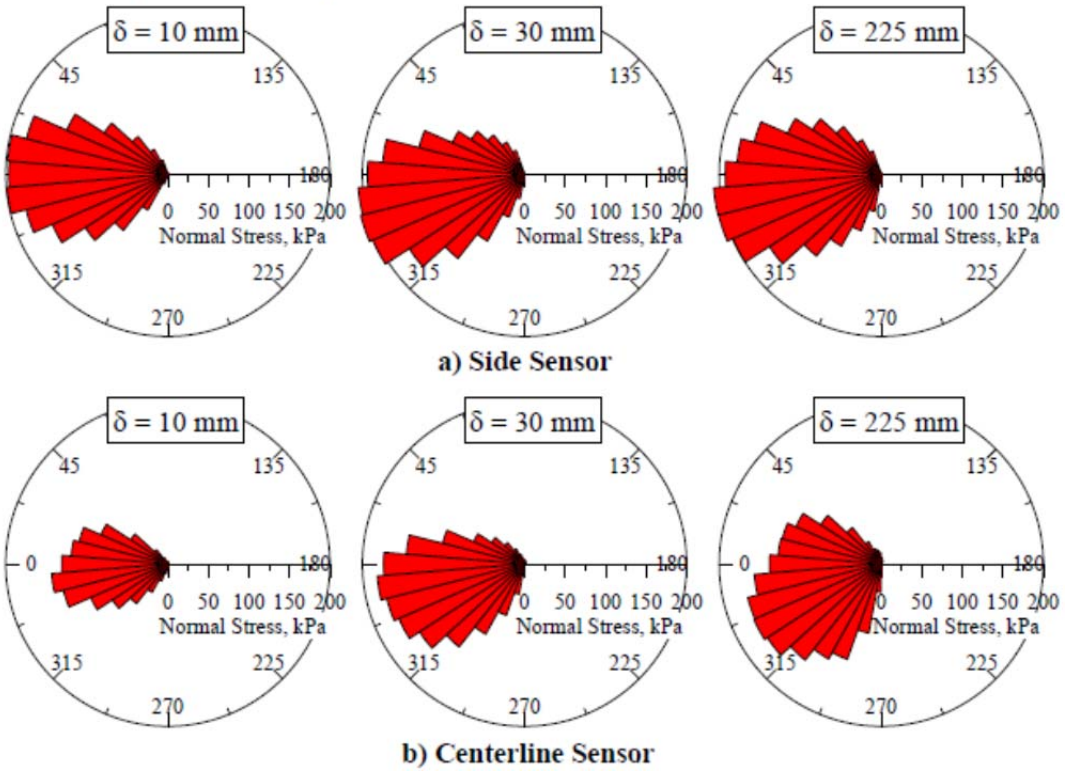

Figure 1.4.15. Distribution of normal Pressure Measured by Tactile Force Sensors (NEESR Final Report 2008).

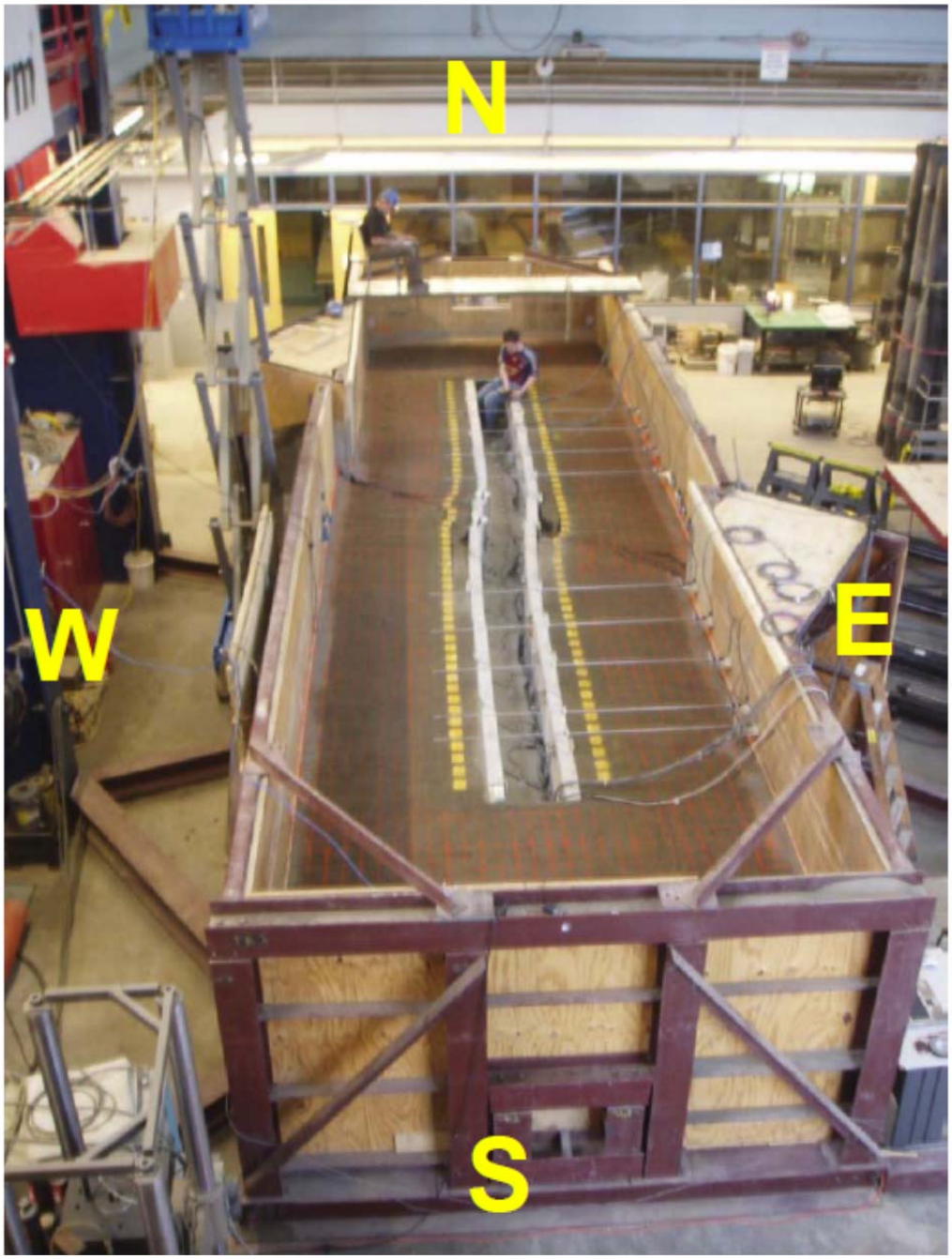

Figure 1.4.16. Test Basin at Cornell for the pipeline embedded in concrete blocks test (NEESR Final Report 2008).

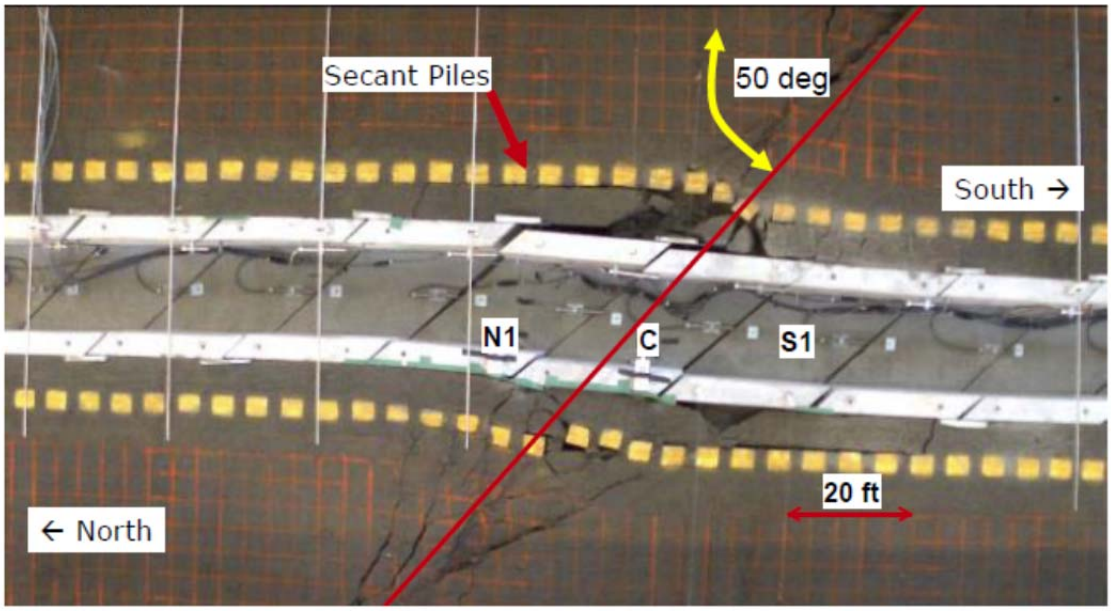

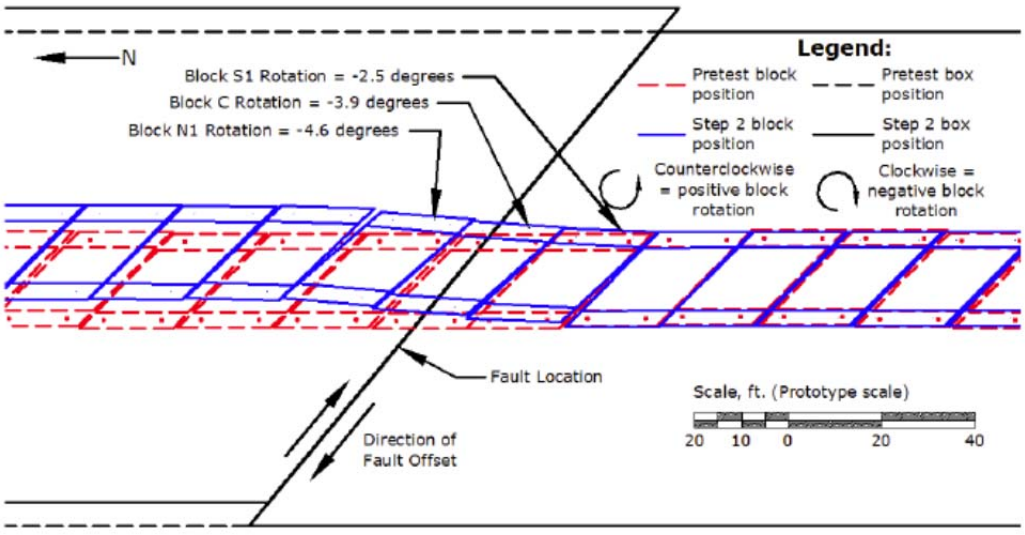

Figure 1.4.17. Photo and drawing of the basin at 2m of fault displacement

(NEESR Final Report 2008).

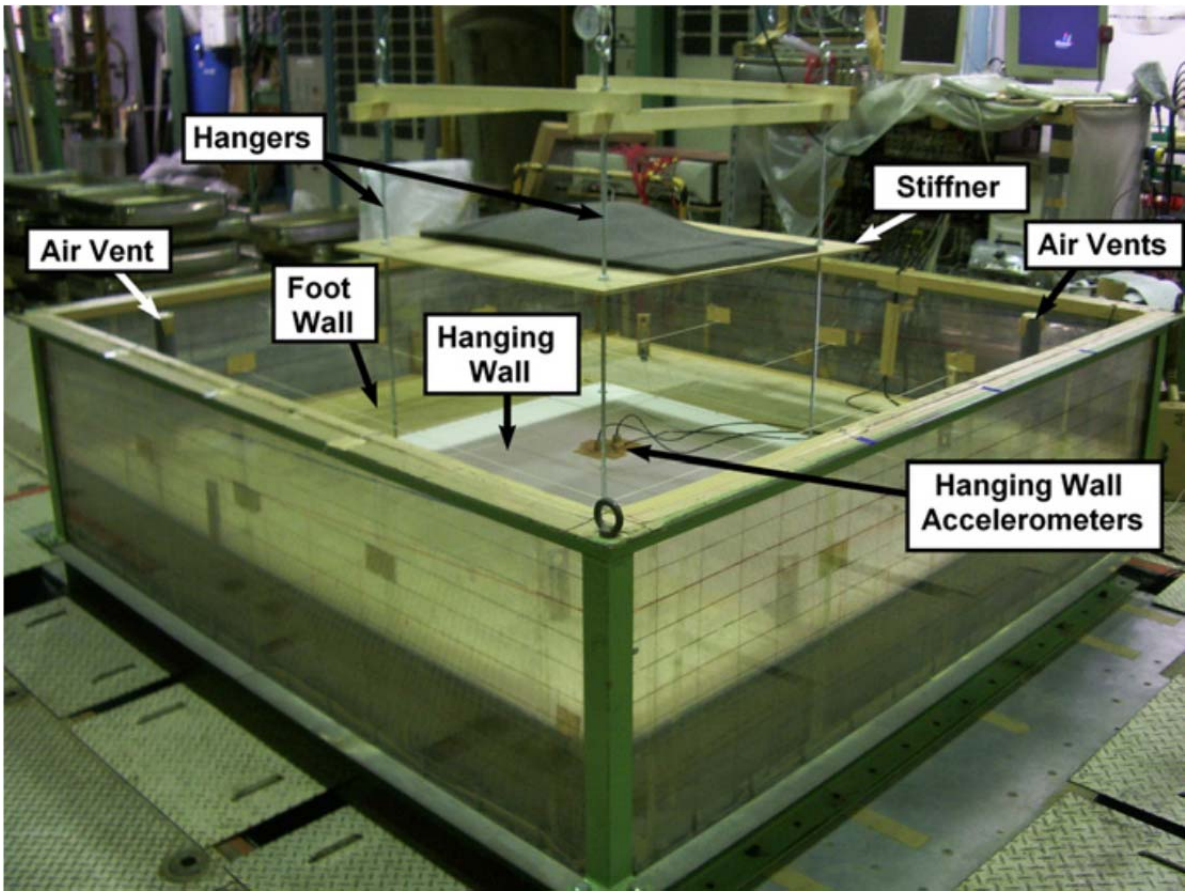

Figure 1.4.18. The shaking table of the University of Tokyo, capable of simulating at the same experiment the seismic vibration as well as the fault rupture (Sim et al. 2012).

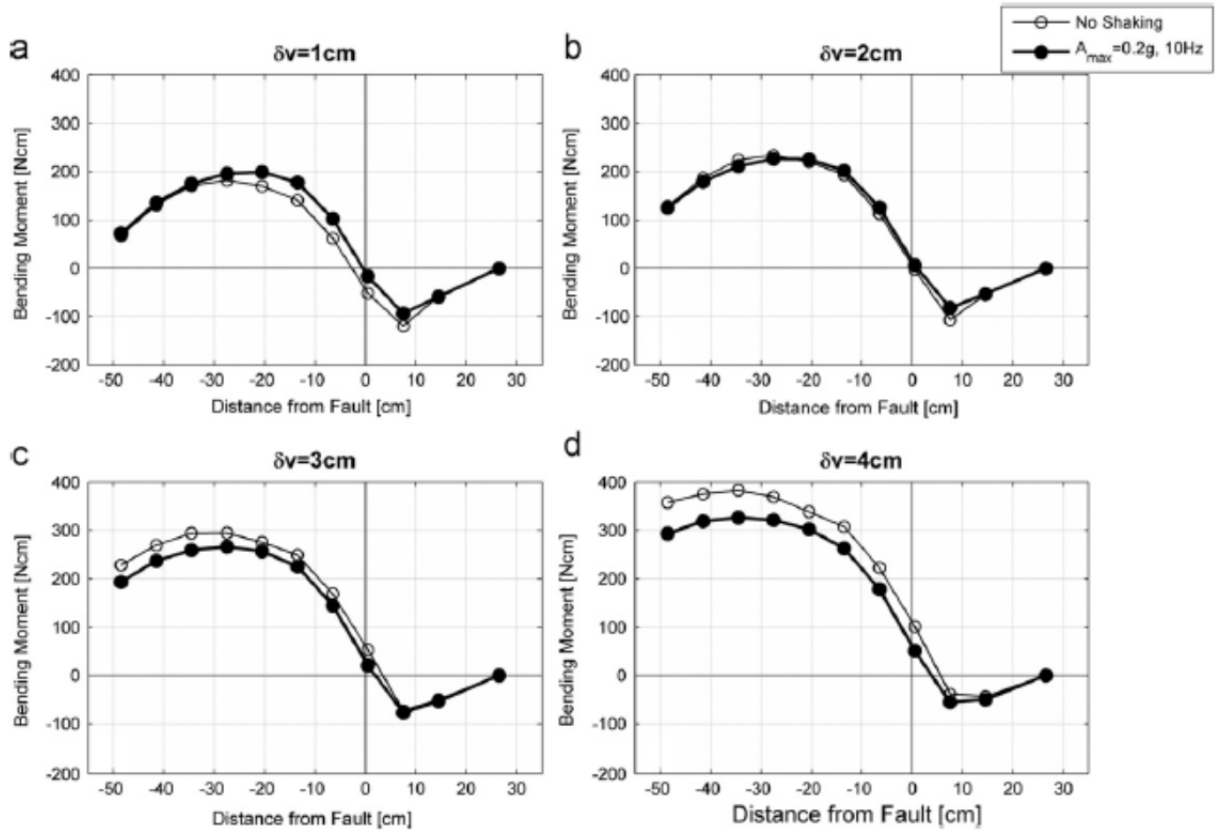

Figure 1.4.19. Bending moment distribution for a pipe crossing the fault at 90° subjected to no shaking and Amax=0.2g, 10Hz at different fault displacements (Sim et al. 2012).

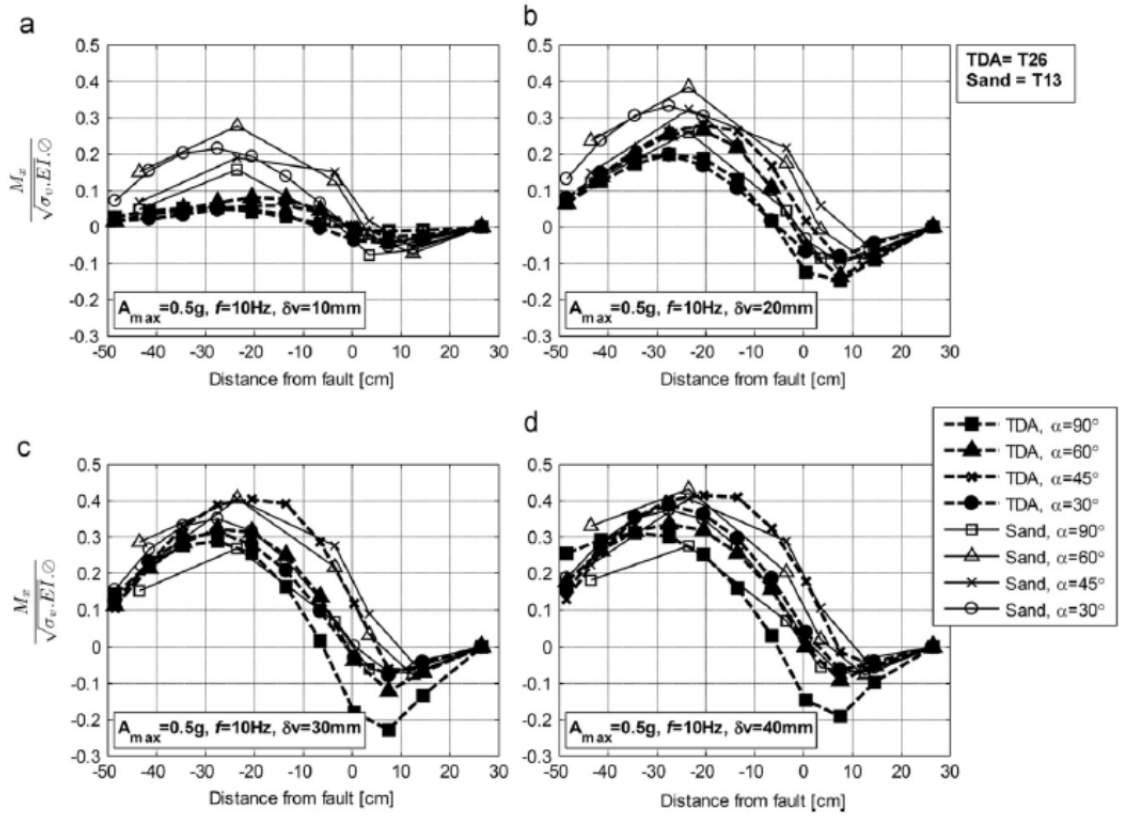

Figure 1.4.20. Comparison of pure sand and TDA trench backfills through normalized bending moment distribution with distance along the pipe axis from the verse subjected to Amax=0.5g, 10Hz at 4 different fault displacements (Sim et al. 2012).

Figure 1.5.1. Pennsylvania, USA, 1872. One of the first gas pipelines running 5 kilometers from Newton Wells to Titusville.(American Oil and Gas Historical Society, aoghs.org)

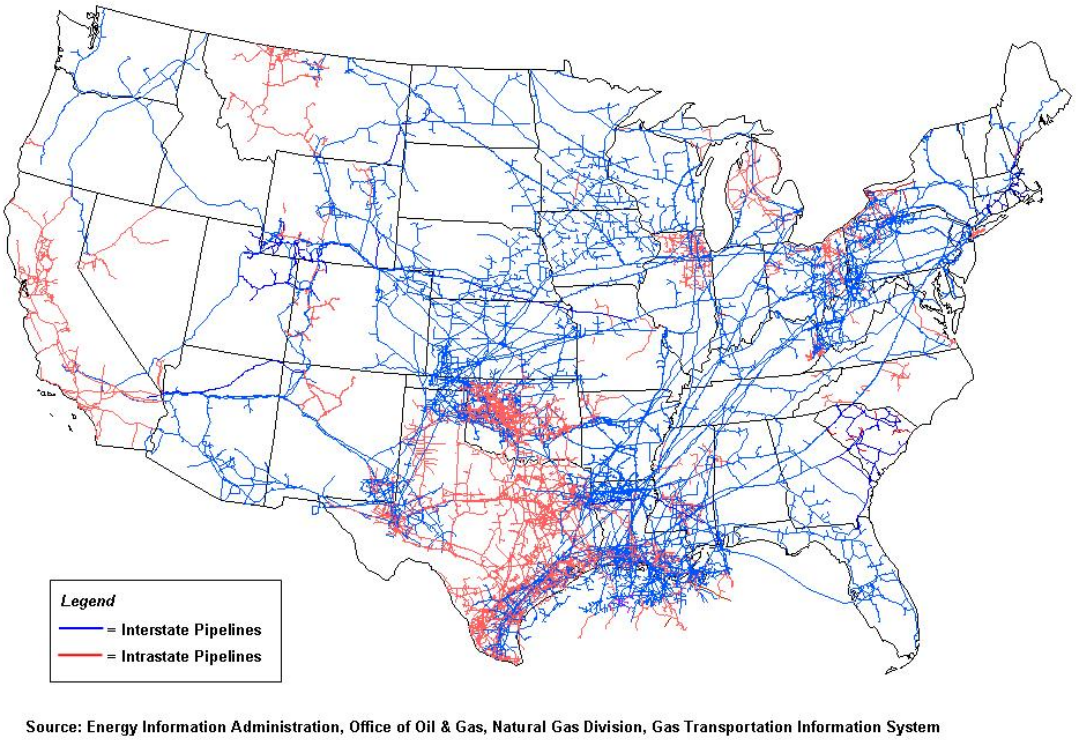

Figure 1.5.2. The gas pipeline network at the USA (API).

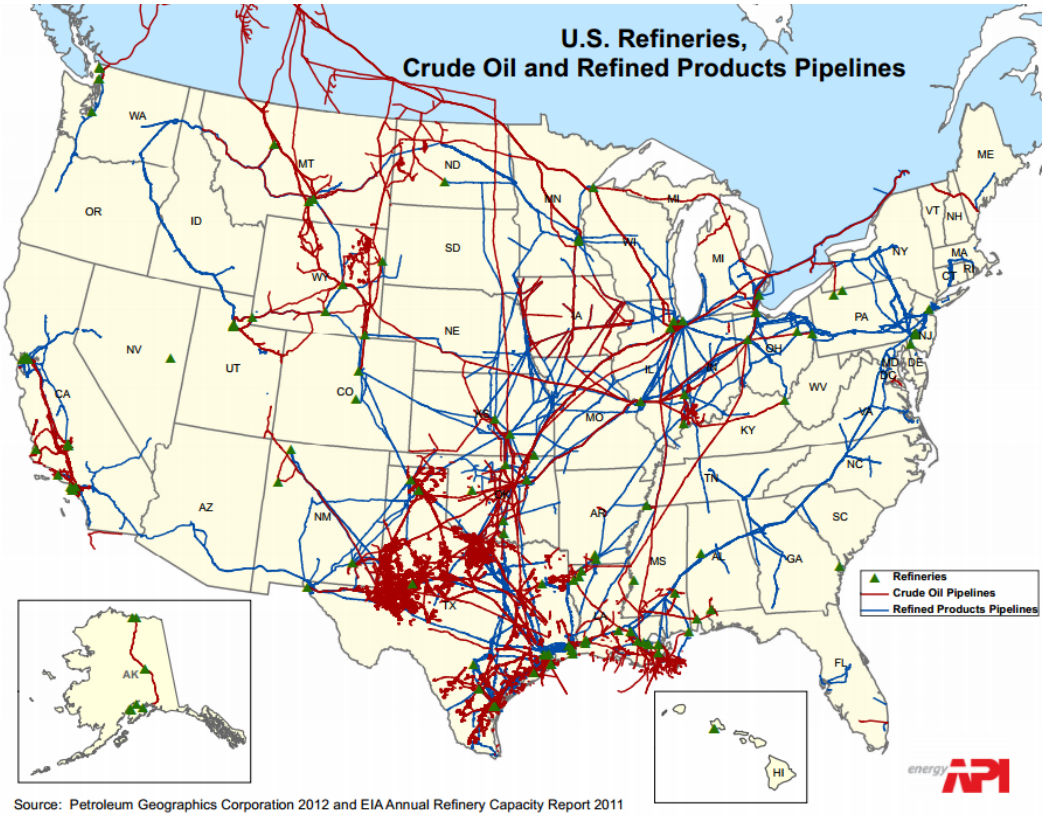

Figure 1.5.3. The oil pipeline network of USA (API).

Figure 1.5.4. Major lifelines at Central Asia (USCC.gov).

Figure 1.5.5. Pipeline network of Central and Western Europe (International Gas Union).

Figure 1.5.6. Major gas pipelines of Russia and Eastern Europe (International Gas Union).

Figure 1.5.7. Fault-induced damage of embedded pipeline during the Manjil earthquake 1990, Iran (Sim et al.2012).

Figure 1.5.8. Large deformation of steel pipe section crossing an active fault (1999 Chi-Chi earthquake, Takada et al.2001).

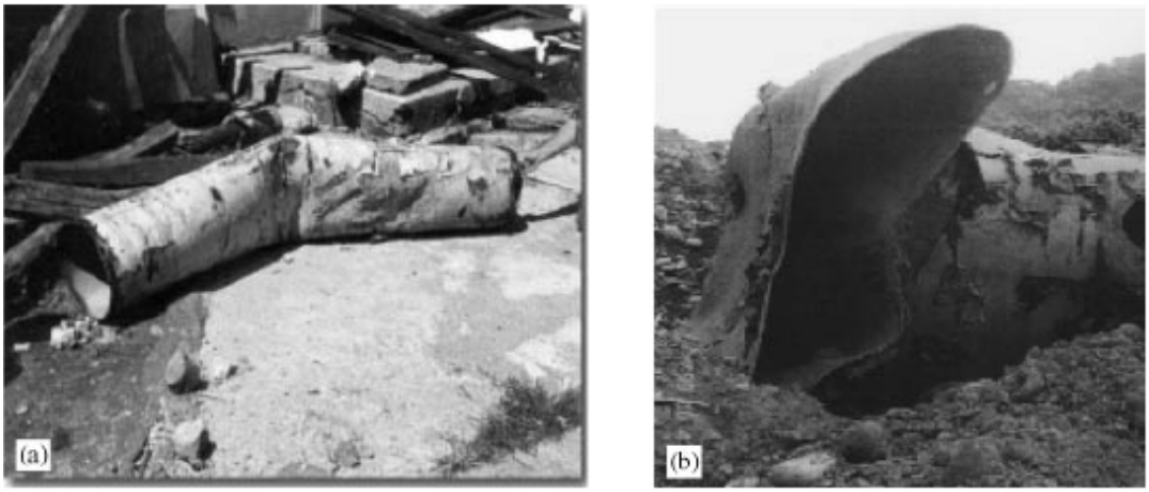

Figure 1.5.9. Failure of steel pipes crossing faults. (a) 1999 Kocaeli earthquake, Turkeu,

(b) 1999 Chi-Chi earthquake, Taiwan. (Takada et al.2001)

Figure 1.5.10. Wrinkled pipeline failed in compression (Takada et al.2001).

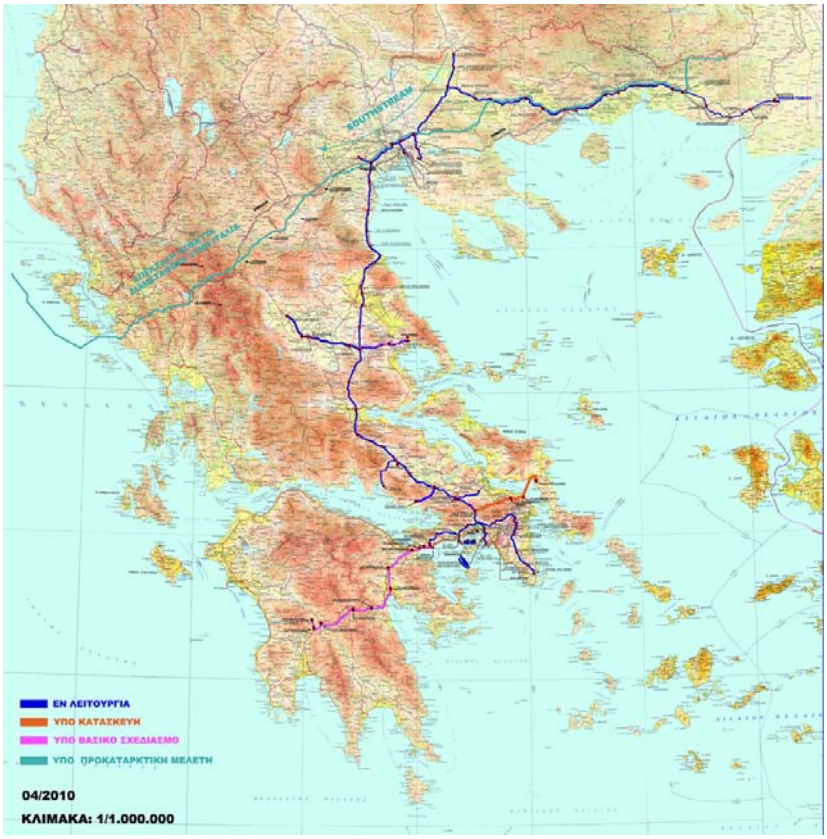

Figure 1.5.11. The main gas pipelines in Greece
(Διαχειριστής Εθνικού Συστήματος Φυσικού Αερίου Α.Ε.).

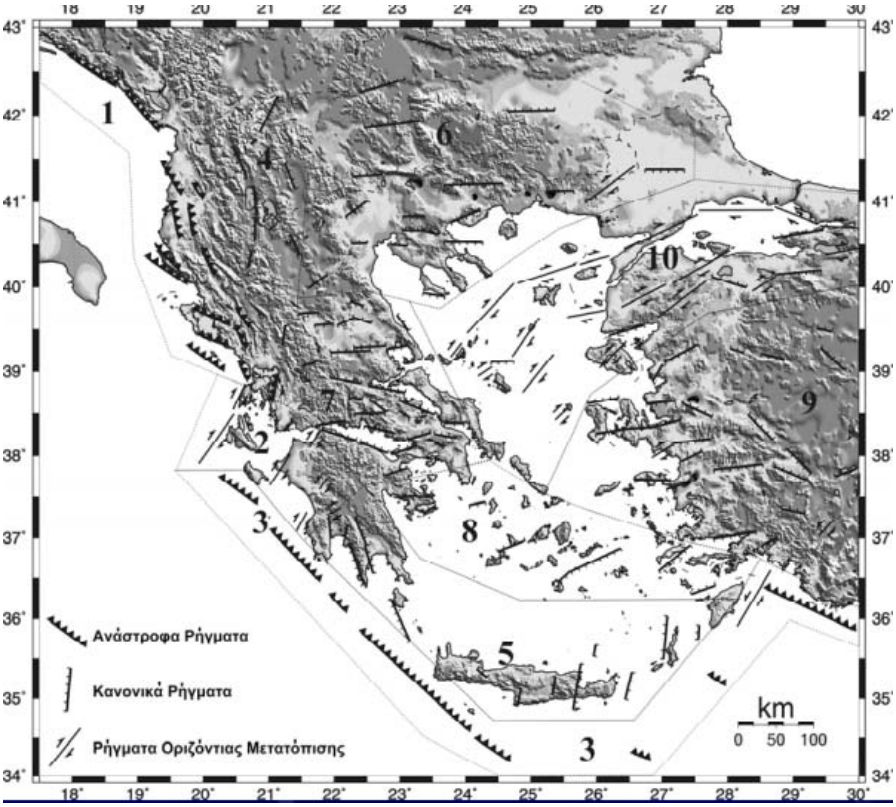

Figure 1.5.12. Major tectonic faults and location map of Greece (Papazachos,1997).

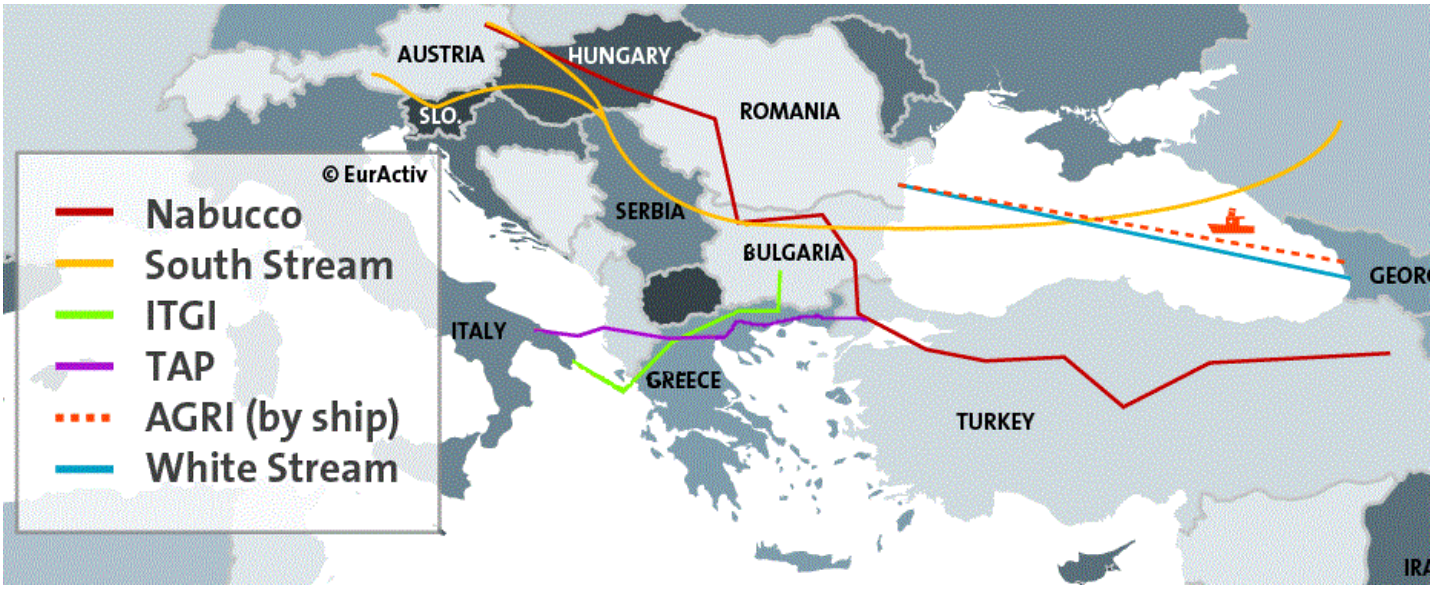

Figure 1.5.13. The "Southern gas corridor". The different proposed plans and their routes (European Commission Project,2009).

Chapter 2
Problem and model definition

2.1 Problem Definition

As already mentioned, relatively limited amount of research has been done regarding the behavior of a pipeline crossing a dip-slip type of fault. The analytical approaches extend to a certain limit, having trouble to describe the problem using formulas because of its complexity. In the strike-slip rupture the soil's passive resistance can be assumed the same along the pipeline. However, in dip-slip cases this is not realistic for the upward movement of the pipe founds less resistance than the downward movement since the soil above the pipeline is of significantly less height (thus less weight, easier to get lifted up by the pipe) and less strength compared to the 'infinite' soil layer under the pipe. Furthermore, another difficulty that occurs when we examine a pipeline subjected to dip-slip fault rupture is an extra added parameter. Unlike, strike-slip fault where there is only one angle of intersection to be examined in dip-slip faults there are two: the angle in plan between the fault and the pipeline, as well as the dip angle of the fault. In addition, analytical studies have difficulties in including the nonlinearity aspects of the problem (either geometrical or material non-linearity) as well as second order effects such as local buckling and ovalization of the pipe that are crucial modes of failure and cannot be neglected. Thus, a rigorous solution of the problem should involve an advanced numerical analysis which can account consistently for the nonlinear stress-strain response of the pipeline steel, the possible forming of gap between the pipeline and the soil, the longitudinal and transverse soil resistance as well as second order effects induced by relatively large displacements. Since such analyses are definitely possible with the available commercial computer codes, many of the researchers approached the problem using numerical methods. The great majority of them used the finite element method simulating the pipe with shell elements and the soil with soil springs. The substitution of soil with soil springs has the advantage of limiting the size of the model and as a result reducing significantly the computational effort and time needed for the analysis. However, soil-springs model, in general, does not take into account either the interaction between the soil

elements or the real propagation of the fault. This is probably the reason why several researchers preferred to use in their models continuum 'brick' elements for the soil. Similarly, the model that we used in this study is a full model that consists of the pipe and the soil represented by shell and continuum 'brick' elements respectively.

Another significant drawback of lots of studies is the boundary conditions of the model and specifically the supports of the pipe at the 2 edges of the model. It is a fact that the deformation caused by the fault rupture to the pipe, as well as the bending stress and strain that occur to the pipe, are concentrated to a relative narrow area (depending on the magnitude of the fault's offset and the pipe and soil properties). However the axial stresses that develop affect a substantially bigger part of the pipe that cannot be fully modeled for computational reasons. Thus, the problem of the boundary conditions arises, which is the subject of Chapter 3.

Investigating the problem of pipe boundaries we try different models and approaches. However, all of those models simulated a normal fault rupture. In Chapter 4 we design a reverse fault model to examine the behavior of the pipe compared to the normal fault case.

In Chapter 5 we focus on the aforementioned problem of fault's propagation. In most of the relative studies where a full model is used, despite the fact that continuum soil elements can depicture the fault's propagation, researchers could design and use a limited model that consisted of the pipe and only a small layer of soil. The limited computational power and the time limits for the completion of the study, commonly, do not allow the use of a bigger and more realistic model that would include a soil layer of 20, 40 meters or more. To overpass this problem we extract results from a 2D free-field model, where faults propagate from the bedrock to the surface through a soil layer of realistic width, and then we integrate them into the hybrid-full 3D model. This method combined the 3D accuracy with the realistic fault propagation of the fault without the high computational force and time a big 3D model would need.

In Chapter 6, we examine the effect of an elastic-plastic with hardening stress-strain relation for the pipe steel, whereas in Chapter 7, we investigate the effect of the internal pipe pressure both for elastic-perfectly plastic and for hardening steel behavior.

Finally, in Chapter 8, we gather the most significant conclusions of our study and propose additional factors and parameters that could be examined in a future research.

2.2 Model and Method of Analysis

As already stated, in order to conclude to a final model we tested several different approaches. The following paragraphs include the general properties and conditions that are common for all the models we used (unless stated otherwise).

2.2.1 Finite Element Model

Geometry of the model

The analyses for the investigation of the problem were conducted in three-dimensional space using the finite element code ABAQUS v.6.11.

The dimensions of our basic model are 60 x 10 x 5 m. The pipeline is placed at the center of our model and its diameter is 0.9144m (3feet). In all of our tests, we maintained the same angle of intersection between the fault and the pipeline investigating only the effect of the dip angle of the fault. For the model definition procedure the angle of the fault was selected equal to 60^{o}. The fault movement was integrated in the model by moving a part of the base and the corresponding side **(Figure 2.2.1)**, according to the wanted fault angle, while the rest of the base

remained immovable. Specifically, the boundary conditions of our model are depicted in **Figure 2.2.2.** Concerning the conditions at the pipe edges we tried various approaches which will be discussed in the next chapter.

Type of elements and material properties

SOIL

It is necessary to make clear that the values mentioned in this paragraph were used in order to find a proper model for the problem. More realistic values, as well as parametric analyses are issues that we examine in the next chapters.

The soil body was modeled using 8-node hexahedral continuum elements C3D8, with a corresponding constitutive model, as described in paragraph 2.2.3. The meshing of the soil body is divided in three areas: a 20m area of relatively dense discretization, in the middle of the model where we expect the fault to cross the pipeline, thus the main soil (and pipe) deformations to occur and two other areas of 20m of coarser meshing (**Figure 2.2.2**).

The soil we used was dense dry sand with the following properties.

Elastic Modulus	E	25 MPa
Poisson's Ratio	ν	0.3
Angle of Internal Friction	ϕ	40^o
Dilation Angle	ψ	10^o
Density	ρ	2.1 kg/m^3
Specific Weight	γ	20.6 kN/m^3
Neutral Earth Pressure Coefficient	Ko	0.29

For computational reasons we also implemented to our sand soil model a small cohesion parameter c=2Kpa.

2.2.2 Soil Constitutive Model

Several experimental and numerical studies have shown that post-peak soil behavior is a decisive factor in fault rupture propagation and its possible emergence on the ground surface. Scott and Schoustra (1974) utilizing the FE method and an elastic–perfectly plastic constitutive soil model with Mohr–Coulomb failure criterion, produced results contradicting both reality and experiments. Walters and Thomas (1982) employed a more elaborate nonlinear incremental constitutive model with Drucker–Prager failure criterion, non-associated flow rule, and strain softening to simulate reverse fault rupture propagation through cohesionless soil. Comparing their analysis results with benchmark small-scale tests, they proved that laborator reality could only be reproduced with a non-associated flow rule and strain softening. Bray (1990) and Bray et al. (1994), utilizing a FE code with a hyperbolic nonlinear elastic constitutive law, also achieved satisfactory agreement with experiments. Also successful were the analyses performed by Roth et al. (1982), White et al. (1994), Nakai et al. (1995), Loukidis (1999), and Erickson et al. (2001), all of which made use of the finite-difference (FD) method with an elastoplastic constitutive model, Mohr–Coulomb failure criterion, and strain softening. Similar constitutive models have been employed successfully to model the failure of embankment dams and the delayed collapse of cut slopes in stiff clay (Potts et al. 1997). Following a thorough review of the literature (Anastasopoulos 2005, Anastasopoulos et al. 2007) we adopted a similar elastoplastic Mohr–Coulomb constitutive model with isotropic strain softening.

Elastic behavior

The elasticity form that we implemented in our model is linear isotropic elasticity where the stress-strain relationship is given by:

$$\begin{Bmatrix} \varepsilon_{11} \\ \varepsilon_{22} \\ \varepsilon_{33} \\ \gamma_{12} \\ \gamma_{13} \\ \gamma_{23} \end{Bmatrix} = \begin{bmatrix} 1/E & -\nu/E & -\nu/E & 0 & 0 & 0 \\ -\nu/E & 1/E & -\nu/E & 0 & 0 & 0 \\ -\nu/E & -\nu/E & 1/E & 0 & 0 & 0 \\ 0 & 0 & 0 & 1/G & 0 & 0 \\ 0 & 0 & 0 & 0 & 1/G & 0 \\ 0 & 0 & 0 & 0 & 0 & 1/G \end{bmatrix} \begin{Bmatrix} \sigma_{11} \\ \sigma_{22} \\ \sigma_{33} \\ \sigma_{12} \\ \sigma_{13} \\ \sigma_{23} \end{Bmatrix}.$$

The elastic properties are completely defined by giving the Young's modulus, *E*, and the Poisson's ratio, ν. (The shear modulus, *G*, can be expressed in terms of *E* and ν as

$$G = E/2(1+\nu).$$

Plastic behavior: yield criteria

Mohr-Coulomb

The Mohr-Coulomb criterion assumes that yield occurs when the shear stress on any point in a material reaches a value that depends linearly on the normal stress in the same plane. The Mohr-Coulomb model is based on plotting Mohr's circle for states of stress at yield in the plane of the maximum and minimum principal stresses. The yield line is the best straight line that touches these Mohr's circles.

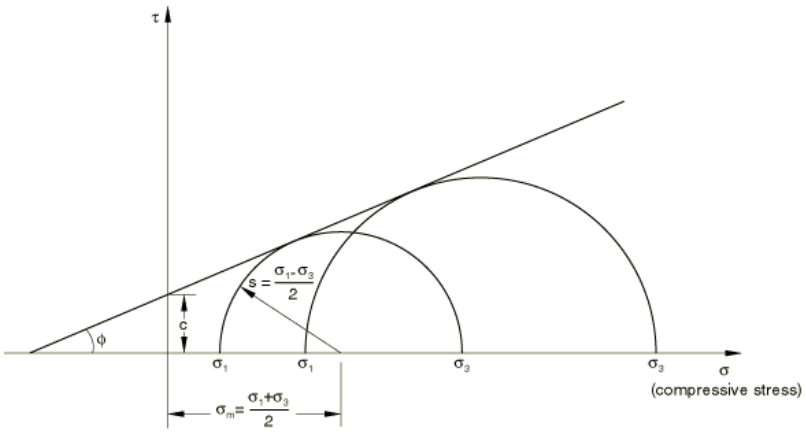

Therefore, the Mohr-Coulomb model is defined by

$$\tau = \sigma \tan\phi + c$$

where σ is negative in compression. From Mohr's circle,

$$\tau = s\cos\phi$$
$$\sigma = \sigma_m + s\sin\phi$$

Substituting for τ and σ, multiplying both sides by cosϕ, and reducing, the Mohr-Coulomb model can be written as

$$s + \sigma_m \sin\phi - c\cos\phi = 0$$

where

$$s = \frac{1}{2}(\sigma_1 - \sigma_3)$$

is half of the difference between the maximum principal stress, σ_1, and the minimum principal stress, σ_3 (and is, therefore, the maximum shear stress),

$$\sigma_m = \frac{1}{2}(\sigma_1 + \sigma_3)$$

is the average of the maximum and minimum principal stresses, and ϕ is the friction angle.

The Mohr–Coulomb criterion in three dimensions is often expressed as

$$\begin{cases} \pm\dfrac{\sigma_1-\sigma_2}{2} = \left[\dfrac{\sigma_1+\sigma_2}{2}\right]\sin(\phi)+c\cos(\phi) \\ \pm\dfrac{\sigma_2-\sigma_3}{2} = \left[\dfrac{\sigma_2+\sigma_3}{2}\right]\sin(\phi)+c\cos(\phi) \\ \pm\dfrac{\sigma_3-\sigma_1}{2} = \left[\dfrac{\sigma_3+\sigma_1}{2}\right]\sin(\phi)+c\cos(\phi) \end{cases}$$

For general states of stress the model is more conveniently written in terms of three stress invariants as

$$F = R_{mc}q - p\tan\phi - c = 0$$

where

$$R_{mc}(\Theta,\phi) = \frac{1}{\sqrt{\varepsilon}\cos\phi}\sin\left(\Theta+\frac{\pi}{3}\right)+\frac{1}{3}\cos\left(\Theta+\frac{\pi}{3}\right)\tan\phi$$

ϕ is the slope of the Mohr-Coulomb yield surface in the p–$R_{mc}q$ stress plane ,the friction angle of the material

C is the cohesion of the material; and

Θ is the deviatoric polar angle defined as

$$\cos(3\Theta) = \left(\frac{r}{q}\right)^3$$

$p = -\dfrac{1}{3}trace(\sigma)$ is the equivalent pressure stress,

$q = \sqrt{\frac{3}{2}(S:S)}$ is the Mises equivalent stress,

$r = \left(\frac{9}{2} S \cdot S : S\right)^{\frac{1}{3}}$ is the third invariant of deviatoric stress, and

$S = \sigma + pI$

is the deviatoric stress.

The friction angle, ϕ, controls the shape of the yield surface in the deviatoric plane as shown in **Figure 2.2.4**. The tension cutoff surface is shown for a meridional angle of Θ=0. The friction angle range is $0 \le \phi \le 90$. In the case of ϕ=0 the Mohr-Coulomb model reduces to the pressure-independent Tresca model with a perfectly hexagonal deviatoric section. In the case of ϕ=90° the Mohr-Coulomb model reduces to the "tension cutoff" Rankine model with a triangular deviatoric section and

$R_{mc} = \infty$ (this limiting case is not permitted within the Mohr-Coulomb model described here).

Isotropic cohesion hardening is assumed for the hardening behavior of the Mohr-Coulomb yield surface. The hardening curve describes the cohesion yield stress as a function of plastic strain.

Plastic flow on the Mohr-Coulomb yield surface

The flow potential, *G*, for the Mohr-Coulomb yield surface is chosen as a hyperbolic function in the meridional stress plane and the smooth elliptic function proposed by Menétrey and Willam (1995) in the deviatoric stress plane:

$$G = \sqrt{\left(\varepsilon c\,|_0 \tan\psi\right)^2 + \left(R_{mw} q\right)^2} - p\tan\psi$$

where

$$R_{mw}(\Theta, e) = \frac{4\left(1-e^2\right)\cos^2\Theta + \left(2e-1\right)^2}{2\left(1-e^2\right)\cos\Theta + \left(2e-1\right)\sqrt{4\left(1-e^2\right)\cos^2\Theta + 5e^2 - 4e}} R_{mc}\left(\frac{\pi}{3}, \phi\right)$$

and

$$R_{mc}\left(\frac{\pi}{3}, \phi\right) = \frac{3 - \sin\phi}{6\cos\phi}$$

ψ is the dilation angle measured in the *p*–R_{mw}q plane at high confining pressure and can depend on temperature and predefined field variables.

$c|_0$ is the initial cohesion yield stress.

Θ is the deviatoric polar angle defined previously.

ε is a parameter, referred to as the meridional eccentricity, that defines the rate at which the hyperbolic function approaches the asymptote (the flow potential tends to a straight line in the meridional stress plane as the meridional eccentricity tends to zero); and

e is a parameter, referred to as the deviatoric eccentricity, that describes the "out-of-roundedness" of the deviatoric section in terms of the ratio between the shear stress along the extension meridian ($\Theta = 0$) and the shear stress along the compression meridian ($\Theta = \frac{\pi}{3}$).

A default value of 0.1 is provided for the meridional eccentricity, ε.

By default, the deviatoric eccentricity, *e*, is calculated as

$$e = \frac{3 - \sin\phi}{3 + \sin\phi}$$

where ϕ is the Mohr-Coulomb friction angle; this calculation corresponds to matching the flow potential to the yield surface in both triaxial tension and compression in the deviatoric plane. This flow potential, which is continuous and smooth, ensures that the flow direction is always uniquely defined. In our models we used non-associated flow rule. A family of hyperbolic potentials in the meridional stress plane and the flow potential in the deviatoric stress plane are shown in **Figure 2.2.5.**

Strain Softening

As depicted by the following equations, strain softening is introduced by reducing the mobilized friction angle φ_{mob} and the mobilized dilation angle ψ_{mob} with the increase of octahedral plastic shear strain where φ_p and φ_{res}=ultimate mobilized friction angle and its residual (or critical state) value; ψ_p=ultimate dilation angle; and γ_f^p =plastic octahedral shear strain at which softening has been completed. The model is incorporated in the finite-element code ABAQUS 2011 through a user subroutine.

$$\varphi_{mob} = \begin{cases} \varphi_p - \dfrac{\varphi_p - \varphi_{res}}{\gamma_f^p}\gamma_{oct}^p & \text{for } 0 \le \gamma_{oct}^p < \gamma_f^p \\ \varphi_{res} & \text{for } \gamma_{oct}^p \ge \gamma_f^p \end{cases}$$

$$\psi_{mob} = \begin{cases} \psi_p \left(1 - \dfrac{\gamma_{oct}^p}{\gamma_f^p} \right) & \text{for } 0 \le \gamma_{oct}^p < \gamma_f^p \\ \psi_{res} & \text{for } \gamma_{oct}^p \ge \gamma_f^p \end{cases}$$

Figure 2.2.6 shows a typical variation of the stress ratio, τ/σ_v, and volume change (expressed through vertical displacement δ_y of the top platen) with respect to the imposed horizontal displacement δ_x in a direct shear test of dense Toyoura sand [based on data of Shibuya et al. (1997)]. Soil response can be divided in four characteristic phases**.**

1. *Quasielastic behavior* (OA): Up to Point A the soil deforms quasielastically (Jewell and Roth 1987). Some nonlinearity is clearly observed, but without any dilation. δx_y is defined as the horizontal displacement for which $-\delta y / \delta x > 0$.

2. *Plastic behavior* (AB): From Point A to B the soil "yields", enters the plastic region, and dilates. Peak conditions are reached at Point B. δx_p=horizontal displacement for which τ/σ_v=max.

3. *Softening behavior* (BC): From Point B to C the soil experiences softening. Right after the peak, a single horizontal shear band develops at mid height of the specimen (Jewell and Roth 1987; Gerolymos et al. 2007). Softening is completed at Point C, and δx_f=horizontal displacement for which $-\delta y / \delta x \approx 0$.

4. *Residual behavior* (CD): Shearing is accumulated along the developed shear band.

2.2.3 Pipeline properties

The pipeline was modeled using shell elements S4R, a robust, general-purpose quadrilateral element that is suitable for a wide range of applications (**Figure 2.2.7**). These elements provide accurate solutions in all loading conditions for thin and thick shell problems. Thickness change as a function of in-plane deformation is allowed in their formulation. They do not suffer from transverse shear locking, nor do they have any unconstrained hourglass modes. These elements consider finite membrane strains. In geometrically nonlinear analyses in Abaqus/Standard the cross-section thickness of finite-strain shell elements changes as a function of the membrane strain based on a user-defined "effective section Poisson's ratio," ν.The thickness change based on the "effective section Poisson's ratio" is calculated as follows.

In plane stress $\sigma_{33} = 0$; linear elasticity gives

$$\varepsilon_{33} = -\frac{\nu}{1-\nu}(\varepsilon_{11} + \varepsilon_{22})$$

Treating these as logarithmic strains,

$$\ln\left(\frac{t}{t_0}\right) = -\frac{\nu}{1-\nu}\left(\ln\left(\frac{l_1}{l_1^0}\right) + \ln\left(\frac{l_2}{l_2^0}\right)\right) = -\frac{\nu}{1-\nu}\ln\left(\frac{A}{A_0}\right)$$

where *A* is the area on the shell's reference surface. This nonlinear analogy with linear elasticity leads to the thickness change relationship:

$$\frac{t}{t_0} = \left(\frac{A}{A_0}\right)^{-\frac{\nu}{1-\nu}}$$

For ν = 0.5 the material is incompressible; for ν = 0 the section thickness does not change**.**

Like before, the middle part of the pipeline has a more refined mesh with a size of shell elements 3.2cm x 9cm instead of 20cm x 9cm which is the element size for the rest of the pipe (**Figure 2.2.7**).

Although the diameter of the pipe D remained the same in all of our tests, the thickness of the pipe t ranges between 0.00635m and 0.0127m giving 4 different D/t ratios.

Diameter	0.9144 m / 36''			
Thikness	0.00635m / 0.25''	0.00762m / 0.3''	0.009525m / 0.375''	0.0127m / 0.5''
D/t	144	120	96	72

The pipe we used is an API 5L X65 steel pipe, which is widely used in the oil and gas industry.

API 5L Grade	Yield Strength min. ksi / Mpa	Tensile Strength min. ksi / Mpa	Yield to Tensile Ratio max.	Elongation min. %
X65	65 / 450	77 / 530	0.93	18

Elastic modulus	E_s	210 Gpa
Poisson's Ratio	v	0.3
Density	ρ	7.8 kg/m^3

As a first approach we assumed elastic- perfectly plastic baviour of the steel whereas in a later chapter we integrated the original hardening behavior of the material as given by the American Petroleum Institute.

The friction coefficient of the pipe-soil interface was chosen equal to 0.42.

2.2.4 Modes of pipeline failure

The main concern of the pipeline design is to ensure that there would be no loss of containment. It is also crucial to maintain the pipeline functional. In order to quantify the amount of damage a buried pipeline can endure it is necessary to adopt appropriate criteria which will pose certain limits and make clear whether the pipeline is safe and operational or not. Traditionally, the pipeline design has been based on the criteria of the "allowable stress". However, steel is a ductile material capable of sustaining significant amount of inelastic deformation. Thus, under the severe deformations caused by the fault rupture the pipeline exhibits important inelastic deformation. Considering that, it is reasonable to determine the limit states according to the strain and deformation levels rather than to stress values. Based on the paper of Vazouras et.al(2012) we categorize the performance limit states as follows **(Figure2.2.9)**:

a) tensile strain in the longitudinal direction of the pipeline that causes pipe wall rupture
b) local buckling
c) excessive distortion of the pipeline cross-section (ovalization)

A) Maximum tensile strain

Determination of tensile strain capacity of a pipeline is of primary importance for establishing an efficient strain-based pipeline design procedure. In the absence of serious defects and damage of the pipeline, the tensile capacity is controlled mainly by the strength of the girth welds, which are usually the weakest locations due to weld defects and stress/strain concentrations. Tensile strain limits are experimentally determined through appropriate tension tests on strip specimens and in wide plates. For design purposes, a simple and straightforward approach for determining tensile strain limit of girth welds in

pipeline is provided by the Canadian CSA Z662 pipeline design standard, through the following equation that considers surface-breaking defects:

$$\varepsilon_{Tu} = \delta^{(2.36-1.583\lambda-0.101\xi\eta)}(1+16.1\lambda^{-4.45})\,(-0.157 + 0.239\xi^{-0.241}\,\eta^{-0.315})$$

where:

ε_{Tu} : the ultimate tensile strain capacity in %

δ : the Crack-Tip Opening Displacement. CTOD is a measurement of the stretching across the crack tip just before rapid growth starts at the crack and is used as a standard measurement of toughness of the weld. ($0.1 \le \delta \le 1$)

λ : the yield-to-tensile strenght ratio. ($0.7 \le \lambda \le 0.95$)

ξ : the ratio of defect length over the pipe wall thickness equal to (2c/t). ($1 \le \xi \le 10$)

η : the ratio of defect height over the pipe wall thickness (α/t). ($\eta \le 0.5$)

Considering a slightly defected pipe with δ=0.3, λ=0.85, ξ=1 and η=0.1 the critical tensile strain is equal to ε_{Tu} = 3.5%.

This is very close to the value proposed by Eurocode 8, EN 1998-4 and by ASCE MOP 119 where the proposed tensile strain limit is 3% for steel welded pipes.

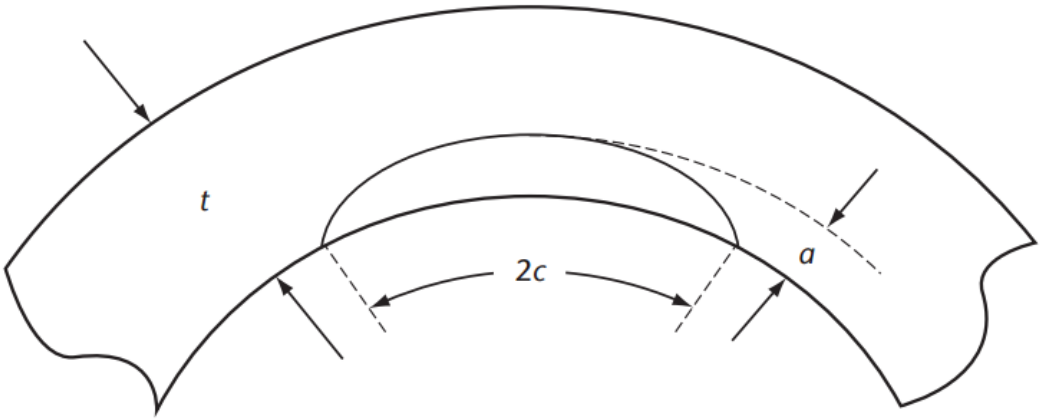

A planar surface-breaking defect in the pipe wall.

CSA Z662 pipeline design standard also provides an equation for buried defects:

$$\varepsilon_t^{crit} = \delta^{(1.08-0.612\eta-0.0735\xi+0.364\psi)}\left(12.3-4.65\sqrt{t}+0.495t\right)$$
$$(11.8-10.6\lambda)\left(-5.14+\frac{0.992}{\psi}+20.1\psi\right)\left(-3.63+11.0\sqrt{\eta}-8.44\eta\right)$$
$$\left(-0.836+0.733\eta+0.0483\xi+\frac{3.49-14.6\eta-12.9\psi}{1+\xi^{1.84}}\right)$$

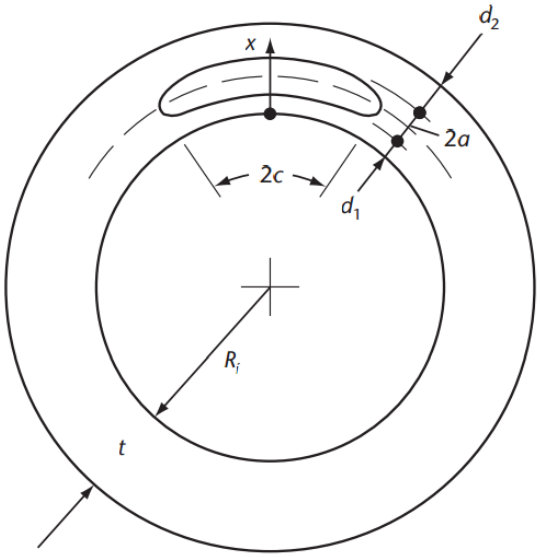

A planar buried defect in the pipe wall.

where:

δ,λ,η,ν : as previously defined

ψ : ratio of defect depth to pipe wall thickness (d/t).

Using the previous values and assuming ψ=0.1 for a 12.7mm thickness pipe one obtains ε_t^{crit}=4.5%. Although we do not take into consideration effects of temperature, strain rate, prior strain history and strain aging these equations give quite conservative values as stated in the CSA regulations. Based on the above equations and on the proposed values of the international regulations we investigate the problem using two values of critical tensile strain **3%** and **5%**.

B) Local Buckling

Under ground-induced actions, together with the development of tensile strains on the pipeline wall, compressive strains due to pipe bending deformation may also occur. When compressive strains exceed a certain limit, pipeline wall exhibits structural instability in the form of local buckling. In the presence of buckling the pipeline may still fulfill its transportation function, provided that the steel material is adequately ductile. However, the buckled area is associated with significant strain concentrations and, in the case of repeated loading (e.g. due to variations of internal pressure or temperature), fatigue cracks may develop, imposing a serious threat for the structural integrity of the pipeline. Therefore, the formation of a local buckle or wrinkle can be considered as a limit state. Extensive research on axial compression and bending of steel pipe segments has demonstrated that compressive strain limits for steel pipes depend on the diameter-to-thickness ratio (D/*t)*, the yield stress of steel material σ_y, the presence of internal or external pressure, as well as the initial imperfections and the residual stresses.(karamanos et al). The local buckling strain ε_{Cu} can be estimated using the following design equation, adopted by the CSA Z662 specification:

$$\varepsilon_{Cu} = 0.5\left(\frac{t}{D}\right) - 0.0025 + 3000\left(\frac{\sigma_h}{E}\right)^2$$

with

$$\sigma_h = \begin{cases} \dfrac{pD}{2t}, & if \dfrac{pD}{2t\sigma_y} \le 0.4 \\ 0.4\sigma_y, & if \dfrac{pD}{2t\sigma_y} > 0.4 \end{cases}$$

Where σ_h is the hoop stress and p is the internal pipe pressure.

C) Distortion of pipeline cross-section

Significant distortions of the pipeline cross-section even though may not harm the integrity of the pipe should be examined as a mode of failure since above a certain limit the pipeline is no longer functional. A simple and efficient measure of cross-section distortion is ovalization which we quantifie using the flattening parameter f and consider as a limit value f=0.15 as also adopted by the Dutch specification NEN 3650.

$$f = \frac{D_o - D'}{D_o}$$

D_o : the initial diameter of the pipe

D’ : the minimum diameter of the final distorted cross-section

Figures of Chapter 2

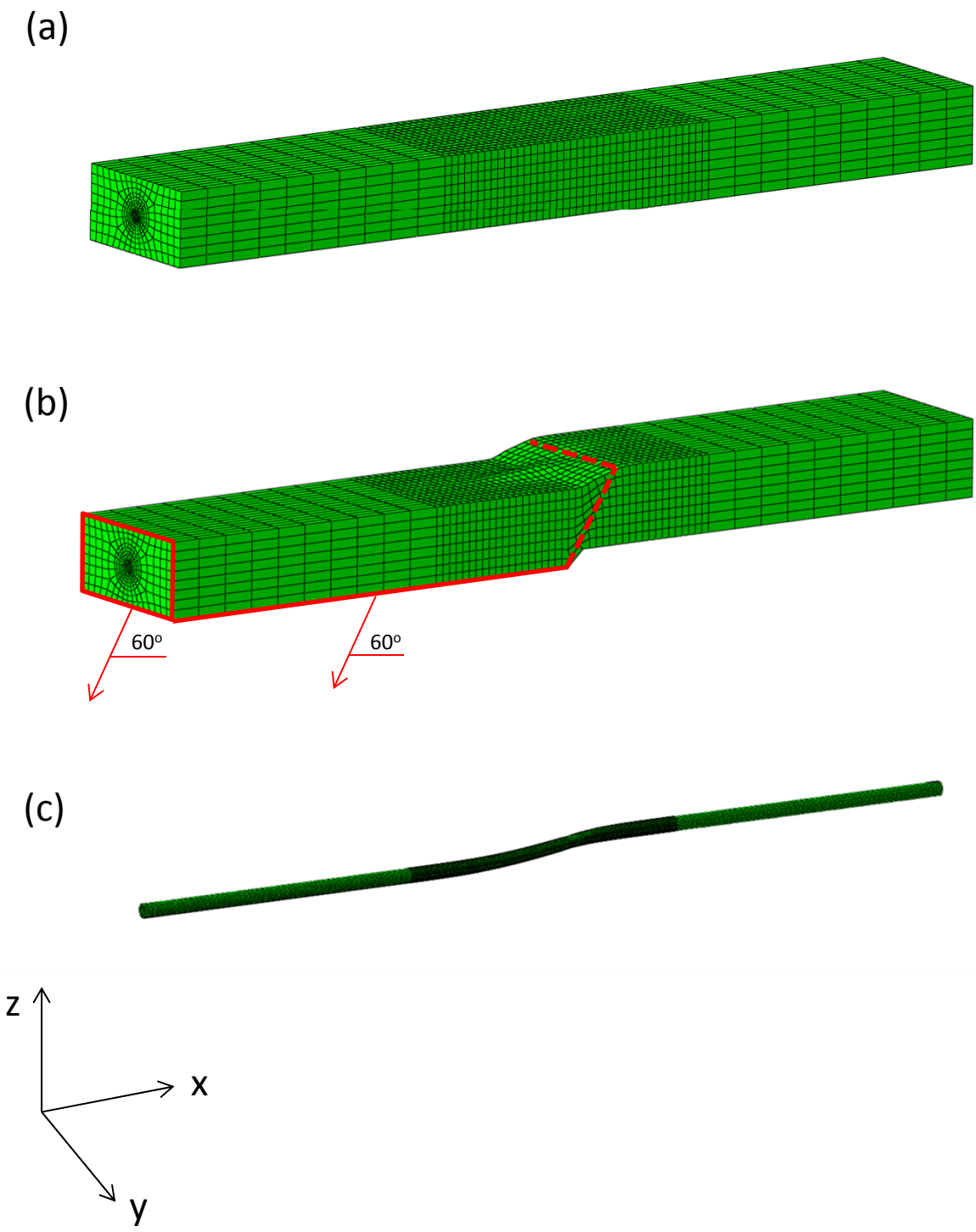

Figure 2.2.1. (a) The basic model of our study. (b) The fault was induced by moving a part of the base and the corresponding side at the left edge of the model. (c) The distorted shape of the pipe.

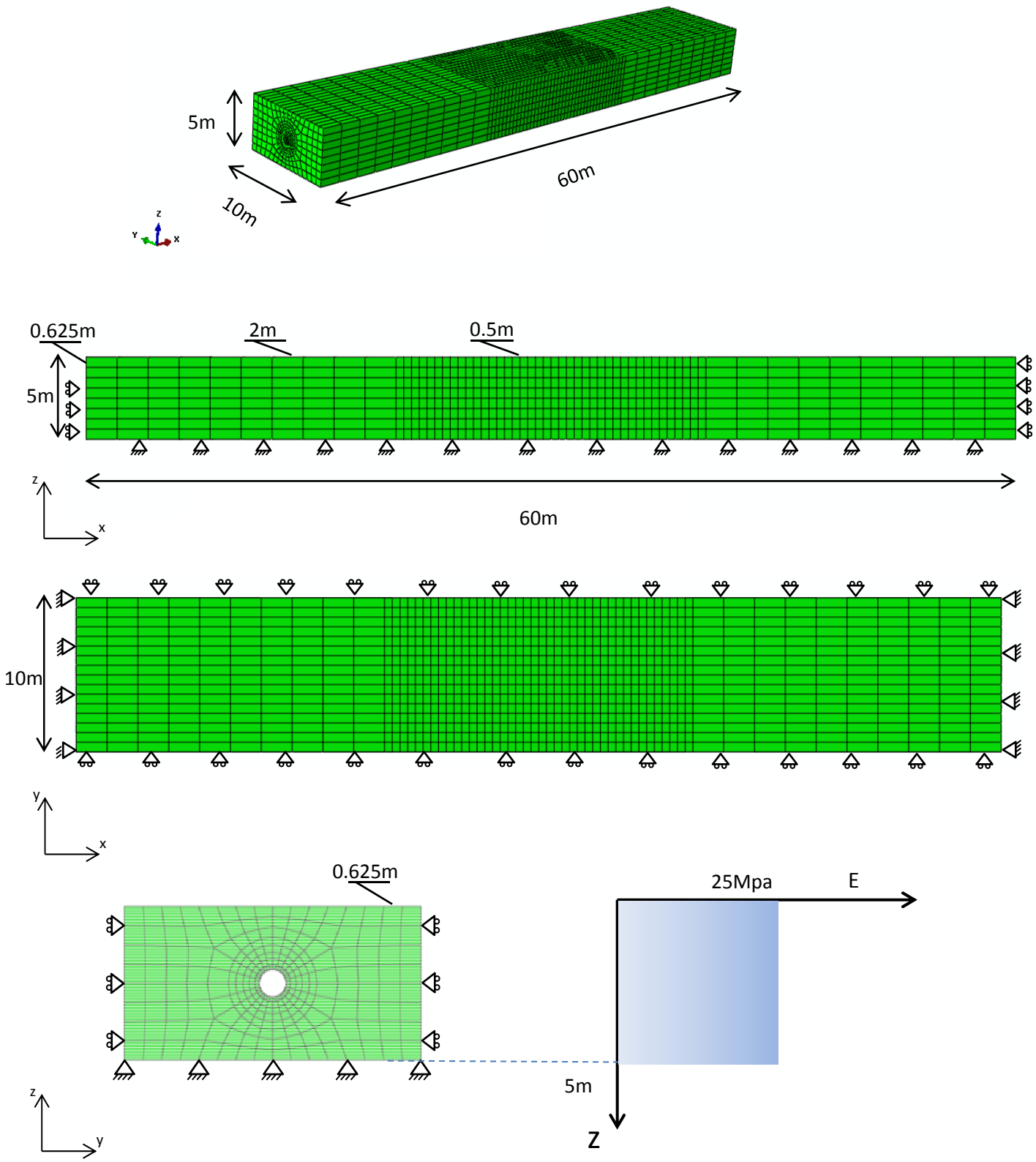

Figure 2.2.2. The soil part of the model, its various cross-sections with their properties, dimensions and boundary conditions.

(a)

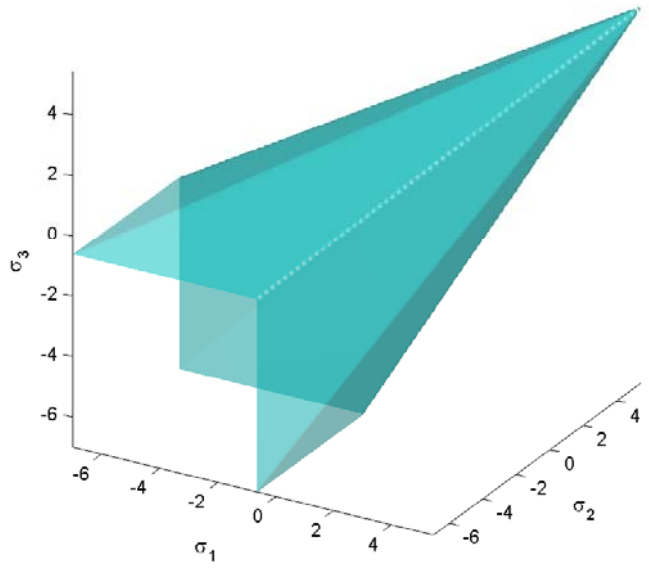

(b)

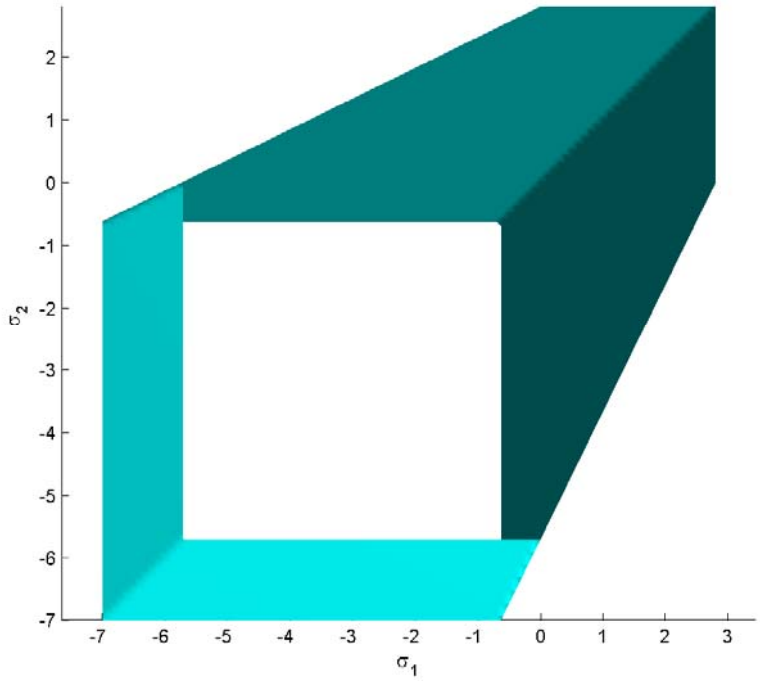

Figure 2.2.3. (a) View of Mohr-Coulomb failure surface in 3D space of principal stresses. (b) Trace of the Mohr-Coulomb yield surface in the σ_1-σ_2 plane.

(a)

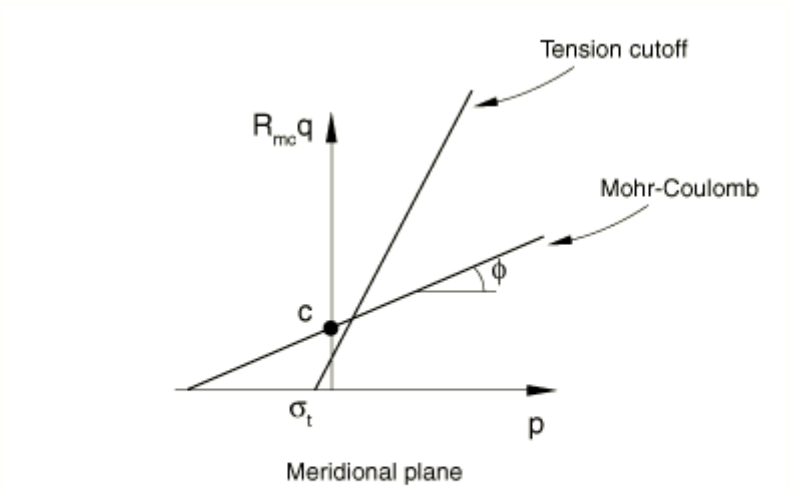

(b)

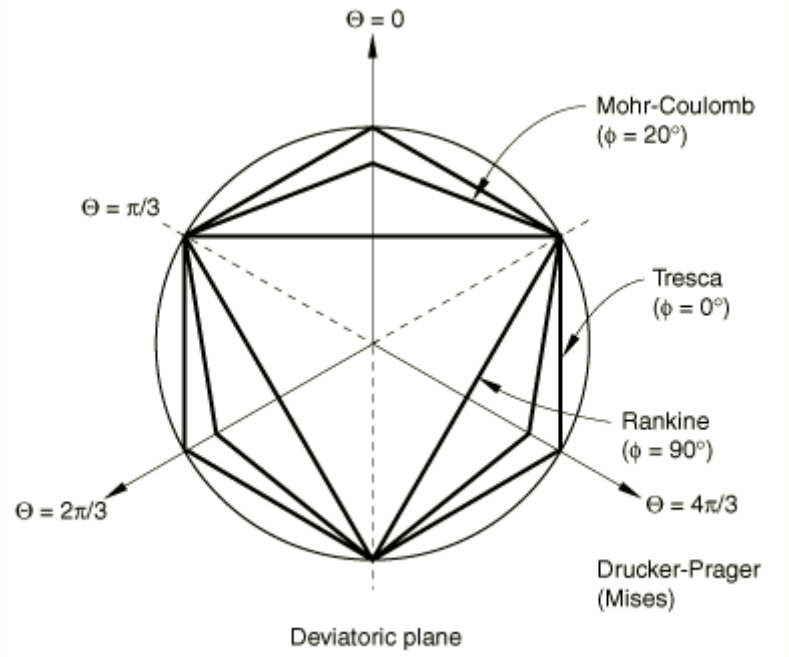

Figure 2.2.4. Mohr-Coulomb and tension cutoff surfaces in (a) meridional and (b) deviatoric planes..

(a)

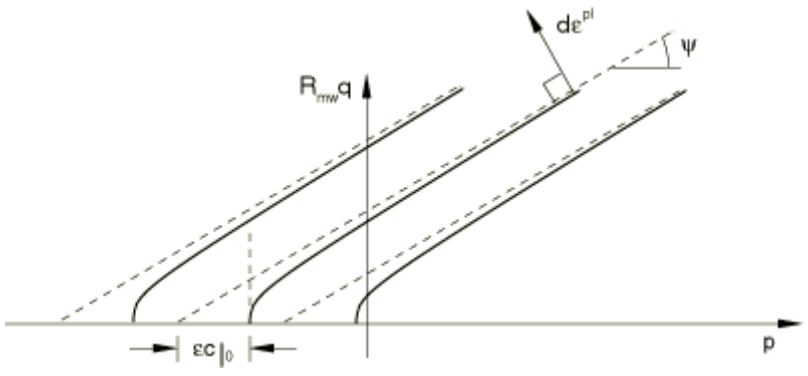

(b)

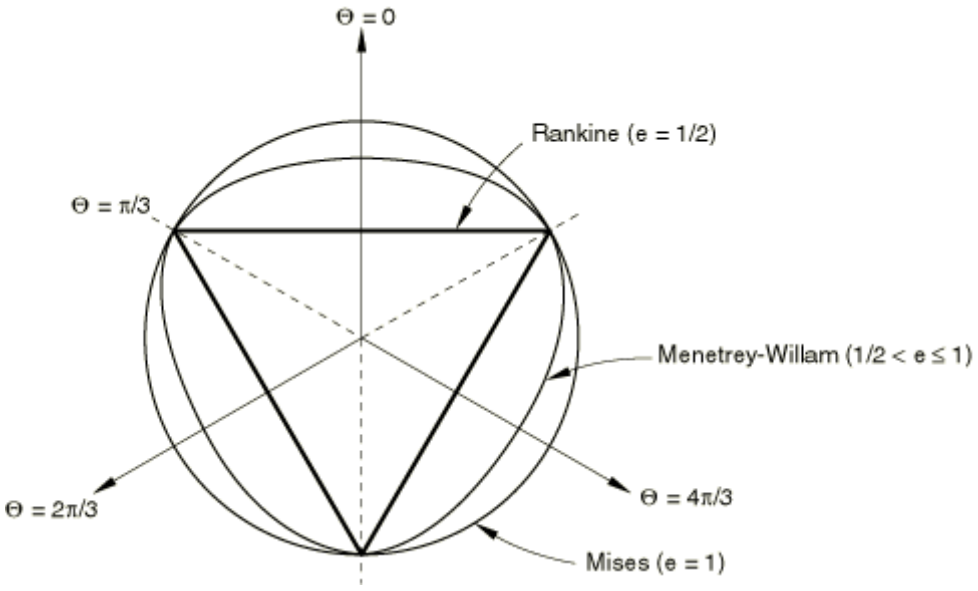

Figure 2.2.5. (a) Hyperbolic potentials in the meridional stress plane and (b) the flow potential in the deviatoric stress plane.

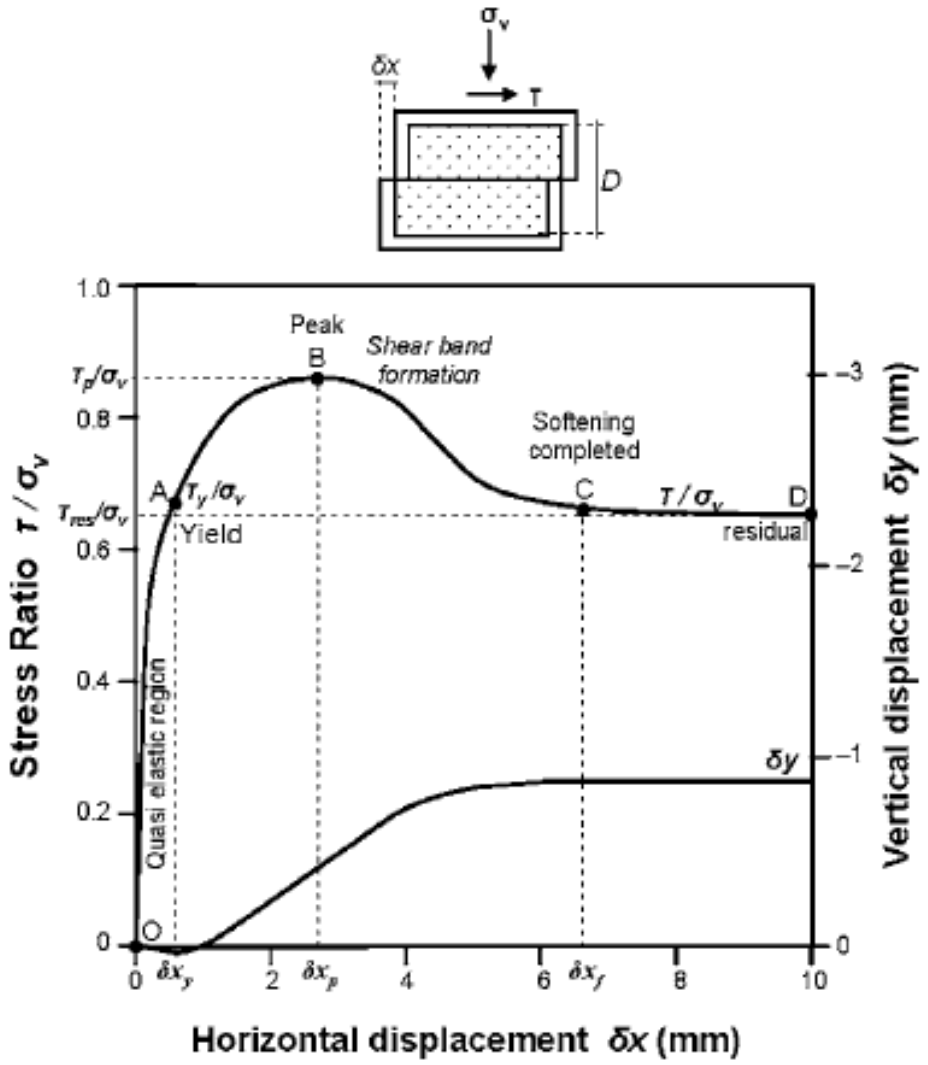

Figure 2.2.6. A typical variation of the stress ratio, τ/σ_v, and volume change (expressed through vertical displacement δy of the top platen) with respect to the imposed horizontal displacement δx in a direct shear test of dense Toyoura sand [based on data of Shibuya et al. (1997)].

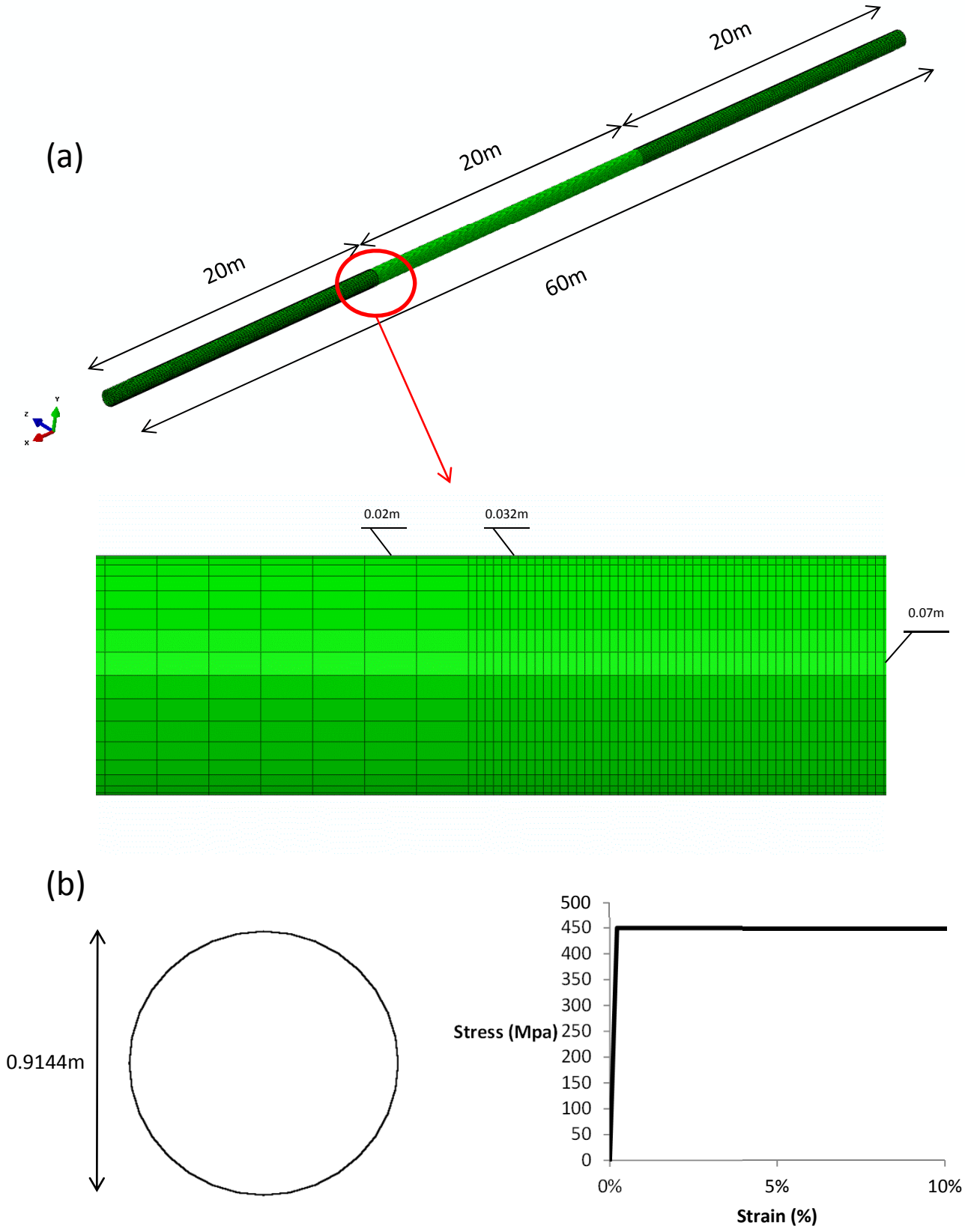

Figure 2.2.7. (a)The pipe as designed in our model. divided in three parts , according to the needed density of meshing, (b) The pipe cross-section and the diagram that described the stress-strain relation of the pipe steel.

(a)

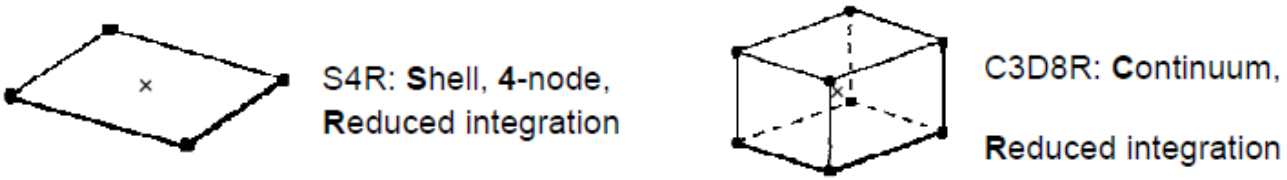

(b)

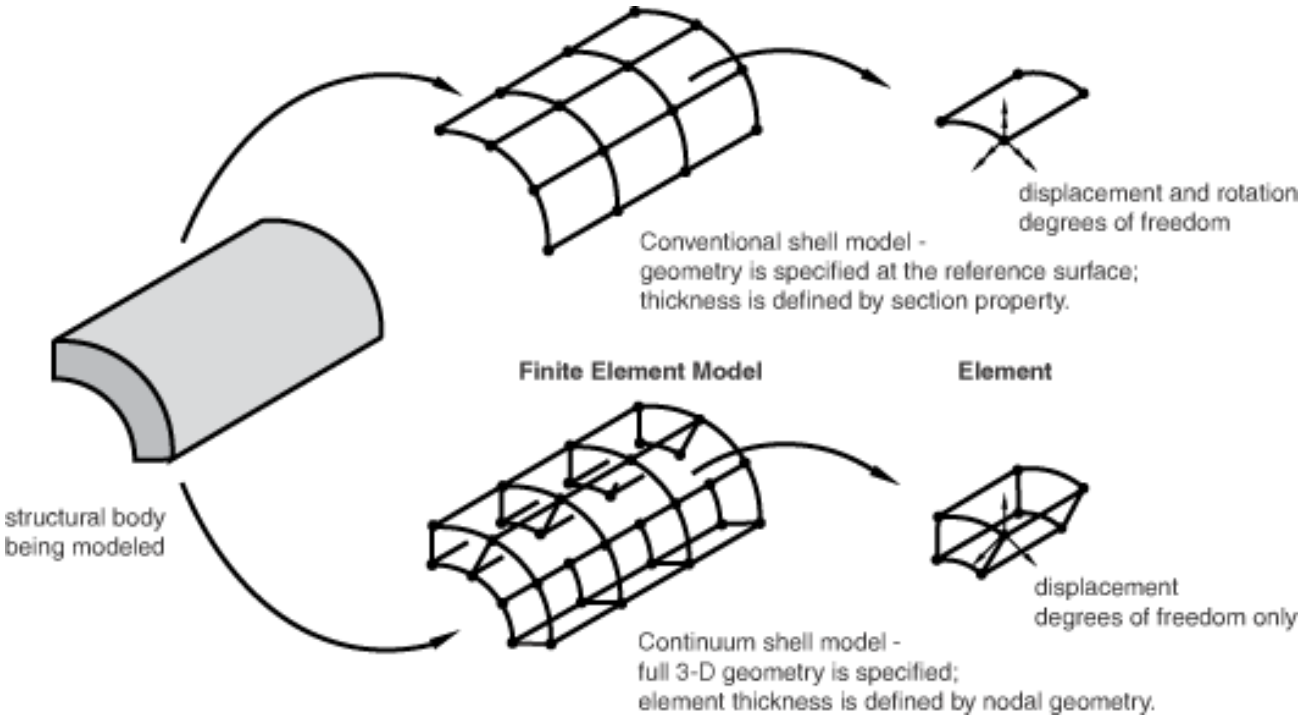

Figure 2.2.8. (a)The elements used in our basic model. Shell elements for the pipe and continuum 'brick' elements for the soil. (b) Comparison of shell to continuum elements (Abaqus Documentation).

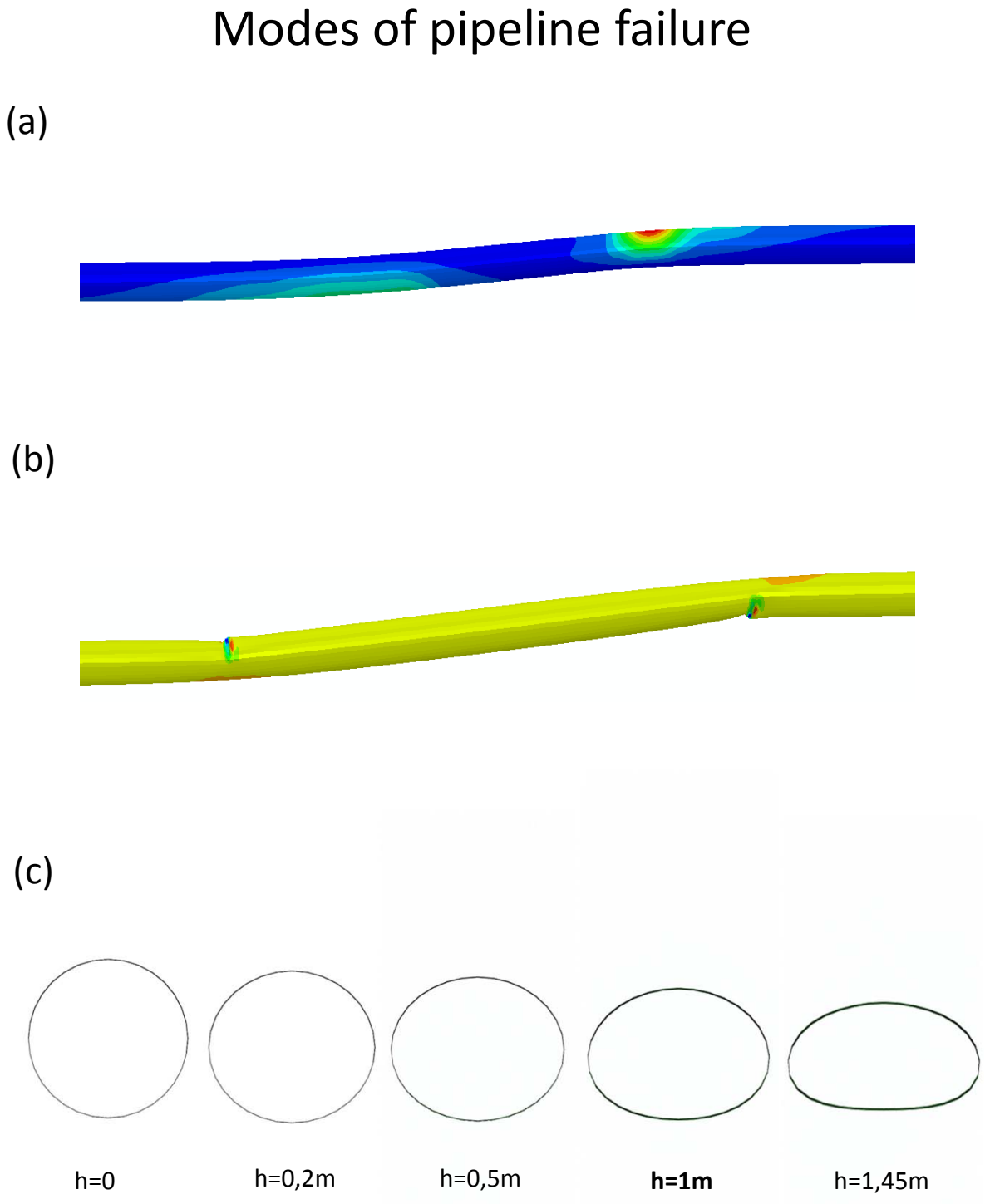

Figure 2.2.9. (a) Excessive tensile strain, (b) Local buckling, (c) The development of the ovalization of the pipe cross-section with respect to the vertical fault displacement h. The critical state beyond which the pipe is considered as non operational corresponds, for this example to h=1m , [D/t=144, steel with hardening behavior, Hybrid-Beam Model (Chapter 6)].

Chapter 3
Pipe boundaries

Introduction

As already mentioned, the boundary conditions of this kind of problems is yet to be answered. A very large model would be needed if we wanted to capture the real pipe-soil interaction and pipe behavior. Such a big model would be, at least, time consuming, hence, all of the researchers had made an assumption about the boundary conditions that they should apply to the model. Usually, the pipe edges are considered as fixed to the marginal sides of the model. Nonetheless, we decided not to take that assumption as granted and to examine different boundary conditions for the pipe edges. Apart from the free and fixed conditions that we examined, we designed a hybrid model that addresses to the boundary problem by combining the previous full model with beam elements that represent the continuation of the pipe and extend for a kilometer, starting from the edges of the pipe, and soil springs attached to those beams as the surrounding soil. In the following paragraphs of the chapter, we present all the steps and all the different models we tried, before ending up with the most realistic and reliable simulation.

We examine four different cases, testing a normal fault and a pipeline of variable thickness.

3.1 Free Pipe Ends Model

In these analyses, we release all the degrees of freedom of the pipe edges. Initially, during the first few centimeters of fault movement, the pipe is under tensile stress that is caused primarily by the friction between the pipe and the soil because of their trend for relative movement. Very soon, the bending mechanism starts to prevail. The deformed shape of the pipe indicates two inflection points (**Figure 3.1.1**) that is in absolute accordance with the analysis stress and strain results (**Figure 3.1.3**). In those two bending areas, tensile and mostly compressive strains start to concentrate, until the point where the compression causes local buckling to occur, firstly in the footwall and later in the hanging wall (**Figure 3.1.2**).

At this point, it is important to describe the way we define and observe the commencement of the local buckling phenomenon -which is our failure criterion- apart from the visual observation of concentrated wrinkling of the pipe. We can spot the start of buckling both at the strain-position diagram, which demonstrates the strain distribution along the pipe for various fault offsets (**Figure 3.1.4**) and at the strain-fault offset diagram at the point of the pipe where the buckling occurs (**Figure 3.1.5**). Concerning the first diagram, as the fault offset augments the compressive axial strains increase as well, having a substantially bigger ratio of increase at the area where buckling will occur, forming a bell shaped strain distribution. When buckling begins, additional fault movement causes not only a general increase of compressive strains but also a decrease of axial strains at certain points of that area which in later steps can even turn to tensile strains. The start of buckling can be defined even more simply, by the later diagram we mentioned, just by pointing out the moment (point) when the increase ratio of compressive strains augments greatly and strains begin to increase almost vertically compared to their previous mild trend of increase.

The results obtained are presented in **Figures 3.1.4**-**3.1.8**.

As we can observe in **Figure 3.1.6**, smaller D/t ratio pipes (thicker pipes since we maintain the same diameter) can endure bigger fault offsets and bigger compressive strains before the appearance of buckling. It is also demonstrated that, even though buckling did not have the exact same form in all D/t cases, it occurs inside a relatively short area of 1m very close to the pipe fault intersection point. This indicates that hypothetically if we knew the fault's plane we could presume the buckling area despite D/t ratio (about 1-2 diameters length from the fault-pipe intersection). However, bedrock at 5m depth is not very realistic, so the above conclusion could be not of great interest and will be reviewed in Chapter 5.

Even though, our approach, as defined in Chapter 2, concentrates on strain based criteria we examined, as well, the axial force (N) and moment (M_Y) distribution along the pipe. Since the pipeline is simulated using shell elements, different values of forces and moments can be expected, not only along the pipe's length but along the cross-sections of the pipe as well. For this reason, we examined and edited the output data for different points of the pipe's cross-section. The axial forces and moments along the top and bottom pipe fibers are demonstrated in **Figures 3.1.7** and **3.1.8** respectively.

Concerning the axial forces diagram, the distribution of forces is in absolute agreement with the previous diagrams of axial strains, making the two bending areas easy to observe. Apart from that, the axial force at the pipe edges (and at the adjacent area) is practically zero, something we clearly expected since we had designed the pipe edges to be free. Another interesting observation we can make by looking these graphs is that as the fault displacement increases so do the values of the axial force. At some characteristic areas, after a certain value the axial forces remain stable and these areas start to expand. These areas correspond to the pipe parts where sliding between the pipe and the soil has occurred and the aforementioned maximum value that the axial forces can obtain is the marginal friction force. The exact value of this maximum force is not easy to be calculated, since, it depends not only on the friction coefficient of the pipe-soil interface and the vertical (to the pipe) soil pressure but on the exact surface (thus the exact length) of

the pipe that is activated and tends to move relatively to the surrounding soil. As we also expected, the maximum friction value for the lower part of the pipe is slightly bigger because of the bigger depth and the added weight of the pipe. Finally, we can notice that, after buckling appears, the axial forces of that area are destabilized and decreased. This decrease is caused by the wrinkling that occurs during buckling and causes at some points the compression to increase and at other points to decrease (even to turn into tension).

Regarding the moment diagrams there are few points to be made. Unlike the axial force distribution, moment is practically the same along any pipe cross-section. That does not apply, obviously, to the phase when buckling occurs, which has as a result very different values of moment between the top and bottom fiber, but again, only at the limited area of buckling.

Finally, we examined the distribution of soil pressures along the pipe and its cross-sections. Using the data output from ABAQUS and an algorithm written in MATLAB we obtained the graphs of external pressure distribution along the pipe cross-section. **Figure 3.1.9** presents the pressure distribution for three cross sections, A, B and C, located at the hanging wall, at the middle of the model and at the footwall respectively. As it is demonstrated, at the area where the fault intersects the pipeline (B), gaping occurs at the very first steps of fault displacement (indicated by the zero soil pressures at the lower part of the pipe cross-section) whereas, at the areas A and C it takes significantly more fault movement for pipe-soil contact loss to occur. Specifically, during the first steps of small fault movement, the pressures around these areas are almost geostatic. Further movement causes the loss of contact firstly in the hanging wall and afterwards in the footwall part.

3.2 Fixed Pipe Ends Model

Apart from integrating all the aforementioned properties and geometries in our model, we restrained, in addition, all the degrees of freedom of the pipe end cross-sections. This would be indeed a valid approach if we could prove that the stresses of the pipe have already been nullified, before reaching the limits of our model, thus, that there would be not significant changes between our model and a bigger one that would include a longer pipeline. It is a fact that we didn't expect this to happen in a 60m model mainly because of the axial stresses that occur and have, in general, a wide area of action. However, we found reasonable to run these analyses, both to be sure about our speculation and for further comparison with the other models let alone that this is the most common option between the researchers. The results that came out of this model are demonstrated in **Figures 3.2.1-3.2.9.**

The pipe behavior is defined as follows. The pipe, at first, experiences almost only axial tensile stress. The tensile stresses and strains are initially more intense at two pipe areas, right and left from the point where the fault plane crosses the pipeline. Loss of contact between the pipe and the surrounding soil occurs by the time the fault reaches the pipeline. During almost all of the fault evolution, because of the bending mechanism that occurs, the fibers with the greatest tensile strain are located anti diametrically to those with the smaller tensile strain. In the free ends scenario, those latter areas experience compressive stress and are those where local buckling occurs. Afterwards, the tensile strains continue to increase and reach the margin of the elastic strain. At that area, (the top fibers of the pipe near the fault , in the footwall part) the concentration and the rate of increase of plastic strains augments leading finally to excessive tensile strains beyond 3% and 5% that we have set as limits. From there, even though it is beyond the interest of this study since we consider that the pipe has already operationally failed, the tensile strains continue to increase and a change of loading mechanism is spotted. This specific feature, the transition from prevailing bending to prevailing tension, is discussed in the following case of Hybrid-Beam model.

As we notice in **Figure 3.2.1**, regardless the pipe thickness, all of the pipes reach the failure criteria of 3% and 5% at the exact same fault offset and failure occurs almost at the same point of the pipe. The explanation of the above coincidence lies in the model design. The side of the hanging wall, where the one end of the pipe is fixed, moves the exact same way (direction, value and rate of displacement) as the base of the hanging wall that we move in order to simulate the fault. The displacements of the side were the same for all the analyses of same fault angle. Hence, since the pipe is fixed both to the movable side of the hanging wall and to the immovable side of the footwall we subject it to elongation, causing mainly (at the first steps at least) the same axial deformation (values and rate) despite the thickness of the pipe. So it is normal that the strain limits are reached for all of the D/t ratios at the same fault offset. This happens of course because, as shown by the analyses of this case, the loading mode is very close to pure axial loading. It is possible that under different fault angles we would not have this behavior since the deformation would be even more concentrated and would cause more severe bending and shearing near the fault plane. As a conclusion, in cases where someone would expect significant axial loading it would be clearly wrong to use the fixed ends model.

It is evident, that under an ideal axial stress or strain loading the behavior of the pipe, keeping the elastic modulus E and the length L the same, would be independent of the thickness of the pipe and the geometric area A in general.

$$\left.\begin{aligned} F &= K \cdot x \\ K &= \frac{E \cdot A}{L} \end{aligned}\right\} \quad F = \frac{E \cdot A}{L} \cdot x$$

$$\left.\begin{array}{l} F = \dfrac{E \cdot A}{L} \cdot x \\ \\ F = \sigma \cdot A \end{array}\right\} \quad \sigma = \frac{E}{L} \cdot x \qquad \text{(For } \sigma \leq \sigma_y \text{)}$$

Comparing fixed to free edges scenario, in the latter case the pipe at the hanging wall follows only a percentage of the movement magnitude of the adjacent soil whereas the pipe on the footwall is dragged towards the direction of the hanging wall, in contrast to the surrounding soil of the footwall that remains relatively stable. Hence, now that we designed the pipe ends to be firmly attached to the surrounding soil we provoke axial tensile stress to the pipe having as a result bigger tensile stresses and more tensile behavior in general. This is the reason why in the free ends case the bending mechanism prevails leading to local buckling failure while in the fixed ends scenario the tensile stress does not allow the compressive strains and as a consequence the buckling to occur, leading to excessive tensile strain failure. However, we cannot be sure which of those two assumptions is closest to the reality just by comparing them. For this reason we designed a more sophisticated model that addresses to this problem as described in the following paragraph.

Regarding the axial forces (**Figures 3.2.5-3.2.7**.) and moment (**Figure 3.2.8**), schematically, things do not differ a lot from the previous case of free edges. However, as mentioned before, fixed edges cause tensile behavior having as a result large values of tensile axial force at the pipe ends (instead of zero in the previous case) and along the pipe in general, which remain tensile during all of the fault movement steps. Soil presses, as well, are not practically affected by the boundary conditions of the pipe (**Figure 3.2.9.**) The only difference spotted is that gaping is less intense, compared to the free ends scenario, something that is attributed probably to the fixed conditions of the pipe end that oblige the pipe, at that point, to follow the exact same movement of the soil, hence the loss of contact is slightly more limited.

3.3 Hybrid-Beam Model

General geometry

Apart from the previous two extreme cases, we tried to approach the real behavior of the soil-pipe system by making the least simplifications possible. In order to achieve that we neither fixed the pipe edges nor let them free. Instead, we kept the same 60m model and then we expanded it by 1 kilometer from each side (**Figure 3.3.1**). The key point is that, for the expansion parts, we now use beam elements PIPE31 for the pipe and non-linear spring elements SPIRNG2 for the surrounding soil, elements that are commented in the following paragraphs. Specifically, we added beam elements of 1m whose nodes were conjoined with five, non-linear, 1m springs along the vertical, horizontal and axial direction respectively (**Figure 3.3.1**).

Beam element overview

A “beam” is an element in which assumptions are made so that the problem is reduced to one dimension mathematically: the primary solution variables are functions of position along the beam axis only. For such assumptions to be reasonable, it is intuitively clear that a beam must be a continuum in which we can define an axis such that the shortest distance from the axis to any point in the continuum is small compared to typical lengths along the axis. The simplest approach to beam theory is the classical Euler-Bernoulli assumption, that plane cross-sections initially normal to the beam's axis remain plane, normal to the beam axis, and undistorted. This approximation can also be used to formulate beams for large axial strains as well as large rotations. The beam elements PIPE31 are based on such a formulation, with the addition that these elements also allow “transverse shear strain”; that is, the cross-section may not necessarily remain normal to the beam axis. This extension leads to Timoshenko beam theory (Timoshenko, 1956) and

is generally considered useful for thicker beams, whose shear flexibility may be important. We assume that, throughout the motion, the radius of curvature of the beam is large compared to distances in the cross-section: the beam cannot fold into a tight hinge. A further assumption is that the strain in the beam's cross-section is the same in any direction in the cross-section and throughout the section.

In some piping applications thin-walled, circular, relatively straight pipes are subjected to relatively large magnitudes of internal pressure (we examine the effect of internal pressure in Chapter 6). This has the effect of creating high levels of hoop stress around the wall of the pipe section so that, if the section yields plastically, the axial yield stress will be different in tension and compression because of the interaction with this hoop stress. The PIPE elements allow for this effect by providing uniform radial expansion of the cross-section caused by internal pressure. Since consideration of planar deformation only provides considerable simplification in formulating beam elements, beam elements only move in the (X,Y) plane.

Spring element overview

Spring elements couple a force with a relative displacement. SPRING2 is between two nodes, acting in a fixed direction. The relative displacement across a SPRING2 element is the difference between the i^{th} component of displacement of the spring's first node and the j^{th} component of displacement of the spring's second node:

$$\Delta u = u_i^1 - u_j^2,$$

Springs Calibration

The force-displacement relation was obtained by the following procedure. We designed a 3-D F.E. model that included the pipeline and the soil of the aforementioned characteristics and we subjected the buried pipeline to vertical, horizontal and axial displacement. Based on the computed reaction forces and displacements that came out of those push-over analyses, we obtained the spring properties for the hybrid-beam model. The spring force-displacement relation diagrams are shown in **Figures 3.3.2** and **3.3.3.** As we observe, the axial spring (K_A) is activated both for negative and positive axial displacement, whereas, the other four springs are activated only for one direction of displacement and develop no force during displacement towards the opposite one. The horizontal spring (K_H) is the same for both sides, since there is no difference neither regarding the soil properties nor regarding the available soil length at each side, thus, the passive reaction of the soil at the sides is the exact same. On the contrary, the vertical springs differ significantly. The spring that is activated during downward displacement (K_{Vdown}) develops much bigger forces than the upper spring (K_{Vup}) for the passive soil reaction that the limited surface soil layer can develop is significantly smaller than the resistance that is demonstrated by the “infinite” soil layer under the pipe.

Results of Hybrid-Beam model

The results of the analyses conducted with the beam model are illustrated in **Figures 3.3.4-3.3.17.** As it is depicted, this more realistic approach gives substantially different results compared to the previous two methods.

Comparison with the fixed and free ends models.

First of all, it is now proved that the mode of failure for this kind of fault rupture is the excessive tensile strain. This is in absolute disagreement with the results that were taken from the free ends analysis. Free ends model does not take into any consideration the effect of the real effective length of the pipe and of its surrounding soil, which exceeds by far the dimensions of the basic model. Thus, it is clarified that to choose free boundary conditions for the pipe (at least for this kind of problem) is not in accordance with reality.

Compared to the fixed ends scenario, once again great differences are observed. Apart from the mode of failure and the area where failure occurred, that are practically the same in both cases and apart from the general shape of distribution of axial strains at the area of failure that is similar, all the other aspects of these two models differ substantially. Now that the axial forces and deformations have adequate length to be developed and are not limited by the boundaries of the model, the pipe can endure a lot more fault displacement. Significantly for the case of D/t=72 the pipe can endure almost 6 times bigger fault movement (**Figure 3.3.3.**). The pipe now demonstrated bigger resistance, with respect to the fault displacement, simply because it is no longer subjected to such high tensile stress and strains like those that were caused by the fixed pipe boundaries. Comparing the axial forces that develop in this model and in the fixed one, we now observe significantly smaller tensile forces (**Figure 3.3.9.**). Furthermore, unlike the fixed ends results, the 3% and 5% strain limit are now reached for different values of fault offset, unlike the fixed ends case where the critical fault displacement was almost the same for 3% and 5% axial strain (**Figure 3.3.3.**). The only exception concerning this, is the case of D/t=72 where we notice once more a very small distance between the critical fault movement for the 3% axial strain and the critical fault movement for 5% axial strain.

A change of loading mechanism

A possible reason for the above observation is that above a certain limit of relative displacement between the footwall and the hanging wall the deformations become more intense and accumulate along the fault's plane having as a result the change of the critical mode of loading from bending to shearing that resembles to direct shear loading. However, in the fixed ends case, the 3% and 5% limits are reached for almost the same h and for very small values of it. Thus, this change of mechanism is spotted even for limited relative displacement between the hanging wall and the footwall. In addition, as already mentioned, fixed ends case results in an almost ideal axial tensile deformation, something that suggests that the change of mechanism is actually a transition from prevailing bending to prevailing tension. This mechanism provokes a rapid development of strains which has as a result that one or two additional centimeters of vertical fault displacement are enough for the strains to increase from 3% to 5%. The mechanism can be identified firstly by the fact that the critical area moves to the point of pipe-fault intersection, which is at the middle of the modeled pipe where there is, practically, no bending deformation and secondly by the strain distribution that change form and shape. Specifically, as long as the bending prevails and causes the main tensile strain accumulation, the strains are distributed over a relatively large area at the upper part of the pipe, whereas, when the prevailing failure mechanism is tension, strains accumulate along a narrow area. Additionally, tension causes tensile strain all along the critical pipe cross-sections in contrast to the bending mechanism that tends to compress (or at least reduce the tension) half of the pipe cross-section. All of the aforementioned observations are depicted in (**Figures 3.3.6**). Because of this change of loading mechanism we observe two critical points: the one where 3% strain is reached because of bending and the other where 5% strain limit is reached because of shearing (**Figure 3.3.8**).

Effective pipe length, L_{eff}.

Very interesting results came up from this model concerning the affected area of the pipe. This is really important to be examined, since it is of great interest how many meters away from the pipe-fault intersection the effect of the rupture stops, something that would give a picture of how long a F.E. simulation should be or in an actual field case, something that could help make a speculation about how long would be the affected length of the pipe from a potential fault rupture. For these reasons we studied the effective (or affected) length of the pipe L_{eff} related to the vertical fault offset FIGURE and to the D/t ratio. We consider as effective length the length of the pipe that expands from the pipe-fault intersection point to the point where the axial force N is practically zero. Another way to calculate the effective length is by using the point where the axial strains are almost zero. This makes no difference since at that area the pipe behaves totally elastically, hence, stresses (forces) and strains are absolutely proportional. We also calculated the effective length both for the hanging wall part and the footwall part and observed negligible difference (**Figure 3.3.11**). As we notice in **Figure 3.3.12** at the very first steps of fault movement the L_{eff} is augmented almost vertically. After that it follows a parabolic trend until it is finally stabilized. This stabilization occurs because, after a certain fault displacement, the deformation is centralized to the point of fault-pipe intersection and continues to augment in that failure area, until probably the breaking of the pipe, causing no further effect to the pipe away from that area. The fault displacement, at which the axial strains start to increase almost vertically at the point of failure, is the one beyond which the effective pipe length remains practically unchanged. **Figure 3.3.12** also demonstrates that L_{eff} is bigger for smaller D/t ratios thus for thicker pipes. Thicker pipes have bigger moment of inertia, hence, just like in the case of beam on elastic foundation, bigger inertia moment means, logically, larger L_{eff}.

Detachment

It is demonstrated that the boundaries of the pipe do not affect that much the gaping between the soil and pipe, since, once again, the contact between them is lost from the first steps of fault displacement. The occurrence of gaping is demonstrated in **Figures 3.3.13** and **3.3.14**. The best way to locate the loss of contact is to spot the areas where the soil pressures are zero. This is the method we used in **Figure 3.3.14** which shows that detachment occurs and expands mainly in the hanging wall part and that above a certain fault displacement the length of the area of gaping remains stable. The only advantage of **Figure 3.3.13**, where we demonstrate gaping by plotting the different vertical displacements of the pipe and the soil, is that it gives us the exact height of the gaping. However, this is not something of interest since it does not affect the pipe and it is only the area of detachment and the time when it occurs that affect the pipe's behavior. Looking at the cross-sectional soil pressure distribution of **Figure 3.3.15** we notice that gaping may occur not only at the lower part of the pipe but also at the upper part of it. It would be reasonable not to expect gaping to occur at that area, since normally, sand above the pipe, just because of the gravity, should follow pipe's movement and fill any gap that is about to occur. However, as already mentioned in Chapter 2, because of computational reasons, we integrated a small cohesion coefficient (c=2kPa) to our sand which, in combination with possible soil arching effect, restrain the soil above the pipe from collapsing and allows the gaping to occur.

Effect of the pipe to the fault propagation

Regarding the effect to the pipe to the fault propagation and the surrounding soil in general, we do not expect significant differences compared to free-field fault rupture case. As demonstrated in **Figures 3.3.16** and **3.3.17**, the fault's surface outcrop is slightly affected by the intersection with the pipe. The major effect of the pipe is the plastification that induces at the surrounding soil because of its resistance to the

downward movement of the hanging wall and the bulging that occurs because the pipe restrains the soil above from following the displacements of the rest of the soil of the hanging wall.

Effect of the fault angle

The effect of the fault angle is also examined by running the analysis for a 45^{o} fault angle. The comparison between the 60^{o} and 45^{o} fault angle cases is shown in **Figures 3.3.18** and **3.3.19**. Now that we change the fault angle we cannot make pipe resistance comparisons just in terms of vertical fault displacement. For this reason we compare the axial strain development at the critical point for both cases in terms of vertical and horizontal fault displacement and in terms of total magnitude of displacement. As it demonstrated, for the normal fault case, failure occurs earlier for the 45^{o} angle in terms of vertical and total displacement but for both angles failure occurs almost at the same value of horizontal displacement. This observation signifies that the horizontal component of the fault, thus the horizontal displacement of the pipe is the critical one for the failure to occur. This is quite logical, if we consider that the mode of pipe failure, subjected to normal faulting, is the excessive tensile axial strain.

3.4 Equivalent Single Spring model

Based on the previous model, we substituted the beam parts and soil springs with just two springs, one at every pipe end (**Figures 3.4.1.**). The spring calibration was based on the Hybrid Beam model. Specifically, the axial reaction forces at the edges of the pipe were recorded, throughout the fault movement, with respect to the axial displacements. These data was later integrated into the Force-Displacement relation diagram of these axial springs, implying, this way, the effects of a non-limited model without the long beam parts of the previous model that cost in time and computational power.

As depictured in **Figures 3.4.2** and **3.4.3.** , there is not any substantial difference compared to the hybrid beam model, neither regarding the critical fault displacement with respect to the D/t ratio, nor regarding the strain development and distribution.

This ensures that the spring edge model is, indeed, able to capture the behavior of the soil-pipe system, yielding reliable results. However, we decided to proceed our research using the hybrid-beam model, instead of the latter one, partly because of the small (however negligible) differences that occurred and mainly, because by using spring edges we would not had been able to compute useful and important parameters such as the effective pipe length.

Main conclusions of Chapter 3

- The more realistic approach, achieved with the hybrid beam model, proves the high importance of the proper choice of the pipe boundaries. Comparing fixed to free ends case, fixed model does capture the actual mode of failure but, nonetheless, the results differ substantially from those obtained from the hybrid beam model, which we consider and propose as the most reliable model and the one that is the closest to the real conditions. Hence, a model, such as the proposed one, that combines reduced time consumption with realism and reliability, is considered as a correct and practical choice of boundaries in order to simulate pipe-fault systems using a finite element program.

- Pipes of smaller D/t ratios (thicker pipes of the same diameter) are able to withstand larger fault movements.

- According to the results of the hybrid beam model a change of the prevailing loading mechanism occurs. As the fault displacement increases, so does the relative movement between the hanging wall and the footwall, which leads to transition from prevailing bending to prevailing shearing-like loading mechanism.

- Useful results came up by the examination of the effective length of the pipe. Firstly, the effective length of the pipe increases with the increase of fault displacement. However the trend of increase reduces as the fault displacement goes on, until, finally, intense plastification and failure occur at the middle part of the pipe hence the effective length is no longer affected. It is also demonstrated that L_{eff} depends on the D/t ratio and augments as the pipe thickness increases.

- The critical displacement component for the normal fault case, that defines the point when the pipe fails, is the horizontal one.

Figures of Chapter 3

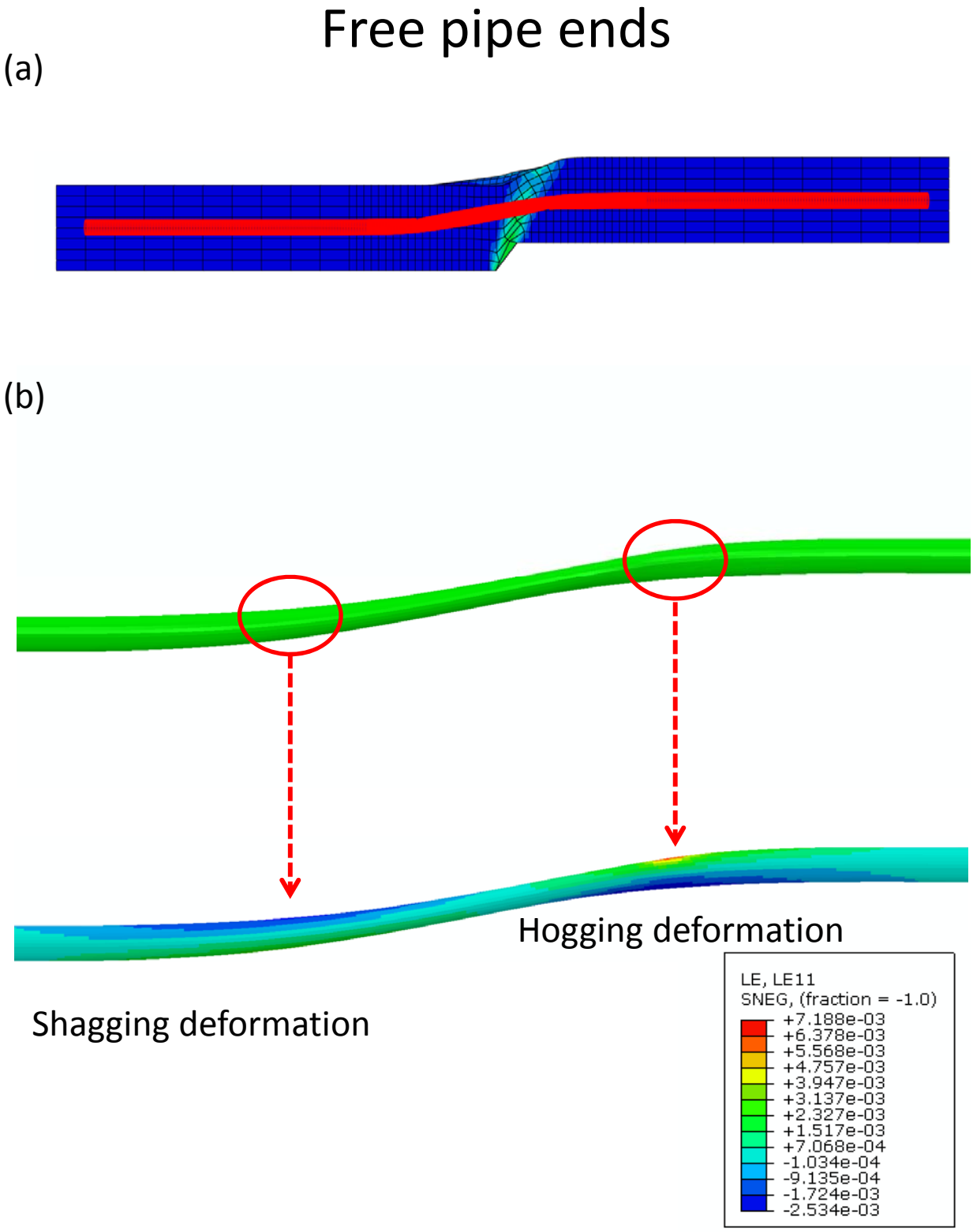

Figure 3.1.1. (a) The deformed model shape . The deformed pipeline is highlighted in red. The pipeline edges are free and the pipe is pulled towards the fault. (b) An example of deformed pipeline and axial strain distribution. The correspondence of the two inflection points of the deformed pipe shape with the strain distribution is depicted.

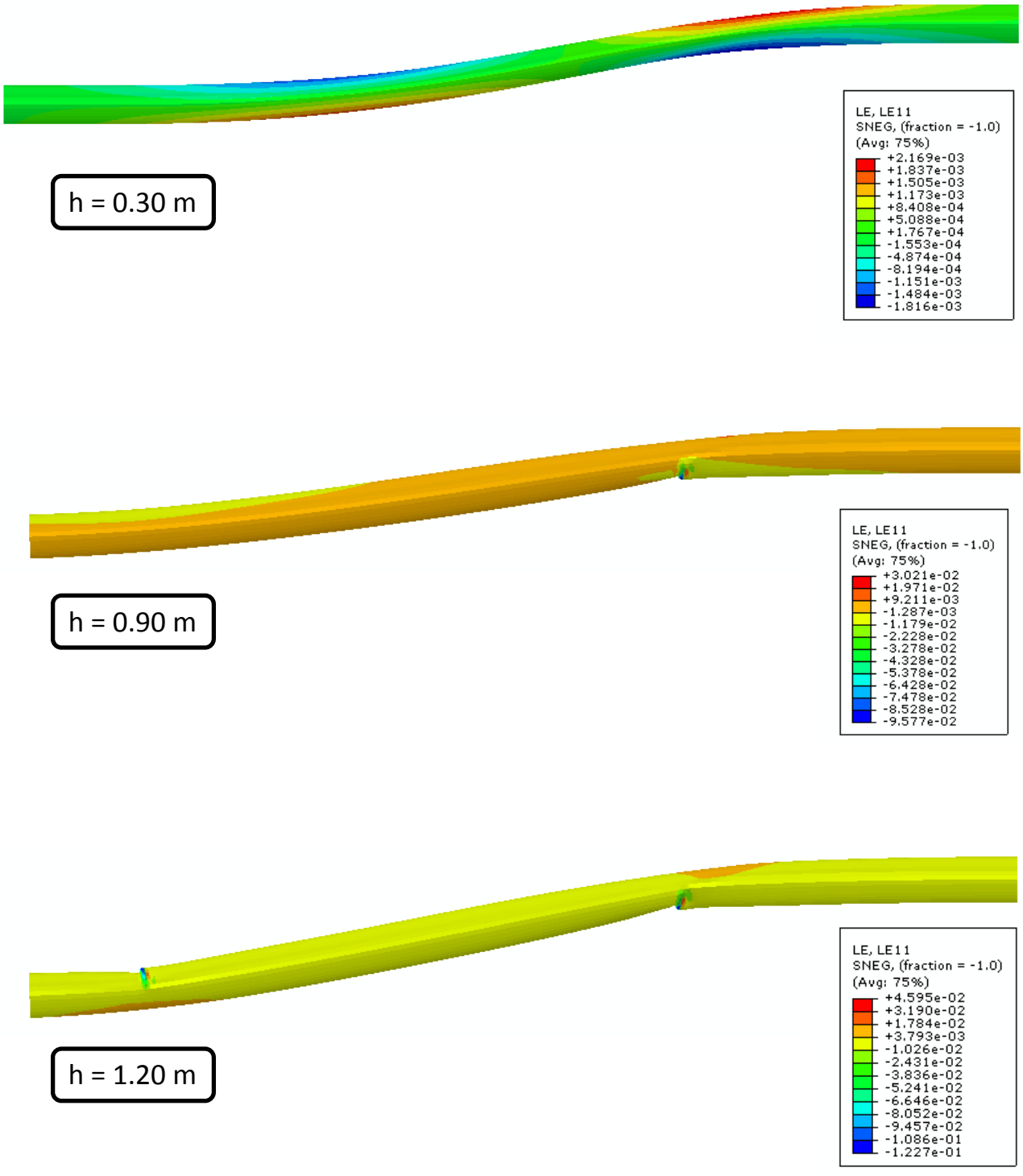

Figure 3.1.2. Axial strain distribution for three vertical fault displacement h. Buckling occurs at two areas making its first appearance in the footwall pipe part (D/t=96, Free ends).

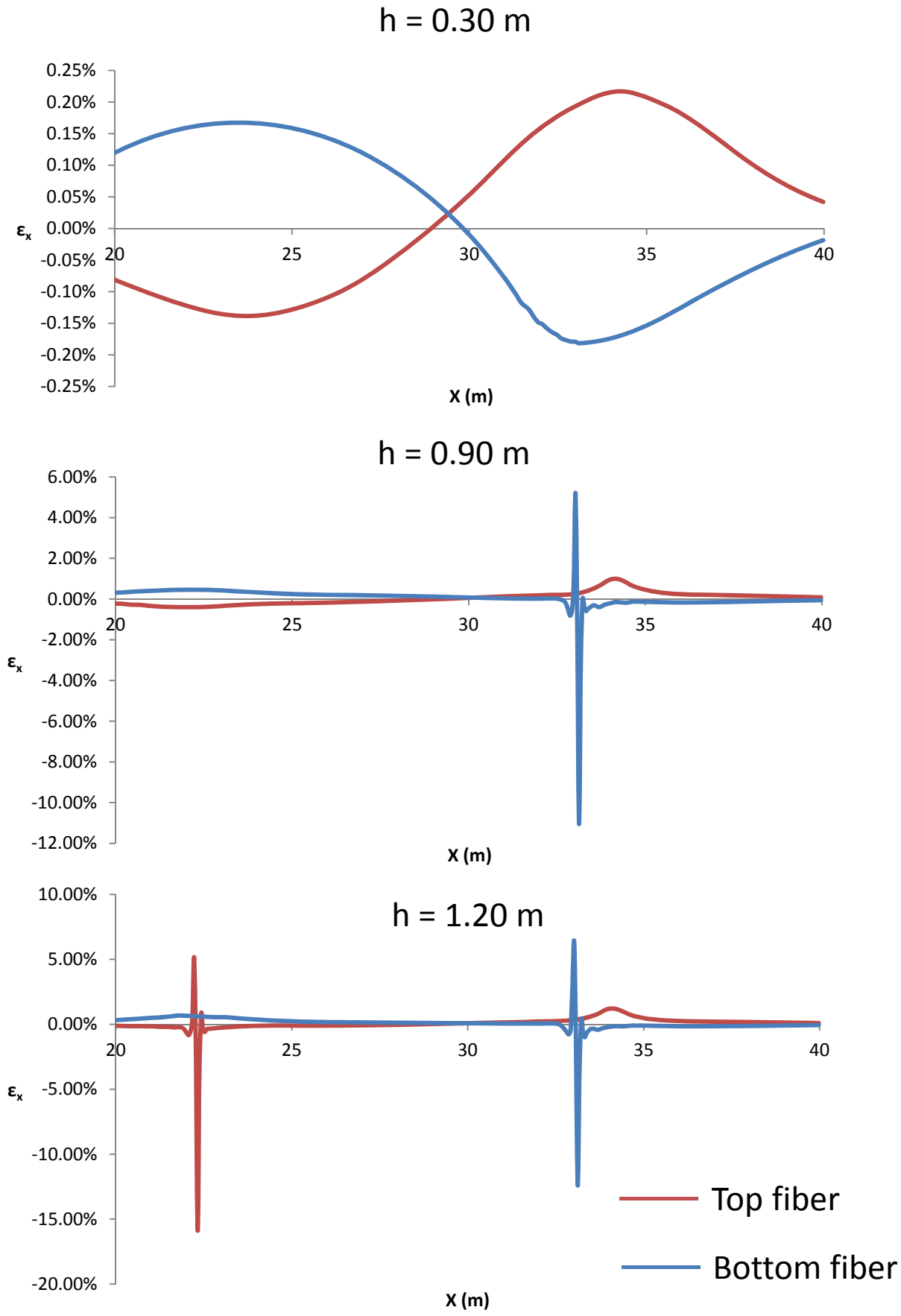

Figure 3.1.3. The axial strain diagrams for the top and bottom pipe fiber along the critical area, that correspond to the deformed shapes of the previous figure.

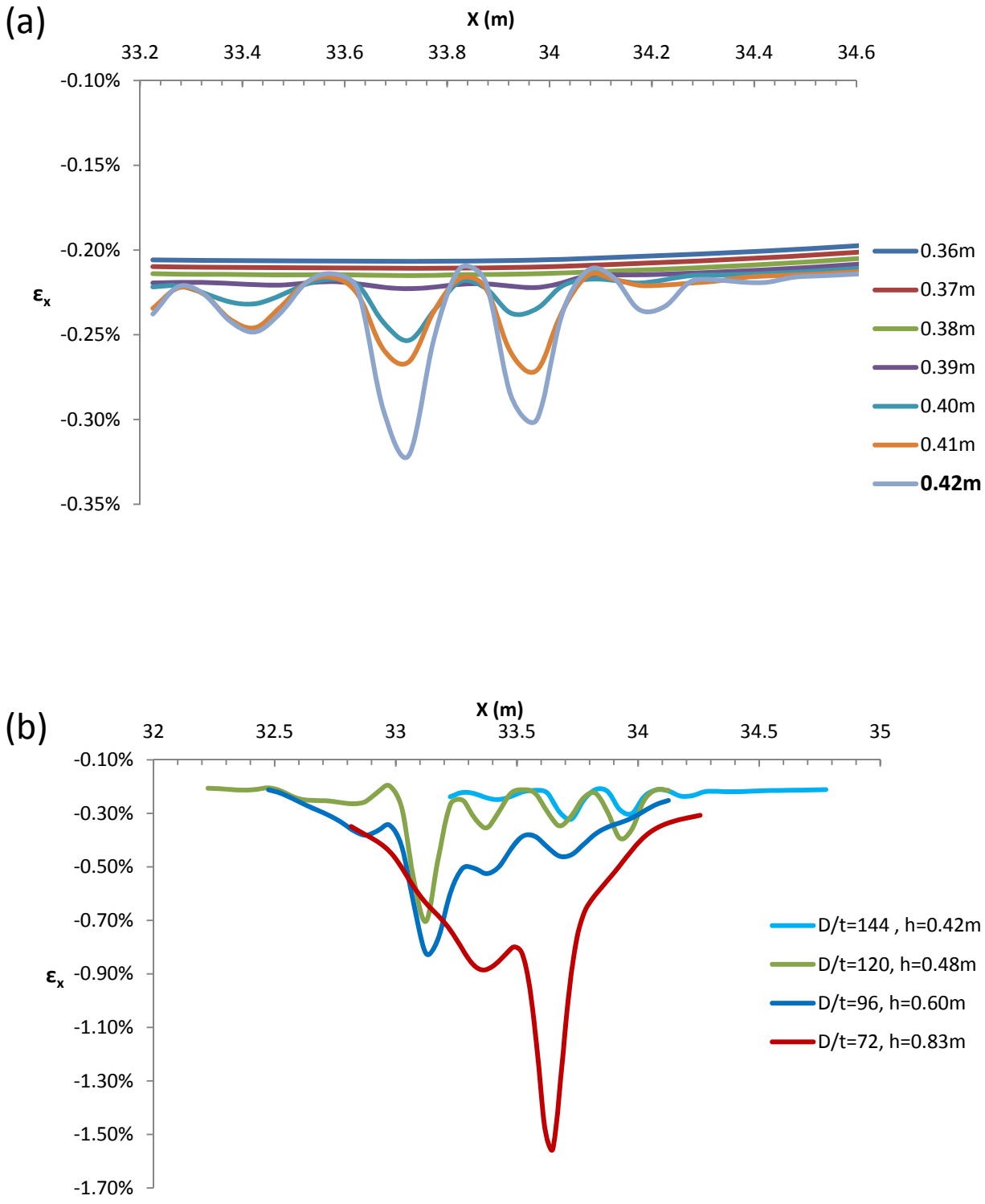

Figure 3.1.4. (a) The evolution of axial compressive strain at the buckling area, as the vertical fault displacement increases.. h=0.42m corresponds to buckling initiation . (D/t=144). (b) Comparison of the axial strains when buckling occurs for four different D/t ratios. (Free Ends)

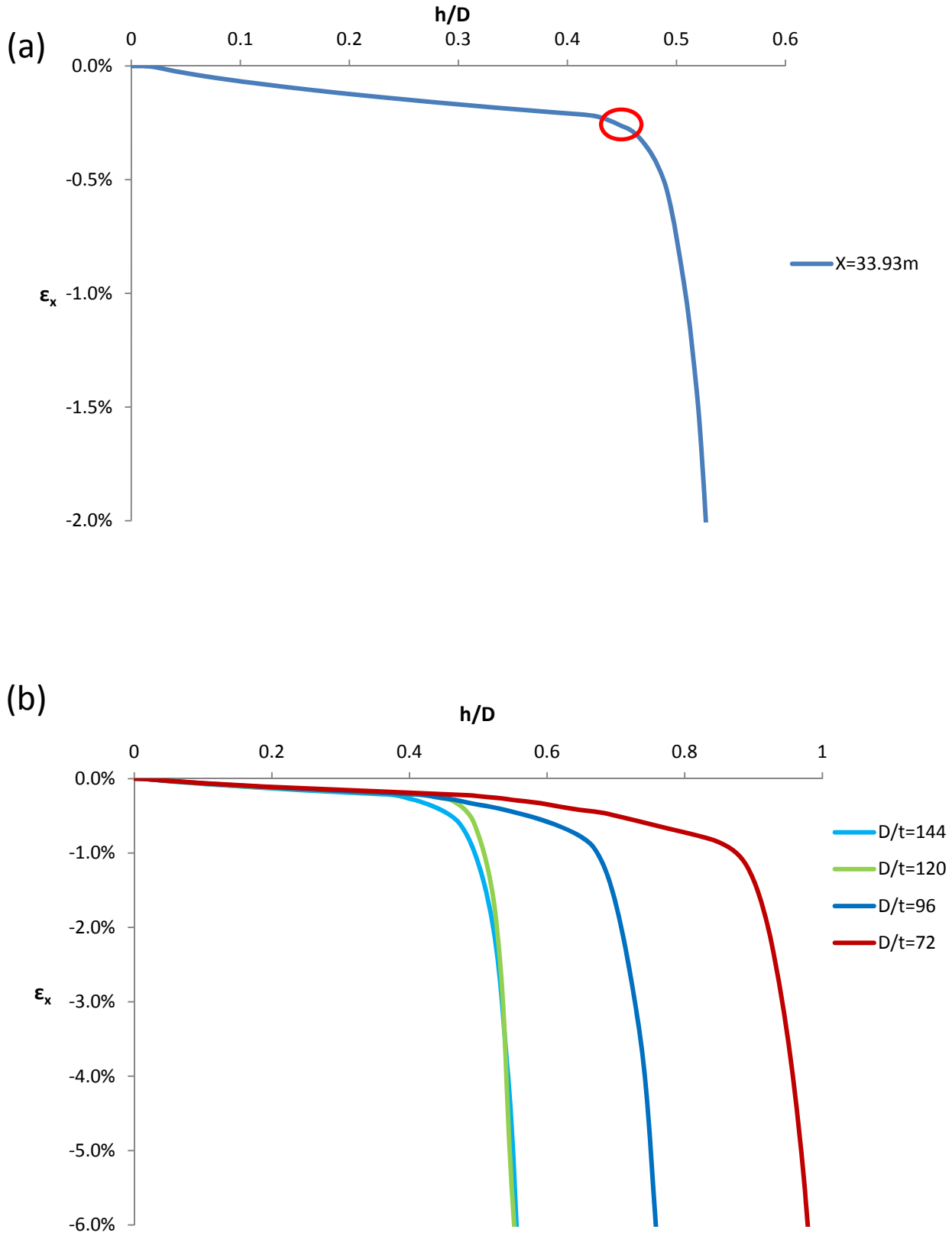

Figure 3.1.5. (a) Axial strain development at the point where buckling occurs (D/t=144). The red circle indicates the start of buckling. (b) Comparison of axial strain developments at the buckling areas for four D/t ratios.(Free ends model)

(a)

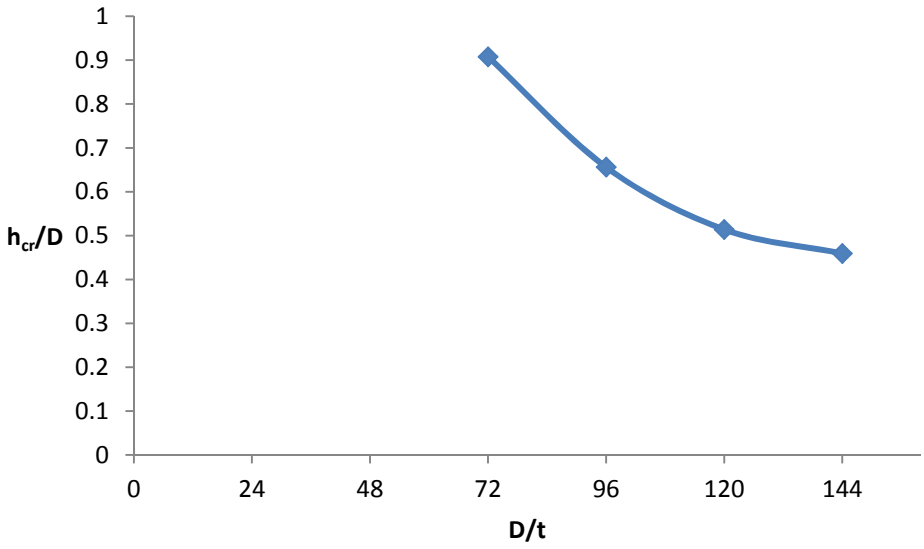

(b)

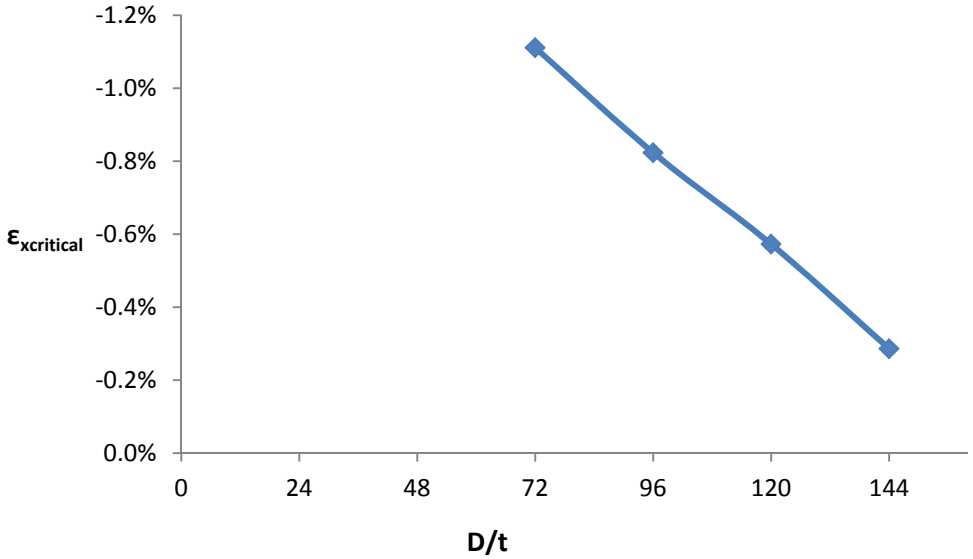

Figure 3.1.6. (a) Vertical critical displacement to pipe diameter h_{cr}/D related to the pipe diameter to thickness ratio for the free ends case. (b) The axial, compressive strain ε_x when buckling occurs for different D/t ratios for the free ends case.

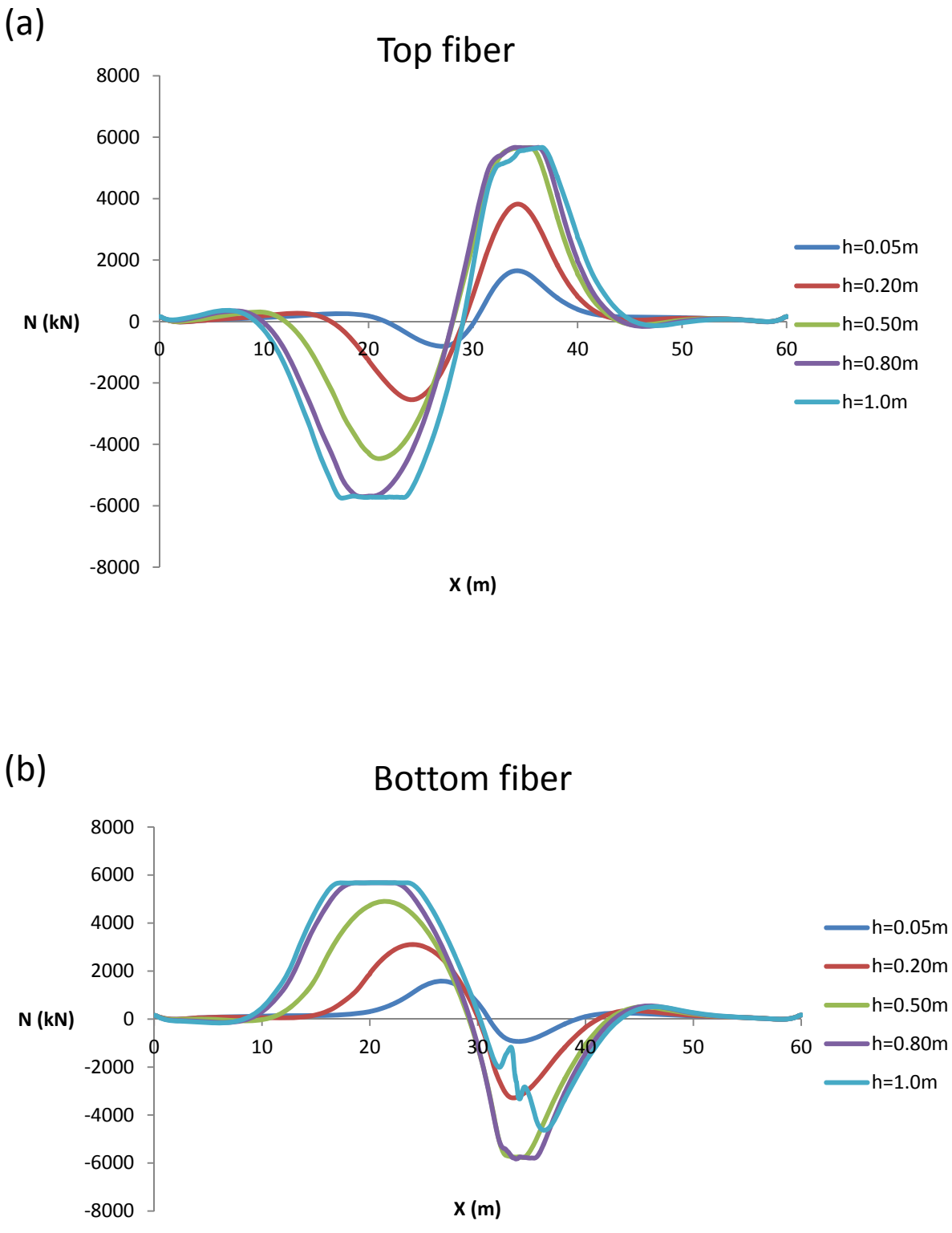

Figure 3.1.7. Axial force distribution and development for five vertical fault displacements for (a) the top and (b) the bottom pipe fiber. (D/t=72, Free ends)

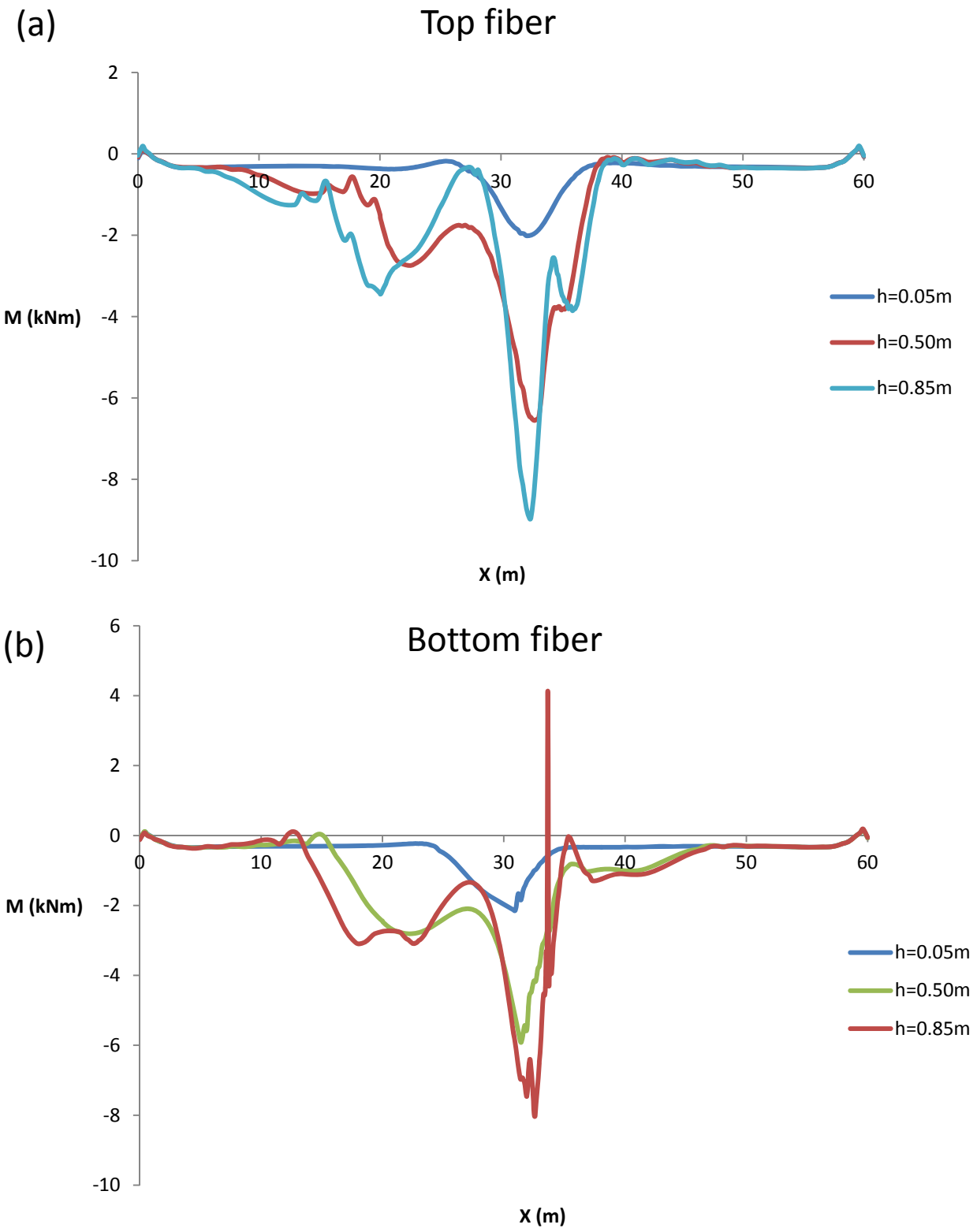

Figure 3.1.8. Moment distribution and development for three vertical fault displacements for (a) the top and (b) the bottom pipe fiber. (D/t=72, Free ends)

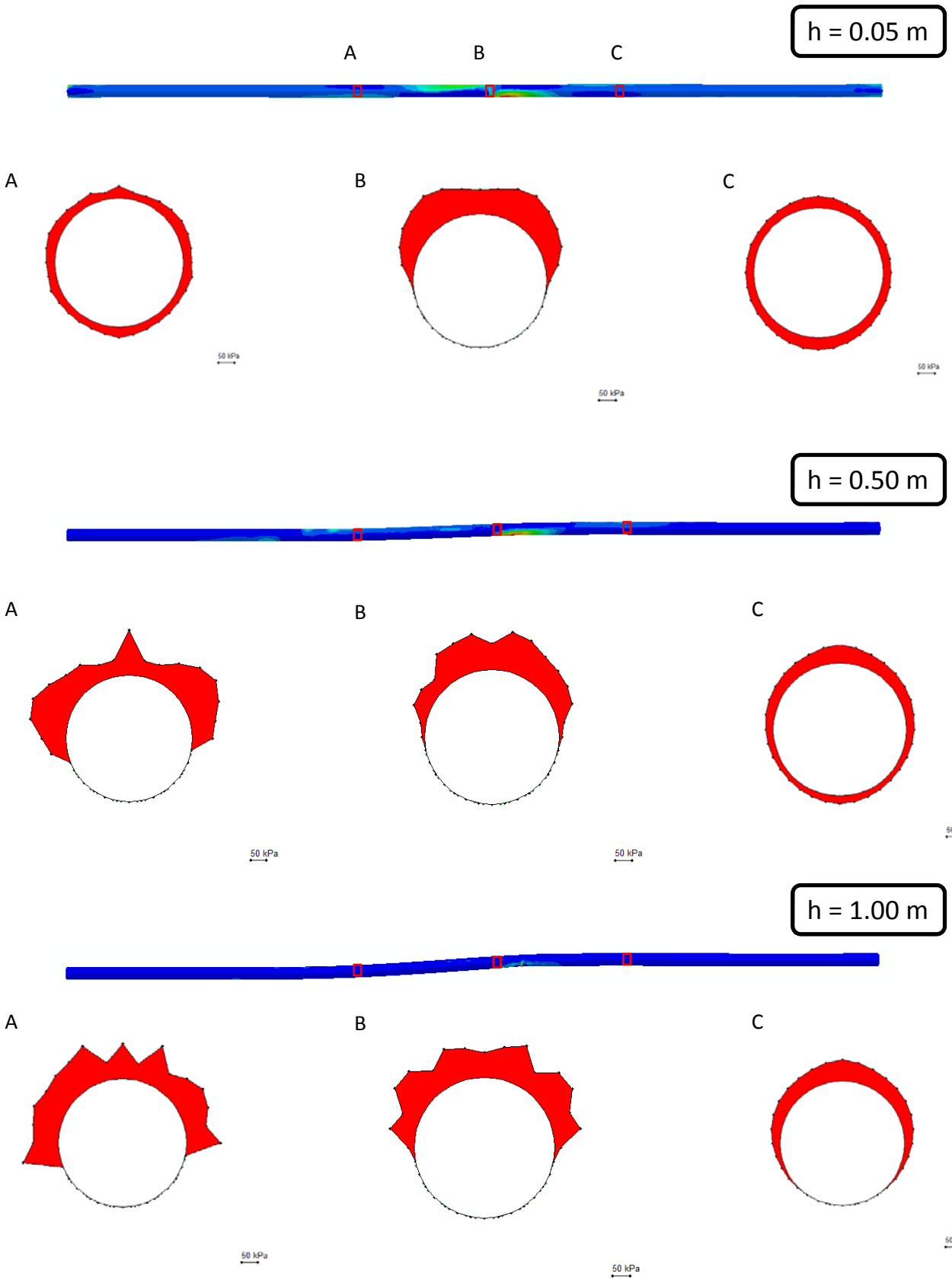

Figure 3.1.9. The soil pressures along three pipe cross-sections (X=20, 40 and 60 m for A,B and C respectively) for three different vertical fault displacements h. (D/t=72)

Fixed pipe ends

(a)

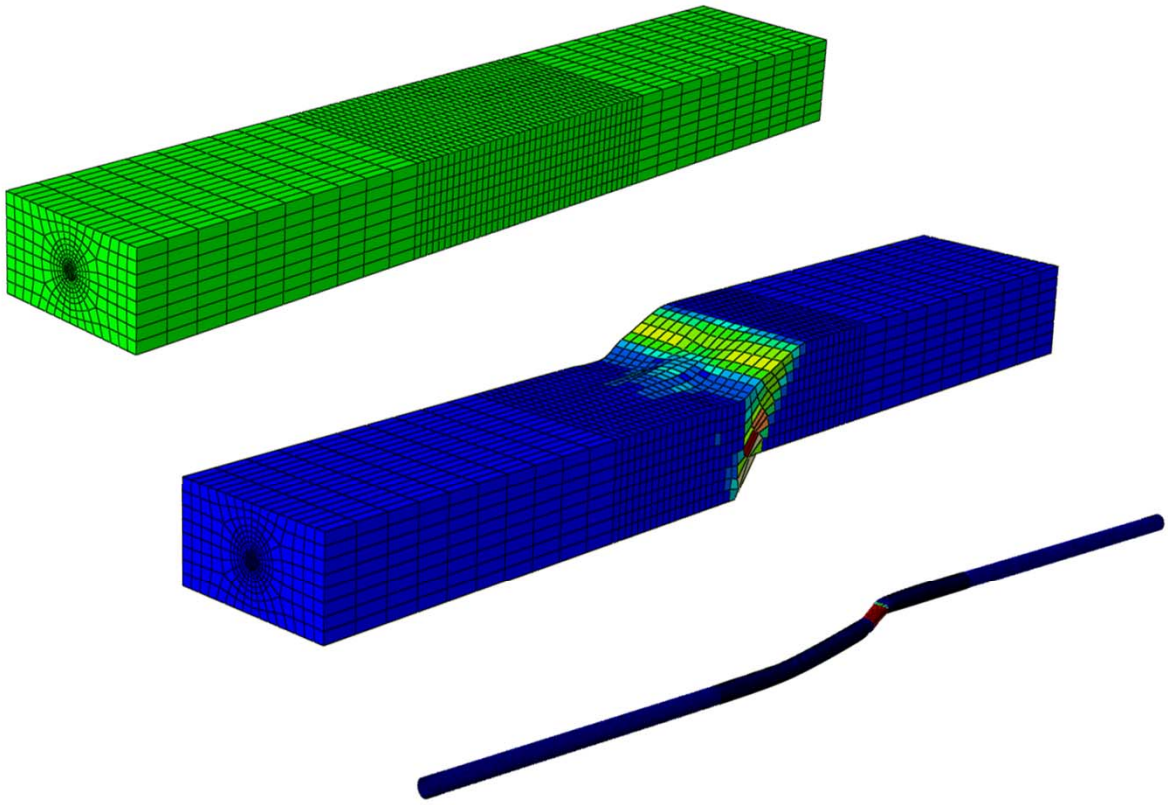

(b)

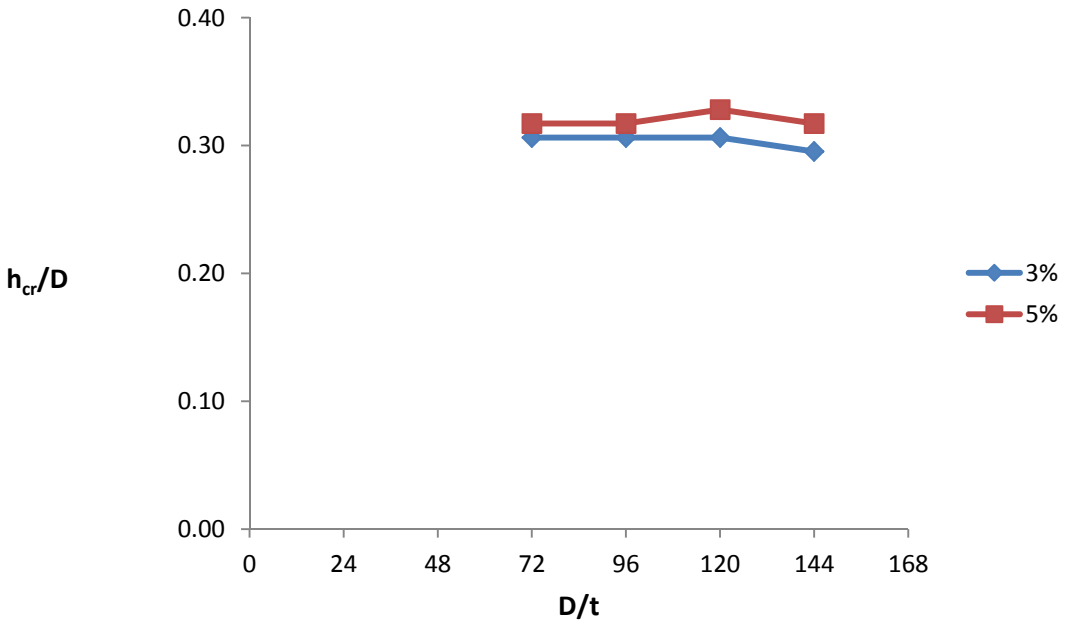

Figure 3.2.1. (a) The undeformed and deformed shape of the Fixed ends model for a normal fault of a vertical movement up to 2m. For this fault offset the pipe is deformed way above the operational strain limits. (b) Critical fault displacement to pipe diameter h_{cr}/D ratio versus the diameter to thickness ratio D/t for D/t=72-114.

(a)

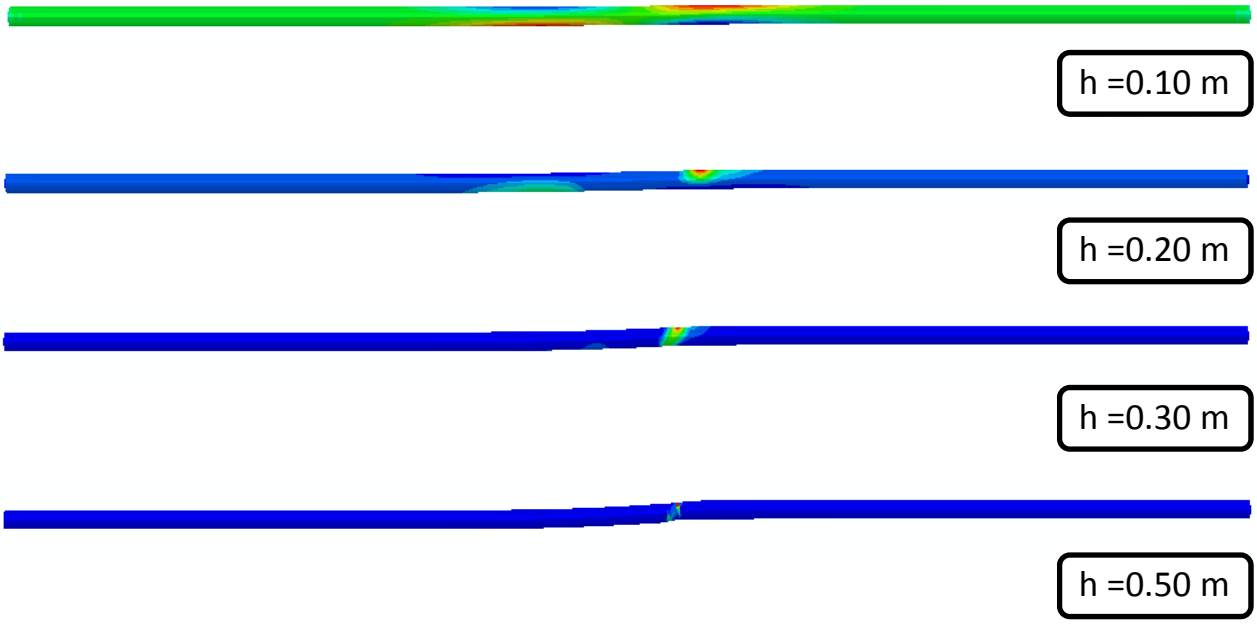

(b)

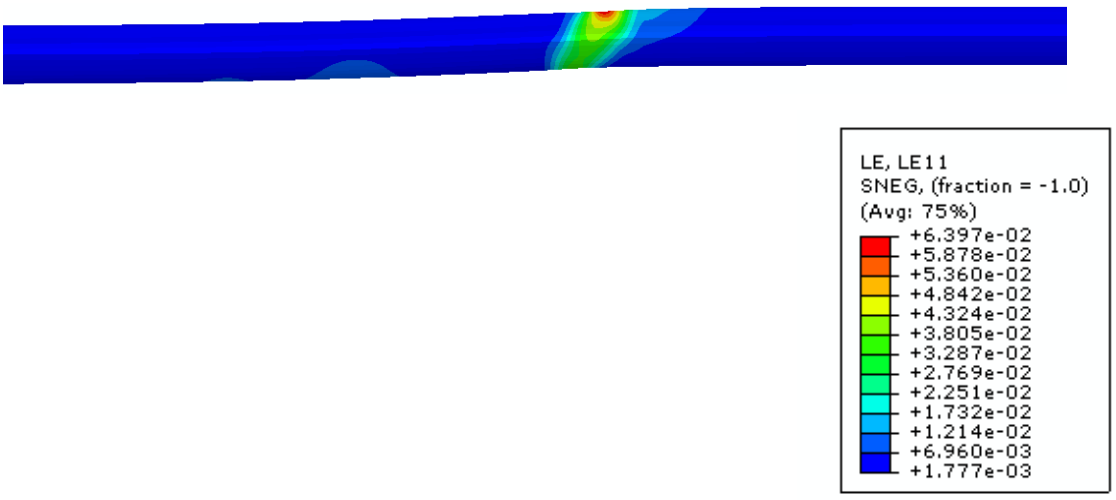

Figure 3.2.2. (a) The deformation of the pipe for four vertical fault. (b) Axial strain at h=0.3m exceeding the upper limit of 5%.(D/t=72, Fixed Ends)

(a)

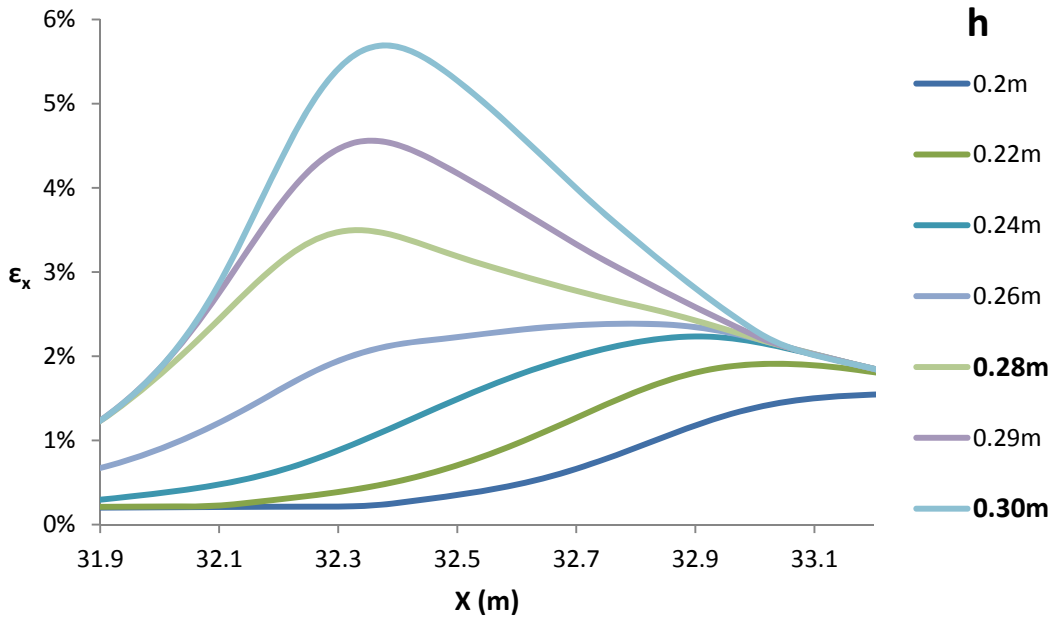

(b)

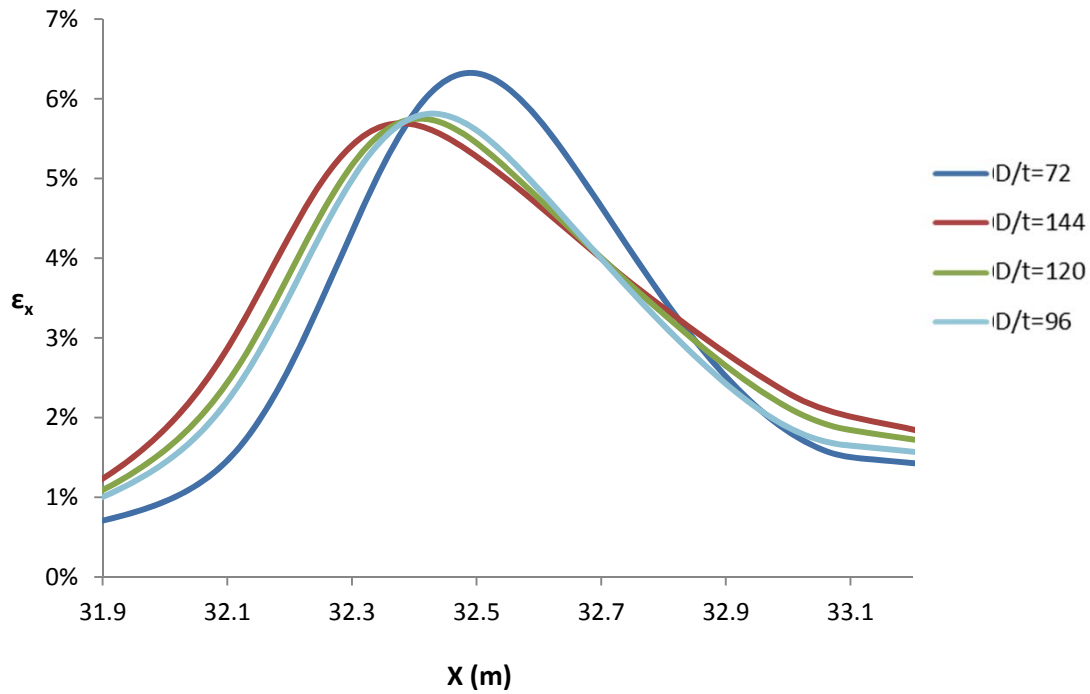

Figure 3.2.3. (a) The evolution of axial tensile strain for vertical fault displacement up to 0.30m with 0.28m and 0.30m corresponding to h_{cr} for 3% and 5% respectively. (D/t=144). (b) Comparison of the axial strains between four different D/t ratios for the critical state of strain values above 5%. (Fixed Ends)

(a)

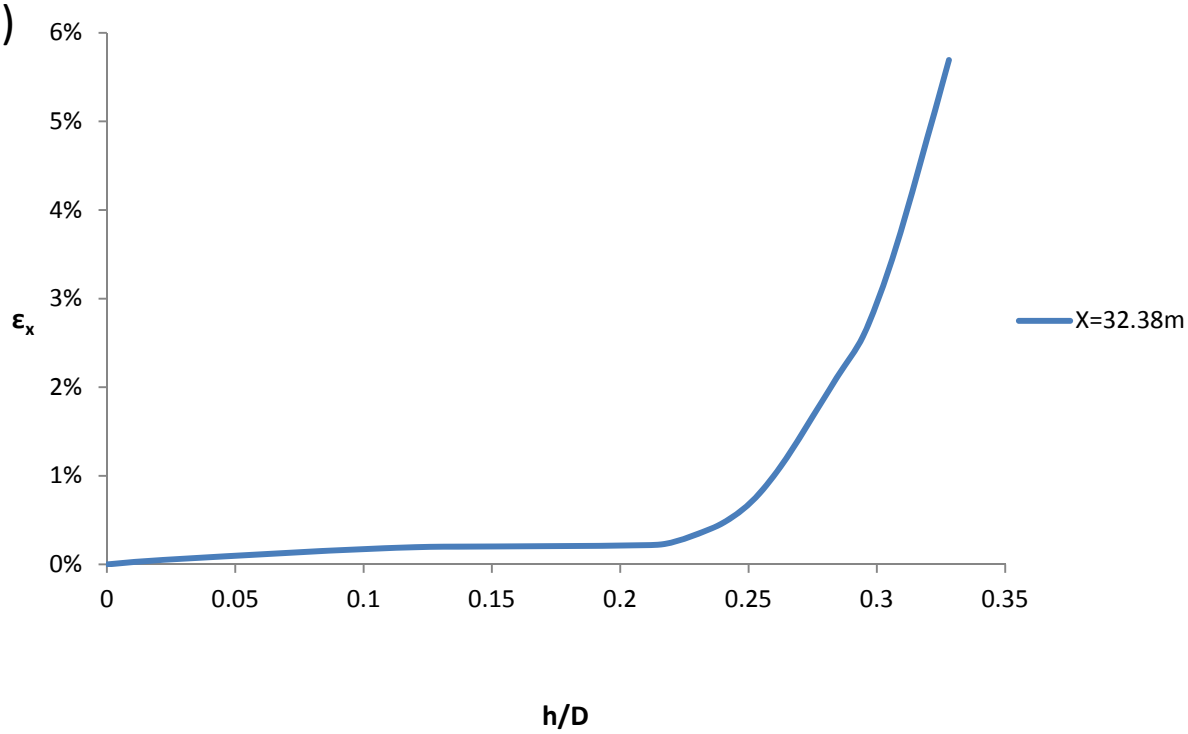

(b)

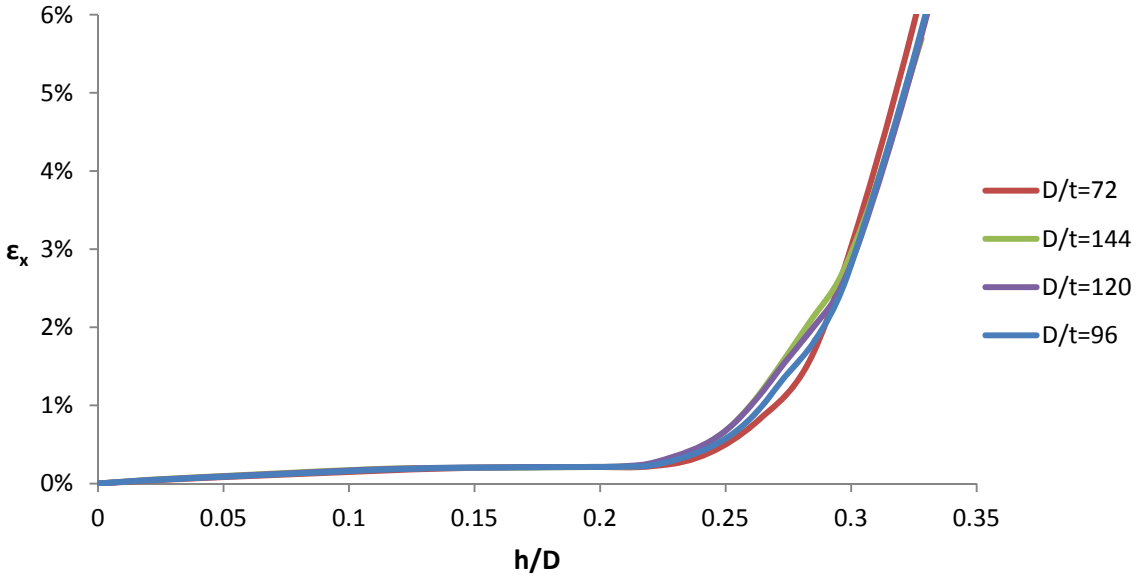

Figure 3.2.4. (a) The axial strain of the most deformed element of the pipe at position X=32.38 versus the h/D ratio. (b) Comparison of the axial strain of the most deformed point of the pipe between four different D/t ratios (Free Ends)

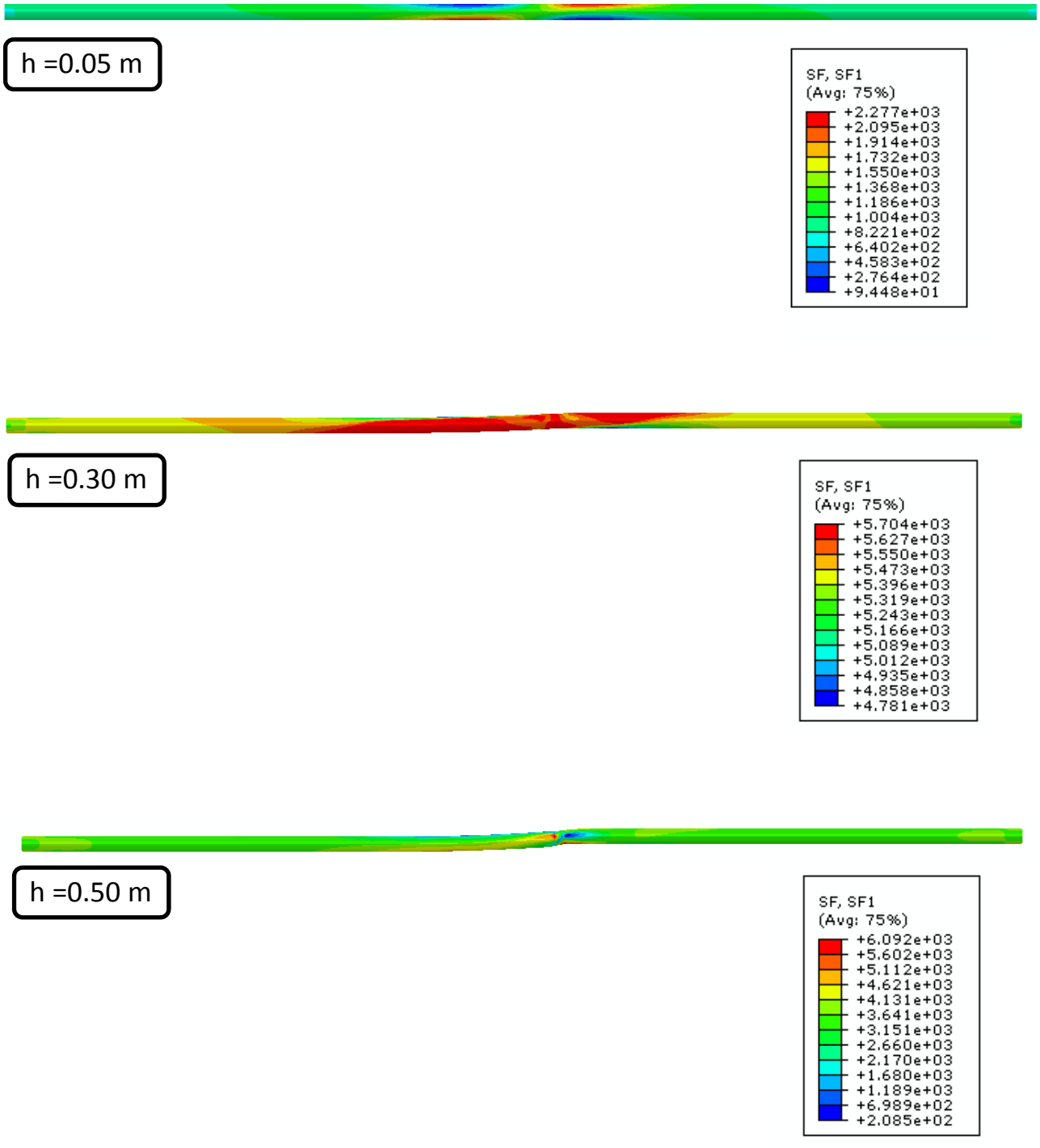

Figure 3.2.5. The distribution of the axial force along the pipeline for three different values of vertical fault movement h. (D/t=72, Fixed ends)

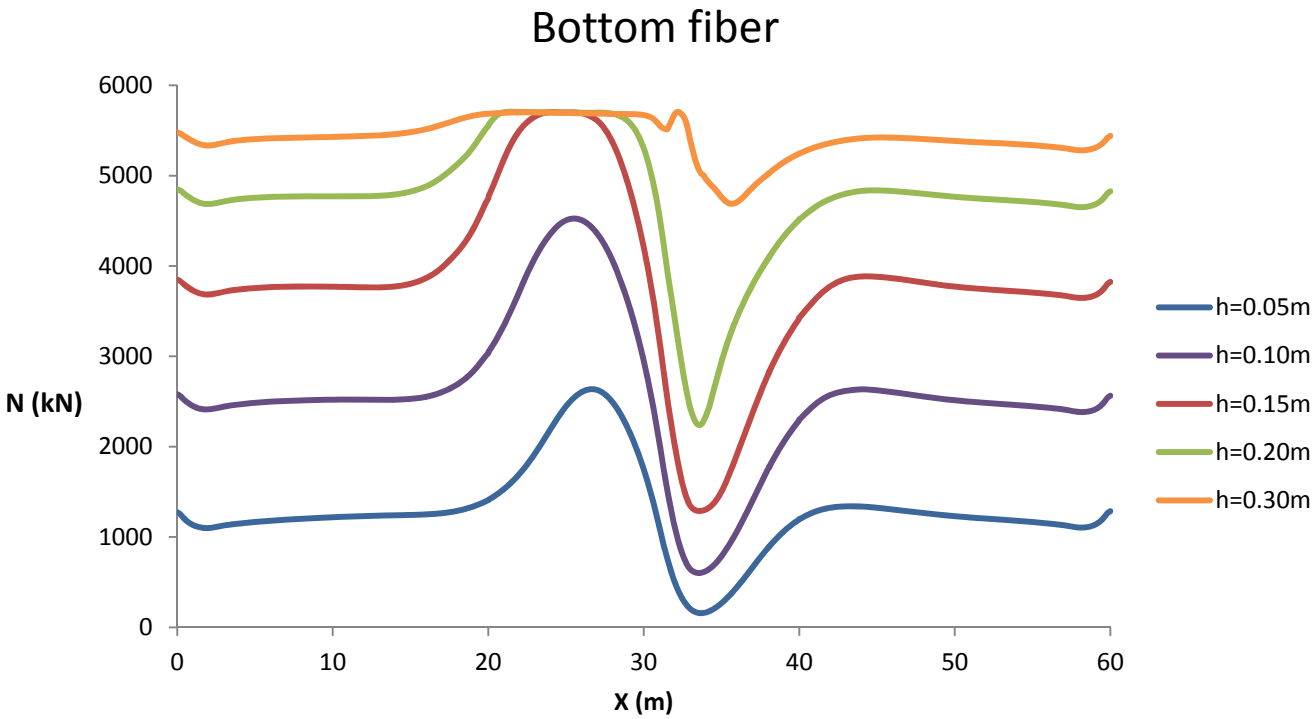

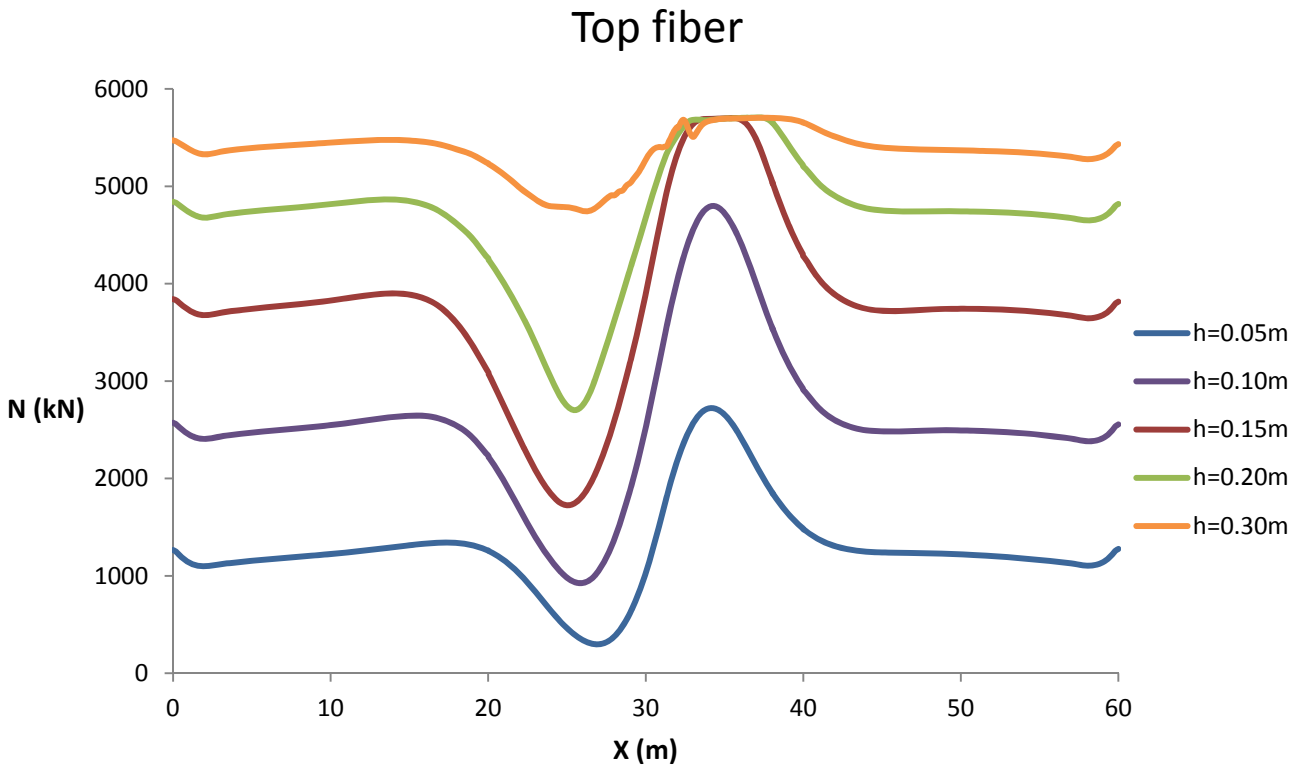

Figure 3.2.6. The distribution of the axial force along the pipeline for five different values of vertical fault movement h. (D/t=72, Fixed ends)

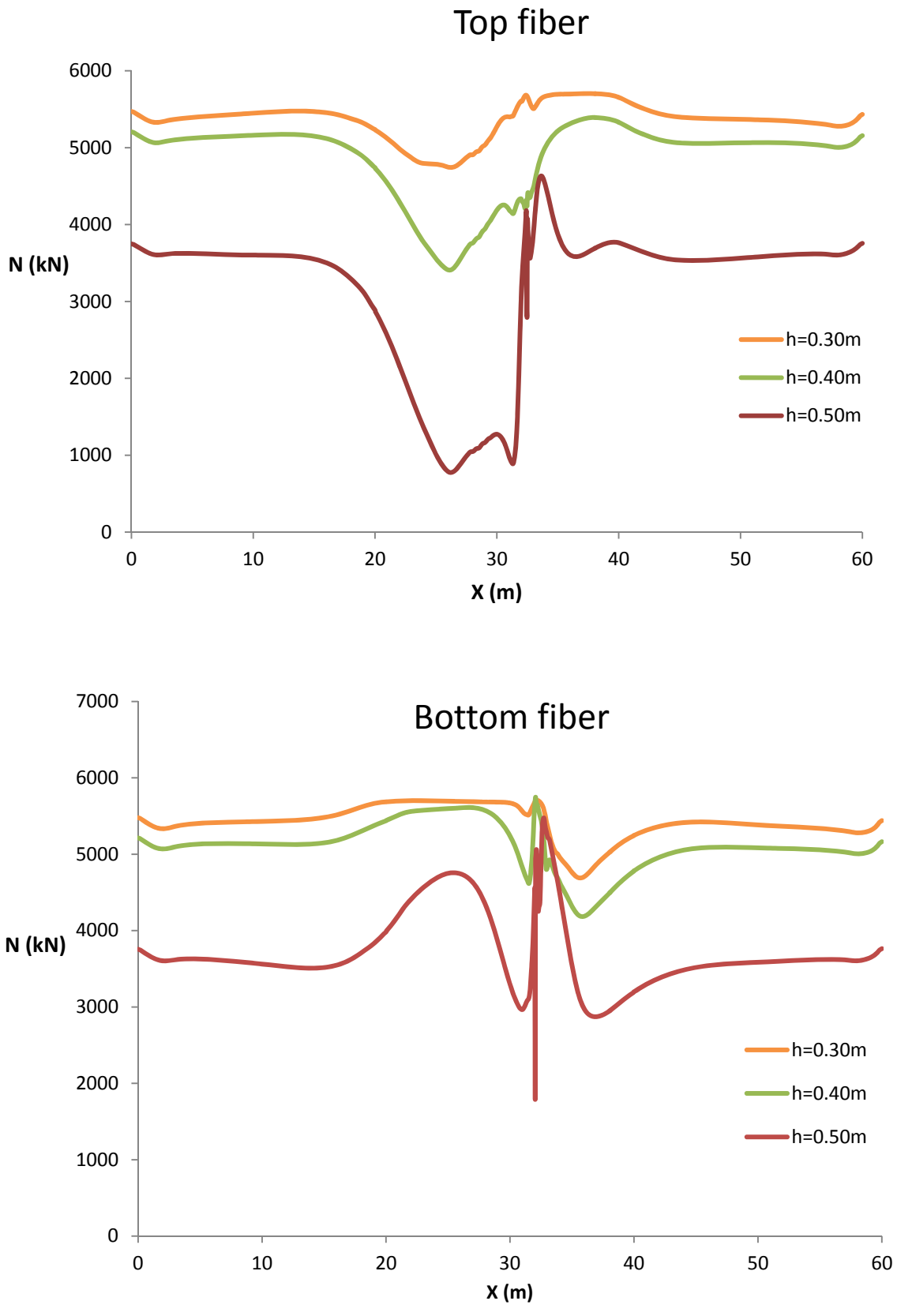

Figure 3.2.7. The distribution of the axial force along the pipeline for three different values of vertical fault movement h. The h=0.30m is the critical displacement above which we observe a general decrease and distortion of the axial force distribution. (D/t=72, Fixed ends)

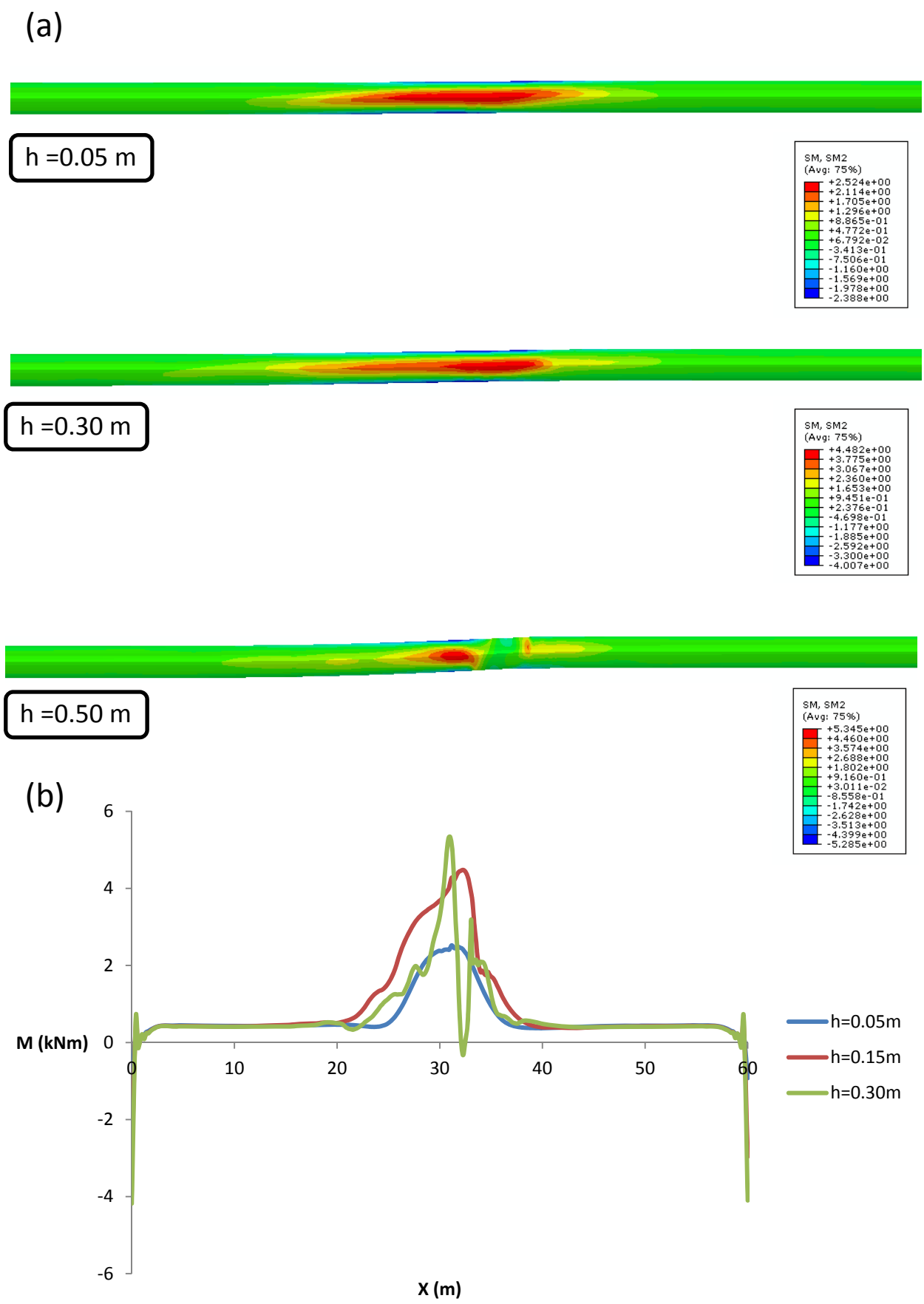

Figure 3.2.8. (a) Schematic distribution of moment along the pipeline and (b) diagrammatic distribution of moment along the middle pipe fiber., for three fault displacements.
(D/t=72, Fixed ends)

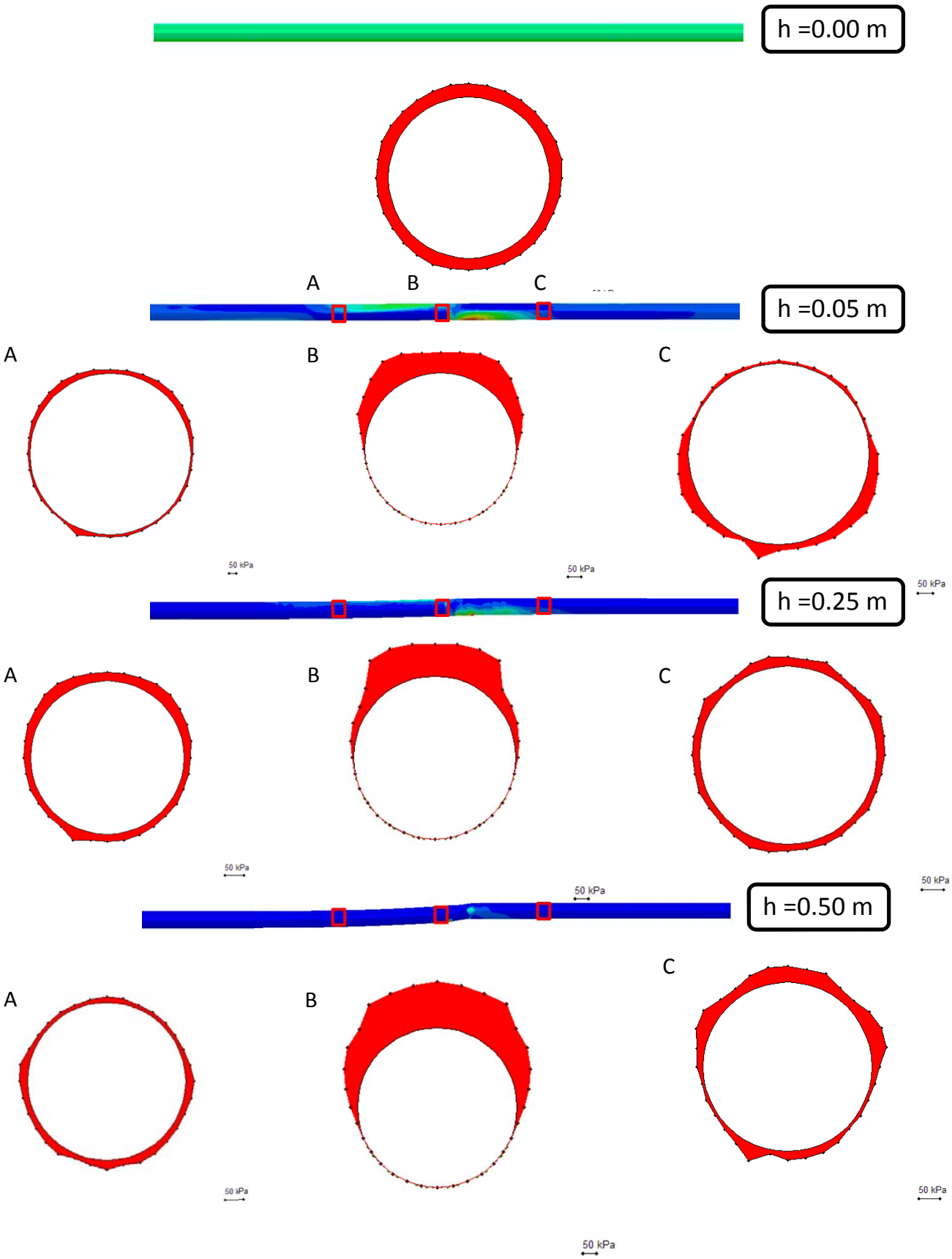

Figure 3.2.9. The distribution of soil pressures along the pipeline and along the pipe cross-section a three points A,B and C (X=20, 40 and 60m respectively) for four vertical fault displacements h. (Dense sand, D/t=72, Fixed ends)

Hybrid-Beam model

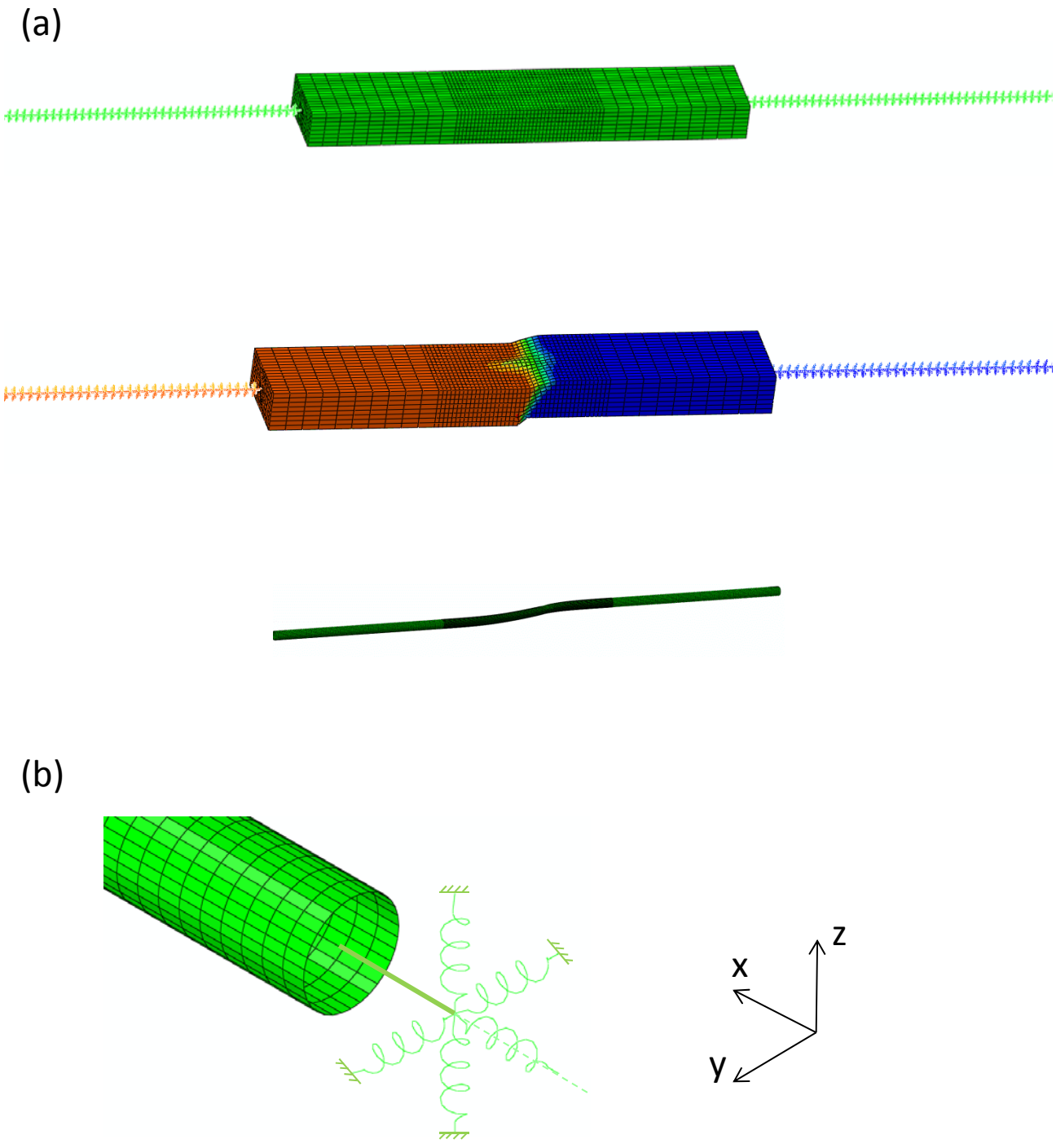

Figure 3.3.1. (a) The hybrid-beam model, initial and deformed shape . (b) Detail of the beam and spring elements connected to the pipe end.

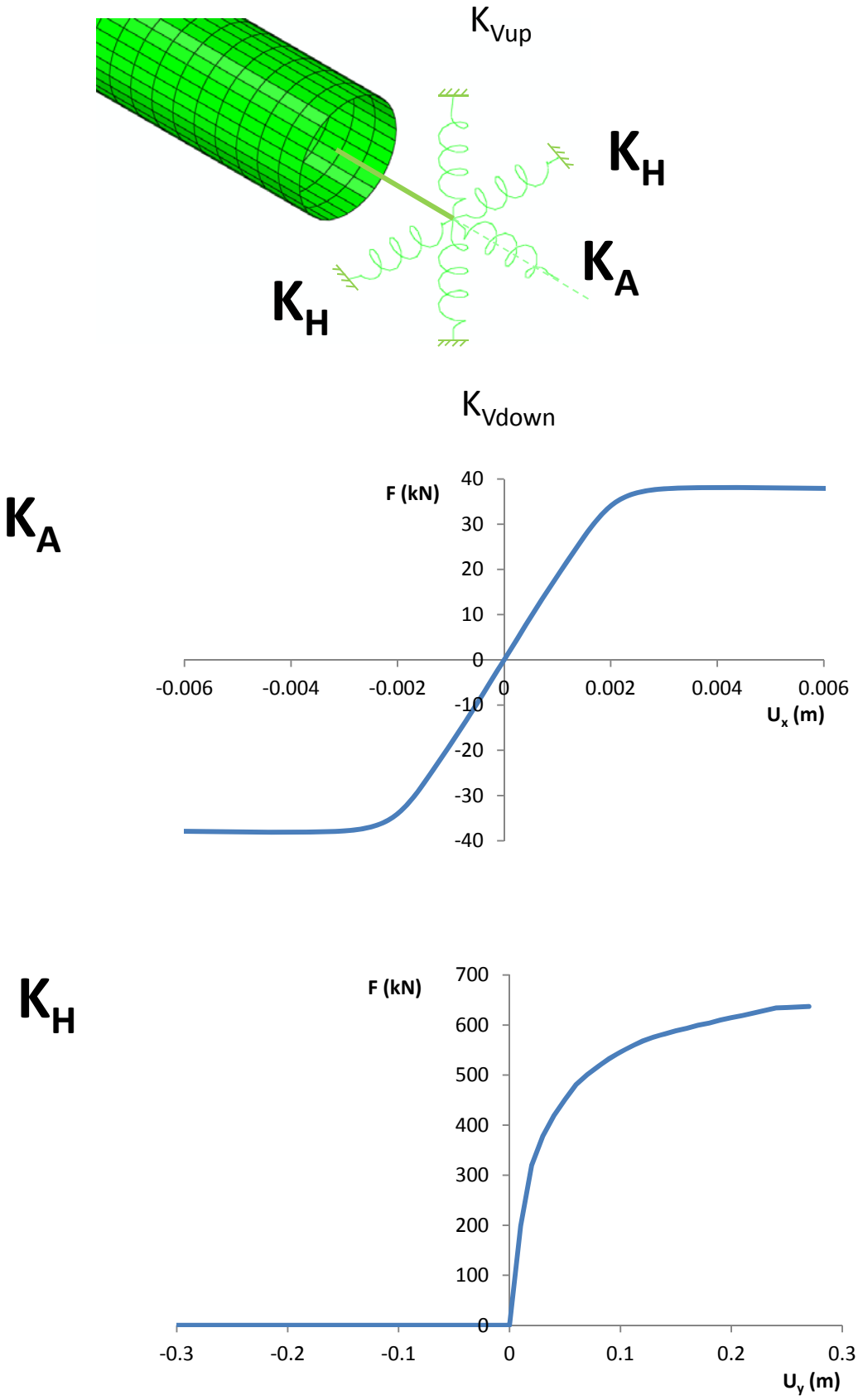

Figure 3.3.2. Spring force with respect to the axial displacement (K_A) and to the horizontal displacement (K_H).

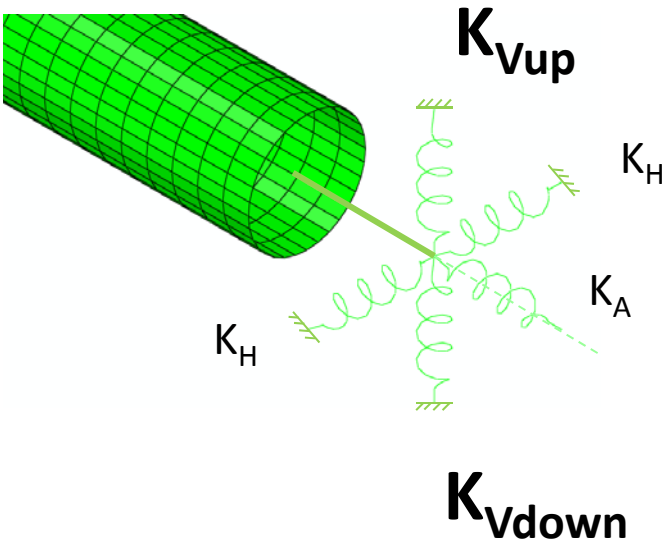

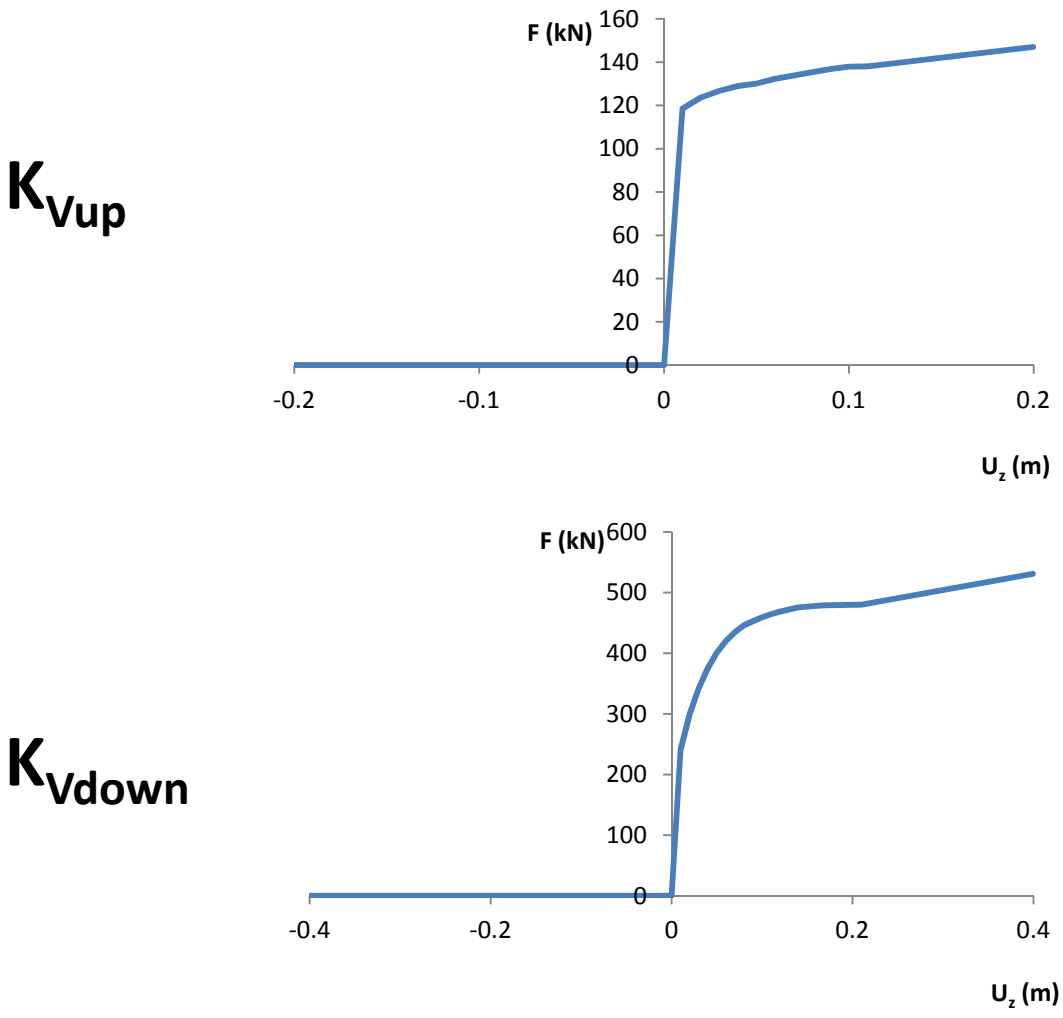

Figure 3.3.3.. Spring force with respect to the vertical displacement U_z for the two vertical springs that are activated by upward (K_{Vup})and downward (K_{Vdown}) movement respectively. The forces of the downward spring are greater because of the bigger passive soil resistance that develops against downward movement in comparison with the smaller soil resistance that the limited surface soil layer activates against the upward movement of the pipe.

(a)

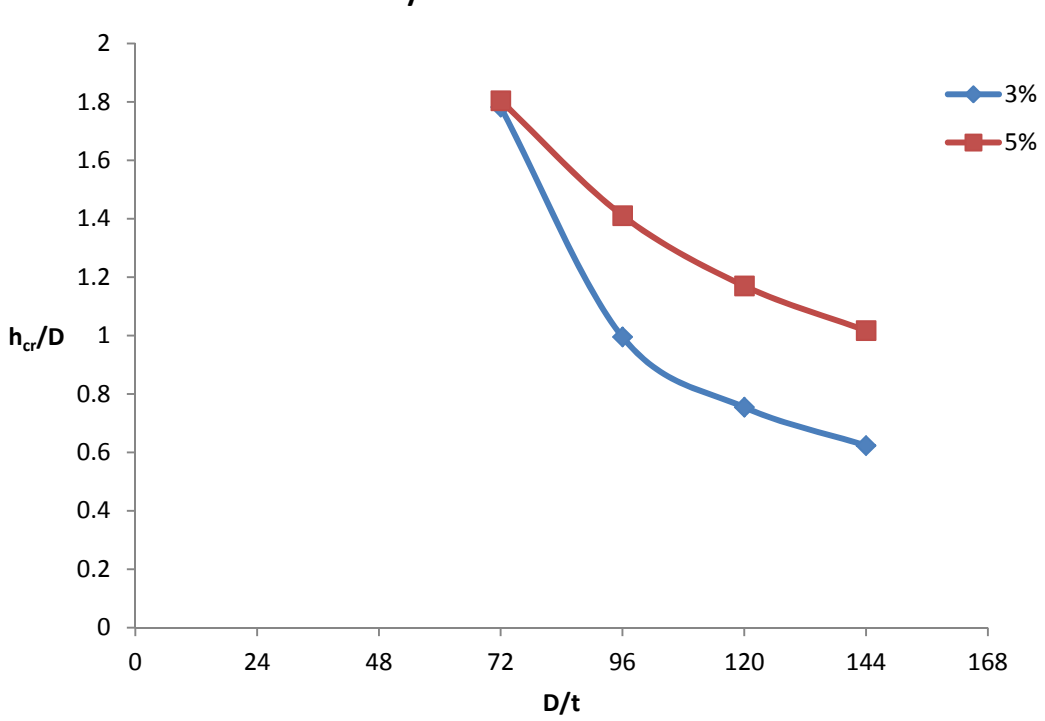

(b)

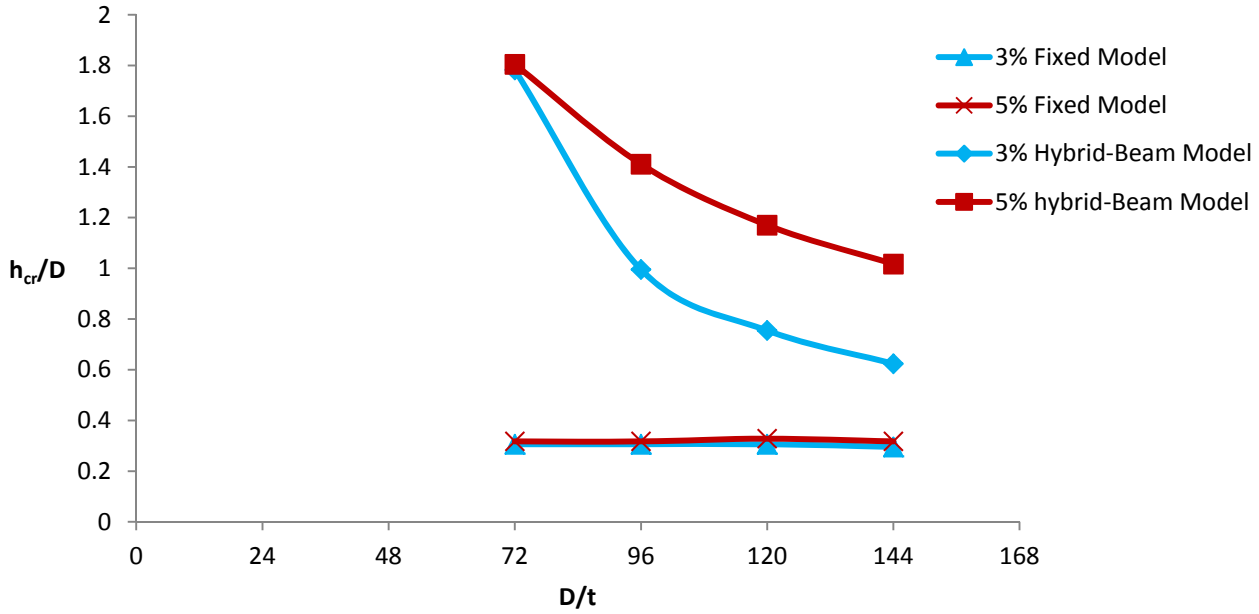

Figure 3.3.4. (a) Vertical critical displacement to pipe diameter h_{cr}/D related to the pipe diameter to thickness ratio for the Hybrid Beam model. (b) Comparison of the previous diagram with the relative one of Fixed ends model.

(a)

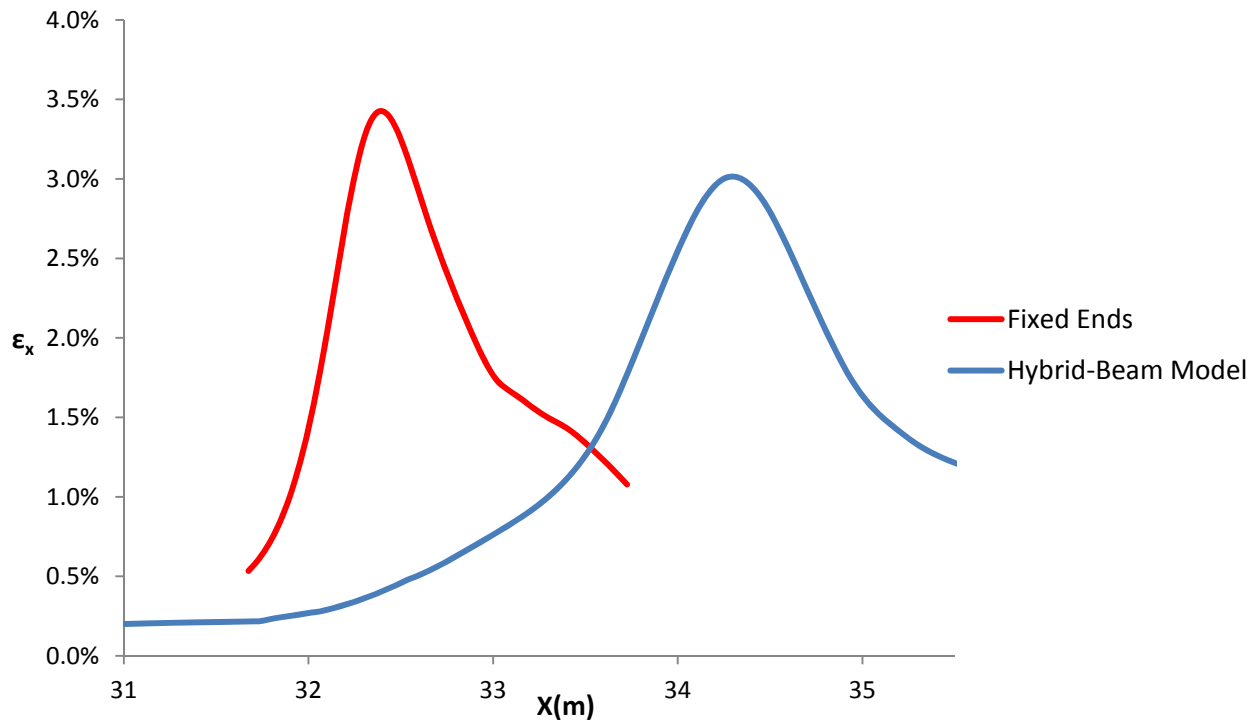

(b)

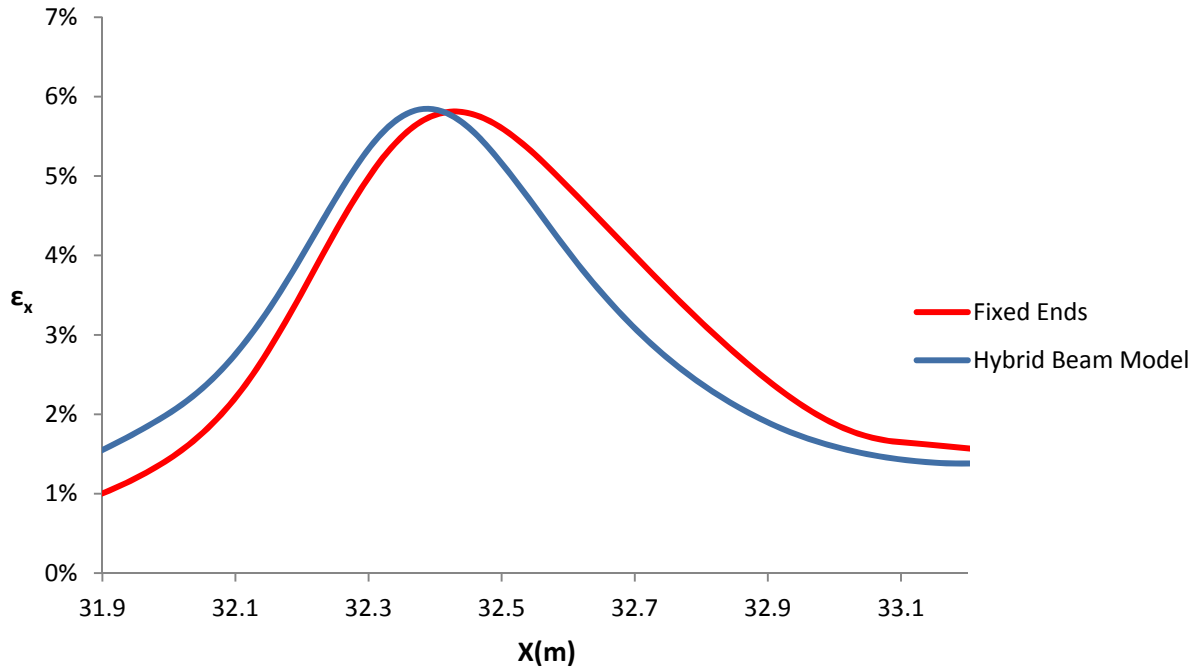

Figure 3.3.5. Comparison of the axial strain distribution between the Fixed ends model and the Hybrid Beam model, at the two critical states of (a) 3% tensile strain and (b) 5% tensile strain. (D/t=96)

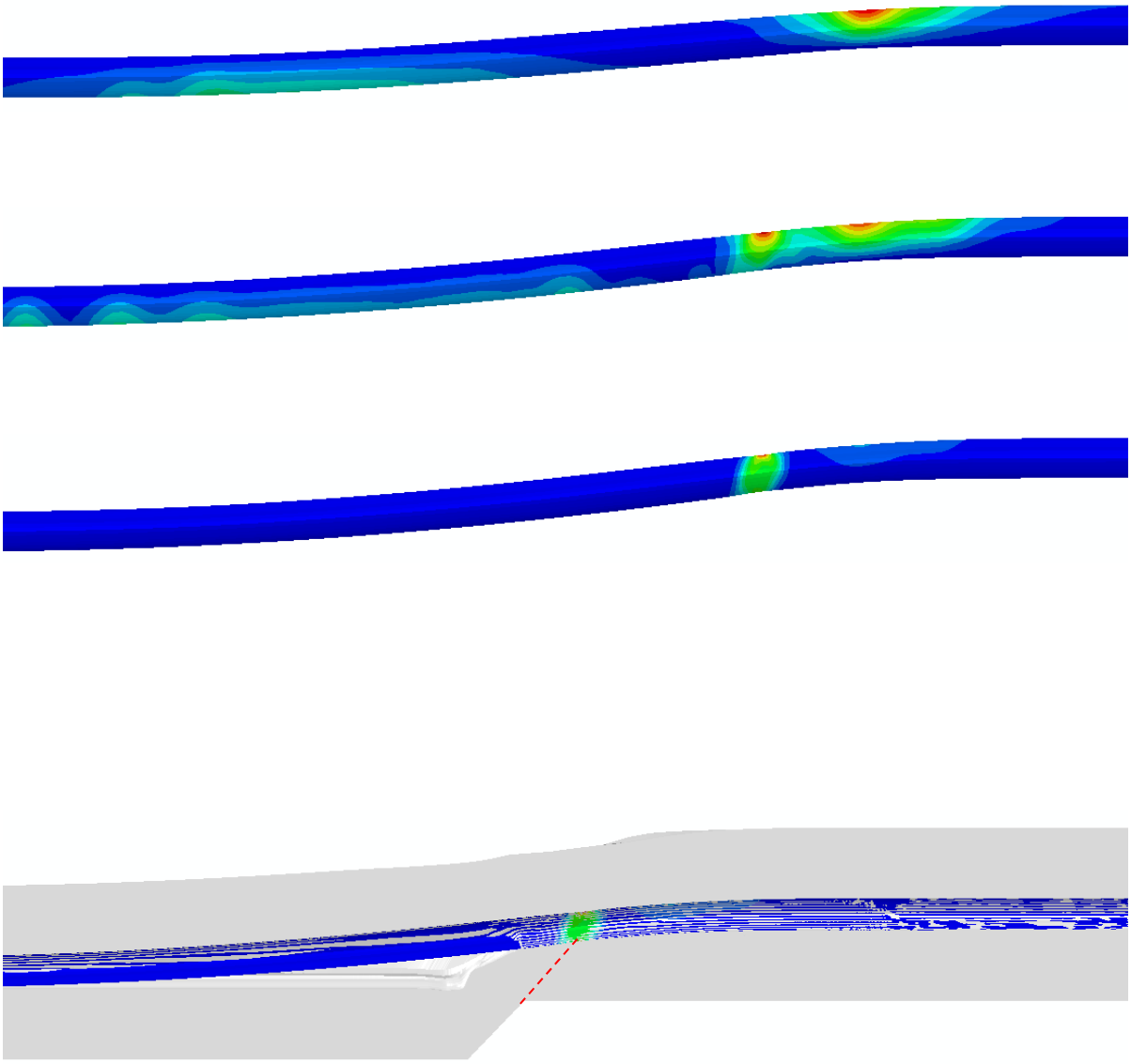

Figure 3.3.6. Bending mechanism prevails from the beginning of fault displacement until the point where the big relative displacement of the hanging wall and the footwall causes the change of the loading mechanism.

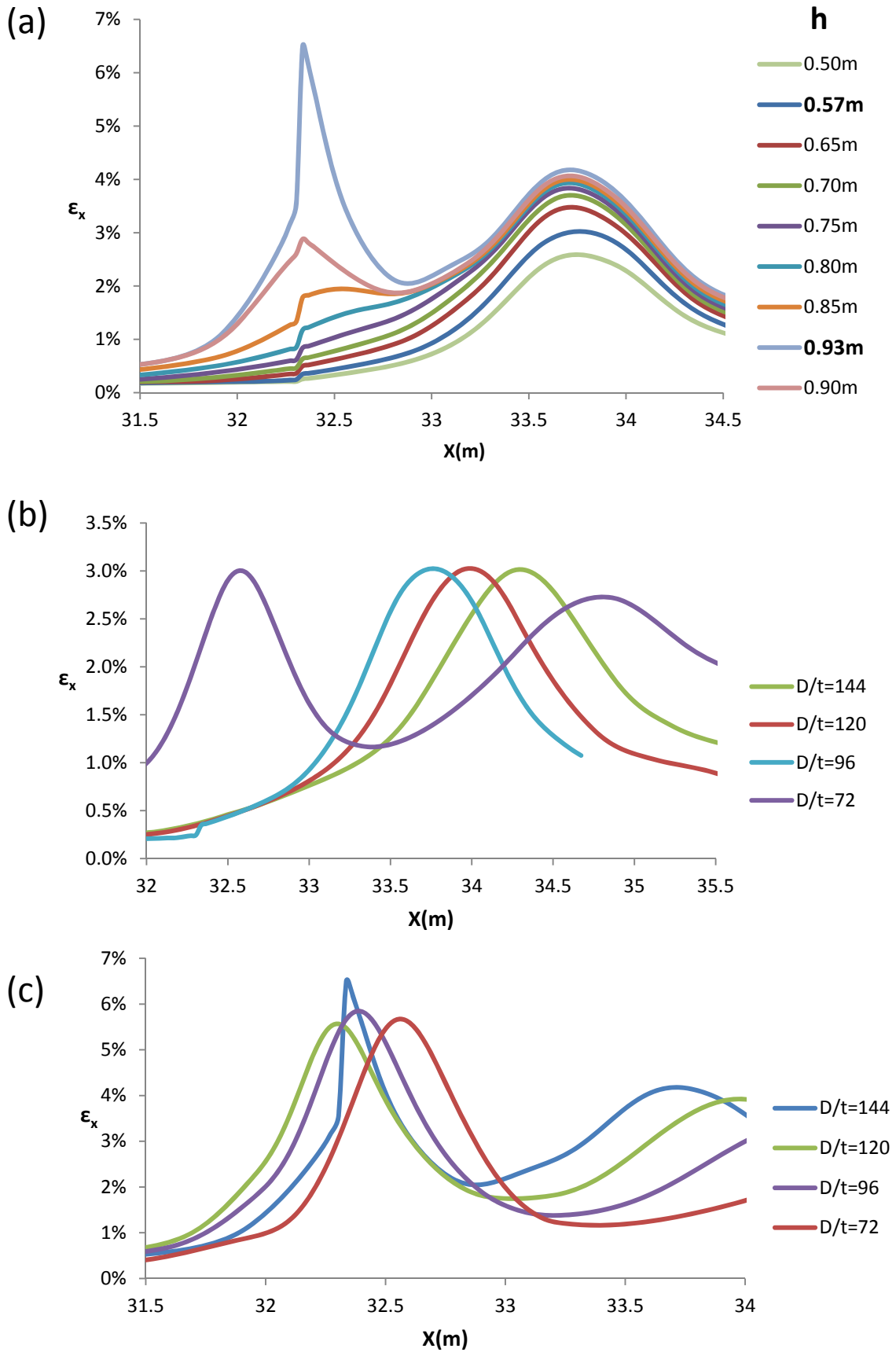

Figure 3.3.7. (a) Axial tensile strain distribution and development along the critical area (D/t=144). Comparison of axial tensile strain distribution between the four different D/t ratios for the limit states of (b) 3% tensile strain and (c) 5% tensile strain.

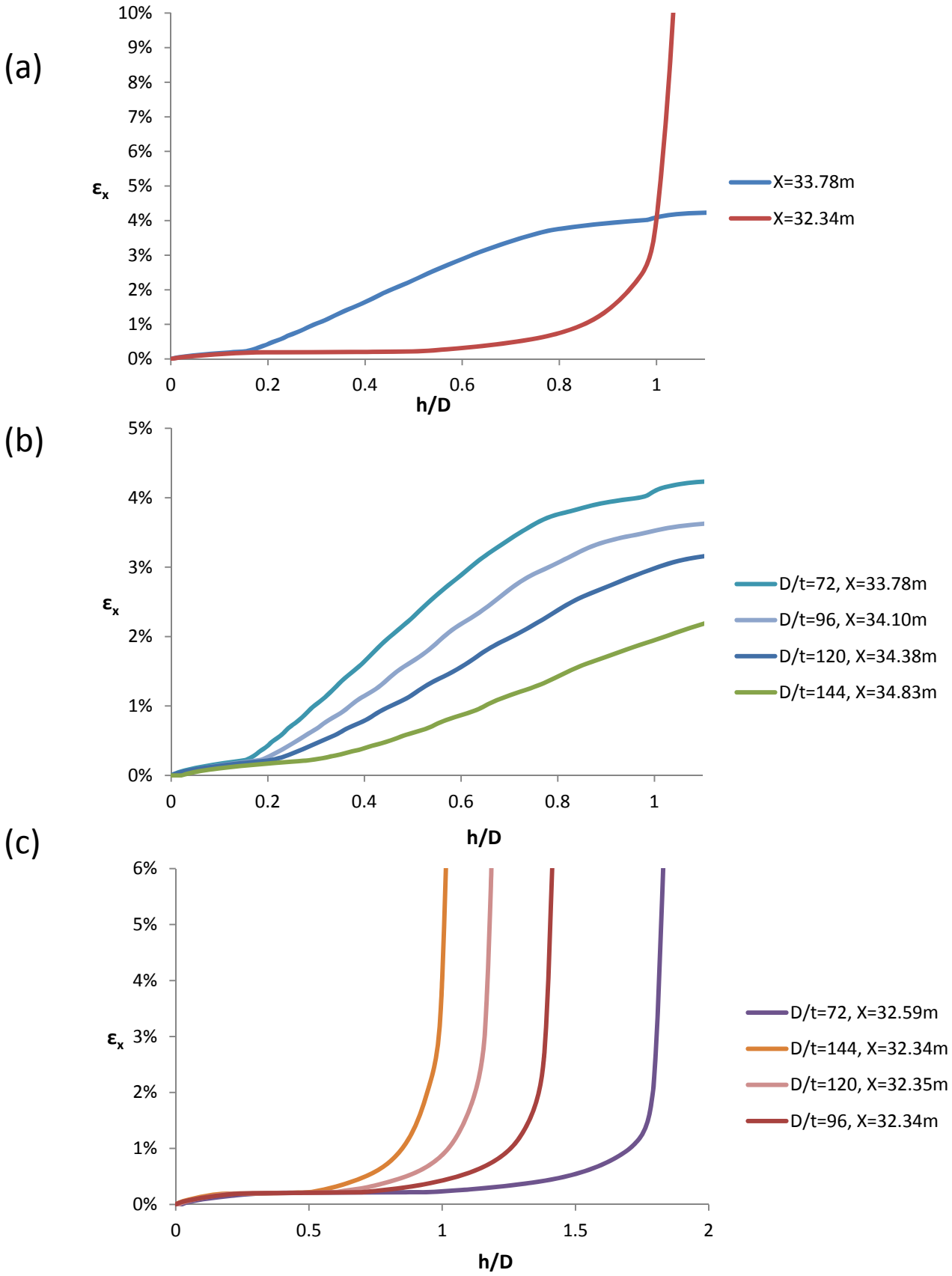

Figure 3.3.8. (a) Axial tensile strain development with respect to the vertical fault displacement to diameter ratio at two points X=33.78 and X=32.34m where the limits of 3% and 5% tensile strain are reached , caused by bending and shearing respectively (D/t=144). (b) The axial strain development at the points where the 3% tensile strain is reached for four D/t ratios. (c) The axial strain development at the points where the 5% tensile strain limit is reached for four D/t ratios.

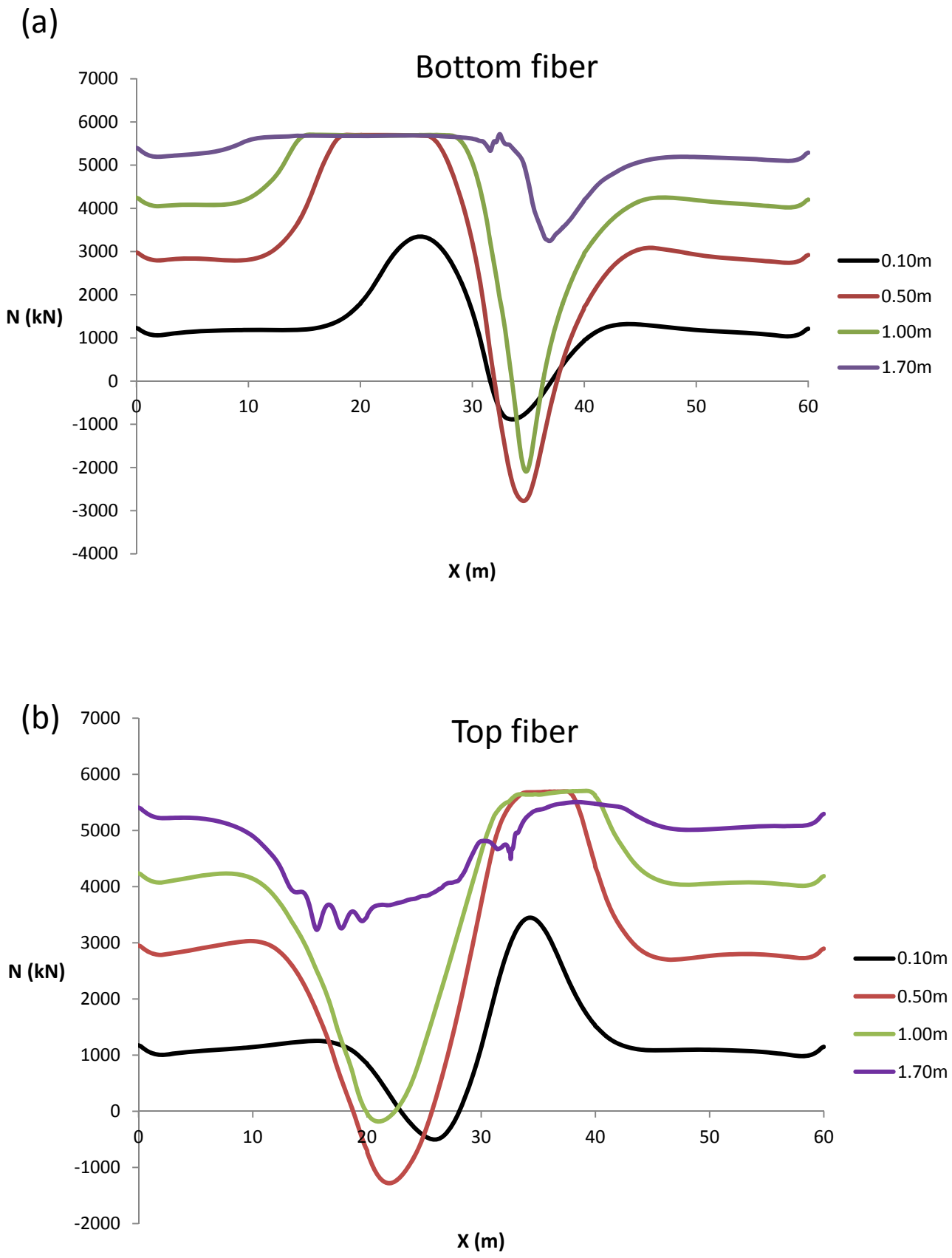

Figure 3.3.9. Axial forces along (a) the top and (b) the bottom pipe fiber, for four values of vertical fault displacement.

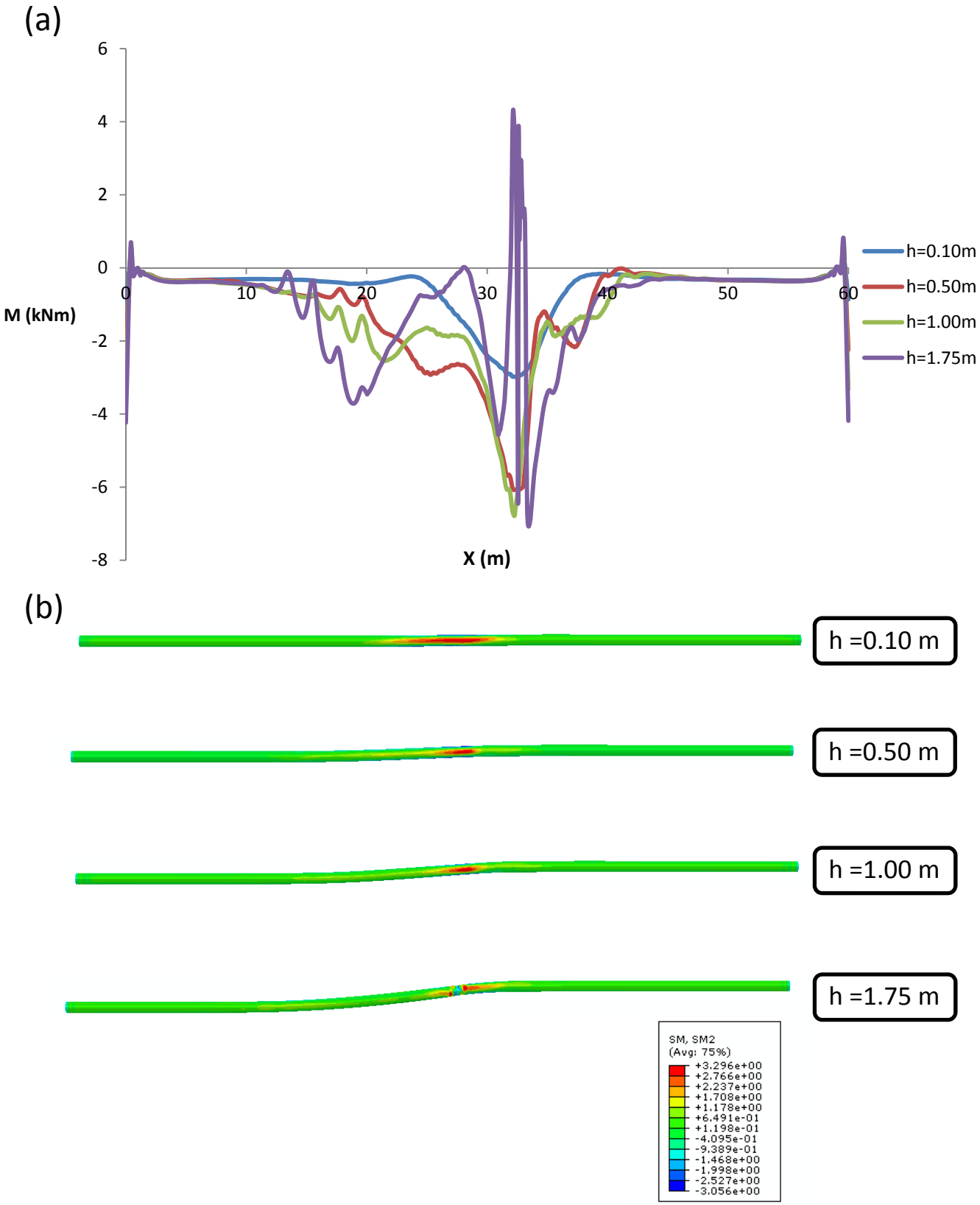

Figure 3.3.10. (a) Diagrammatic distribution of moment along the top pipe fiber and (b) schematic display of moment values along the pipe.(D/t=72)

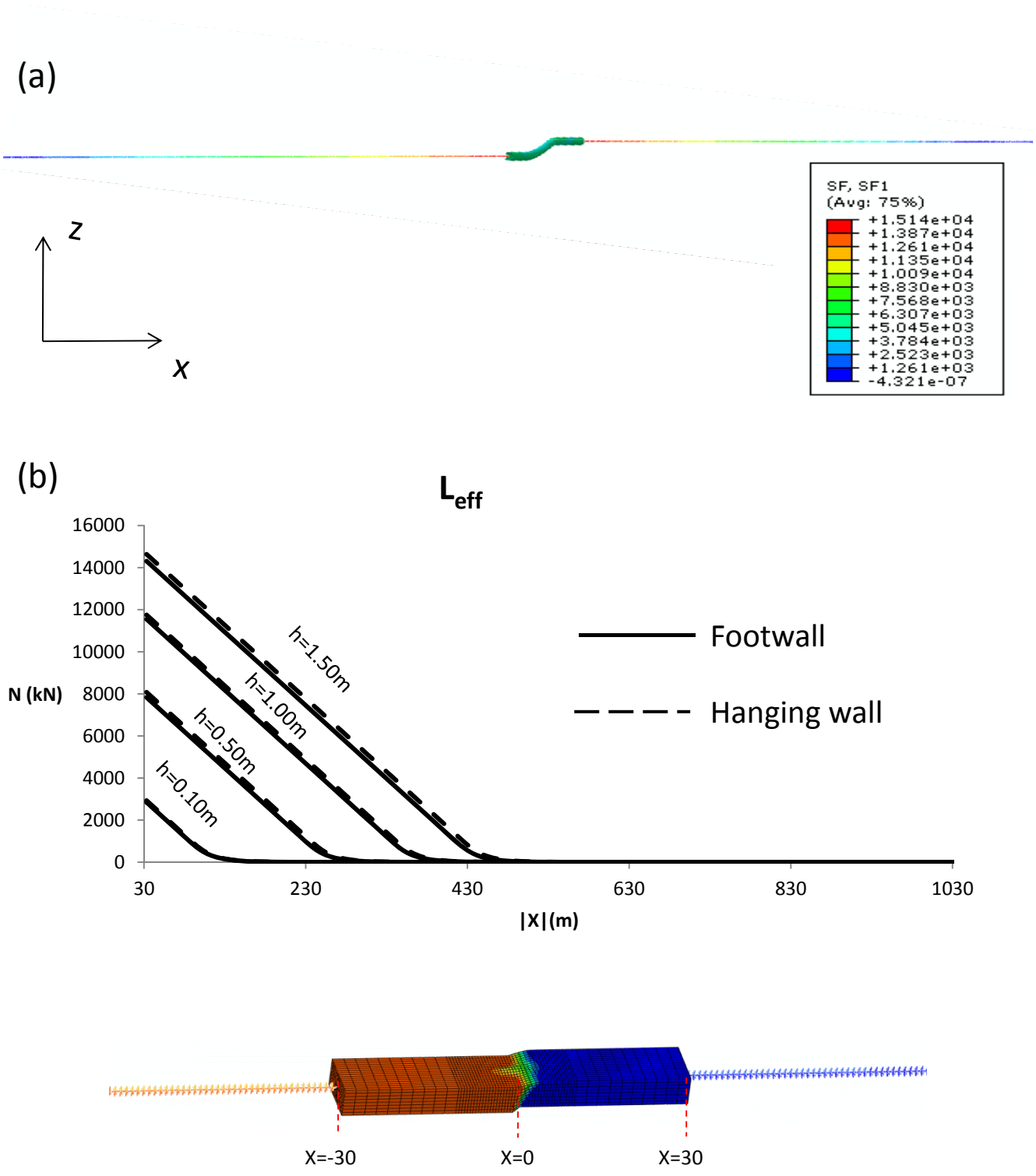

Figure 3.3.11. (a) The axial force distribution along our model. We consider as L_{eff} the length of the segment that extends from the fault-pipe intersection point (practically at the middle of the model) to the point where the axial force is almost 0. (b) Comparison of the axial forces along the two beam parts of the model at the hanging wall and at the footwall respectively., no significant difference is observed.

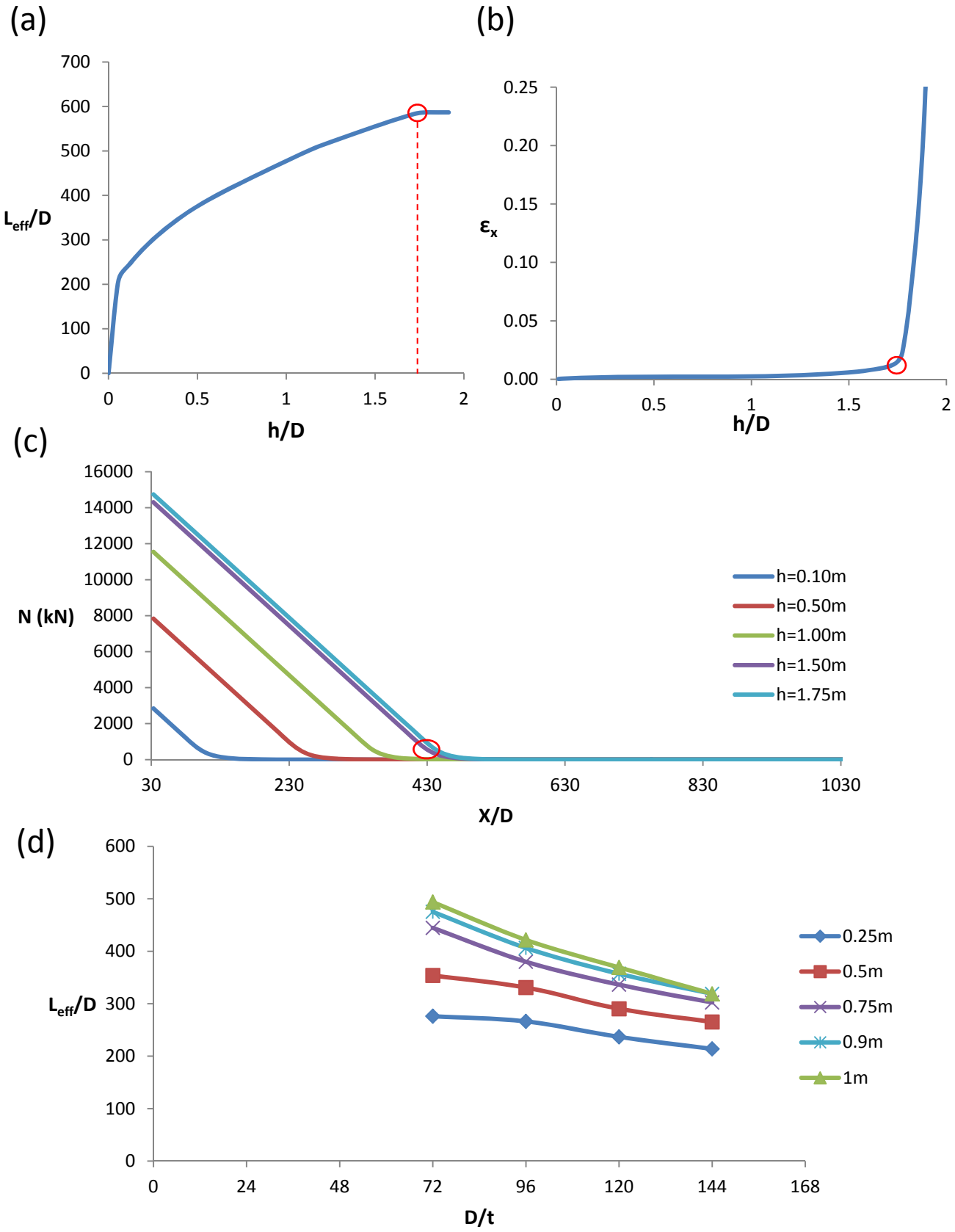

Figure 3.3.12. (a) The effective length (hanging wall side) with respect to the vertical fault displacement . (b) The axial tensile strain at the point of failure. (c) The axial forces along the beam elements of the hanging wall for five values of h. The increase rate of Leff remains stable for a few centimeters of fault displacement and then decreases as the fault displacement augments. When the tensile strain starts to increase rapidly (point of failure because of shear mechanism) the Leff practically stops increasing. (D/t=72) (d) The effective length Leff with respect to the diameter to thickness ratio D/t.

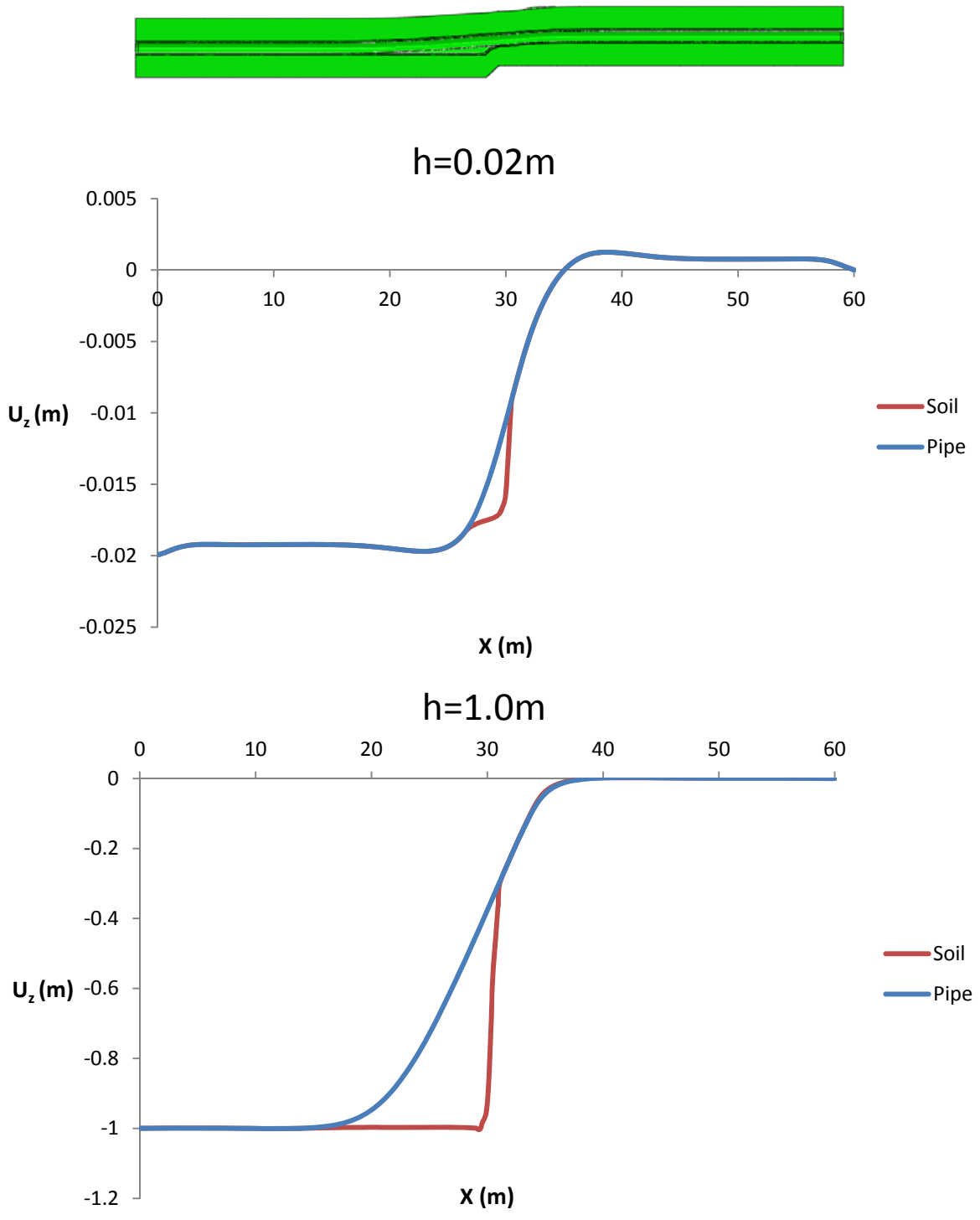

Figure 3.3.13. Detachment of the pipe from the surrounding soil depicted for two values of vertical fault displacement h, by comparing the vertical displacement of the bottom pipe fiber with the vertical displacement of the soil beneath. Gaping occurs almost instantly within the very first centimeters of fault displacement. (D/t=72)

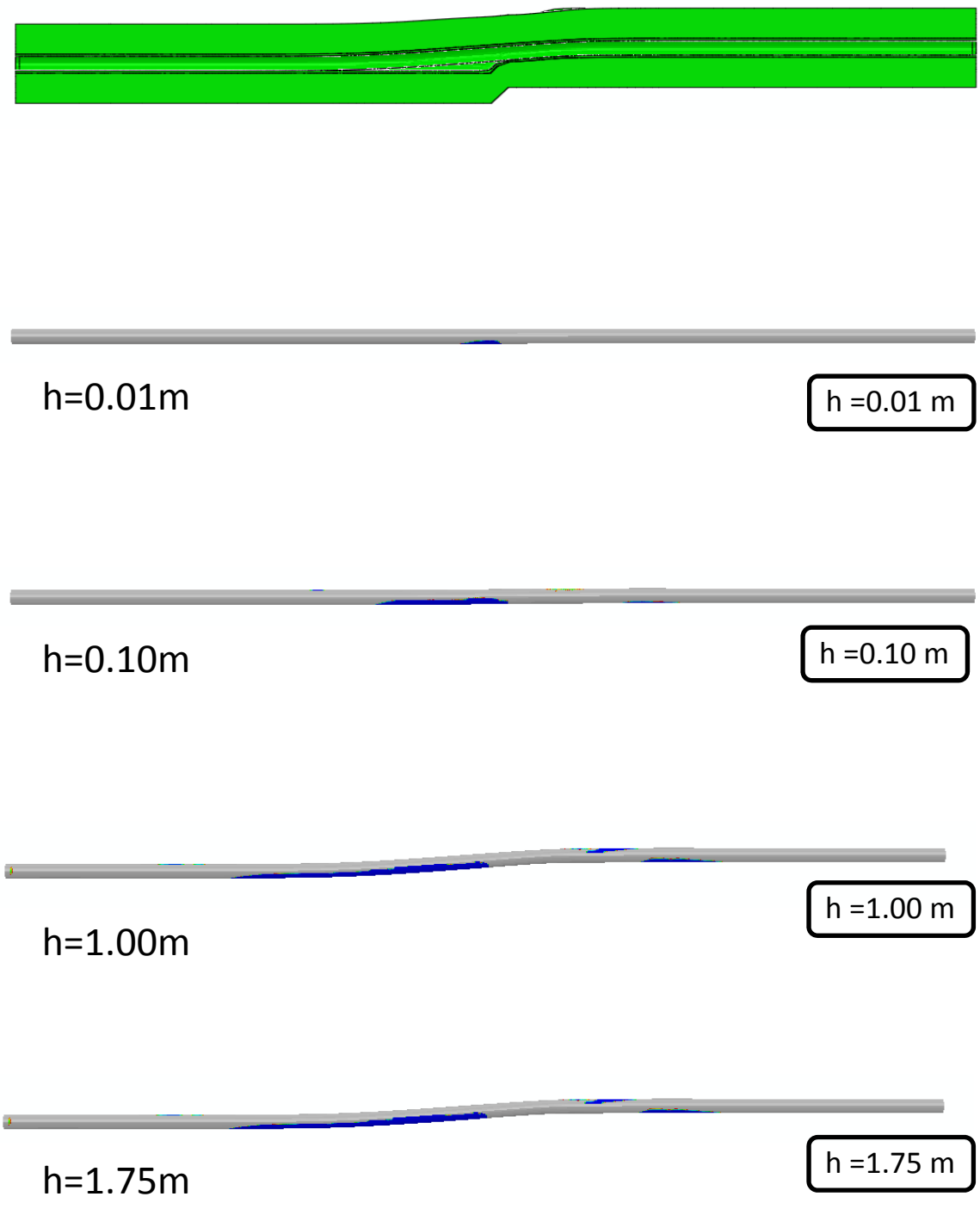

Figure 3.3.14. Pipe detachment from the surrounding soil can be clearly depicted based on the soil pressure on the pipe. When the soil pressure becomes zero (blue areas) ,the loss of contact between soil and pipe is indicated. The gaping is formed from the very beginning of fault displacement, its length increases as the fault displacement augments until a maximum point above which further fault displacement does not affect the length of the gaping area.

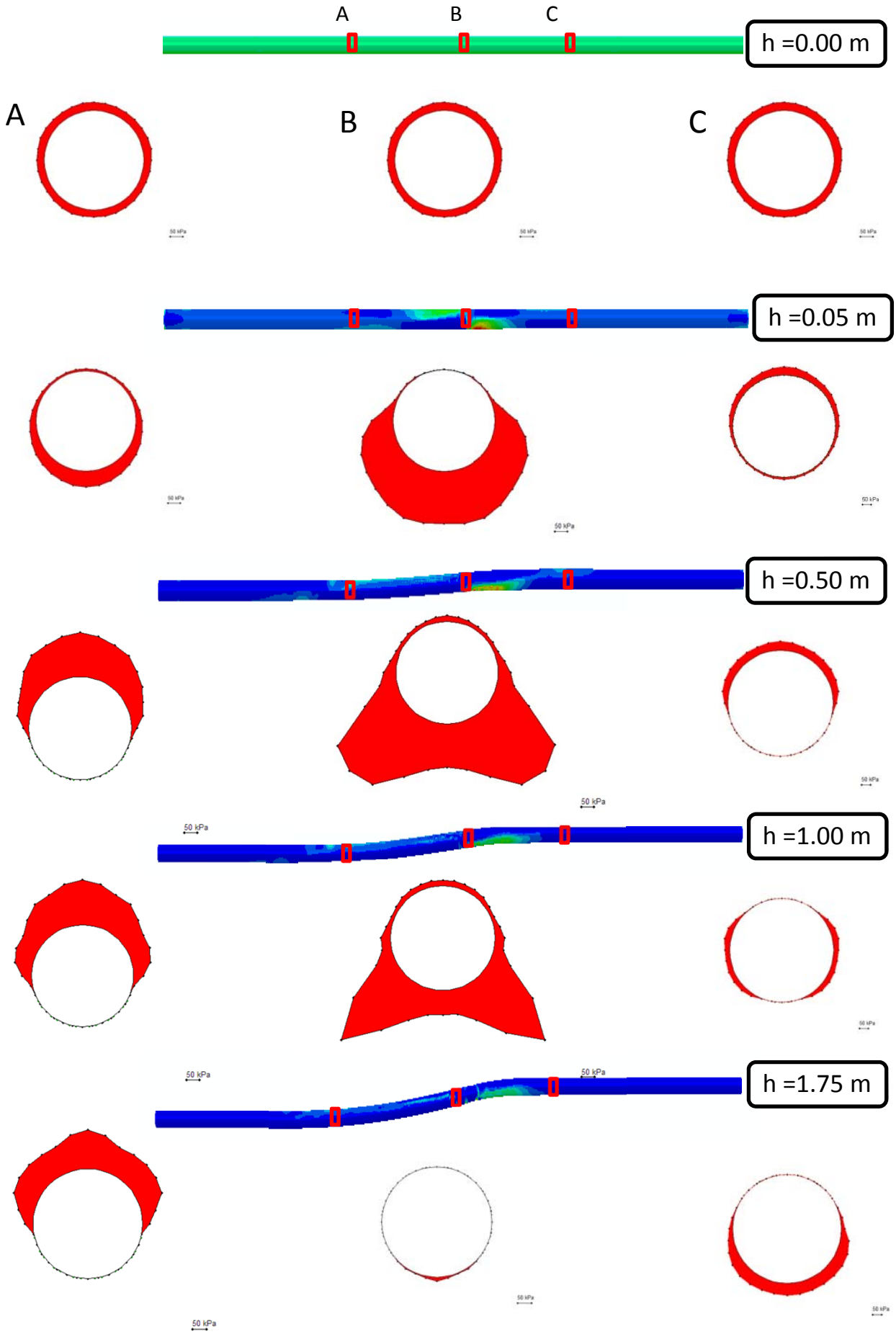

Figure 3.3.15. Soil pressure along three pipe cross-sections A,B and C (X=20,30 and 40m respectively) for several vertical fault displacement h. (D/t=72)

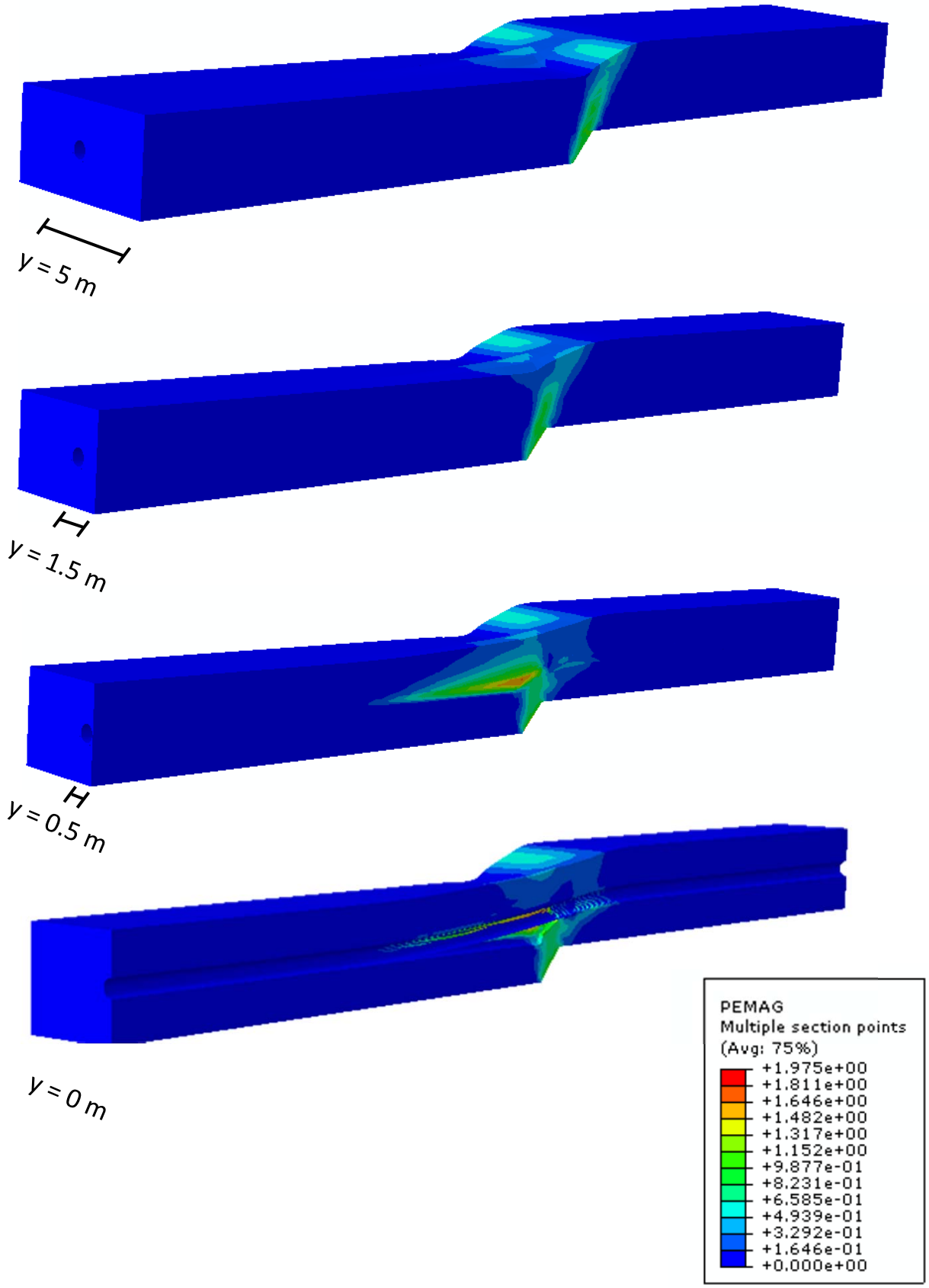

Figure 3.3.16. Magnitude of plastic strains for h=1.75 . Planes of various distances from the pipe are depicted. (y=0 corresponds to the vertical plane of the central pipe axis) (D/t=72).

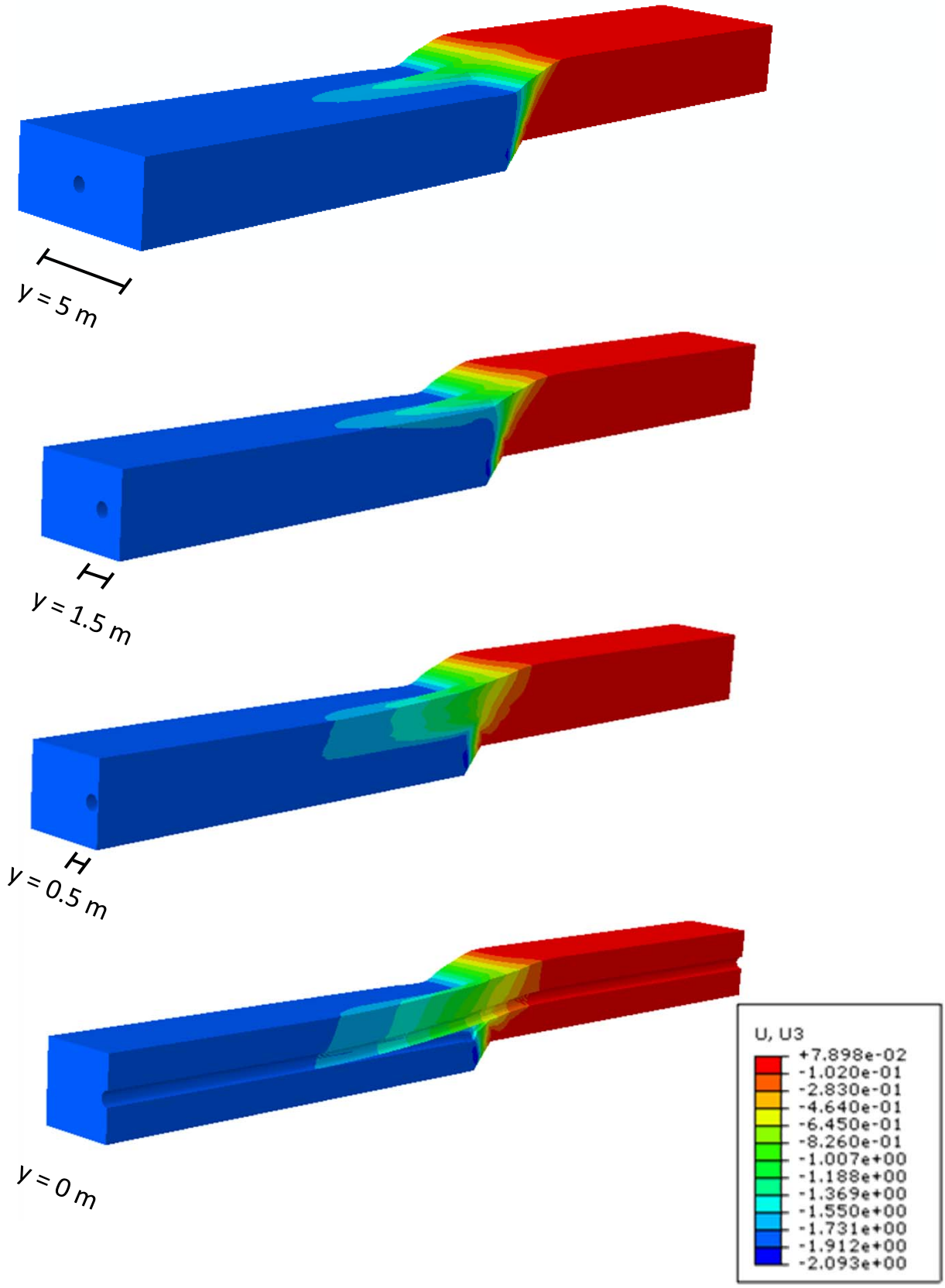

Figure 3.3.17. Vertical displacement distribution for vertical fault displacement h=1.75m. Planes of various distances from the pipe. (y=0 corresponds to the vertical plane of the central pipe axis) (D/t=72).

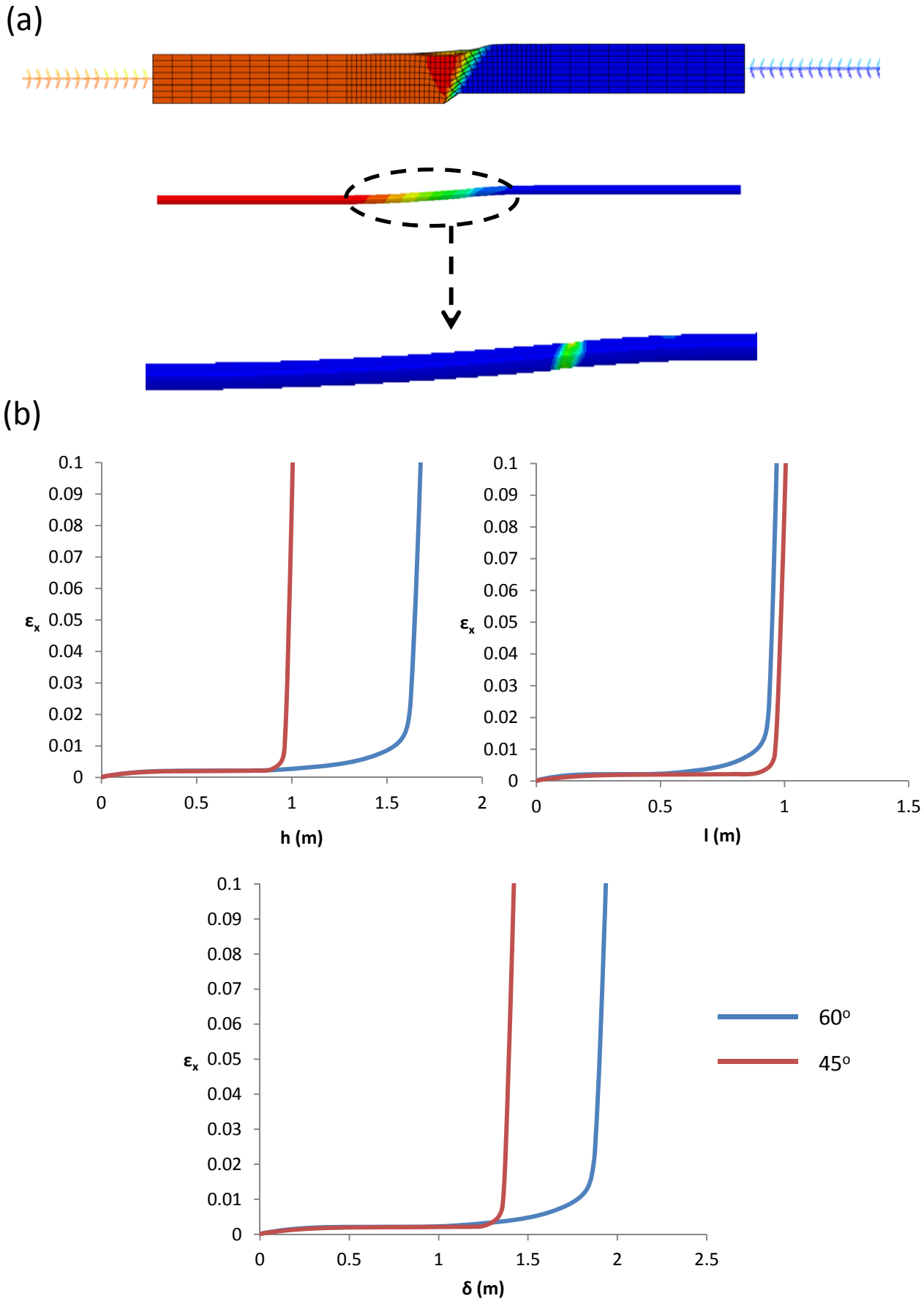

Figure 3.3.18. (a) The deformed soil and pipe for a normal fault of 45°. (b) Comparison between the 60° and 45° normal fault in terms of axial deformation with respect to the vertical fault displacement h, the horizontal fault displacement l and the total magnitude of displacement δ, (D/t = 72).

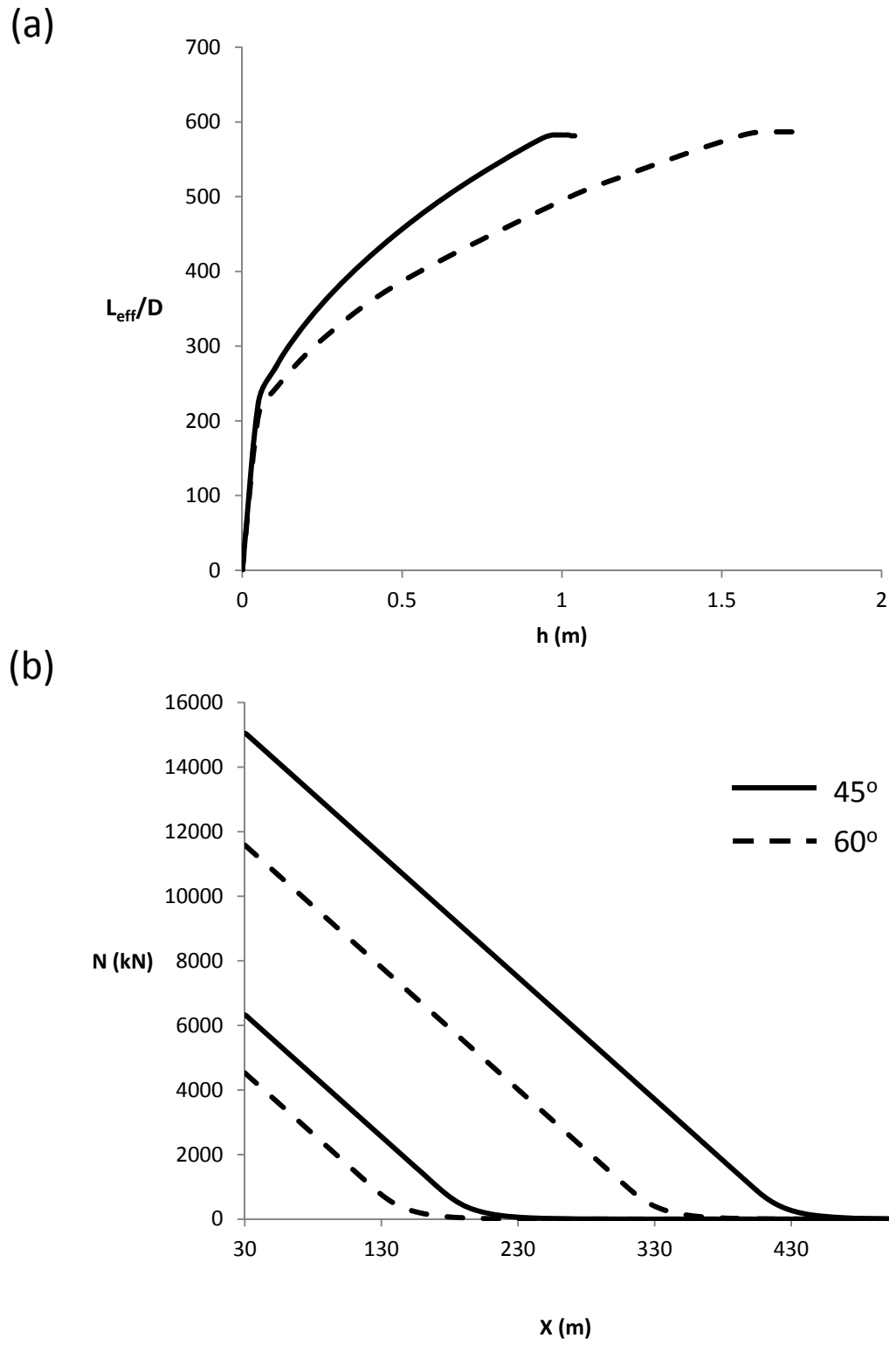

Figure 3.3.19. Comparison of a) the effective pipe length and b) the beam force distribution between the 45° and 60° analyses , for normal faulting (D/t = 72).

Spring Edge Model

(a)

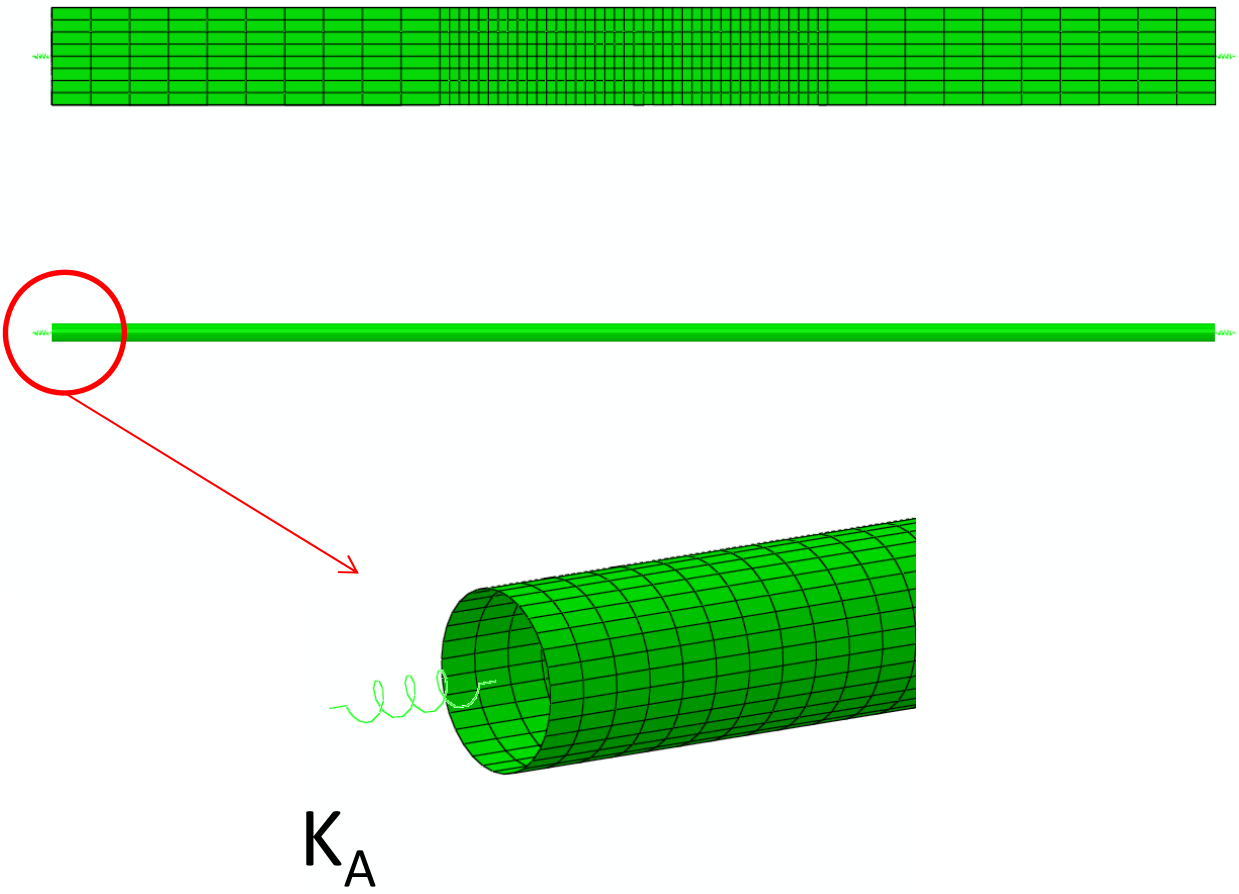

(b)

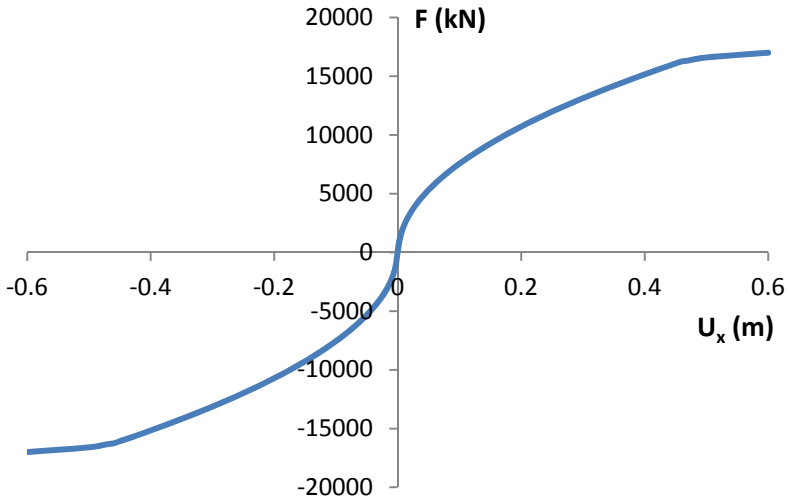

Figure 3.4.1. (a) The Spring edge model where we substituted the beams and soil springs of the Hybrid Beam model with a single axial spring at the edge of the pipe.(b) The axial spring force F with respect to the axial displacement U_x.

(a)

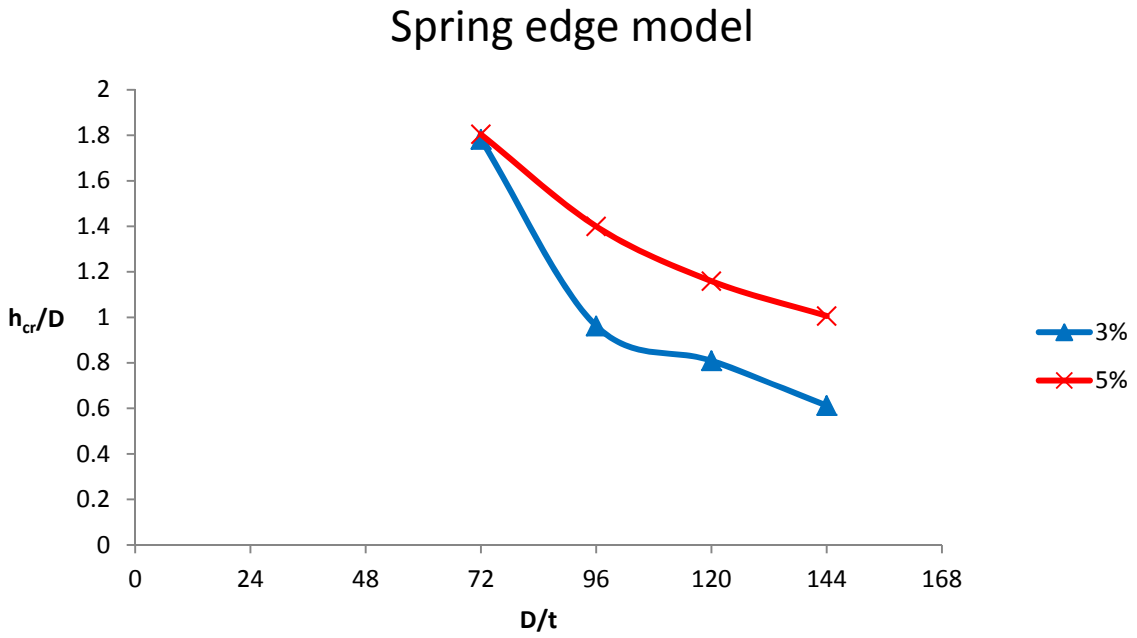

(b)

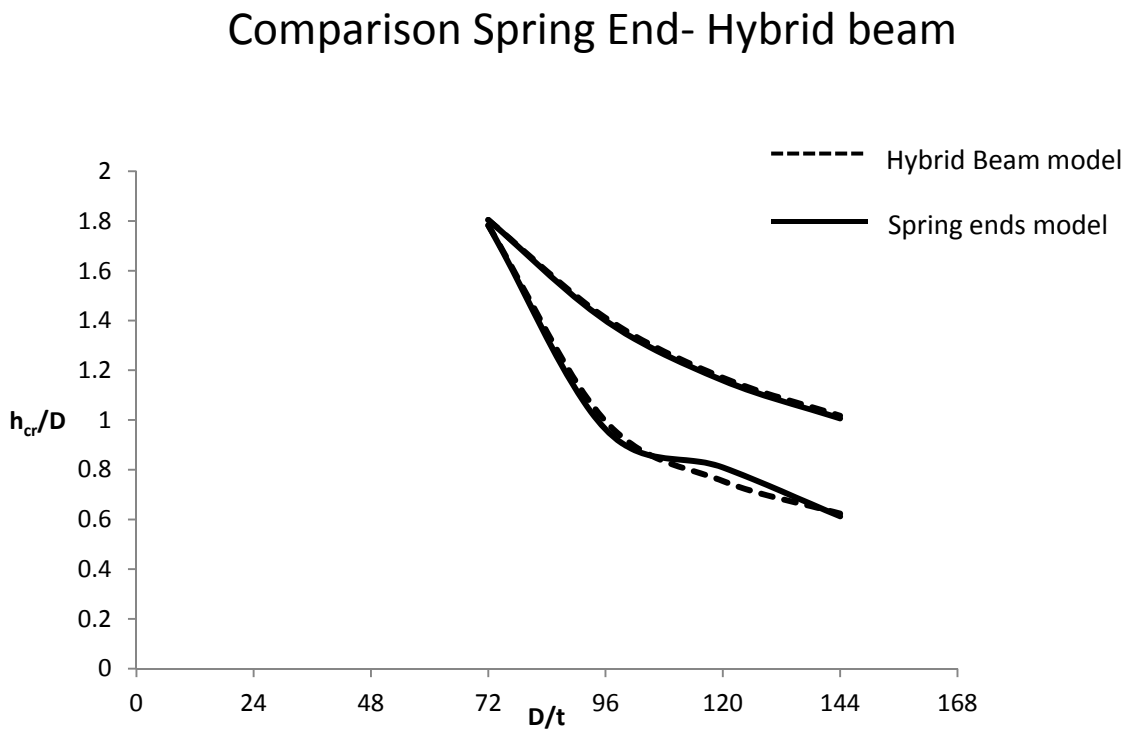

Figure 3.4.2. (a) Critical fault displacement to pipe diameter h_{cr} /D ratio versus the diameter to thickness ratio D/t for D/t=72-114. (b) Comparison of the spring edge model to the hybrid beam model with respect to the critical vertical fault displacement for D/t=72-114.

(a)

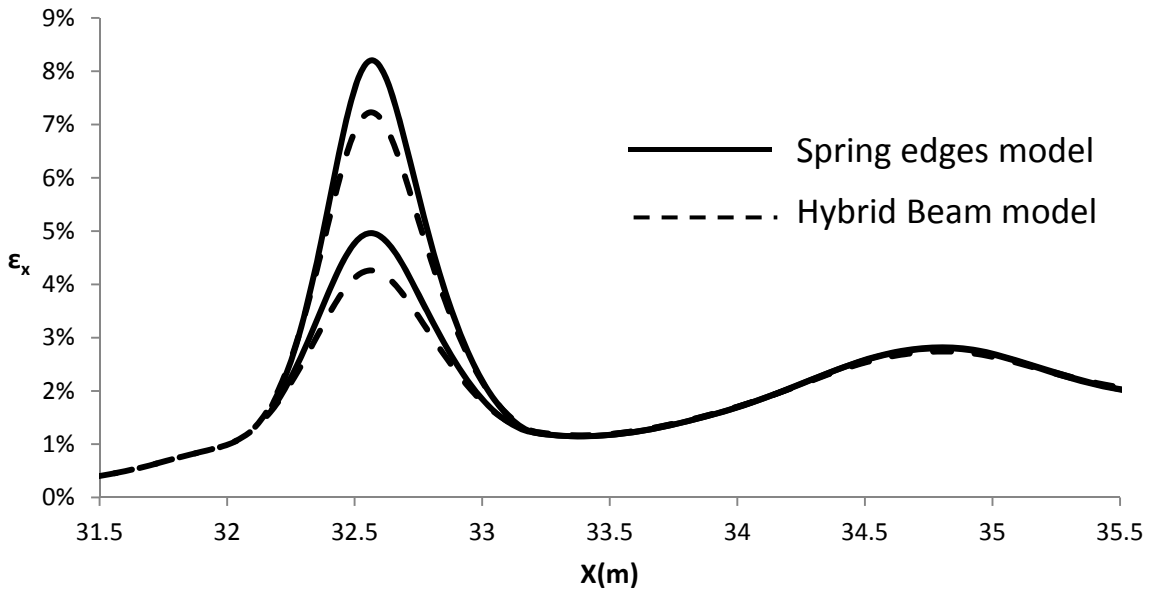

(b)

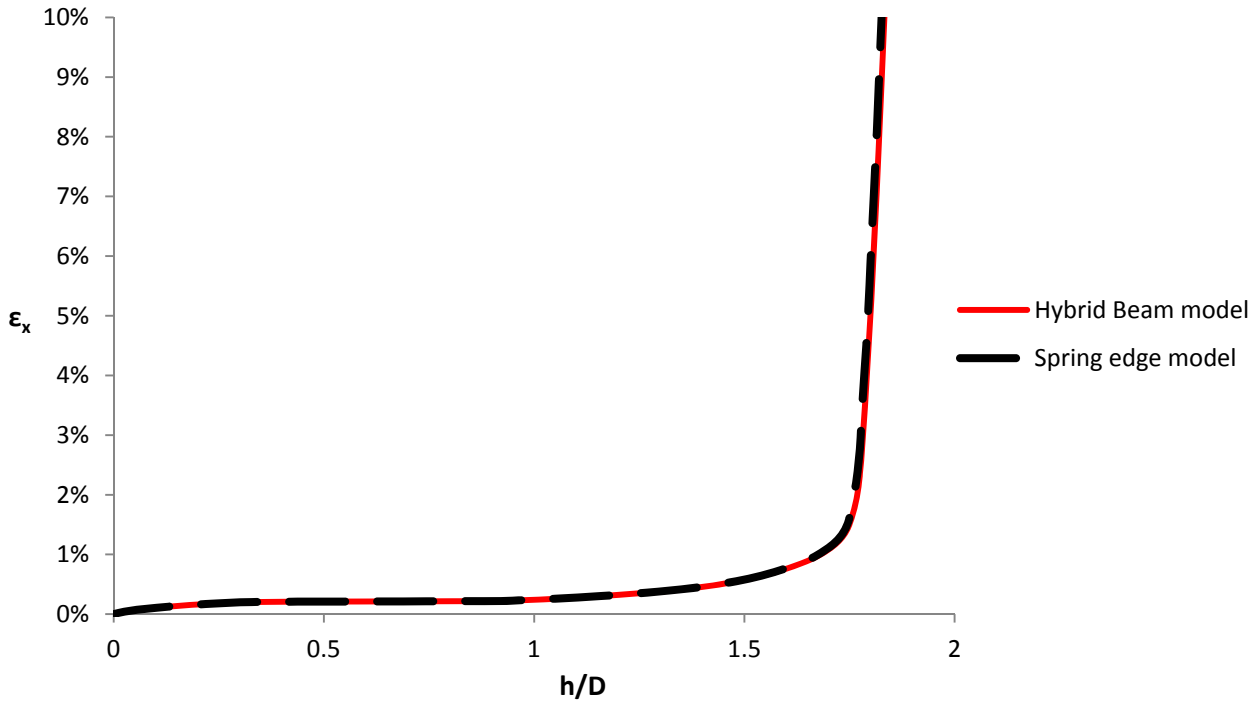

Figure 3.4.3. (a) Comparison of axial tensile strain distribution for vertical fault movement h=1.63 and 1.65m and (b) comparison of the axial tensile strain with respect to the vertical fault movement, between the Spring edges and Hybrid Beam model . (D/t=72)

Chapter 4
Reverse fault rupture

Introduction

In this chapter, we design and examine the behavior of a pipe when subjected to reverse fault rupture. For our analysis we use the hybrid beam model whose reliability has been discussed and proven in the previous chapter. However, we conduct a brief comparison between the results of this model and the results of the models with free and fixed pipe ends, to get a clear view about how close to reality the latter models are.

Model Properties

The models we use in this chapter are practically the same with those of Chapter 2: geometry, elements, constitutive model, and pipe and soil properties are kept the same as in Paragraph 2.2. Two are the major differences implemented in these analyses.

The first is the obvious change of applied movement. Instead of a downward we apply an upward movement keeping, however, the same angle of 60^{o}, in order to be able to directly compare the two cases, normal and reverse.

Secondly, we adjusted the neutral earth pressure coefficient (K_o) changing its value from 0.29 to 1.0. The reason for this change is that, normally in the case of reverse fault, before the occurrence of rupture, horizontal stresses have already increased because of the compressive nature of reverse fault. Hence, in order to capture this initial state we increase the value of K_o to be closer to the passive earth pressure coefficient K_p. Respectively, the normal fault case is of tensile nature thus, the horizontal stresses have already been decreased before the rupture and the value of K_o is chosen to be closer to the active earth pressure coefficient K_a.

4.1 Brief Review of Fixed and Free Ends Model

Free ends model

We present the results (**Figures 4.1.2 - 4.1.4**) only for a certain pipe thickness (D/t = 72). Since we have already concluded that the hybrid beam model is the most reliable, we simply want to briefly demonstrate the divergence of the two models.

As depicted in **Figure 4.1.2** the pipeline fails because of the occurrence of buckling at vertical fault offset h=0.49 m (h/D = 0.54). **Figure 4.1.3** demonstrates the axial strain distribution along the critical area of the pipe. We observe that the majority of the pipe is subjected to compression with the exception of the two inflection areas where tensile stresses and strains appear and where at later h values local buckling occurs. First, buckling appears in the hanging wall side (where hogging deformation appears) and this is when we consider the failure of the pipe. As the fault movement continues a second local buckling occurs at the pipe part in the footwall (where shagging deformation has been formed). The relative axial strain diagrams, for top and bottom fiber, are shown in **Figure 4.1.4.**

Fixed ends model

Once again, we present the results only for a pipe thickness t = 0.0127 m (D/t = 72). Buckling is the mode of failure in this case, as well. Buckling appears firstly in the hanging wall and then in the footwall, like in the previous case. As shown in **Figure 4.1.5,** the critical vertical fault displacement is merely 0.07 m (h/D = 0.08). The huge difference between free-ends and fixed-ends solutions is explained by the fact that reverse fault subjects the pipe mainly to compression and since the boundaries are fixed, the pipe is unable to move and thus the stresses increase more rapidly.

4.2 Hybrid-Beam Model

In contrast with the previous extreme and unrealistic cases of free and fixed ends, this approach addresses to the problem of boundaries in rationally. Without even examining the results of the analysis, we could predict that the failure will occur somewhere between the previous “extreme” approaches. As mentioned before, fixed edges restrain the pipe from moving, thus, compressive stresses increase and buckling occurs early, while free edges allow the pipe to axially move almost freely (affected only by the friction force). Since in both cases failure was due to buckling, we expect buckling to be the failure mode in this case as well. Since the hybrid beam model takes into account the continuation of the pipe, we expect buckling (for D/t =72) to occur for a vertical fault movement between 0.07 m (fixed ends) and 0.49 m (free ends).

Indeed, as shown in **Figures 4.2.1** and **4.2.3** local buckling (for D/t = 72) occurs at 0.25 m of vertical fault displacement h. Similar to the normal fault case, thicker pipes can endure bigger fault displacements (**Figure 4.2.1**) and larger axial strains (**Figure 4.2.4**) before the occurrence of buckling. Again, buckling occurs along a narrow area of about 0.2m length for every D/t ratio.

Effective pipe length, L_{eff}

We define L_{eff} as in Paragraph 3 based on the point where axial forces in the beam parts become zero. In **Figure 4.2.6.a**, a comparison of beam axial forces in the hanging wall and the footwall does not indicate great differences but makes clear that in the footwall the pipe is more stressed compared than in the hanging wall. The effective length increases rapidly during the first steps of vertical displacement (until h/D = 0.06) and then the rate of increase diminishes until the L_{eff} remains practically stable (h/D = 0.38) (**Figure 4.2.6**). In the same figure, the effect of D/t ratio is demonstrated, showing that greater length of pipe is activated for the thicker pipes.

Furthermore, we compare the magnitude and area of effect of the axial beam forces in the footwall and as it is depicted in **Figure 4.2.6.b**, the reverse fault activates greater length of pipe for the same value of dislocation.

Detachment and pipe effects to the soil

The detachment of the pipe from the soil is demonstrated in **Figures 4.2.8** and **4.2.9** in terms of relative pipe and soil vertical displacements and soil pressures, respectively. In the first case, we use the vertical displacements of the lower part of the pipe and of the soil surface beneath the pipe and in the second figure, loss of contact is depictured by the areas where soil pressure is zero. The latter way of display is more efficient since it can demonstrate the detachment areas along the entire pipe surface and not only the lower pipe part. Unlike the normal fault case, reverse rupture causes detachment to occur mainly at the footwall part of the pipe. Detachment can also be demonstrated by plotting the soil pressure around different pipe cross-sections **(Figure 4.2.10)**.

Finally, regarding the general effect of the pipe to the soil, we observe in **Figure 4.2.11**, that the pipe hinders the fault from propagating up to the surface and in **Figure 4.2.12**, we notice that compared to the free-field rupture (y=5m) the pipe provokes additional displacement to the soil since it pushes it upwards and rightwards, according to the fault movement and the pipe deformation.

Effect of the fault angle

The effect of the fault angle is also examined by running the analysis for a 45^{o} fault angle. The comparison between the 60^{o} and 45^{o} fault angle cases is shown in **Figures 4.2.13** and **4.2.14**. Similarly to the relative paragraph of Chapter 3, we examine the pipe resistance in terms of vertical, horizontal and total fault displacement. We observe that, unlike the normal fault case, the critical parameter now is the total fault displacement since in both fault angle cases the pipe fails for the same total fault displacement. This is also quite logical, since the mode of pipe failure when subjected to reverse faulting, is the local buckling. For local buckling to occur it is important the increase of compressive axial strains (caused mainly by the horizontal movement component) as well as the occurrence of bending (caused by the vertical movement component).

Main conclusions of Chapter 4

- Once again, the limited models of fixed and free pipe ends are proven inadequate to capture and describe correctly the behavior of the soil-pipe system in the case of reverse fault rupture.

- The mode of failure for this kind of fault is local buckling, due to the compressive nature of reverse rupture.

- Subjected to reverse fault rupture, pipe can endure significantly less fault movement before the occurrence of failure, compared to normal fault rupture.

- Compared to the normal fault case, reverse fault activates a longer part of the pipe.

- As critical fault movement component, it appears that the critical parameter is the total fault displacement.

Figures of Chapter 4

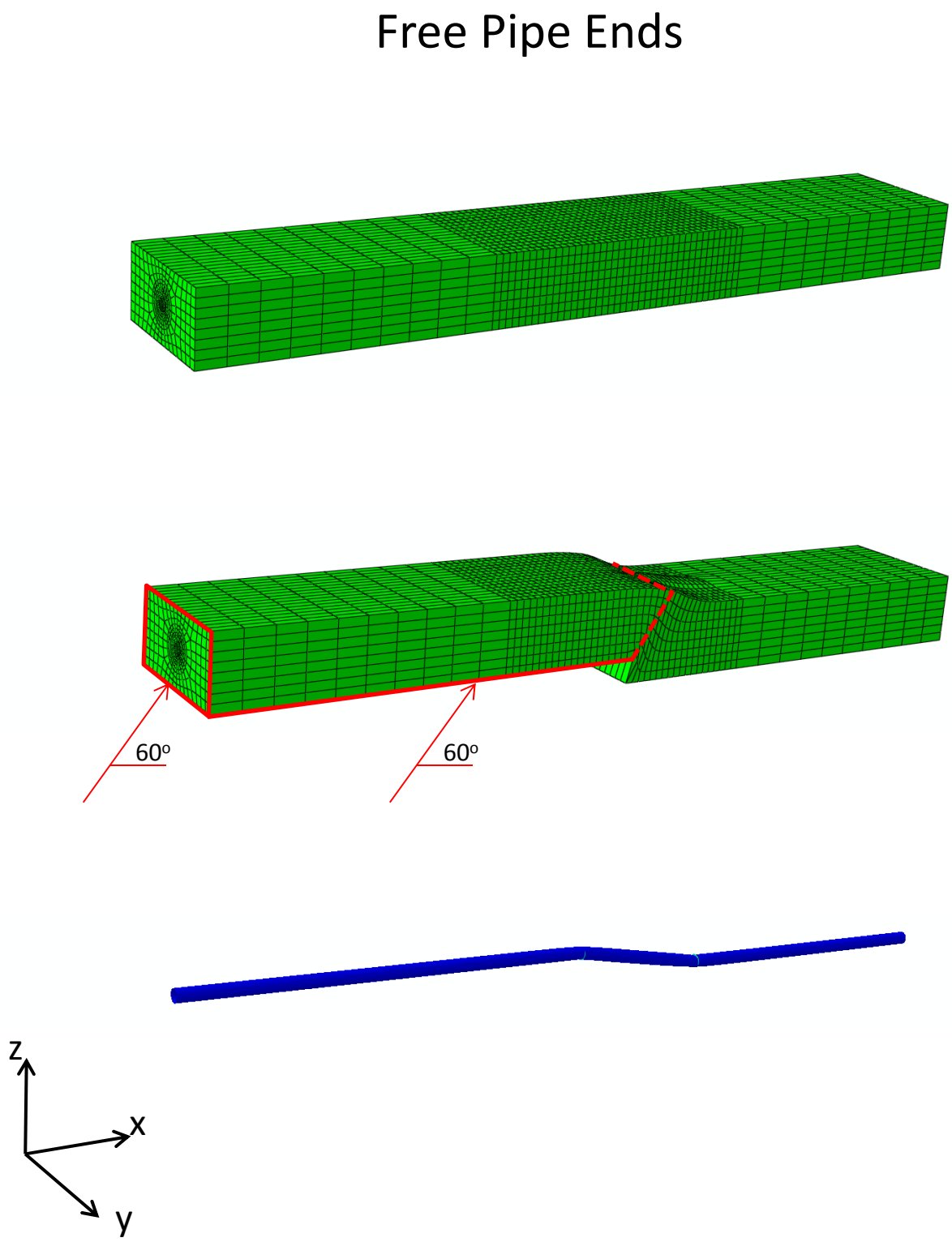

Figure 4.1.1. Simulation of reverse fault rupture, using the basic model of Chapter 3 with free pipe ends.

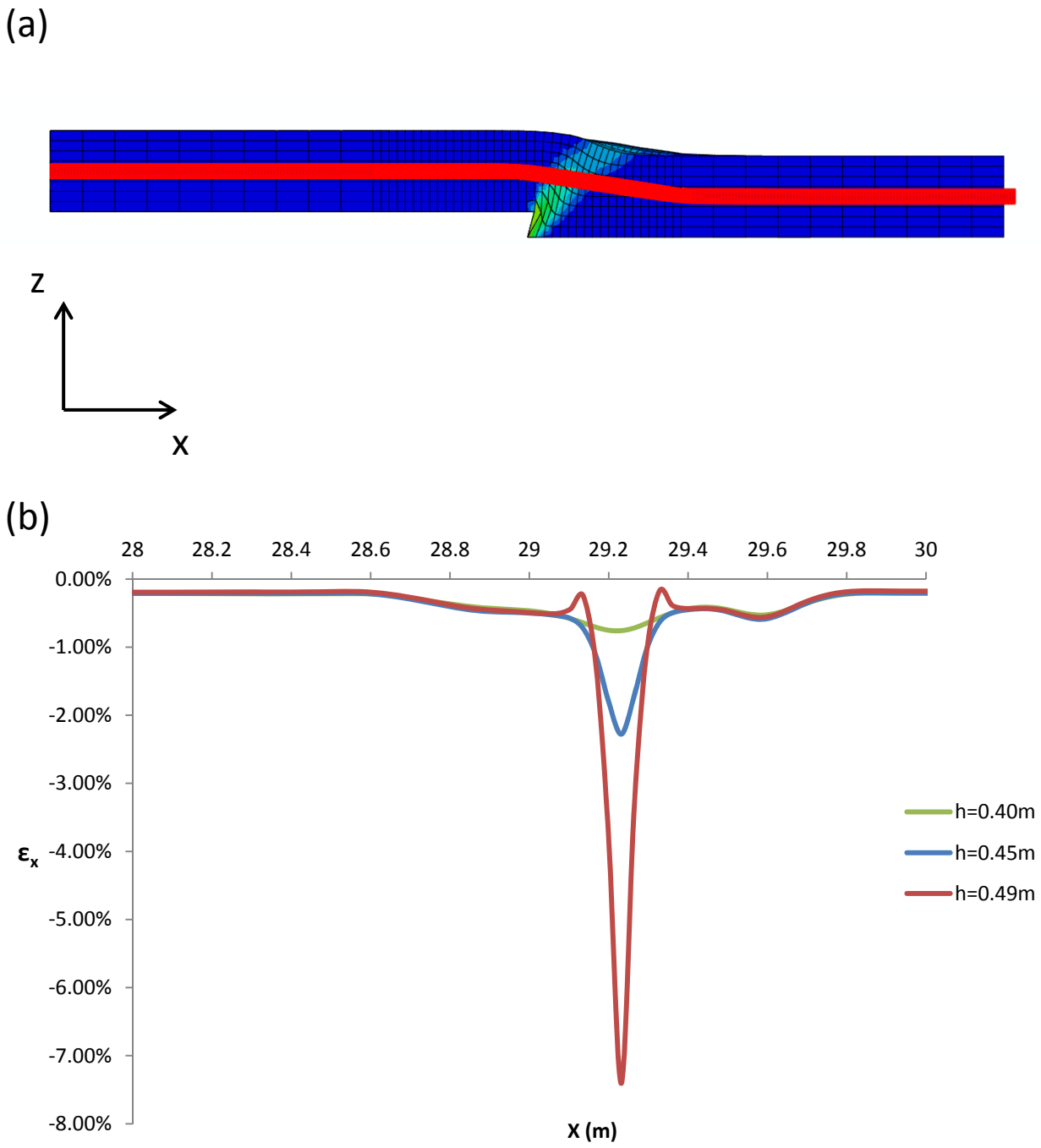

Figure 4.1.2. (a) The deformed pipeline shape is highlighted in red. The relative movement between the pipe and the soil indicates that , if not for the free boundaries of the pipe, a compression would have occurred, caused by the continuation of the pipe , which is not taken into consideration in the free edges model. (b) Axial strain distribution in the critical area. Buckling appears at 0.49 m of vertical fault displacement.

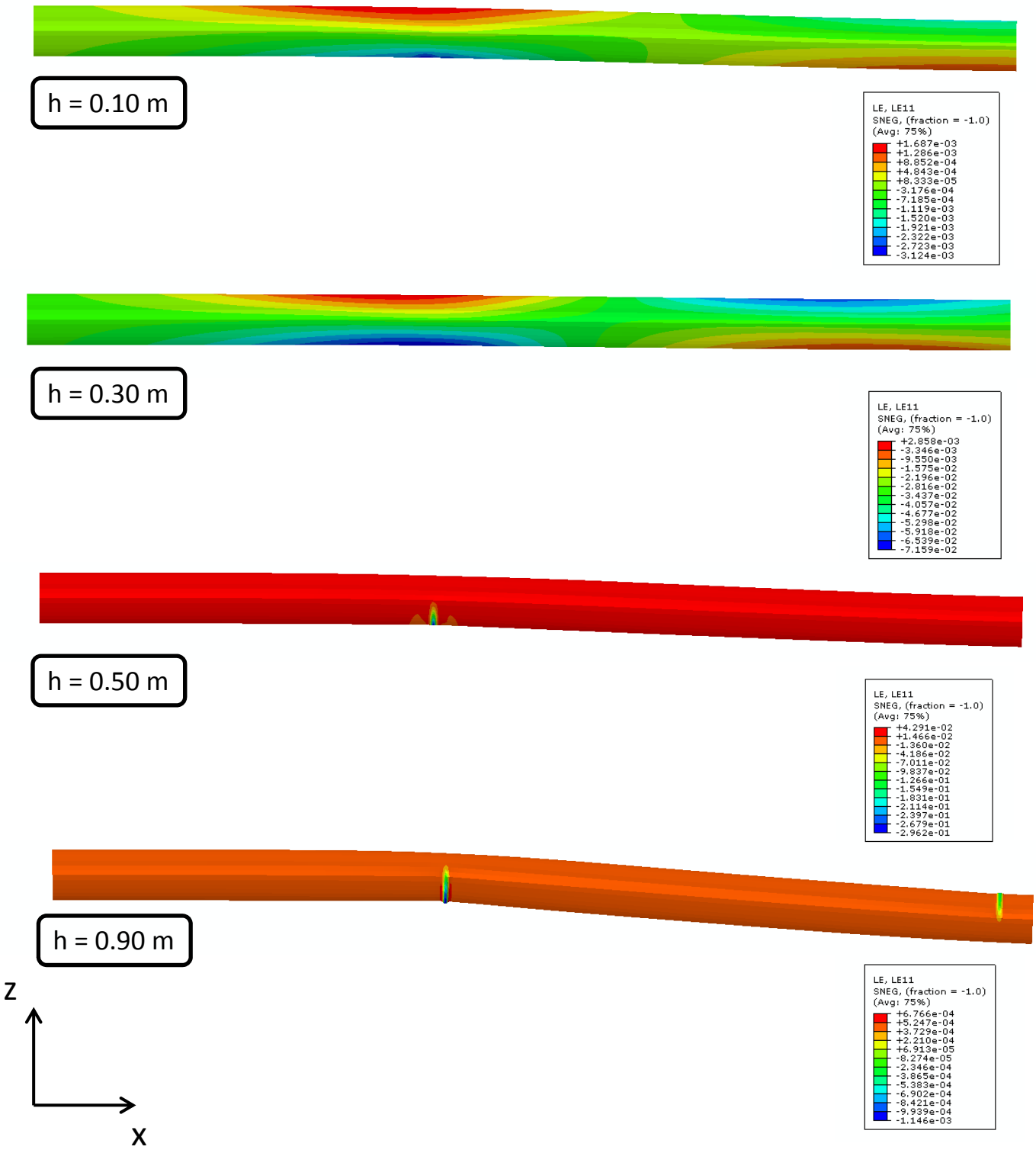

Figure 4.1.3. Axial strain distribution along the pipe for four vertical fault displacements. (D/t = 72,Free ends)

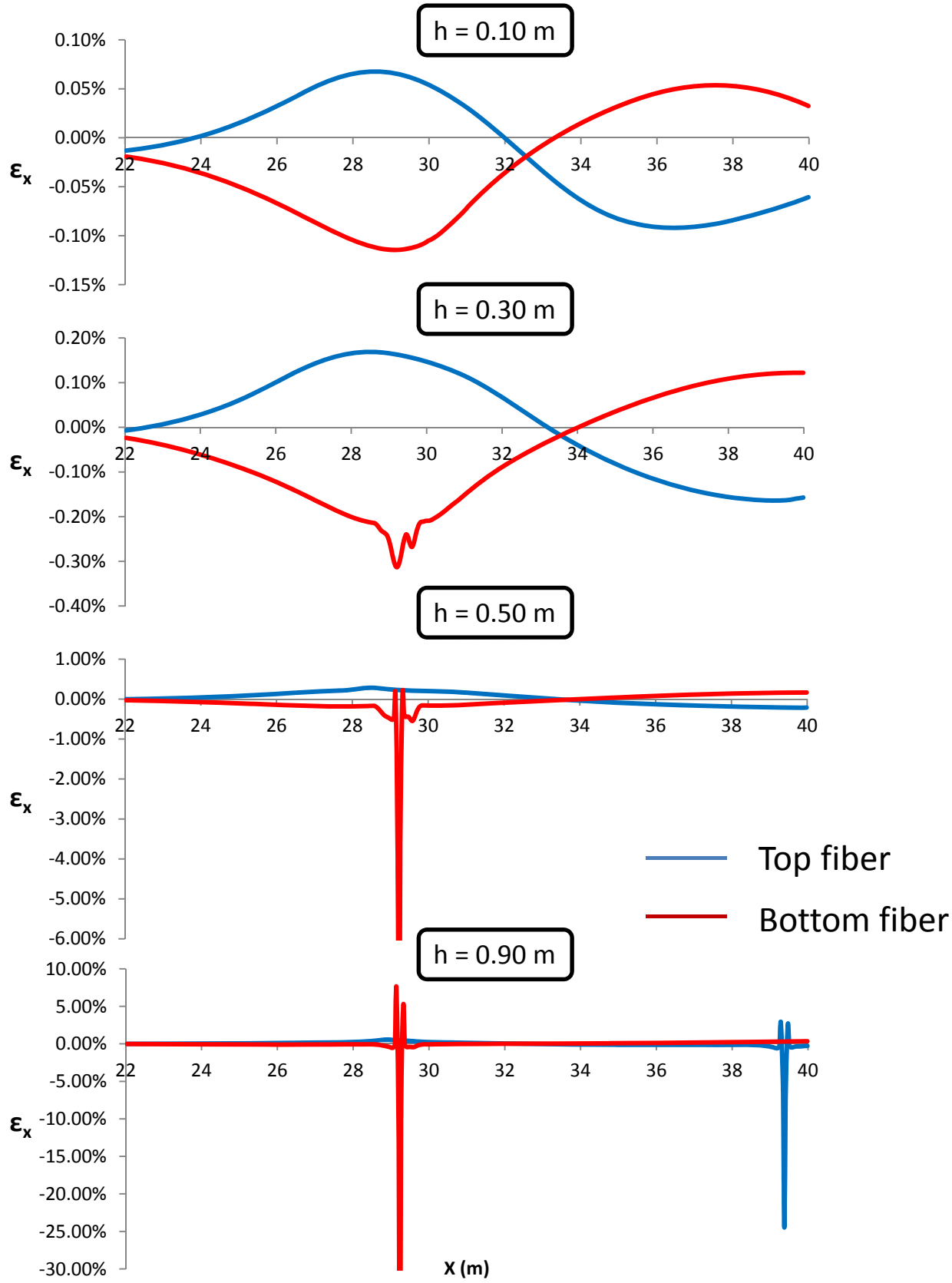

Figure 4.1.4. Diagrammatic axial strain distribution along the critical area for four vertical fault displacements. (D/t = 72,Free ends)

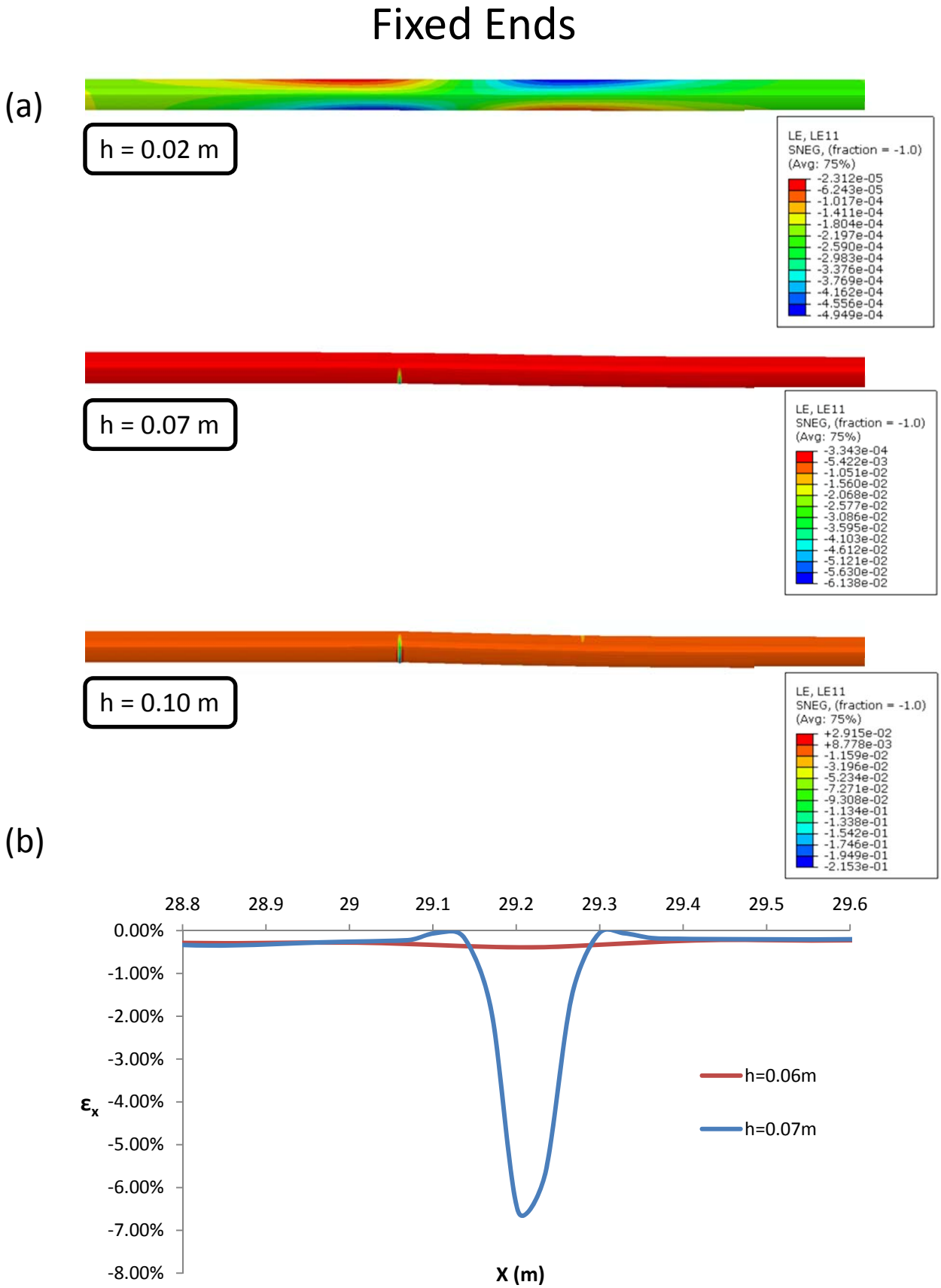

Figure 4.1.5. (a) Axial strain distribution along the critical area. The pipe is under compression from the very beginning of fault movement. (b) Axial strain distribution along the critical area (bottom fiber) when first buckling occurs. (D/t = 72, Fixed ends)

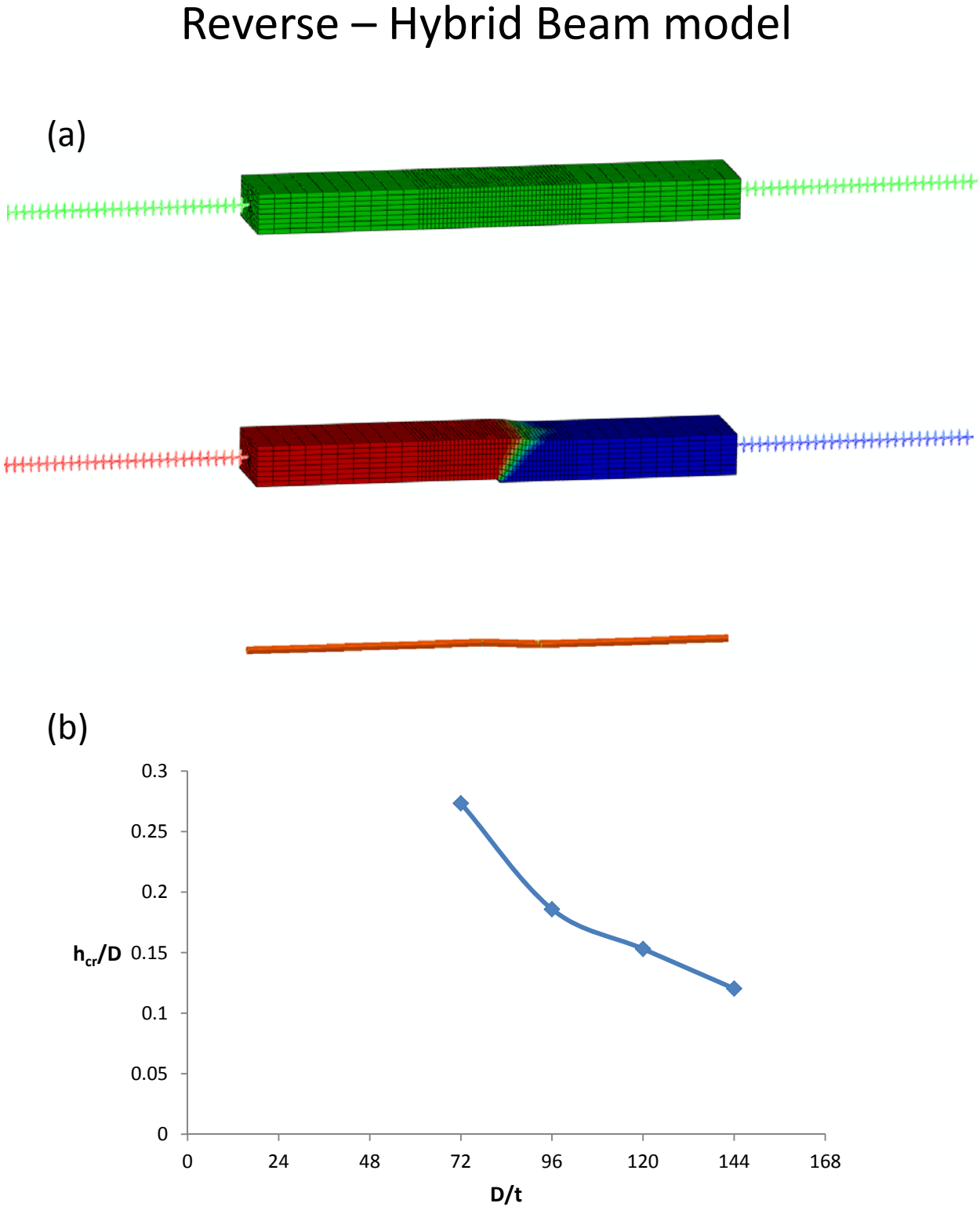

Figure 4.2.1. (a) The aforementioned Hybrid-Beam model used for the simulation of reverse fault motion. (b) The summarized dimensionless results of the analysis in terms of critical vertical fault displacement with respect to the diameter to thickness ratio D/t.

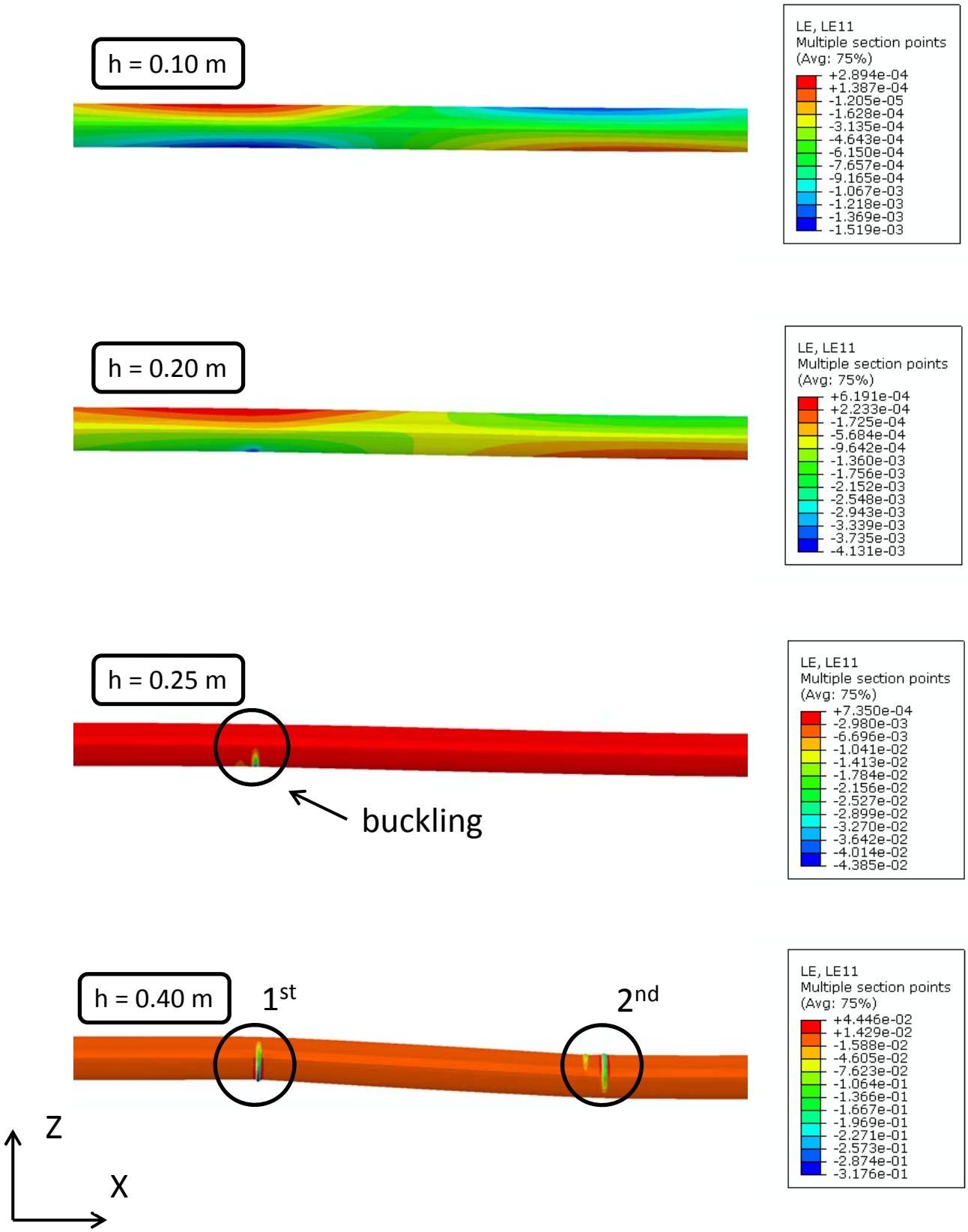

Figure 4.2.2. The axial strain distribution along the critical pipe area (X=25-40 m) for four vertical fault displacements h. (D/t = 72). First buckling occurs in the hanging wall side.

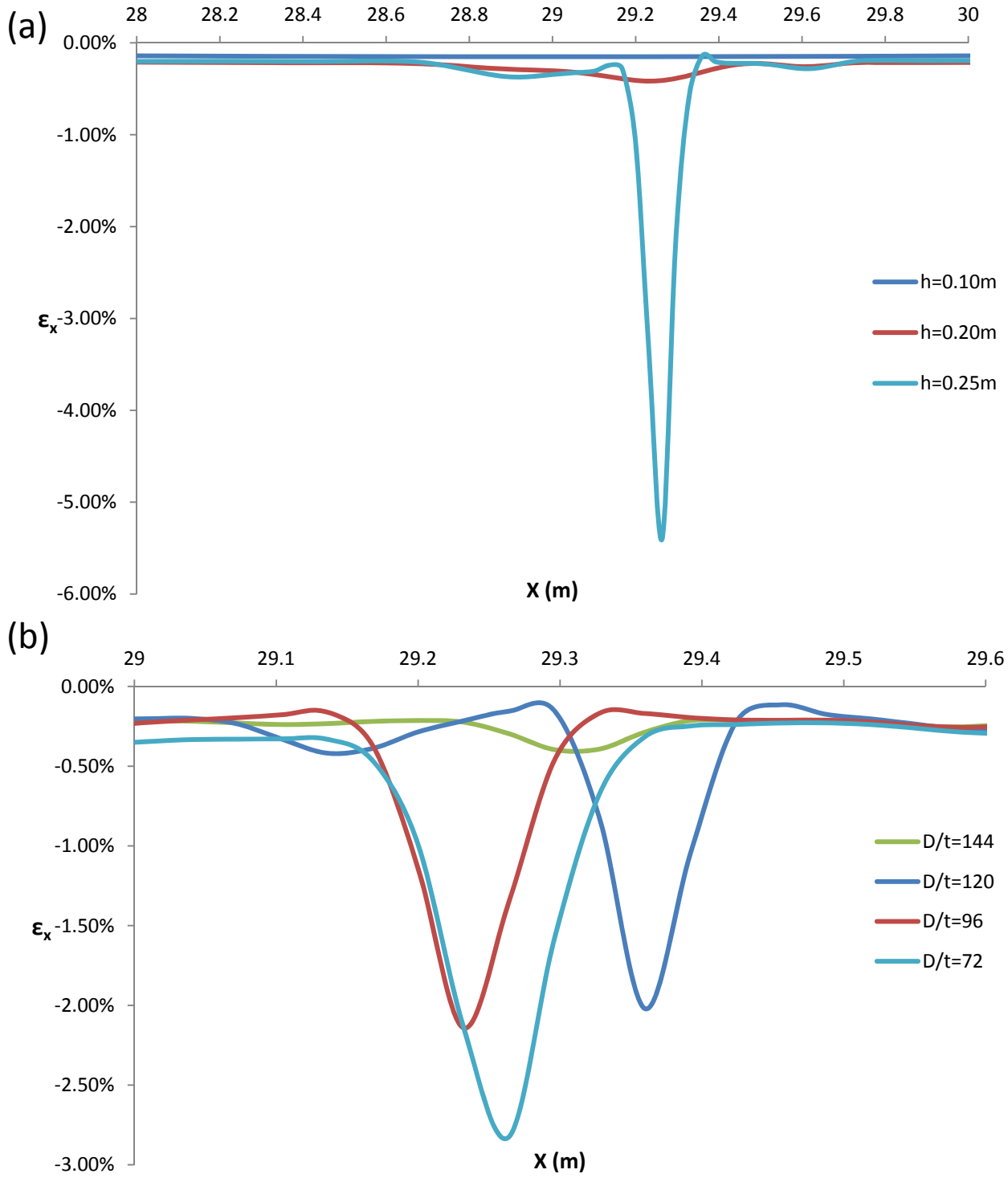

Figure 4.2.3. (a) Axial stain development for three vertical fault displacements, for D/t = 72. (b) Axial strain distribution at the moment of buckling initiation for four D/t ratios..

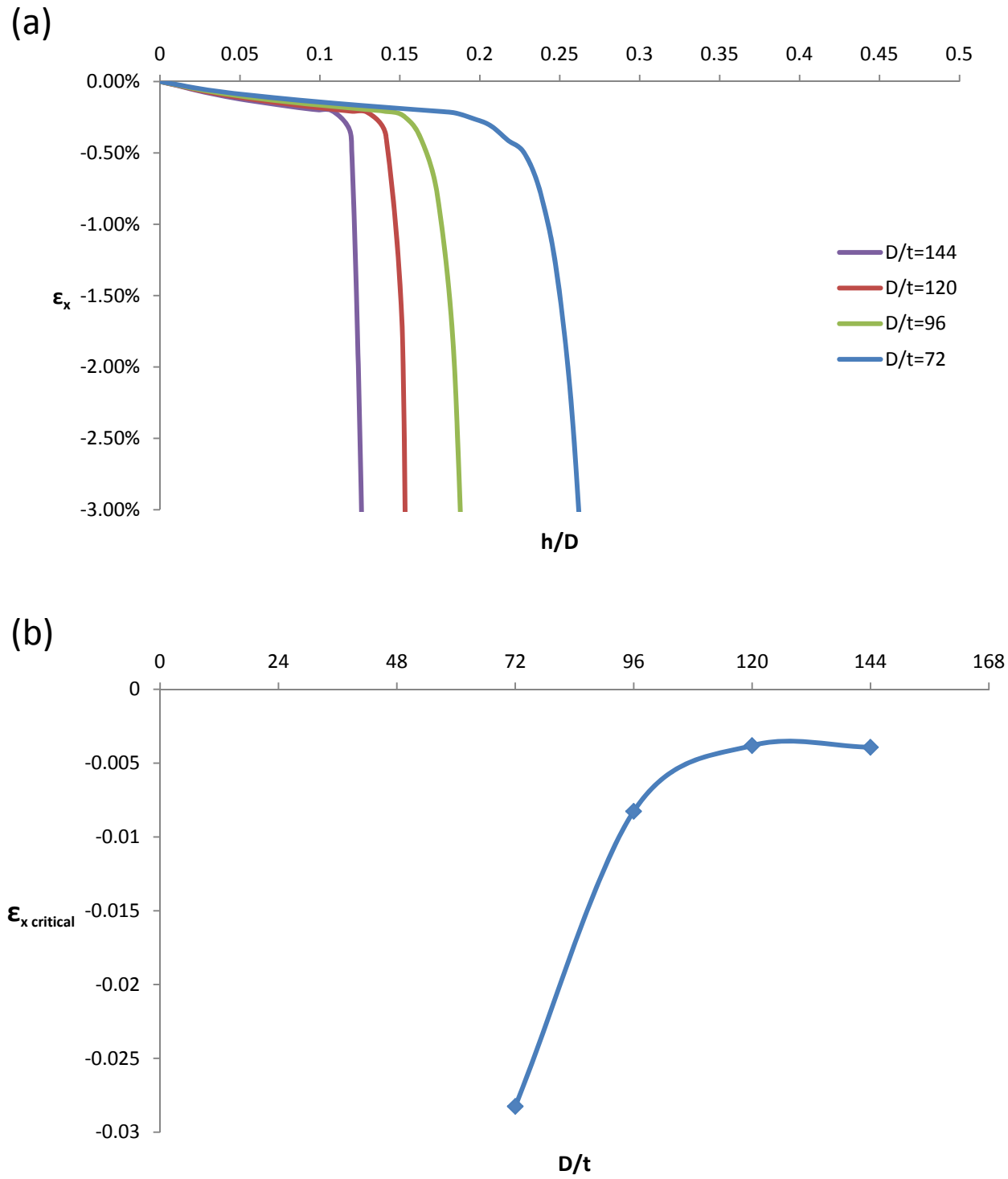

Figure 4.2.4. (a) Axial strain development at the point where buckling occurs for four D/t ratios. (b) The critical axial strain at which buckling occurs , for four D/t ratios.

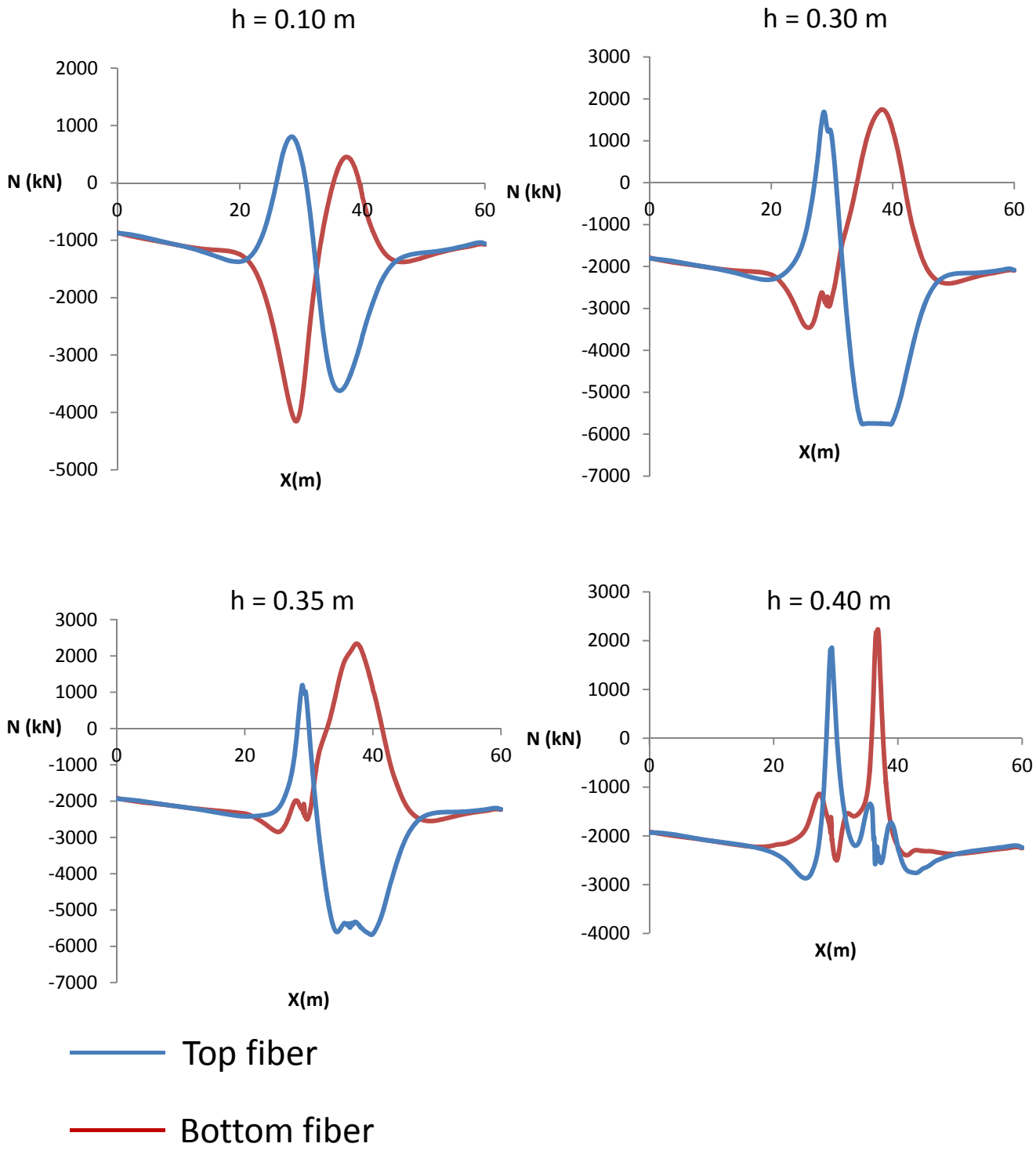

Figure 4.2.5. Axial forces of the upper and lower fiber, for four vertical fault displacements. The selected steps indicate the initial condition, the initiation of the first buckling , the initiation of the second buckling and the axial forces distribution several steps after both of buckling failures have occurred. (D/t = 72)

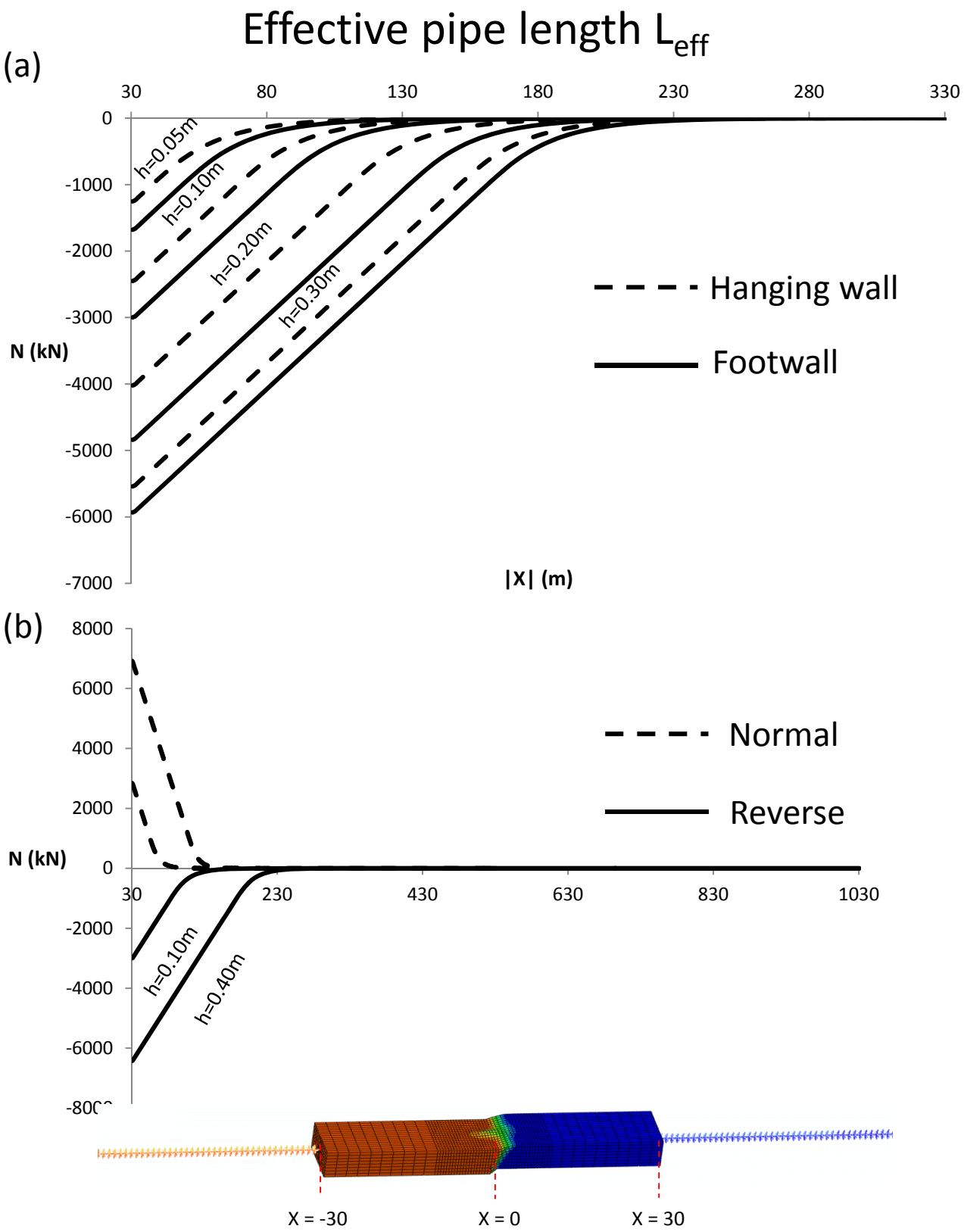

Figure 4.2.6. (a) Comparison of axial forces along the beam in the hanging wall and the footwall. The differences are not large but demonstrate that footwall is more stressed compared to hanging wall. (b) Comparison between normal and reverse cases regarding the effective pipe length . Reverse activates a longer part of the pipe for the same fault displacement.

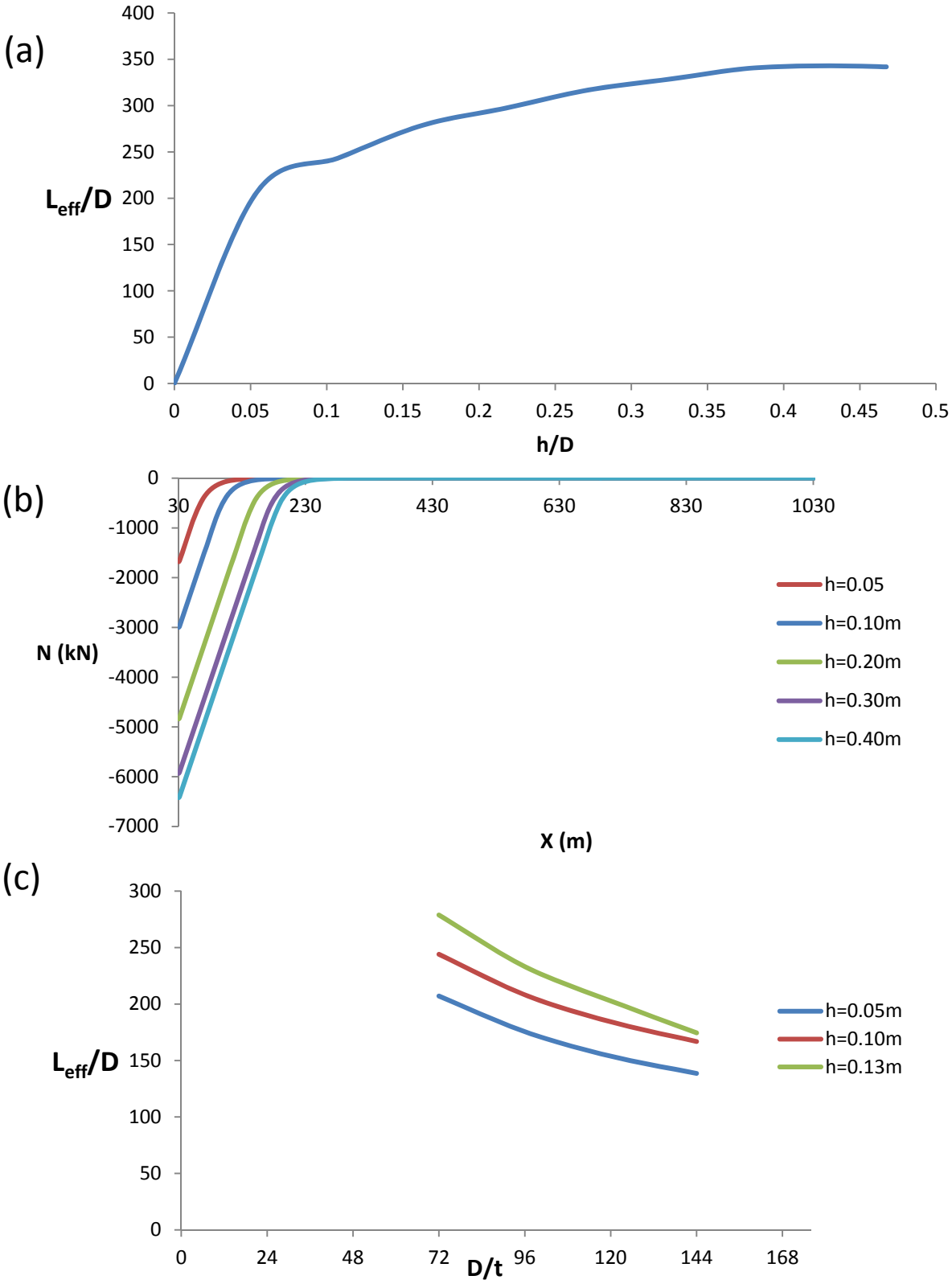

Figure 4.2.7. (a) Effective pipe length as fault displacement increases. Just like with normal fault case, during the first steps the increase is large while, subsequently, the rate of increase diminishes until the L_{eff} gets a maximum value. (b) The development of axial forces, as the fault movement increases ,indicates the value of L_{eff} (D/t = 72). (c) The axial forces along the beam elements in the footwall for three values of h.

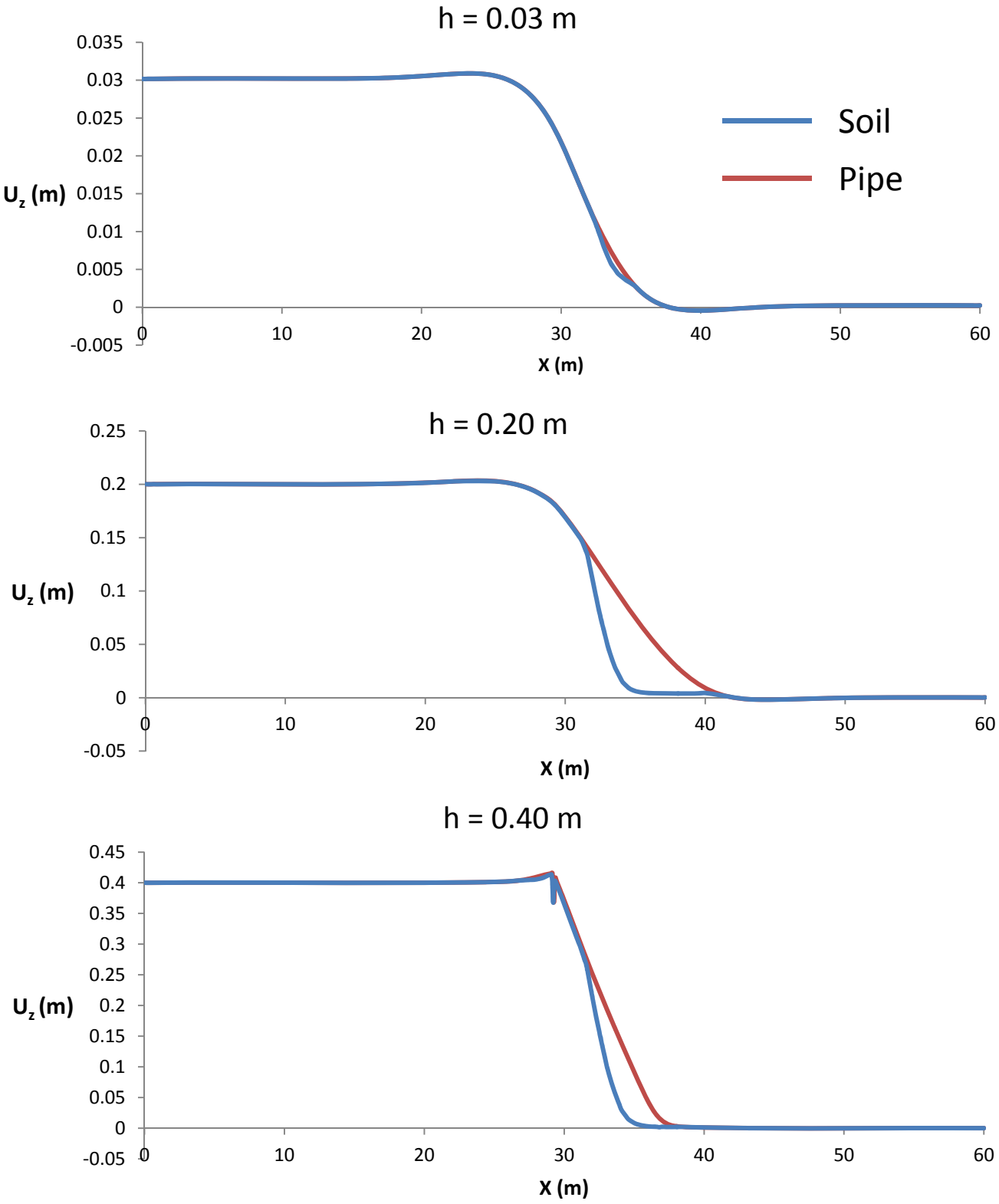

Figure 4.2.8. Detachment of the pipe from the soil beneath it , depicted by plotting and comparing the vertical displacements off pipe and soil (D/t = 72).

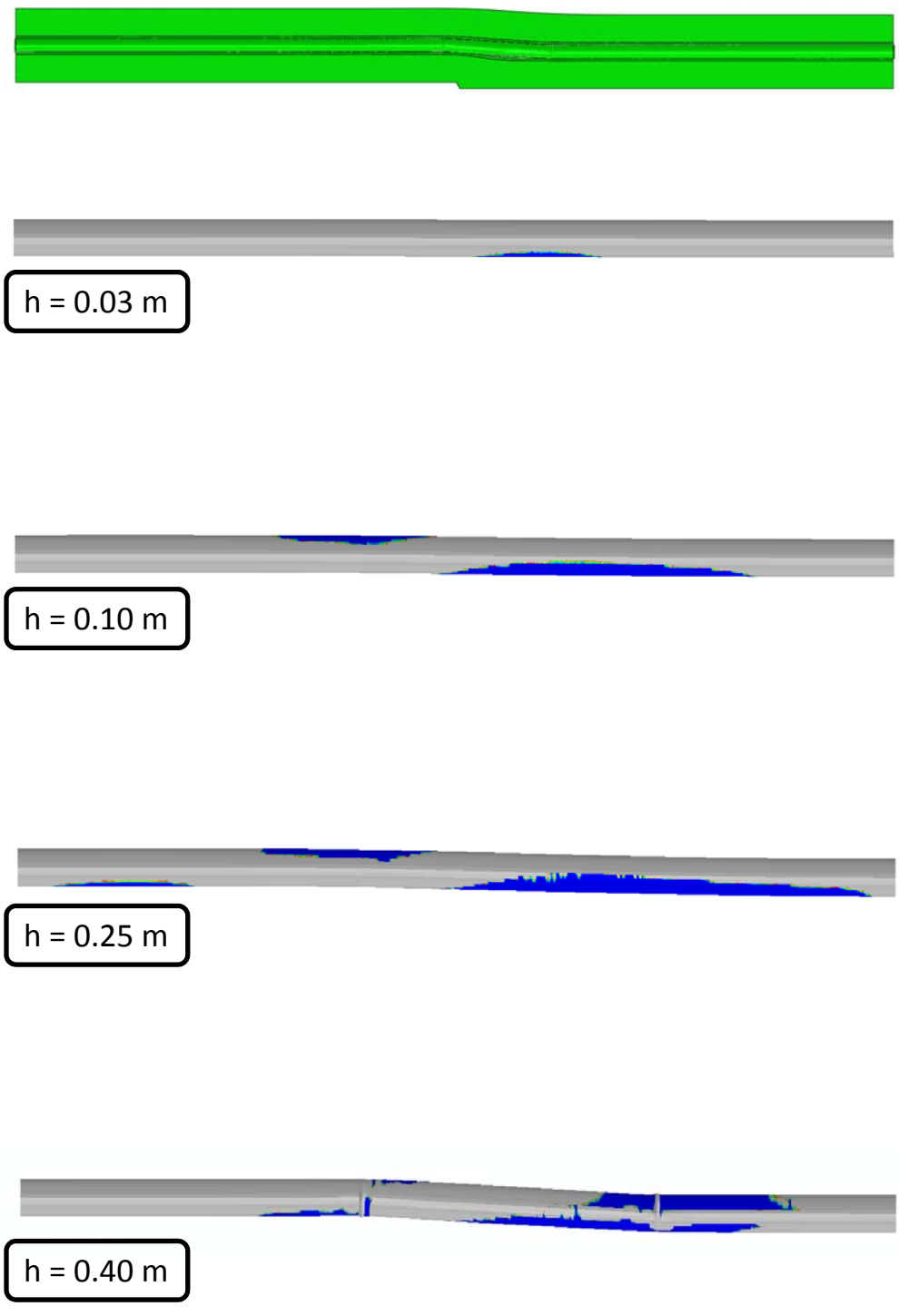

Figure 4.2.9. Detachment of the pipe, indicated by the pipe areas where the soil pressure is zero (blue areas).

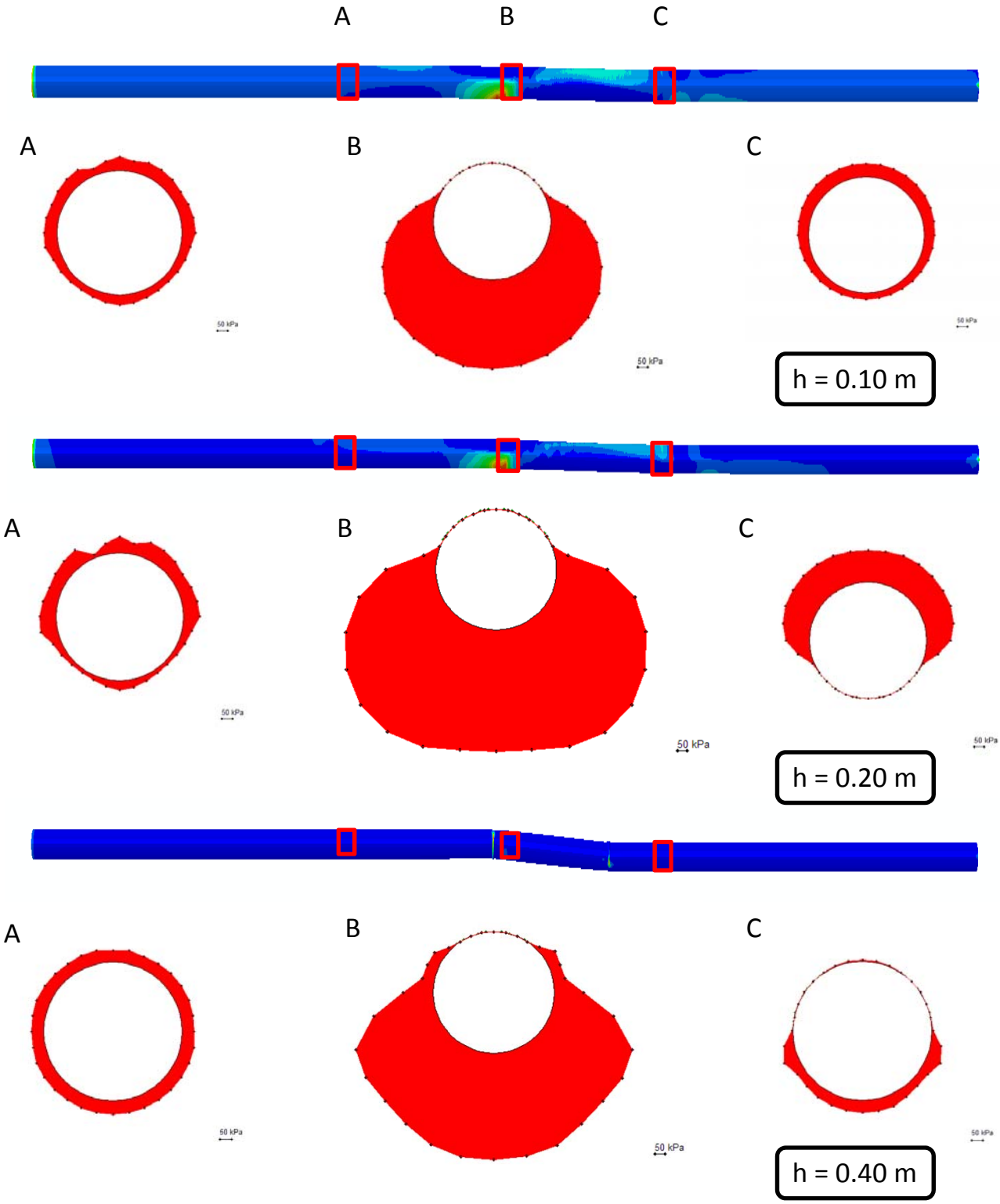

Figure 4.2.10. Soil pressure around the pipe cross-section in three positions A,B and C of X=20,30 and 40m respectively. (D/t = 72)

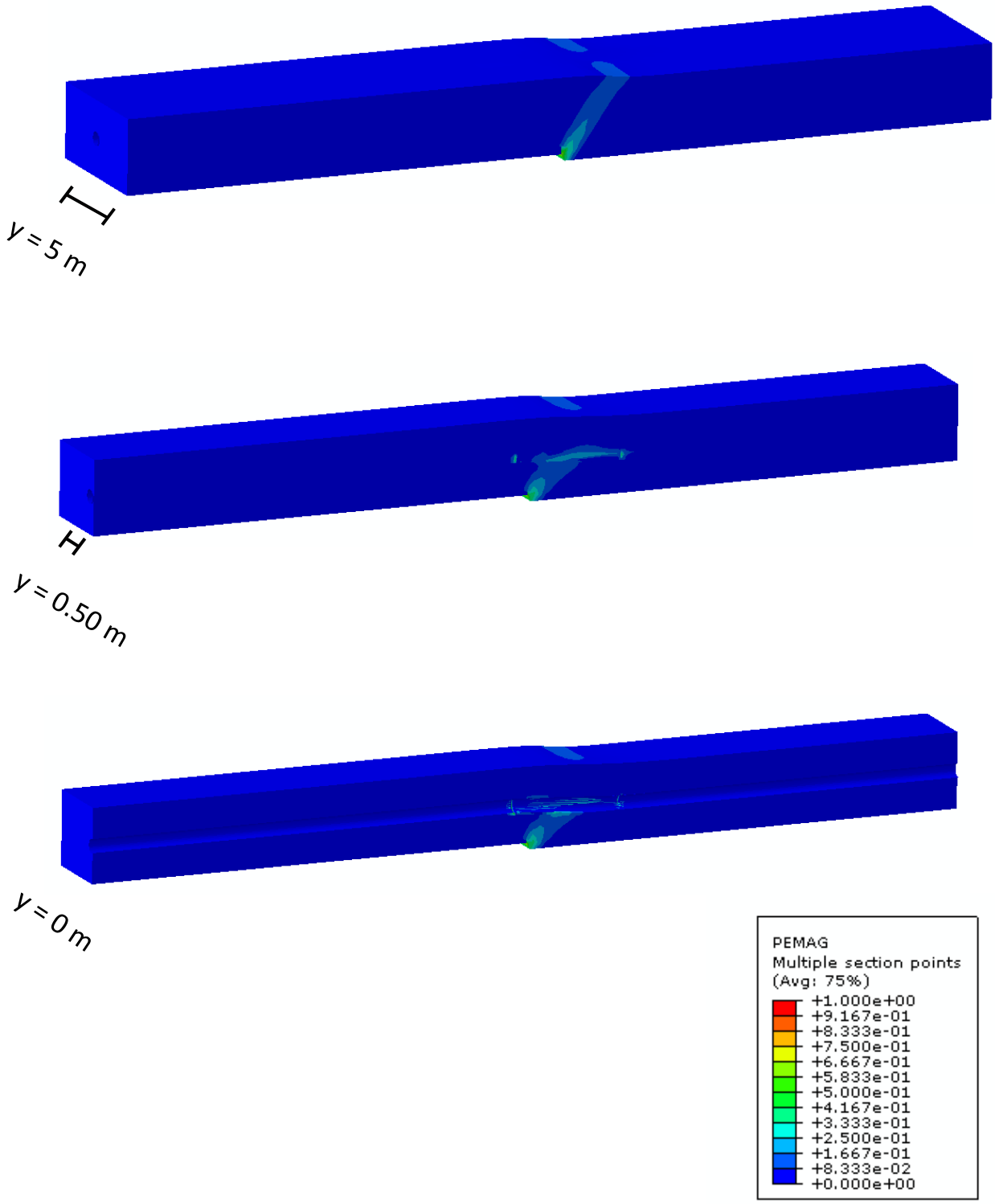

Figure 4.2.11. Magnitude of plastic strains for h = 0.40 m . Planes of various distances from the pipe are depicted. (y=0 corresponds to the vertical plane of the central pipe axis).
No significant lateral effects are spotted.(D/t = 72)

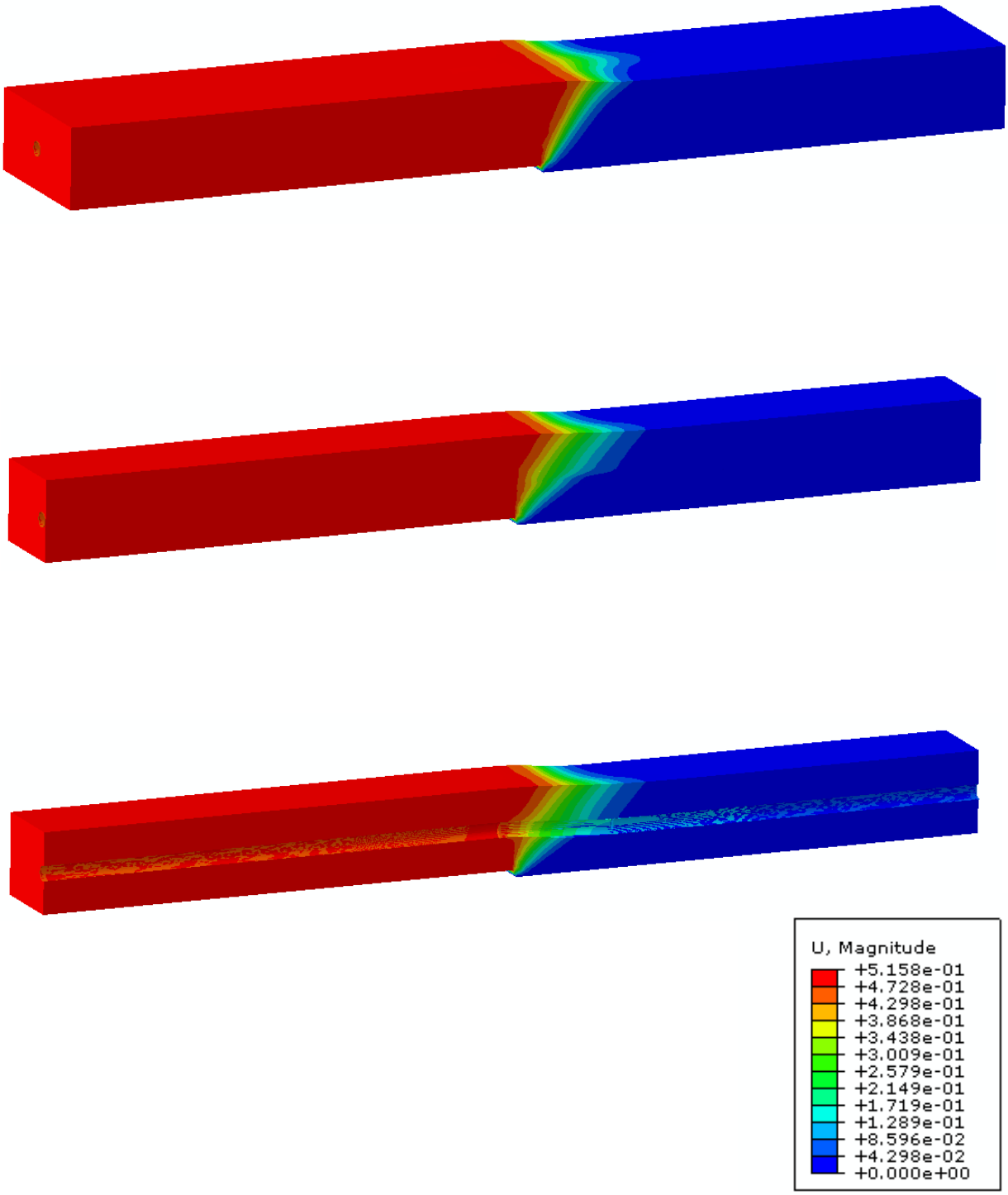

Figure 4.2.12. Vertical displacement distribution for vertical fault displacement h=0.40 m. Planes of various distances from the pipe. (y = 0 corresponds to the vertical plane of the central pipe axis) (D/t=72).

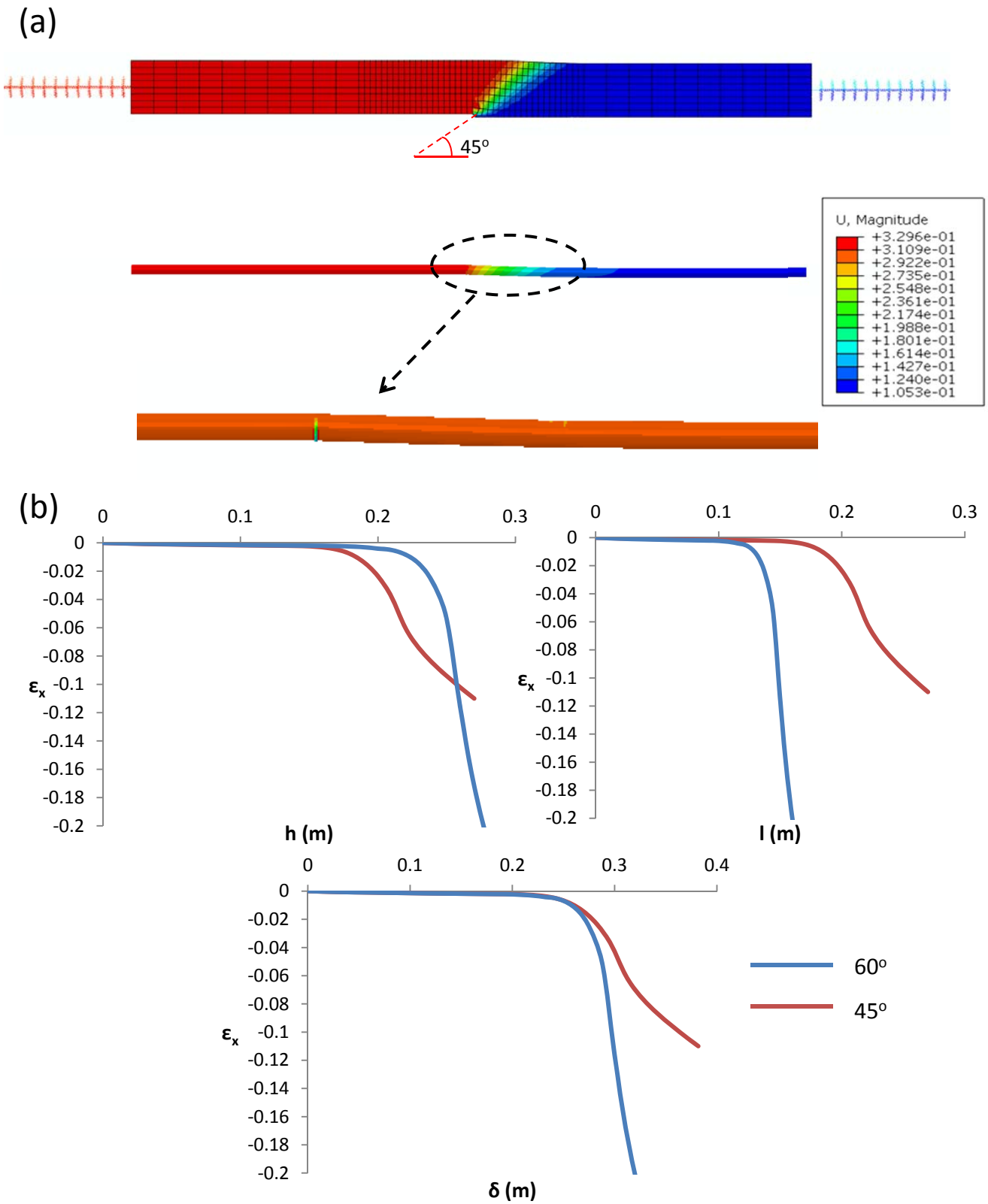

Figure 4.2.13. (a) The deformed soil and pipe for a reverse fault of 45°. (b) Comparison between the 60° and 45° reverse fault in terms of axial deformation with respect to the vertical fault displacement h, the horizontal fault displacement l and the total magnitude of displacement δ, (D/t = 72).

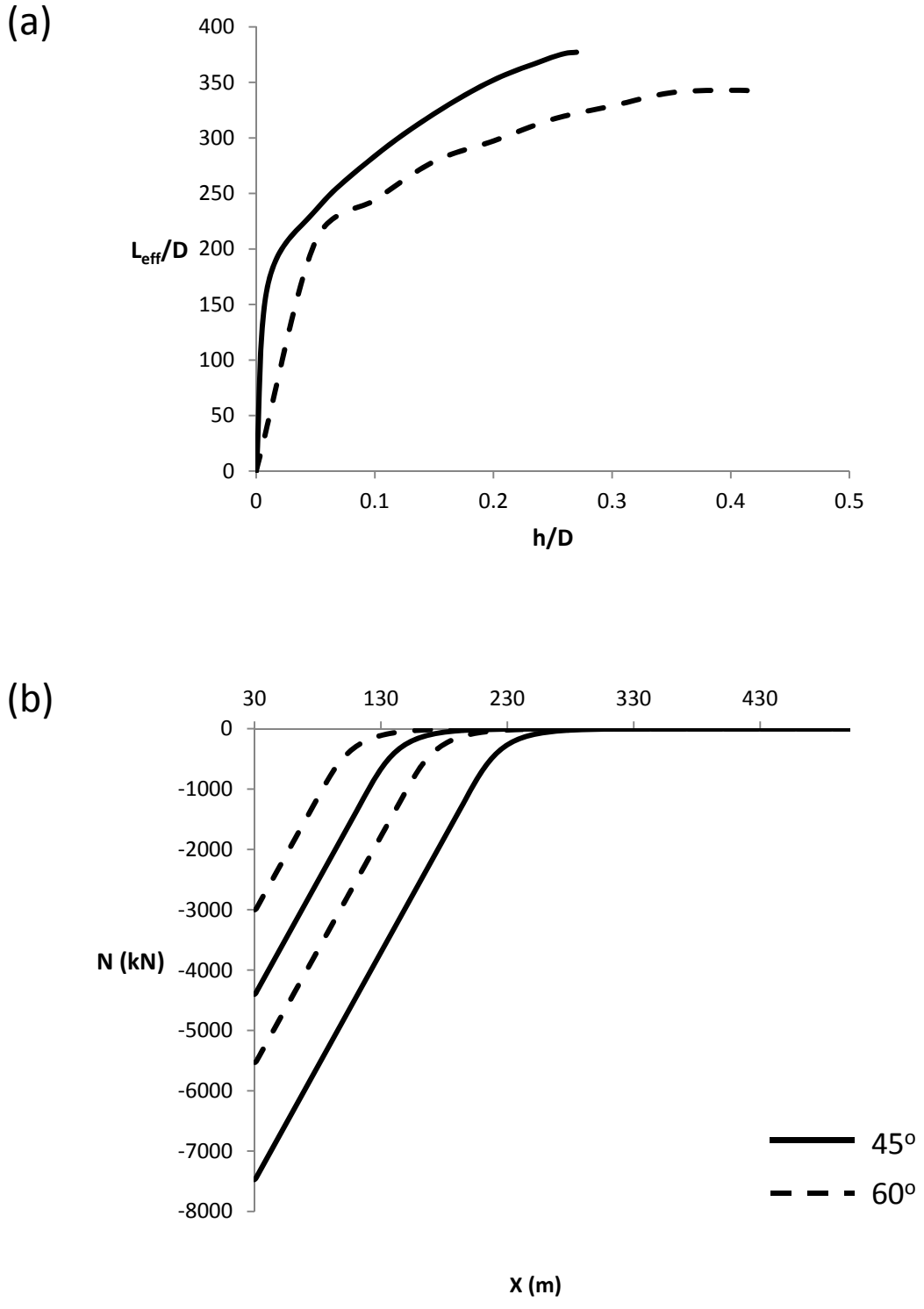

Figure 4.2.14. Comparison of a) the effective pipe length and b) the beam force distribution between the 45° and 60° analyses , for reverse faulting (D/t = 72).

Chapter 5
Soil layer depth effect

Introduction

Having tested and investigated several models for the simulation of the problem we came to the conclusion that the most realistic and reliable one is the hybrid-beam model. The reason is that it does not need any arbitrary assumption about the boundary conditions of the pipe, since it is practically not limited (in the longitudinal direction) and depictures accurately both the affected area and the actual behavior of the pipe. Nonetheless, there are still some aspects of this model that are not in accordance with the common, real conditions. These remaining inaccuracies have to do once again with the size of the model and specifically with the depth of the simulated soil layer. Imposing the bedrock movement just 2.5 meters below the pipe does not allow the fault propagation to evolve naturally. On the contrary, this way the soil and the pipe are subjected to a more centralized and steep deformation compared to the natural one. In addition, a 5 meter surface soil layer with an elastic modulus of 25Mpa cannot be considered realistic. In order to overcome these inaccuracies, to examine the effect of the soil layer depth and at the same time to limit the needed time for the analysis, we designed a two dimensional free field model, subjected to normal and reverse fault rupture and then implemented its results to the 3-D beam model.

5.1 Free-Field model

Model properties and geometry

The model we used is a simple 40m x 160m model consisted of square 1m x 1m continuum CPE4 elements that substitute the soil. Once again, the hanging wall side and one part of the base were moved to simulate a 60^{o} fault rupture (normal and reverse). The purpose of these analyses was to obtain the vertical and horizontal node displacements at 5m depth and then to impose them to the base of the 3-D, 5m deep hybrid-beam model (**Figure 5.1.2**).

Regarding the soil properties, in this chapter, everything but the Young's modulus E distribution, remained the same as in the previous chapters. For the elastic modulus distribution along the depth, it was decided to examine various proposed distribution models and compare them with a linear distribution model which has been proved trustworthy by various researches conducted in our department. Specifically, we compared the distributions of the linear model and of the sand models of Yu and Richart (1984), Iwasaki et al. (1978), Zhou and Chen(2005) and Hardin (1978). As depicted in **Figure 5.1.3**, the parabolic model that approaches better the linear distribution is that of Yu and Richart.

Hence, the comparison was focused on these two models, in order to examine whether or not the parabolic (and more realistic) distribution yields similar results to the linear one, which has already been proved reliable.

The **linear distribution** is, approximately, a simple relation between the depth and the elastic modulus:

$$E(MPa) = 4 \cdot z$$

The **Yu and Richart** model for pure sand is based on the following relation:

$$G_{\max} = A_G \cdot F(e) \cdot (\sigma'_0)^{n_G}$$

where

$$A_G = 7000$$
$$n_G = 0.5$$

depending on the soil type

$$\sigma'_0 = \left(\frac{\sigma'_1 + \sigma'_2 + \sigma'_3}{3} \right)$$
$$\sigma'_1 = \gamma \cdot z$$
$$\sigma'_2 = \sigma'_3 = K_0 \cdot \sigma'_1$$

and

$$F(e) = \frac{(2.17 - e)^2}{1 + e}$$

Where e is the pore index equal to

$$e = \frac{\rho_s}{\rho} - 1 = 0.286$$

It must be clarified that the Yu and Richart model was proposed for dynamic problems, thus, the values we get from the above equations are very large to be implied into our quasi-static problem. Hence, we derived the G_{max} values with an integer in order to obtain smaller values and to achieve relatively similar values to those of the hybrid-beam model of the previous chapters, in order to be able to make valid comparisons.

The results of the comparison, both for normal and reverse fault rupture are presented in **Figures 5.1.4 - 5.1.7,** in terms of surface displacements and surface angular distortion, for an imposed bedrock movement up to 3m. It is quite obvious that the two different soil profiles yielded quite similar results. The final surface displacements are almost identical, whereas the surface shear strain slightly differs between the two profiles. The main difference is that the parabolic profile seems to result to quicker fault propagation to the surface and to a slightly more centralized deformation.

However, the comparisons are close enough to allow the use of the parabolic profile in our 3D model, without expecting any practical differences compared to the linear one.

5.2 Normal Fault Rupture

The 3-D hybrid model is used to examine the pipe behavior, when subjected to a fault rupture that initiates 40m below the surface. The results we obtained are demonstrated in **Figures 5.2.1 - 5.2.8**. It must be clarified, that “40 m model” corresponds to the 3-D Hybrid-beam model of 5 m depth which takes into account a fault that initiates from the bedrock layer, 40 m below the surface, whereas “5 m model” corresponds to the previously described Hybrid-beam model of Chapter 3. In addition, we may refer to “vertical fault displacement” meaning the vertical component of the bedrock movement.

Despite the differences of the 40 m and the 5 m models, the results are quite similar. The axial strain development and distribution is very much alike and the upper limit of 5% axial tensile strain is reached for the exact same values of bedrock vertical displacement. As described in Chapter 3, a transition from prevailing bending to prevailing tension is again spotted (**Figure 5.2.2**). The critical, failure areas of the

40 m model are slightly different and located about 3 m away, compared to the 5 m model. As expected from the aforementioned similarities, substantial differences are not spotted either in terms of axial forces (**Figure 5.2.4**).

Regarding the effective pipe length, it appears that the length of the activated pipe is the same towards the hanging wall and the footwall side. Compared to the 5 m model of Chapter 3, the L_{eff} is practically the same and differs only during the first 0.2 m of vertical bedrock movement, where the 40 m model demonstrates a much smoother increase of the L_{eff} (**Figure 5.2.5**).

Pipe detachment from the soil was also examined and is presented both in terms of areas of contact loss and in terms of relative soil-pipe vertical displacement (**Figure 5.2.6**). It is clear that, detachment occurs later in the case of 40 m model, but again, it takes only a small bedrock movement (h = 0.08 m) for detachment to occur. For completeness' sake, soil pressures around three pipe cross-sections are presented in **Figure 5.2.7**.

Regarding the substantial differences that occur as a result of the soil layer's depth effect, the different soil displacement distribution is one of the most important factors. As demonstrated in **Figure 5.2.8**, unlike the 5 m model, where the displacements (thus the deformations) are concentrated along a relatively narrow area, in the case of 40 m model, not only the values of displacement are lower for the same bedrock movement, but also the distribution is significantly less steep. This is also depictured by the displacement diagrams of the same figure, where the displacements of the soil right beneath the pipe are compared.

However, the most important difference, from a practical point of view, is that the two models reach the limit of 3% axial strain for totally dissimilar values of vertical bedrock movement h, with the exception of the case of D/t=72. The 40 m model provokes a less intense bending loading, thus, the increase of axial strains because of bending is less rapid. Hence, in the 5m model, the 3% strain limit, which is caused by bending, is reached quicker, before the transition to prevailing tension. On the contrary, in the 40m model, the axial strains caused by bending demonstrate a

milder increase, as a result of the wider displacement distribution, so that the prevailing tension appears before the 3% strain limit is reached. After the change of loading mechanism there is a rapid increase of the axial strains, reaching the 3% and 5% limit, practically for the same h.

This relatively limited difference, in terms of critical bedrock movement, has to do with the nature of normal fault propagation. Because of its tensile nature, (thus active conditions) the rupture propagates relatively rapidly up till the surface. Anastasopoulos et al. (2007) have shown that for normal fault, propagating through dense sand, it takes about (0.75% Z) of vertical bedrock movement for fault outcropping, where Z = the soil layer depth. On the contrary, it takes 3 times bigger bedrock movement for a reverse fault to outcrop (2.5% Z). Indeed we observe limited differences for the normal fault case whereas for the reverse fault, the differences are much greater as shown in the following paragraph.

5.3 Reverse Fault Rupture

The effect of soil layer's depth was also examined for the case of reverse fault rupture. The differences compared to the 5 m model are obvious in every aspect of the obtained results.

Even though local buckling is once again the failure mode, the strain distribution and development are quite different in this case. In **Figure 5.3.2** the strain distribution, as the fault movement increases, is demonstrated and it is obvious that the two inflection points we had in the 5 m model do not appear as quickly and as clearly. Furthermore, the sequence of the occurrence of local buckling is opposite to that of 5 m model and now the first buckling appears in the footwall and the second one in the hanging wall. This is due to the different displacement distribution the pipe is subjected to as shown in **Figure 5.3.3.**

The most significant alteration that occurred concerns the critical fault displacement. As demonstrated in **Figure 5.3.11**, pipe can endure up to 5 times (depending on the D/t ratio) bigger vertical fault movement. The critical axial compressive strains are also greatly larger (**Figure 5.3.5**). The above observation, as well as all the observed differences, is the result of the totally different distribution of displacements, as demonstrated in **Figure 5.3.10**, and of the passive conditions that occur during a reverse fault, which cause slower rupture propagation. In simple words, since the fault movement needed for fault outcropping is about 2.5% of Z (instead of only 0.75% as in normal fault) a deeper soil layer affects much more intensively the results of the reverse fault case. The fault rupture “needs” a lot more of bedrock displacement in order to reach the pipe and in general, in order to reach the same deformation state with the 5m model.

Concerning the pipe detachment, contrary to all the previous cases, loss of contact between the pipe and the soil appears only after 0.60 m of vertical fault displacement (**Figure 5.3.7**). Again, for the sake of completeness, the L_{eff} and the soil pressures along certain pipe cross-section are demonstrated in **Figures 5.3.6** and **5.3.8** respectively.

Main conclusions of Chapter 5

- We examined various parabolic E distributions in order to add realism to our simulation. We concluded that the Yu and Richart distribution is the best among those we examined, since it yields only negligible differences compared to the linear distribution, which has been used various times from our department and has been tested for its reliability.

- As expected, the greatest alteration, between this model and the model of Chapter 3, is the distribution of soil displacement. This is the cause of every observed difference.

- The lower displacement values and the more smooth soil displacement distribution at the level of the pipe lead to larger pipe endurance in terms of vertical bedrock displacement.

Figures of Chapter 5

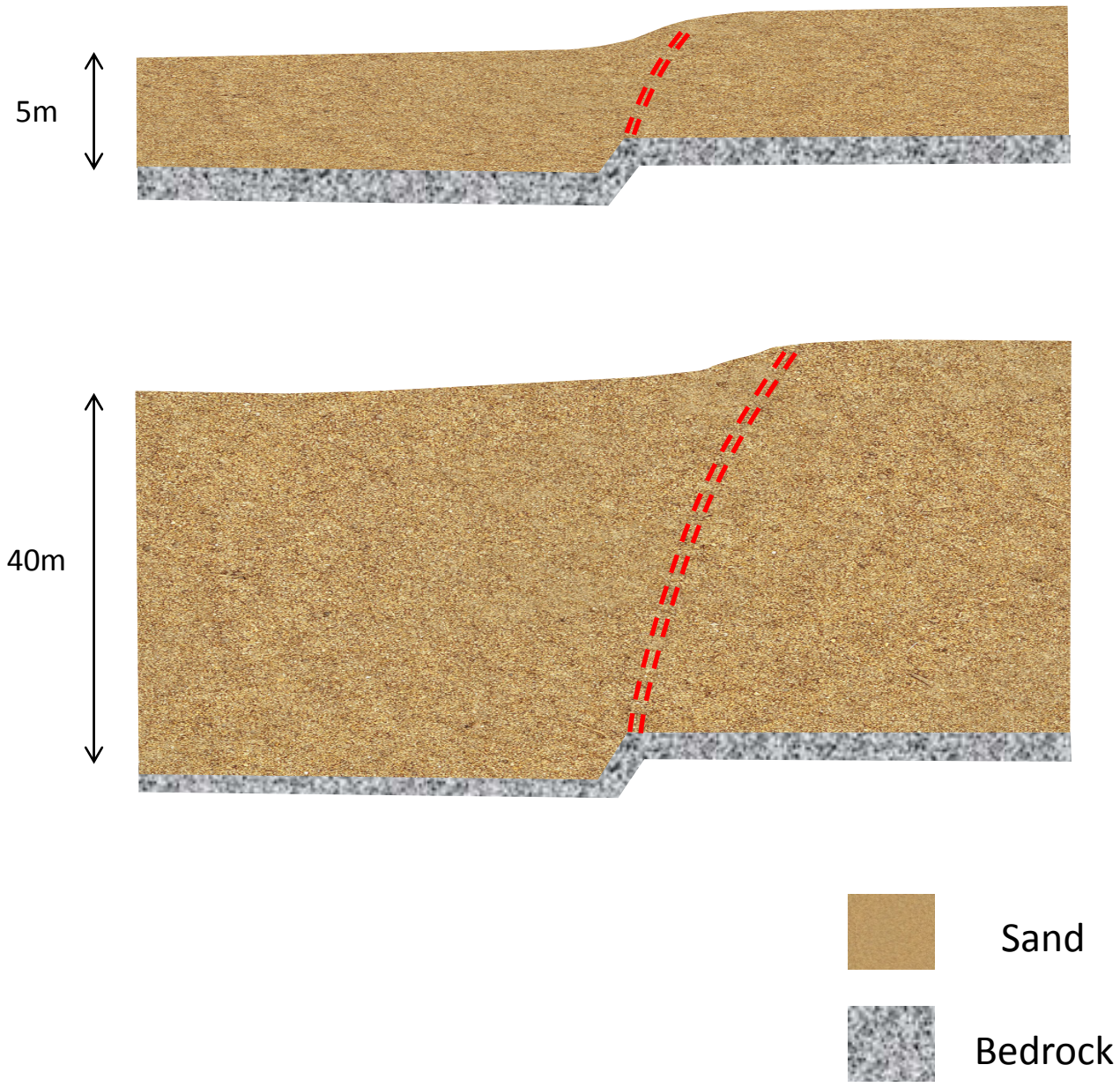

Figure 5.1.1. Two normal fault ruptures, propagating through a surface soil layer of 5 m and 40 m respectively. In Chapter 5, the differences of those two models regarding the pipe behavior are examined, both for normal and reverse faults.

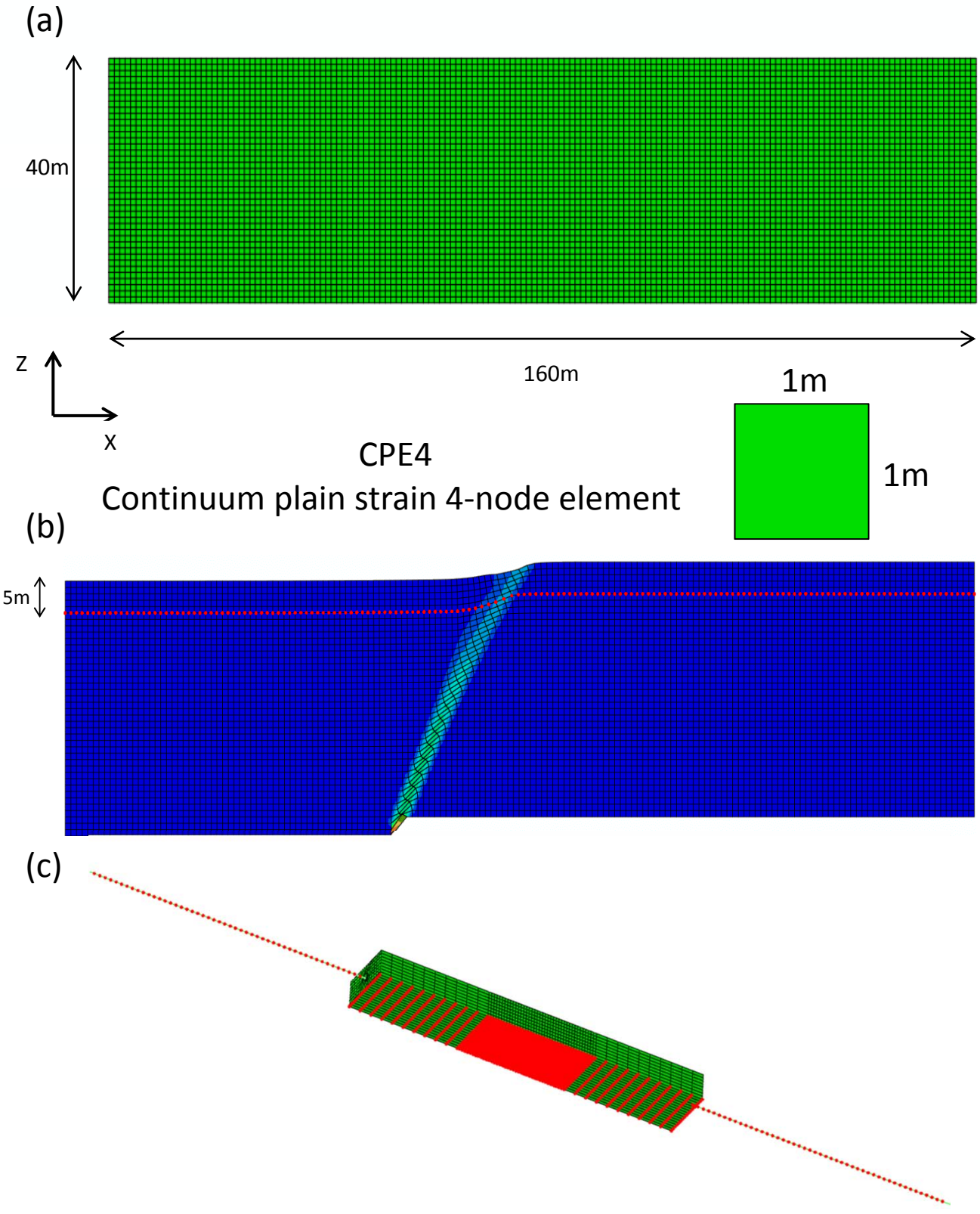

Figure 5.1.2. (a) The 2-D model consisted of square finite elements 1m x 1m.b) The deformed 2D free field model, used for obtaining the displacements during the development of the fault, at level 5m below the surface. Those values where applied to the base of the 3D model (c).

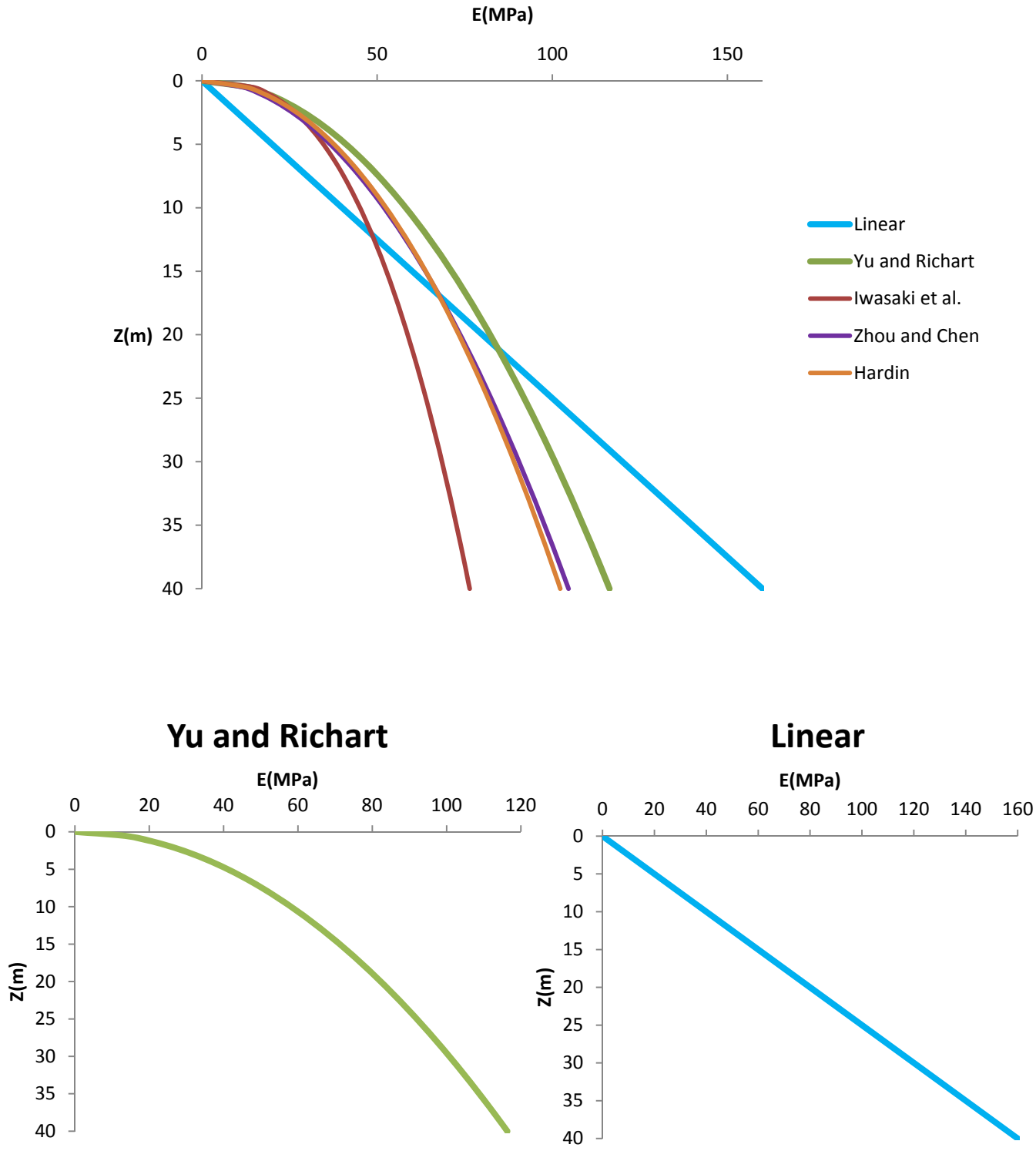

Figure 5.1.3. The distribution of Young's modulus along the depth of our model, according to various proposed models. Yu and Richart's relation was selected to be compared with the linear distribution.

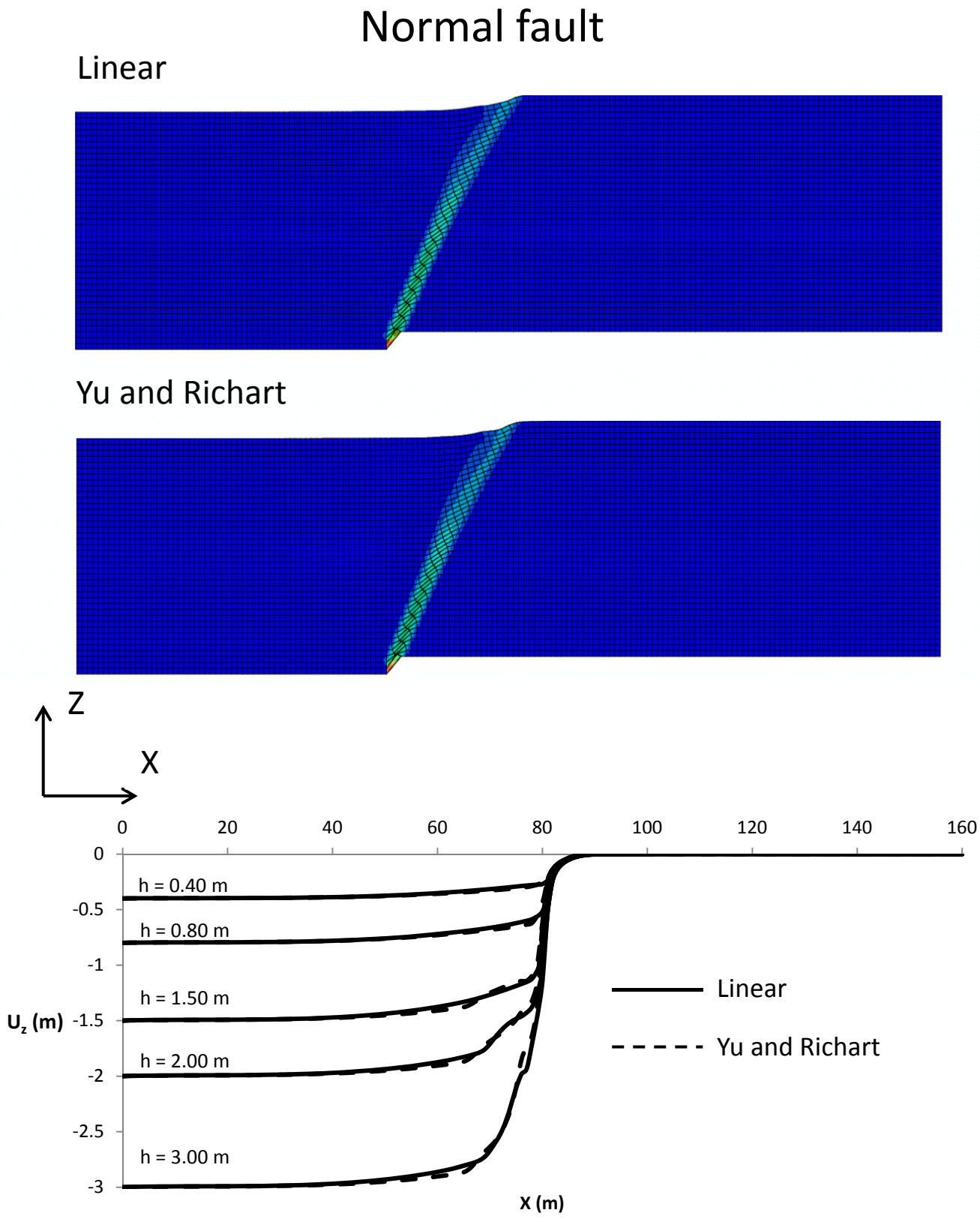

Figure 5.1.4. The deformed models are almost identical for Linear and Yu and Richart distribution. This is also depicted by the comparison of the vertical displacements of the surface of the two models (h = 3 m).

(a)

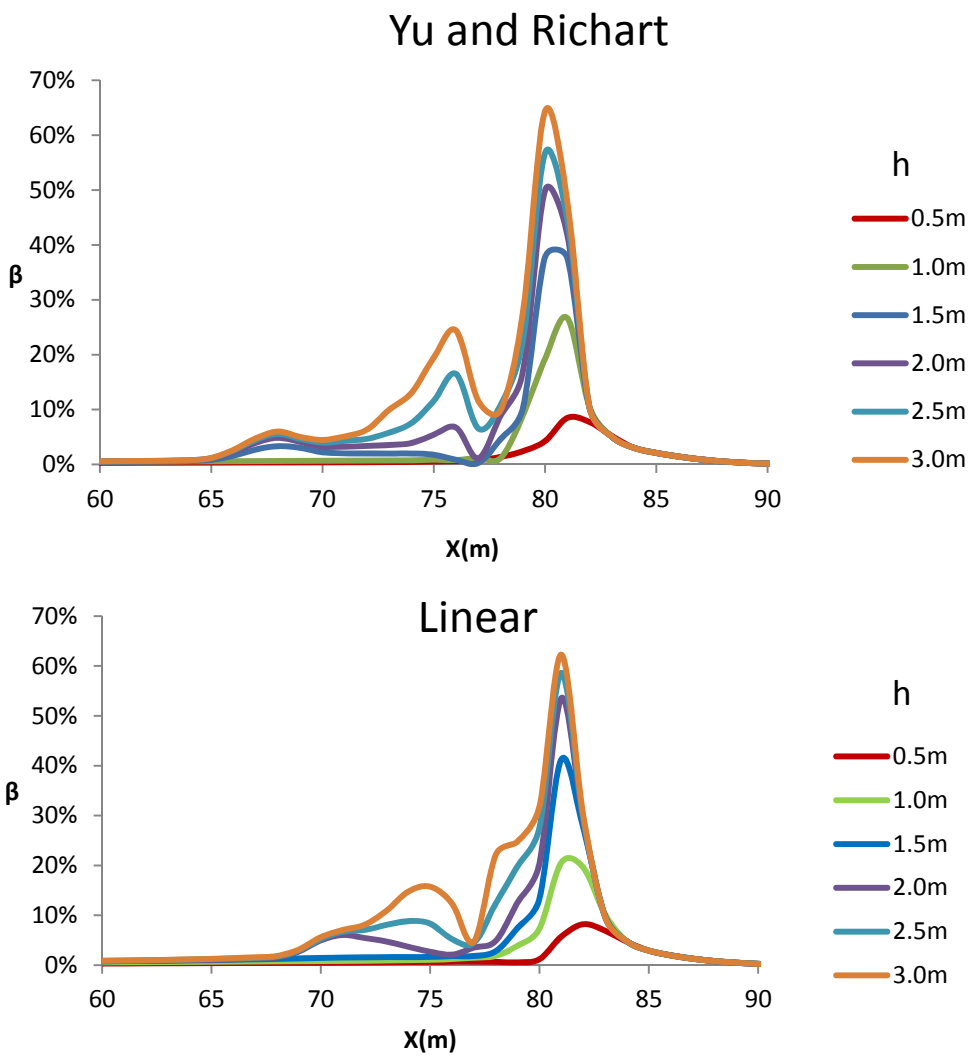

(b)

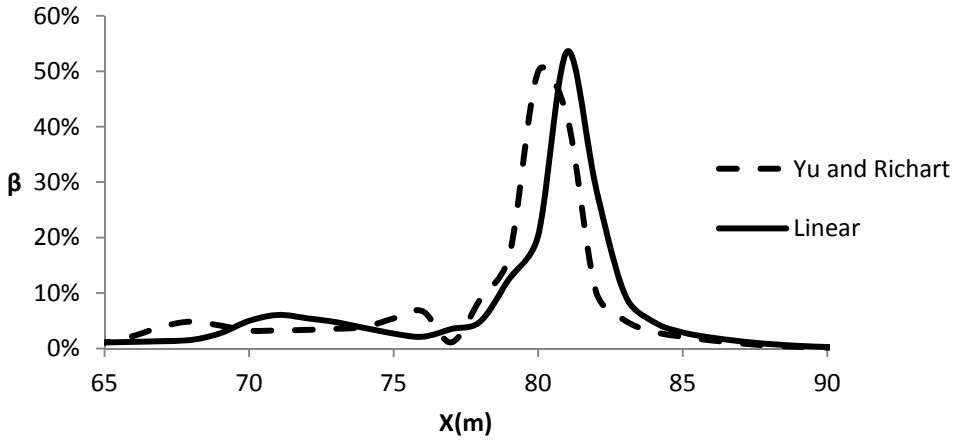

Figure 5.1.5. (a) The development of angular distortion β along the surface area where the fault outcrop appears, for linear and Yu and Richart E distribution. (b) Comparison of the angular distortion β for vertical fault displacement h = 2 m.

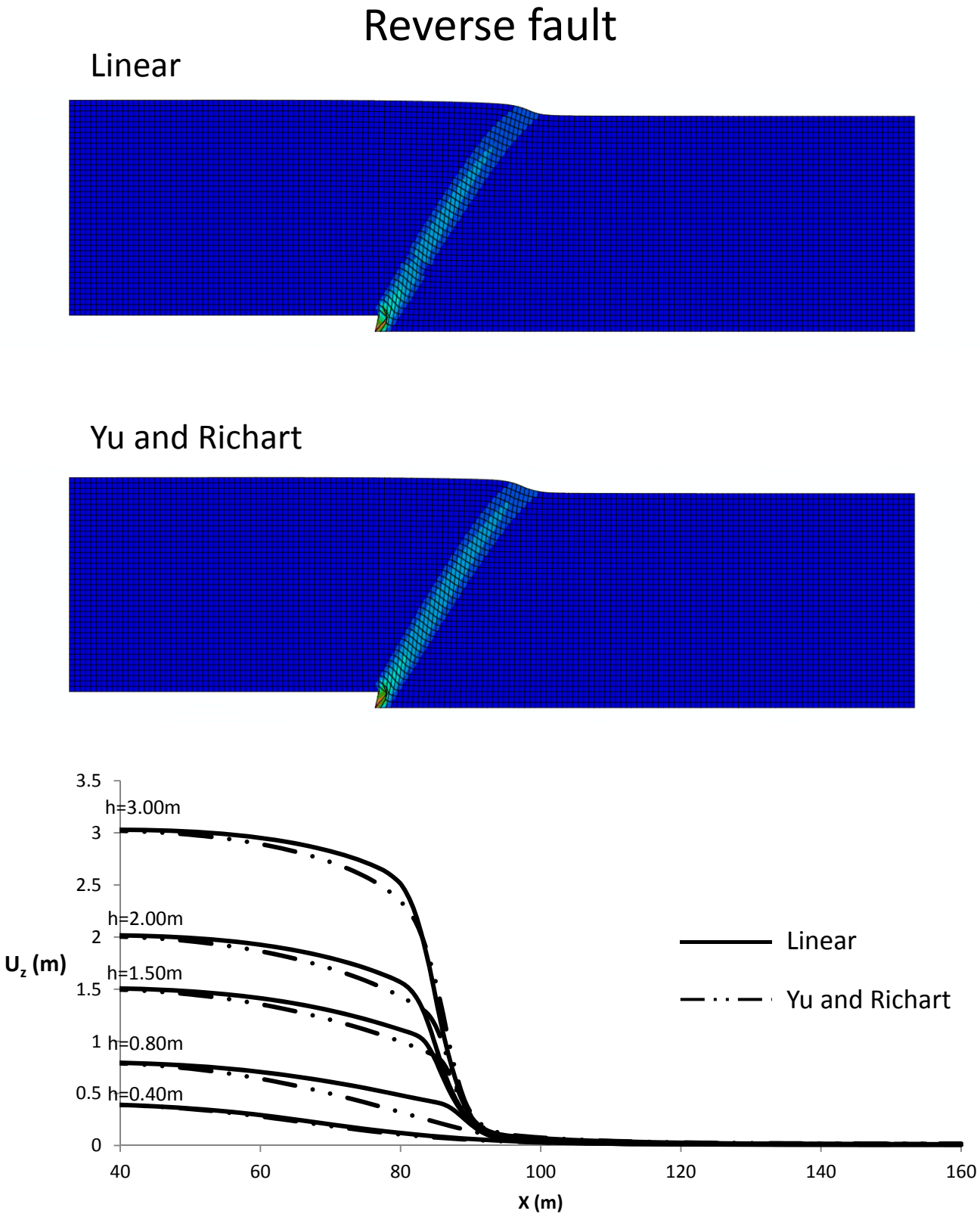

Figure 5.1.6. The deformed models of reverse fault for h = 3 m. The vertical displacements demonstrate no significant differences between linear and parabolic distribution model.

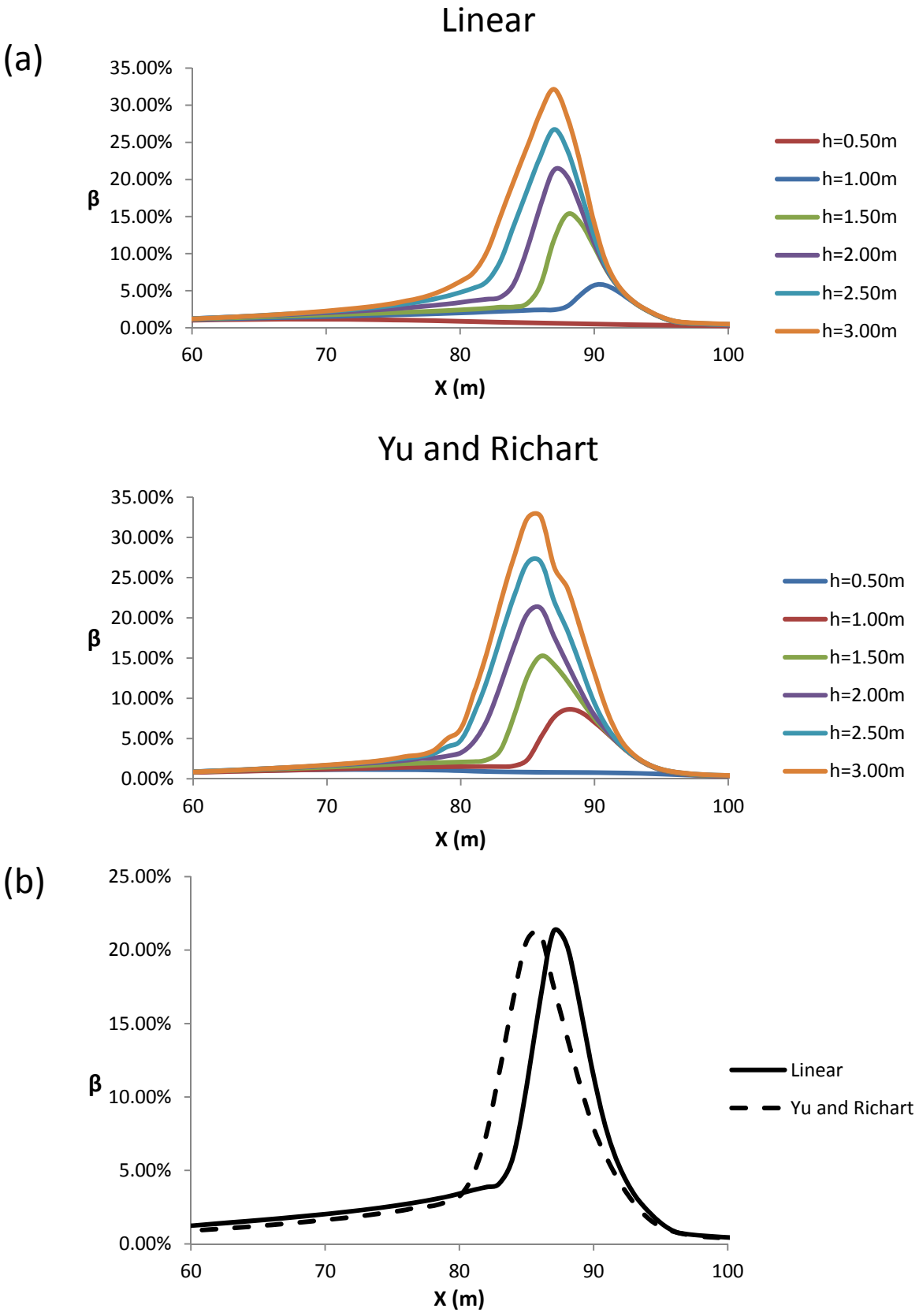

Figure 5.1.7. a) The development of angular distortion β along the surface area where the fault outcrop appears ,for linear and Yu and Richart E distribution. b) Comparison of the angular distortion βfor vertical fault displacement h = 2 m.

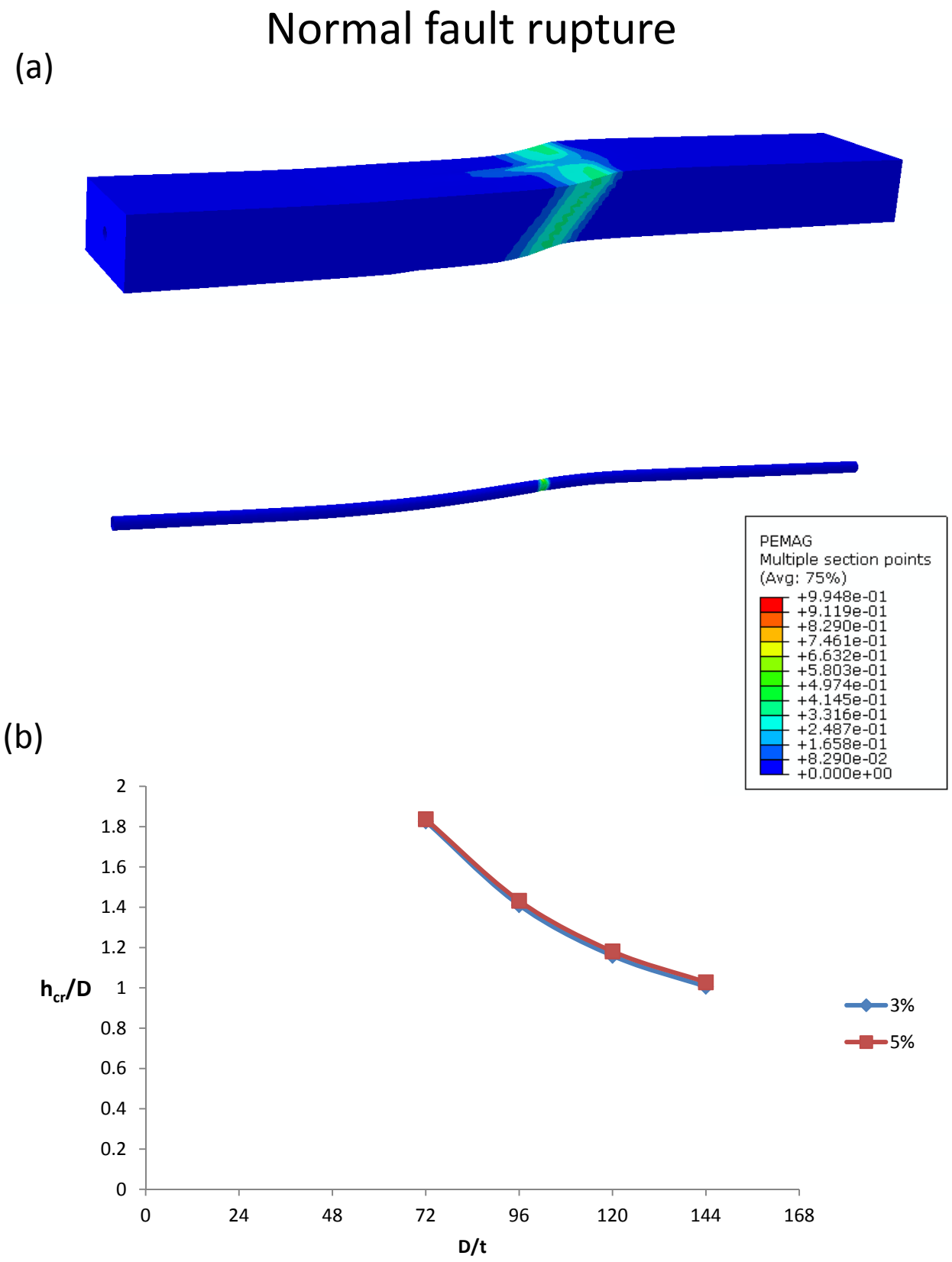

Figure 5.2.1.. (a) The deformed soil and pipe. (b) The critical vertical fault displacement to diameter ratio (h_{cr}/D) with respect to the diameter to thickness ratio (D/t).

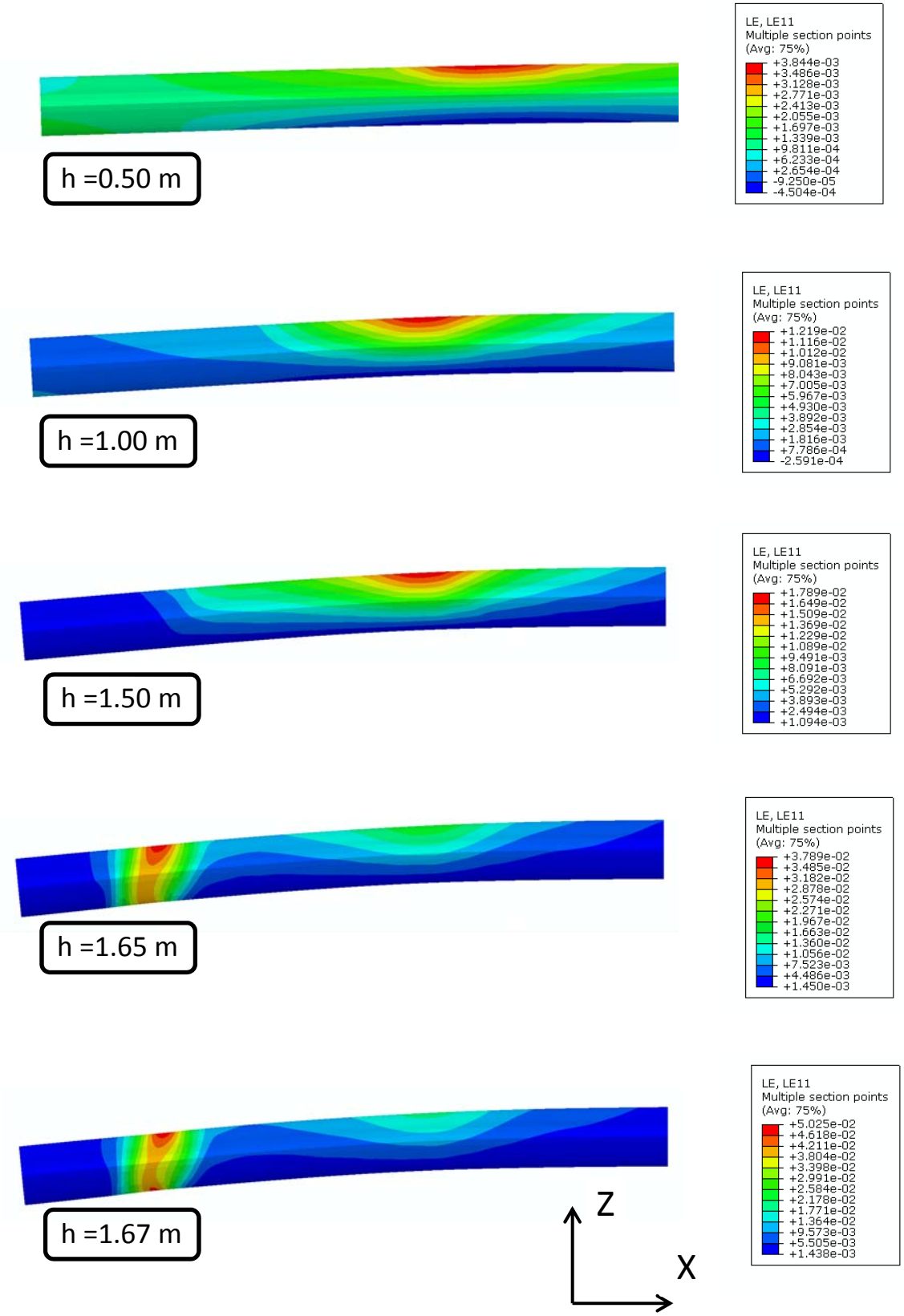

Figure 5.2.2. The axial strain distribution along the critical pipe area (X=27-37 m) for five fault displacements h. (D/t = 72)

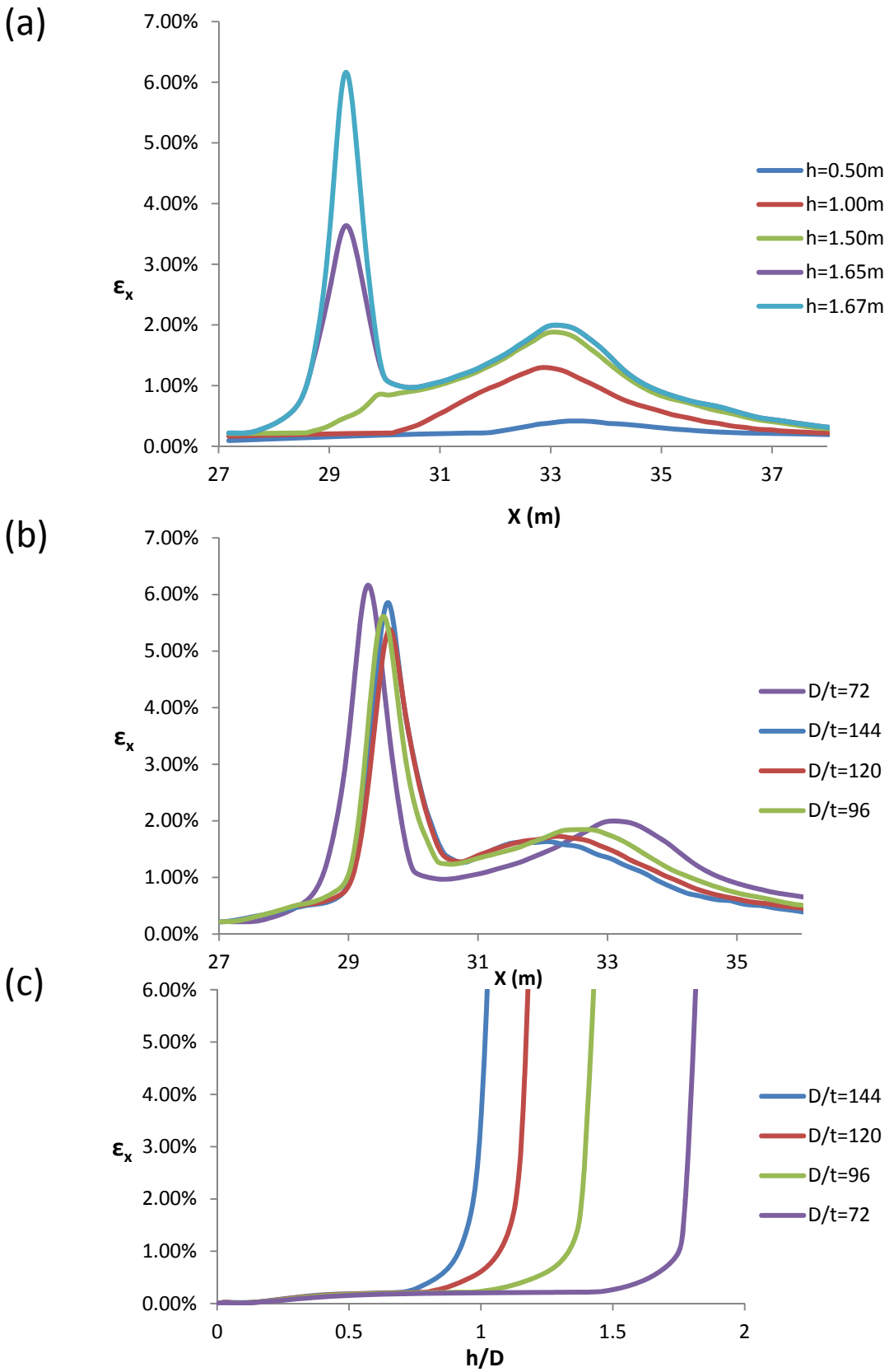

Figure 5.2.3. (a) The axial strain distribution along the critical area for D/t = 72. (b) Comparison of axial strain distribution, when critical state is reached (ε_x=5%), for four D/t ratios. (c) Comparison of axial strain development at the points where the limit strain is exceeded, with respect to the vertical fault offset for D/t=72,96,120 and 144.

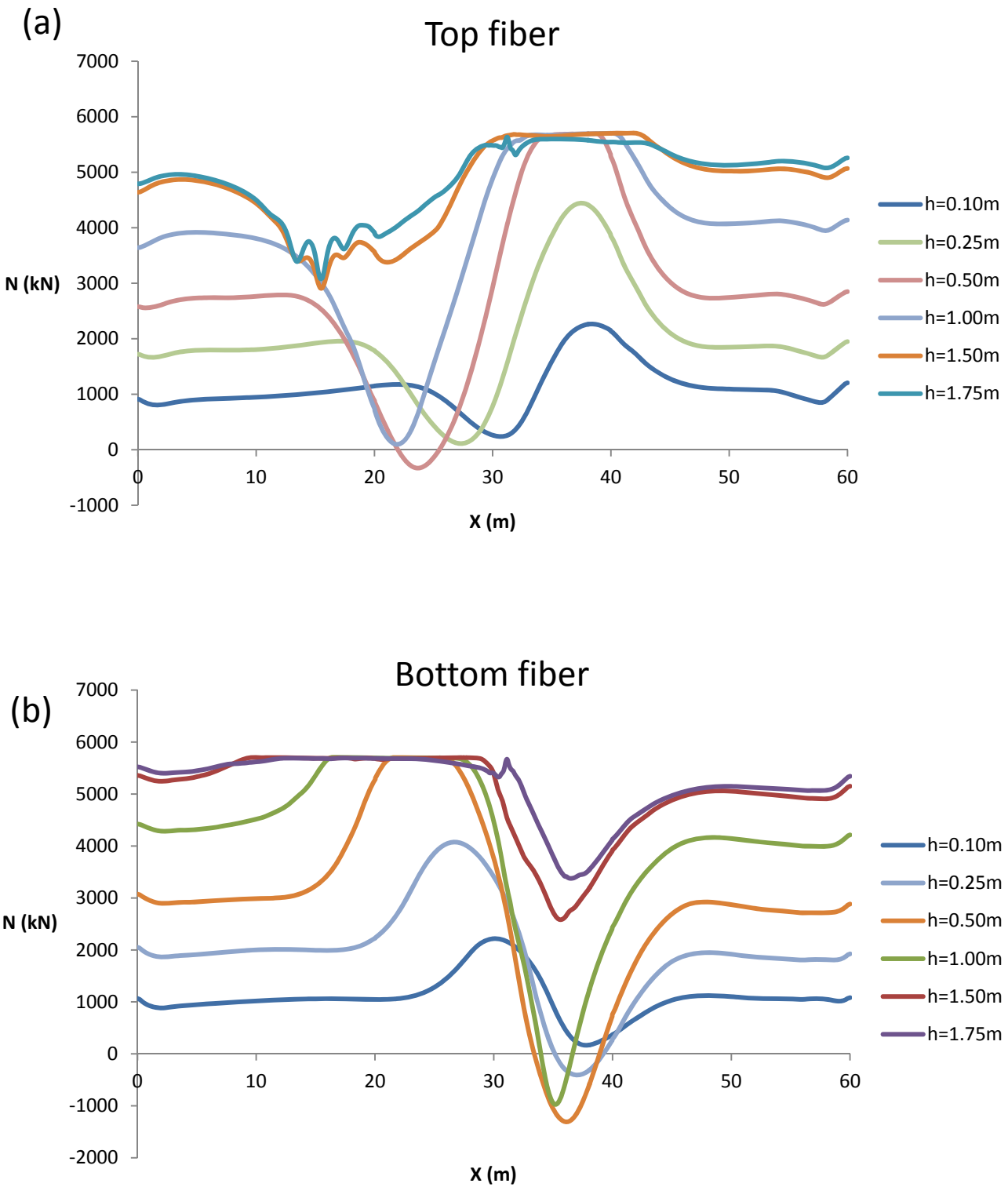

Figure 5.2.4. Axial force distribution and development for six vertical fault displacements for (a) the top pipe fiber (b) the bottom fiber (D/t = 72)

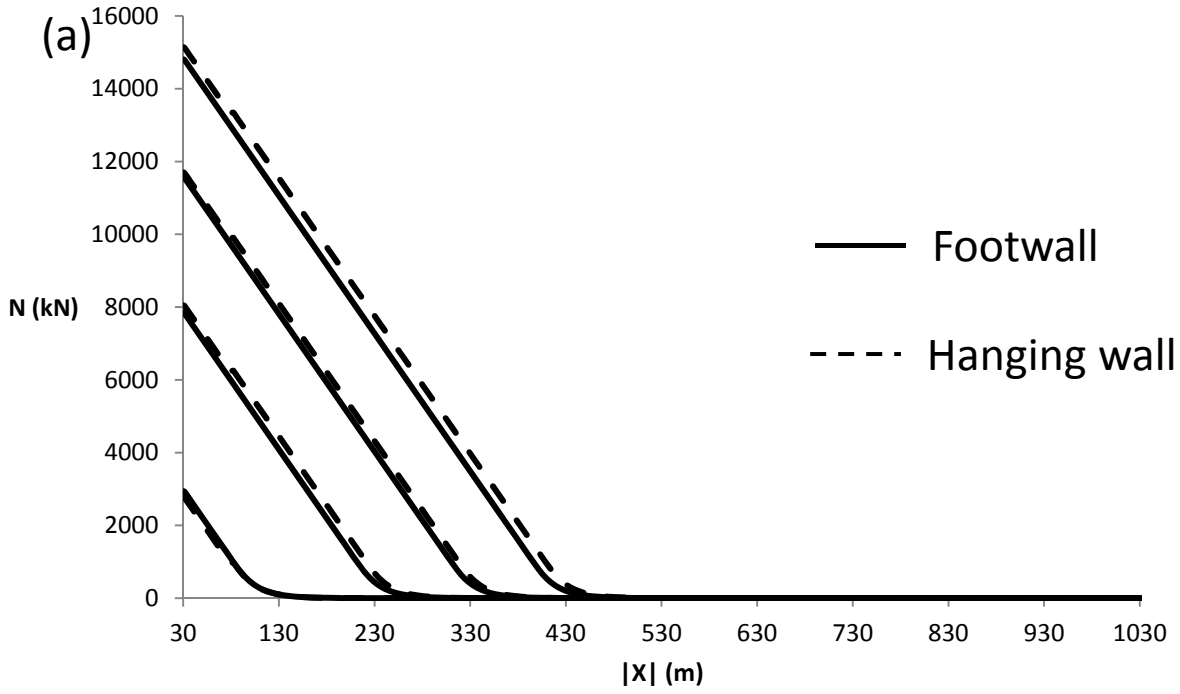

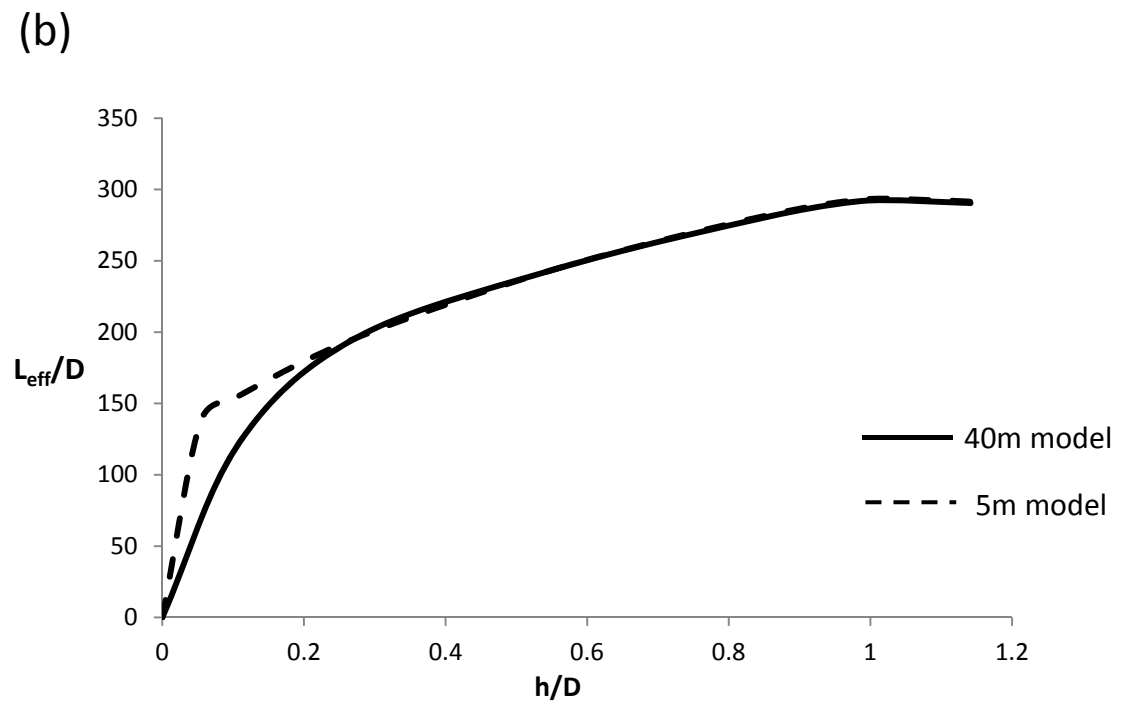

Figure 5.2.5. (a) Axial beam force in the hanging wall and the footwall. No significant difference is spotted. In this diagram, X=0 is considered at the middle of the model, where the fault crosses the pipe, approximately. (b) The activated pipe length with respect to the vertical fault offset (D/t = 144).

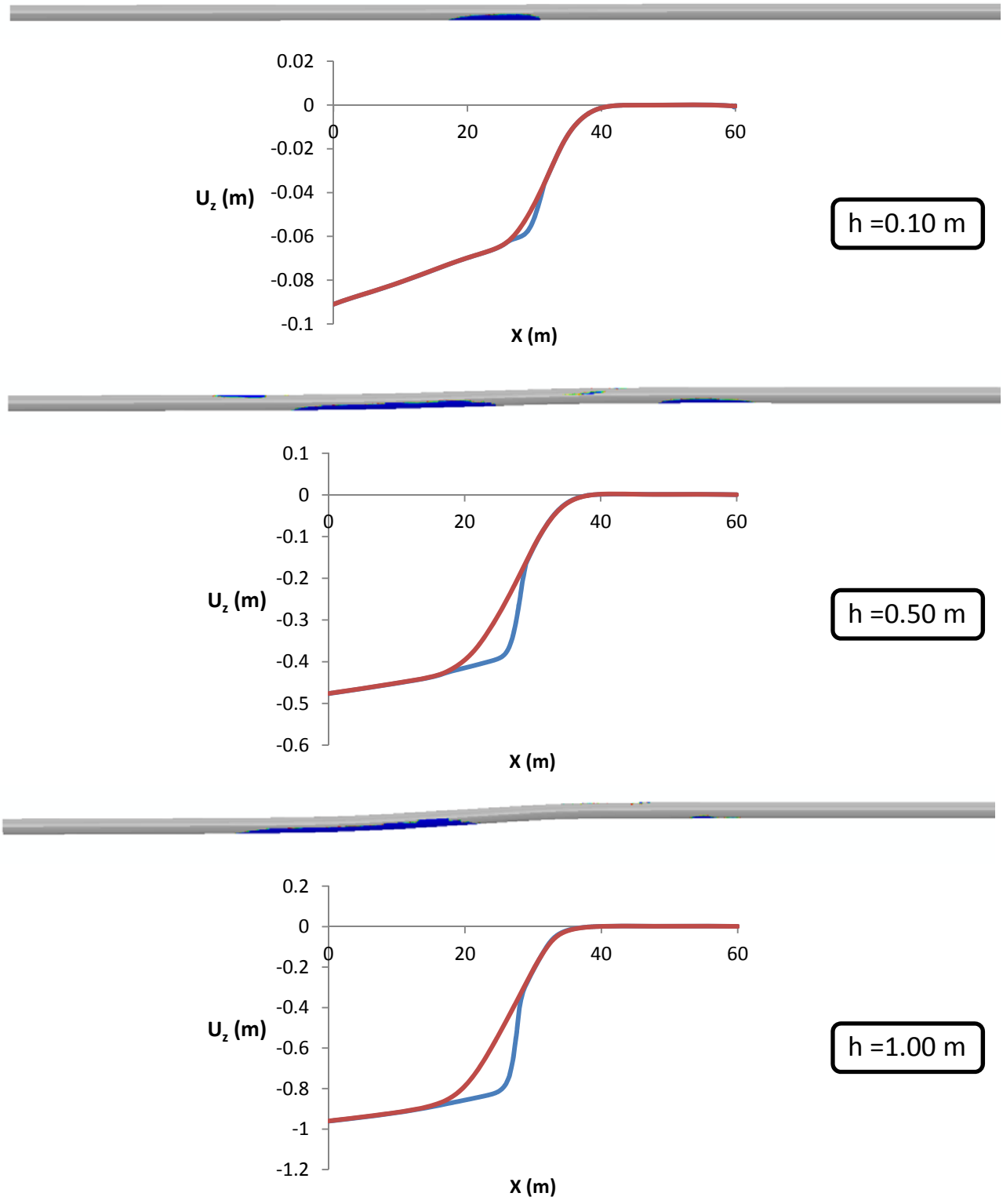

Figure 5.2.6. Pipe detachment areas from the surrounding soil are defined by the blue colored areas. The detachment of the pipe bottom from the soil beneath it, is demonstrated by the diagrams of vertical displacements of the pipe bottom and the soil for three values of vertical bedrock displacement.(D/t = 72)

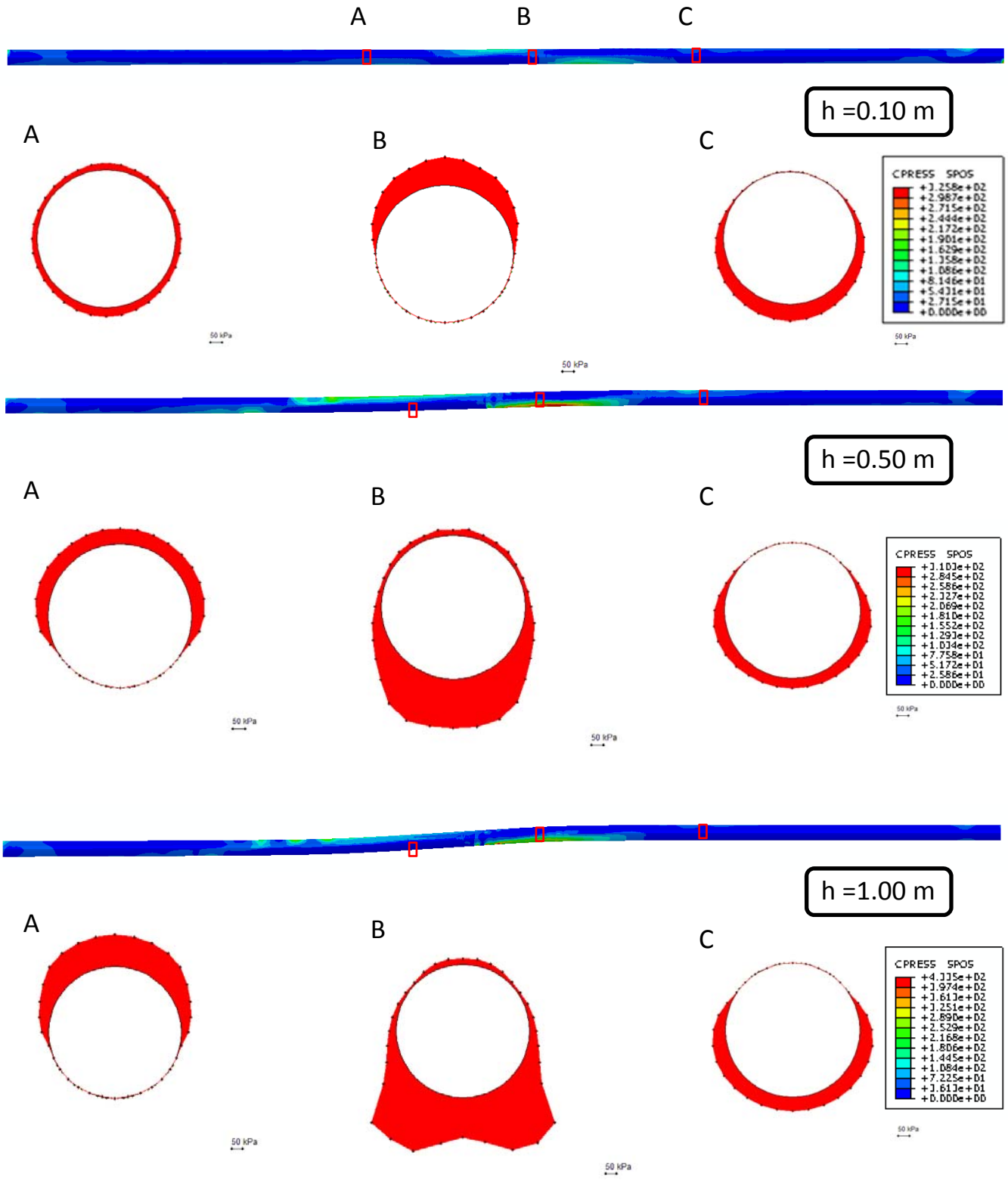

Figure 5.2.7. Soil pressures along the pipeline and soil pressures around three pipe cross-sections A,B and C (X=20,30 and 40 m respectively) for three vertical fault offsets h.

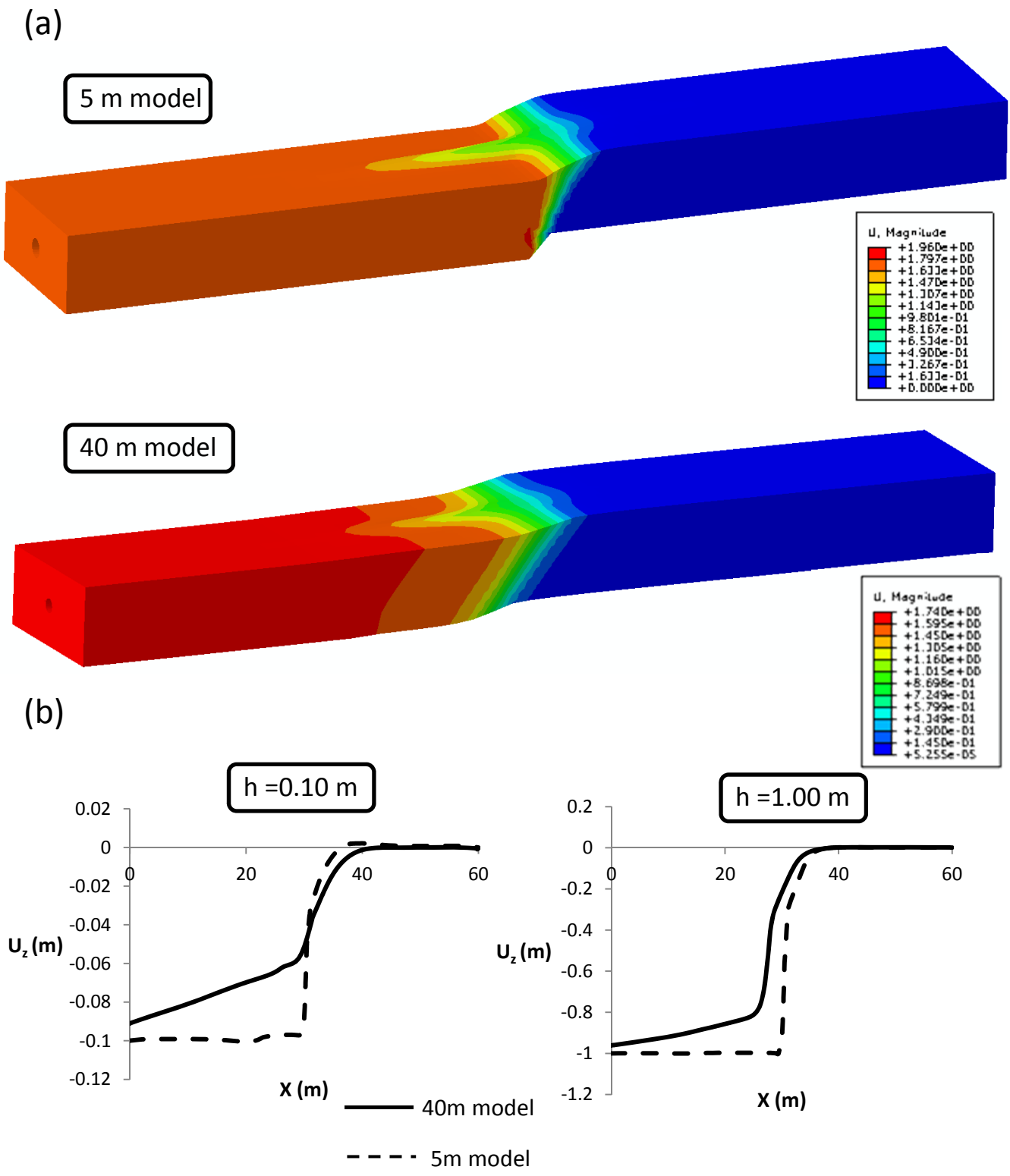

Figure 5.2.8. (a) Displacement distribution for the limited 5 m depth model and the model that takes into account a soil layer of 40 m depth. (b) Comparison of soil vertical displacements beneath the pipe bottom between the 5 m and 40 m model.

Reverse fault rupture

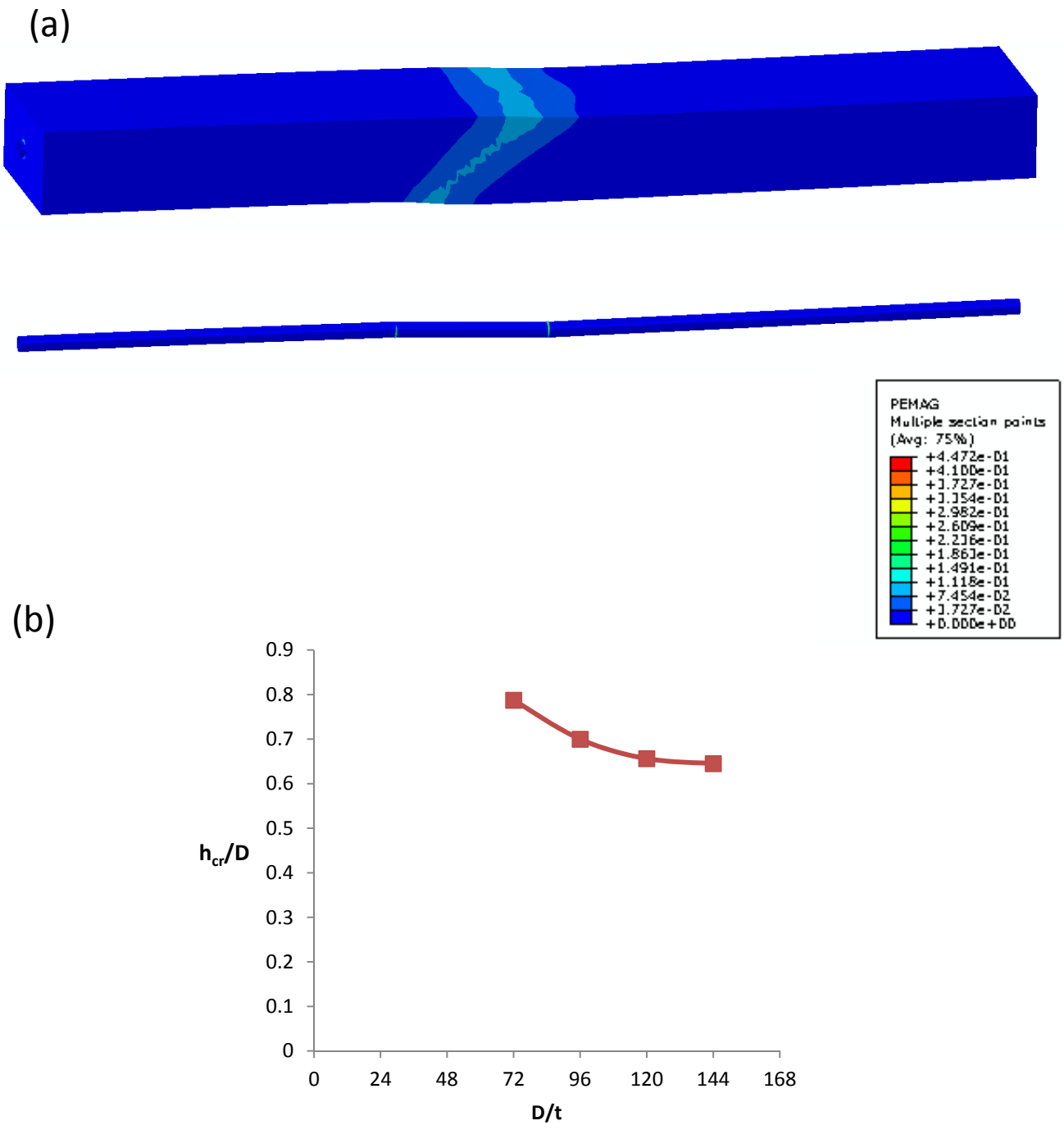

Figure 5.3.1. (a) Plastic strain distribution along the deformed soil and pipe for the reverse fault case. (b) The critical vertical fault displacement to diameter ratio (h_{cr}/D) with respect to the diameter to thickness ratio (D/t).

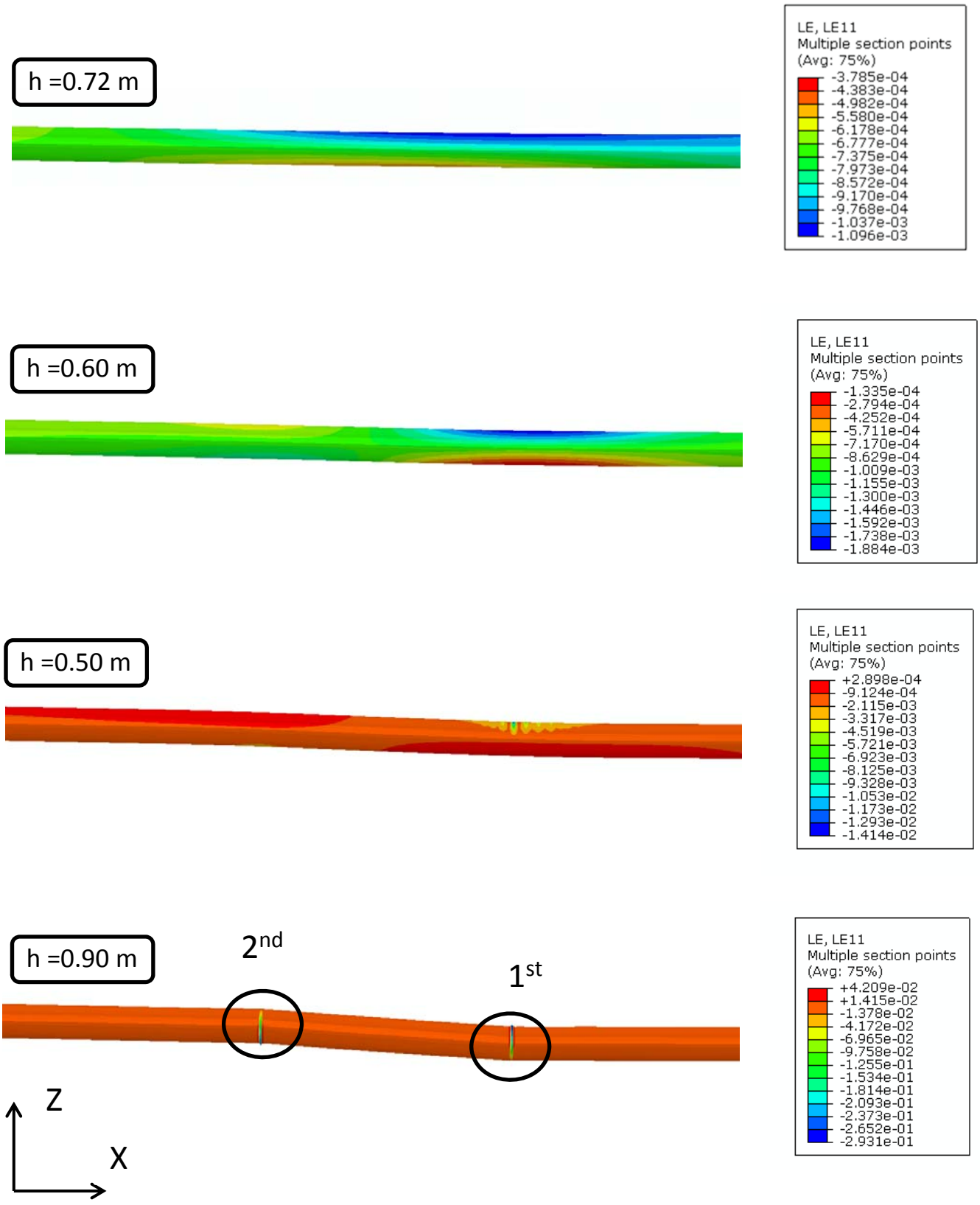

Figure 5.3.2. The axial strain distribution along the critical pipe area (X=13-40 m) for four fault displacements h. (D/t = 72). First buckling occurs in the footwall .

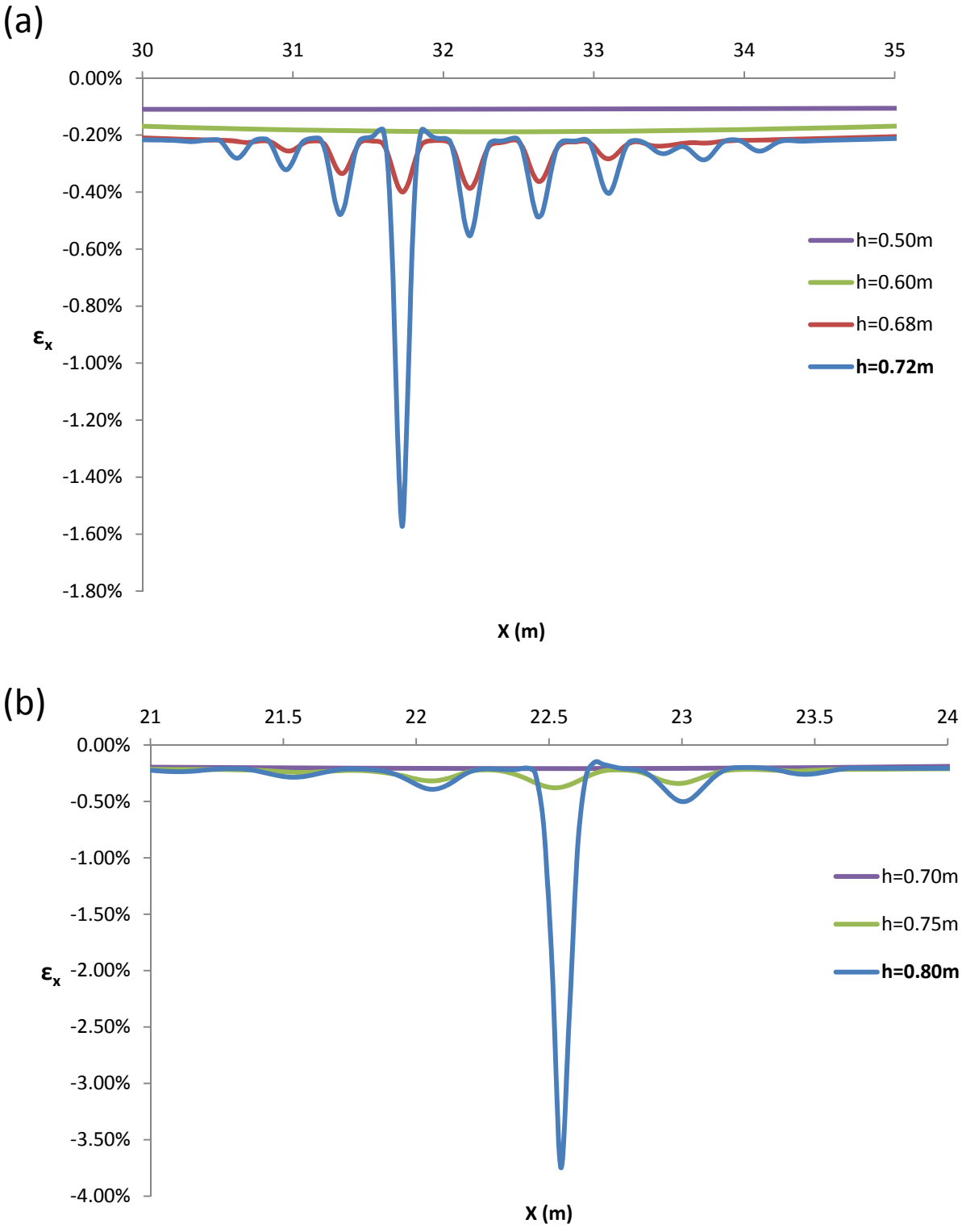

Figure 5.3.3. The distribution of axial strains until (a) the 1st appearance (h = 0.72 m) and (b) the 2nd appearance of buckling (h = 0.80 m). (D/t = 72)

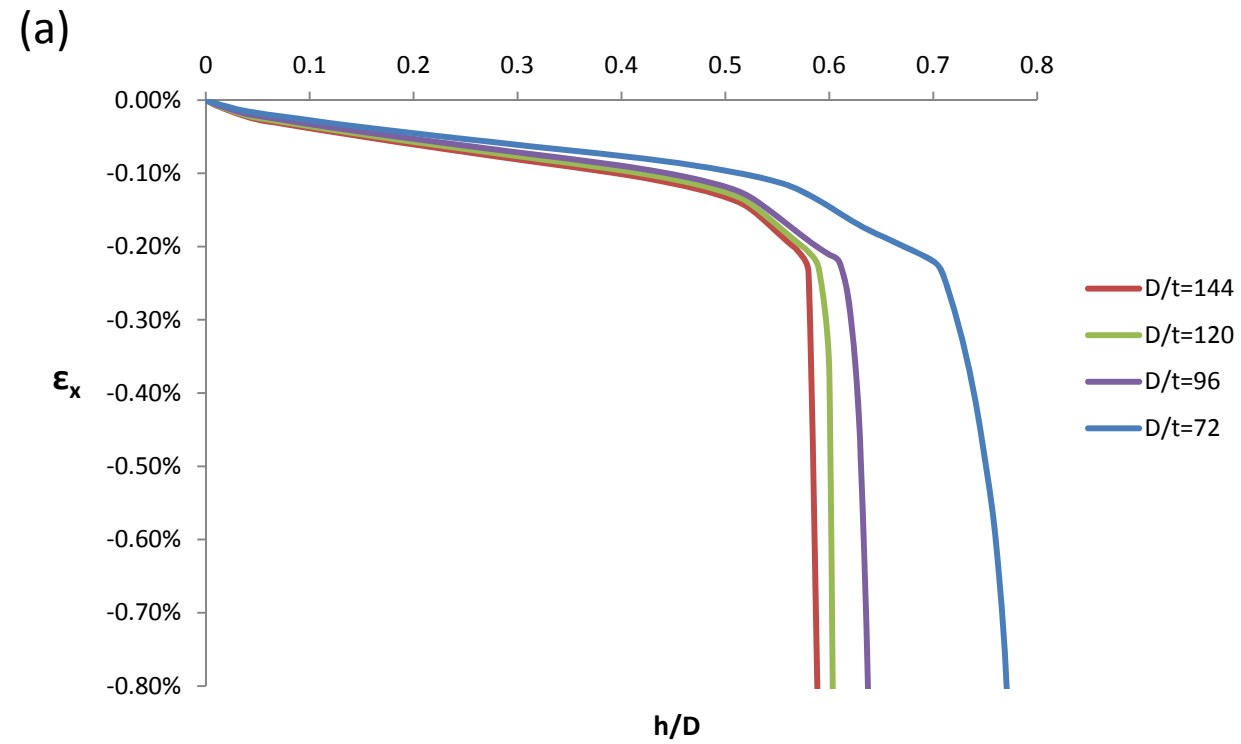

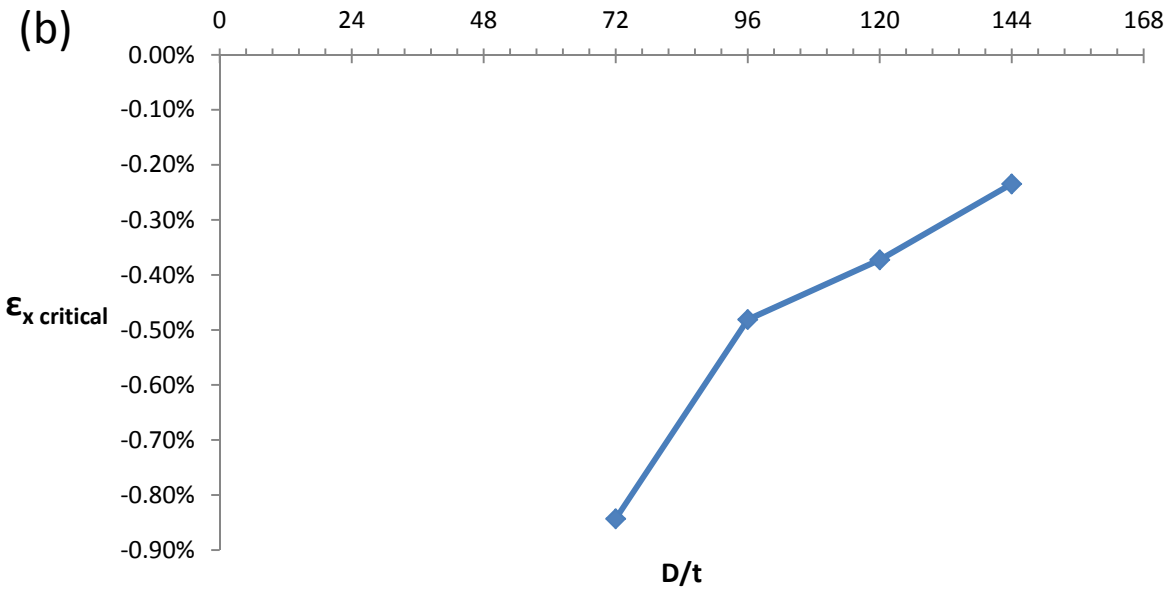

Figure 5.3.4. (a) Axial strain development at the buckling points with respect to the h/D ratio, for D/t=72-144. (b) The critical axial strain values , beyond which buckling occurs., for all the four values of D/t.

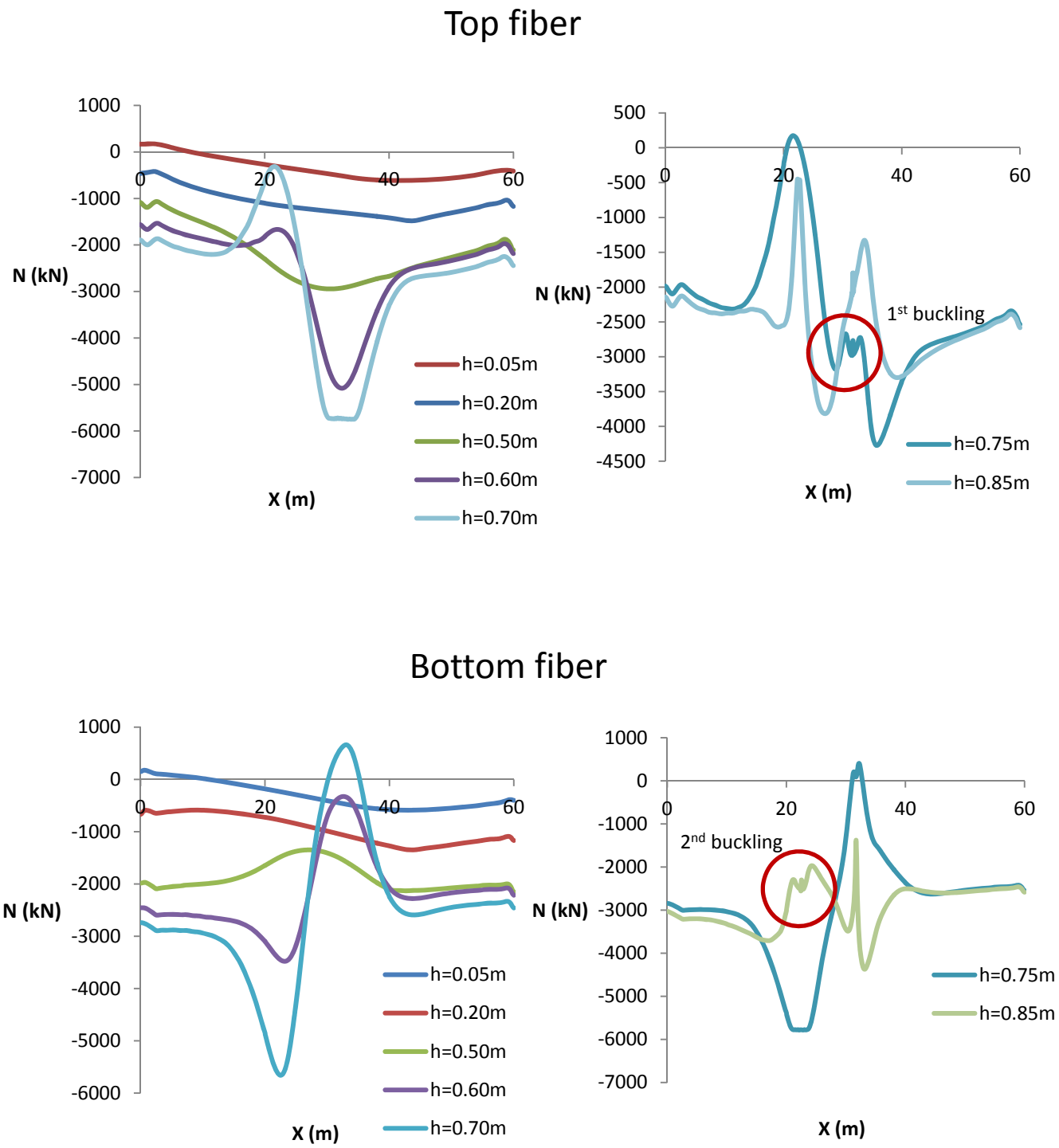

Figure 5.3.5. The axial stain along the bottom and top pipe fiber before and after the occurrence of buckling.

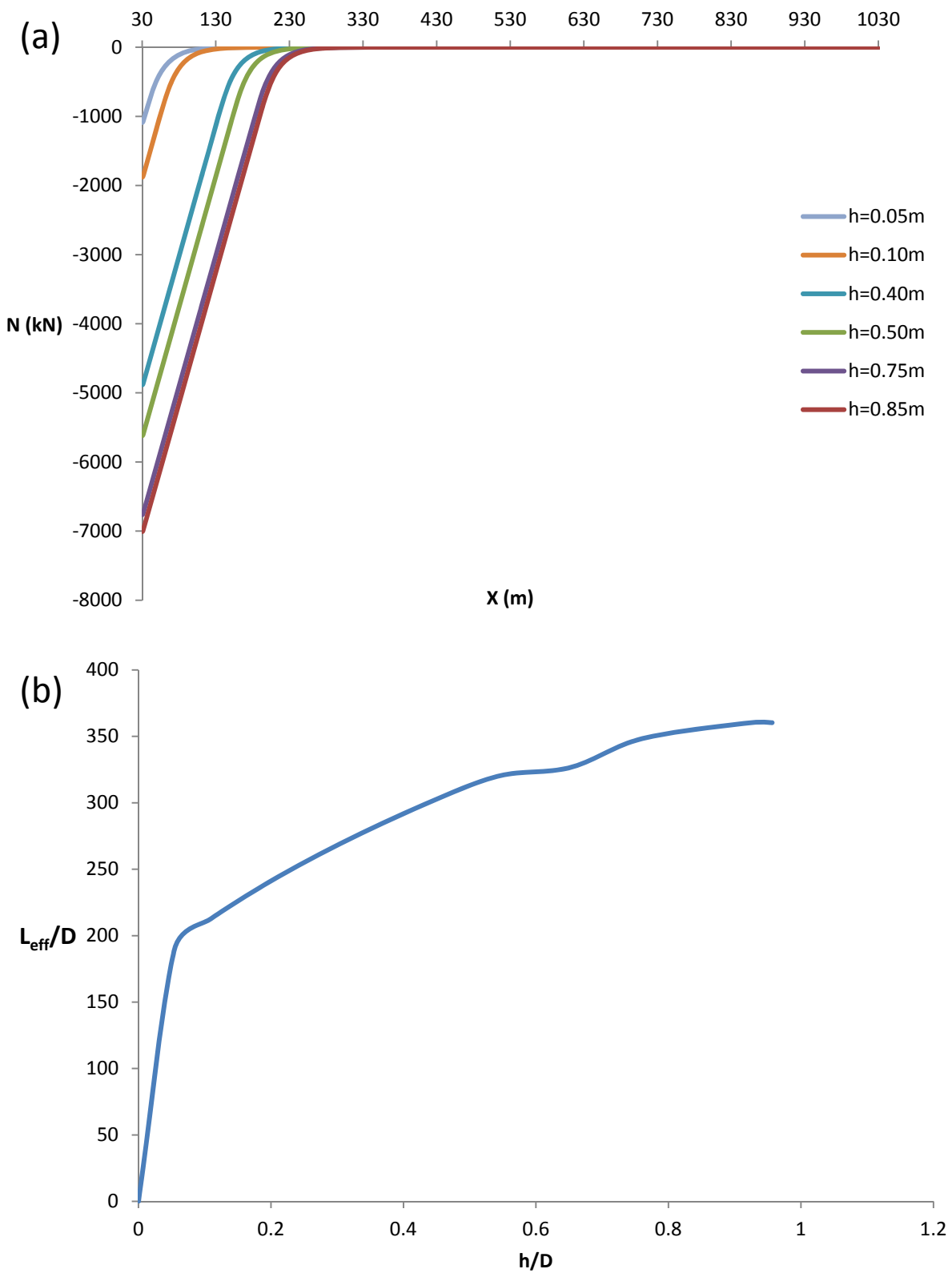

Figure 5.3.6. (a) The axial beam forces in the footwall, demonstrating the activated pipe length with respect to the vertical bedrock displacement. (b) The effective pipe length to diameter ratio with respect to the h/D ratio (D/t = 72).

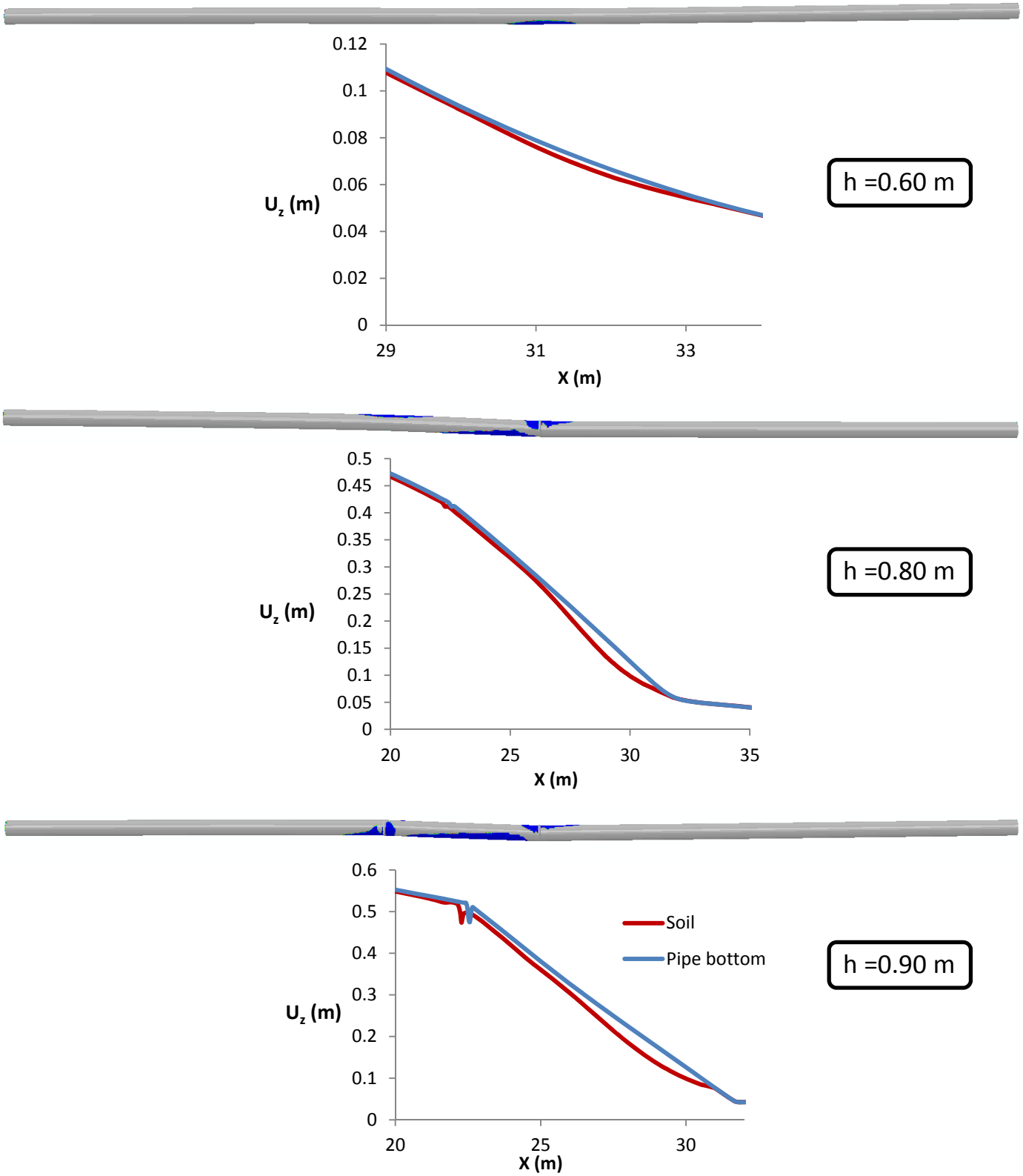

Figure 5.3.7. Detachment areas are defined by the blue colored areas. The detachment of the pipe bottom from the soil beneath it, is demonstrated by the diagrams of vertical displacements of the pipe bottom and the soil for three values of vertical bedrock displacement.(D/t = 72)

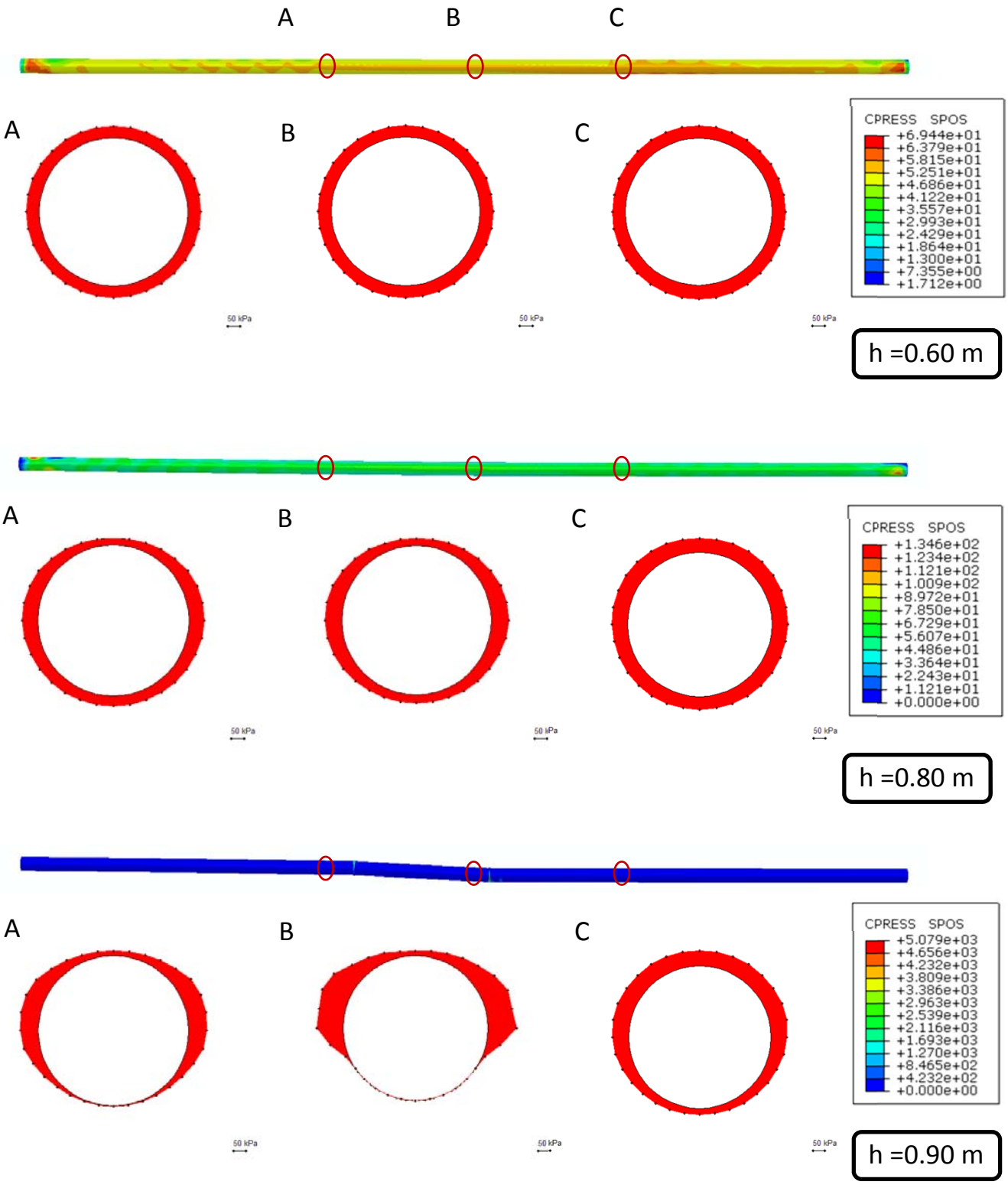

Figure 5.3.8. Soil pressures along the pipeline and soil pressures around three pipe cross-sections A,B and C (X=20,30 and 40 m respectively) for three vertical fault offsets h.

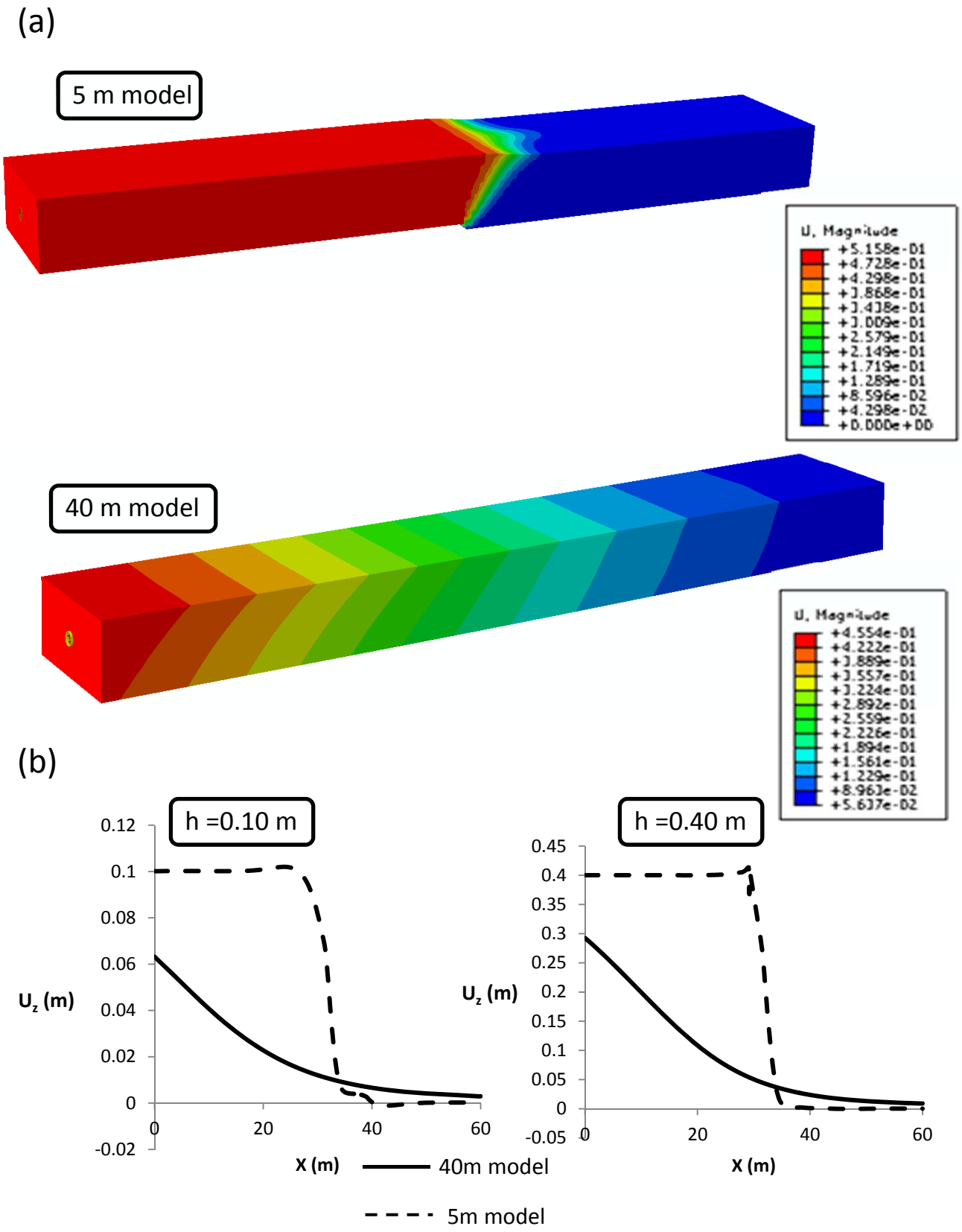

Figure 5.3.9. (a) Displacement distribution for the limited 5 m depth model and the model that takes into account a soil layer of 40 m depth. (b) Comparison of soil vertical displacements beneath the pipe bottom between the 5 m and 40 m model.

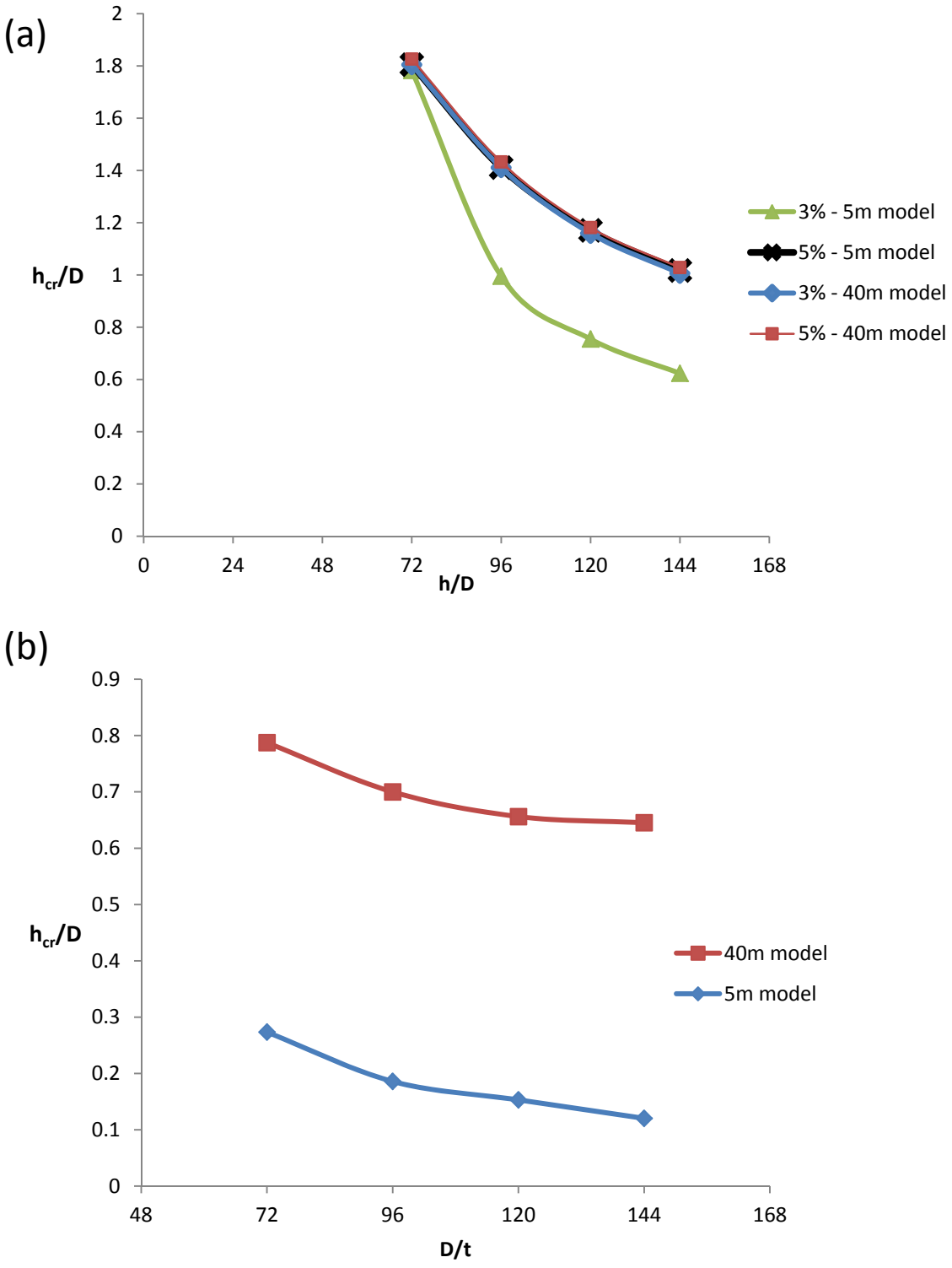

Figure 5.3.10. (a) Comparison of the failure points in terms of h_{cr}/D between the 5 m and 40 m model, for the normal fault case. (b) Comparison of the failure points in terms of h_{cr}/D between the 5 m and 40 m model, for the reverse fault case.

Chapter 6
Pipe steel with hardening behavior

Introduction

In all the previous chapters, the models we examined were based on an elastic-perfectly plastic behavior of the steel pipe material, as described in Chapter 2. However, the original stress-strain behavior, as officially given by manufacturers and institutes (e.g. API), is consisted of a limited elastic brunch, followed by a short plateau which is succeeded by an ascending part, until the ultimate stress of 550MPa is reached, corresponding to approximately 20% of axial strain (**Figure 6.1.1**). This chapter aims at the investigation of the effect that the aforementioned change could have, concerning the pipe endurance and behavior.

6.1 Normal Fault Rupture

The model we use is the Hybrid-Beam model, keeping the same properties as of those described in Chapters 2 and 3, with the exception of the hardening pipe behavior.

The results of the normal fault rupture model can be summarized by the graph given in **Figure 6.1.1.** As it is demonstrated, applying hardening behavior to the pipe material leads to a quite different outcome. As we would have expected, hardening grants the pipe the capability of developing bigger stresses, caused by the strain increase, leading to bigger capacity in terms of critical fault displacement.

What is even more interesting is that, as we can notice at the same figure, another, different mode of failure appears between the strain limit states of 3% and 5% of axial tensile strain. This operational failure occurs due to excessive cross-sectional distortion, also known as cross-section flattening or ovalization, as described in Chapter 2. **Figure 6.1.3** presents the image of such a failure and the development of the cross-sectional flattening.

Hardening results in a different redistribution of stresses and strains, as presented in **Figures 6.1.2** and **6.1.4**, and this is the cause for all the noticed differences. Similarly to the previous model of Chapter 3, above a certain fault displacement, the prevailing loading mode switches from bending to a more shear-like loading, accompanied by a small transposition of the critical area. However, the form of the axial strain distribution is significantly different.

Regarding the length of the pipe that gets activated, results do not demonstrate any great differences. **Figure 6.1.6** proves the aforementioned observation since, the applied hardening behavior has only a slight effect, causing smaller L_{eff}.

6.2 Reverse Fault Rupture

Once again, the Hybrid-Beam model of Chapter 3 is used, applying the hardening stress-strain relation of the steel.

As depictured in **Figure 6.2.1** not only the mode of failure remains the same but also the critical fault displacement is identical to that of the case of elastic-perfectly plastic material. This is quite logical, since local buckling is related to the stability and capacity of a wider area and not only to the strength of a critical cross-section.

The sequence of buckling appearances is not altered since it is only affected by the way we impose the soil displacements. The shape of strain distribution is also slightly altered, especially as regards the 2nd buckling area (**Figure 6.2.3**) where the strain distribution is more wrinkled, declaring the different stress and strain redistribution mode.

Regarding the L_{eff}, hardening does not seem to affect the activated pipe length at all. Similarly to Chapter 4, the footwall beam part of the model gets more stressed and is the one on which we are based in order to compute the L_{eff}. **Figure 6.2.5** shows that the evolution of the L_{eff} for the reverse fault rupture is almost identical to that of Chapter 4.

Conclusions of Chapter 6

- Probably the most important conclusion made in this chapter is that the application of the original hardening behavior of the pipe material is necessary in order to capture the cross-sectional failure mode of ovalization. Ovalization appears only in the normal fault case where tensile stress prevails.

- It has been proved that in the case of normal fault rupture, hardening results in bigger capacity in terms of fault displacement and thus we can claim that is more conservative to ignore it and to apply an elastic-perfectly plastic stress-strain relation. However, the axial strain limits of 3% and 5% are already conservative and taking also in consideration that the elastic-plastic model fails to capture the ovalization failure mode, we propose that hardening should be integrated in model.

- Concerning the affected pipe length the importance of hardening is not of great importance especially in the reverse fault case.

- Hardening, obviously, does not impose any direct alteration to the pipe-soil interaction apart from the limited changes in soil pressures and detachment that are caused by the different deformed shape of the pipe.

- In the case of reverse fault rupture, where local buckling is the mode of failure, no actual differences are spotted and the critical fault displacements are identical to those of the elastic- perfectly plastic case.

Figures of Chapter 6

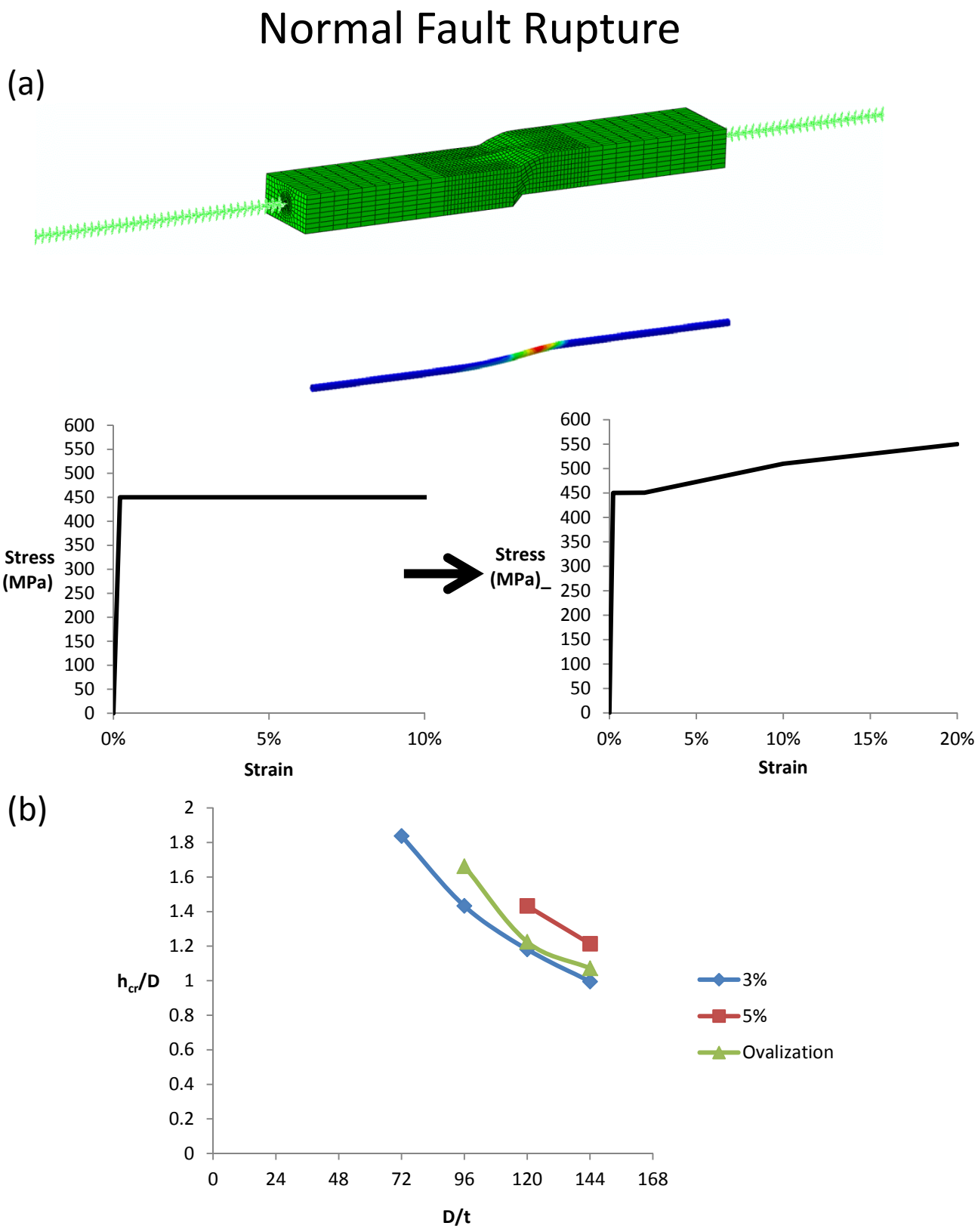

Figure 6.1.1. (a) The deformed model due to normal fault rupture. In this chapter, instead of Elastic-Perfectly Plastic stress-strain relation, we applied the original Elastic-Hardening Plastic behavior of the pipe steel. (b) The summarized dimensionless results demonstrate the critical vertical fault displacement with respect to the D/t ratio, for the axial strain limits of 3% and 5%, as well as, for the failure due to ovalization.

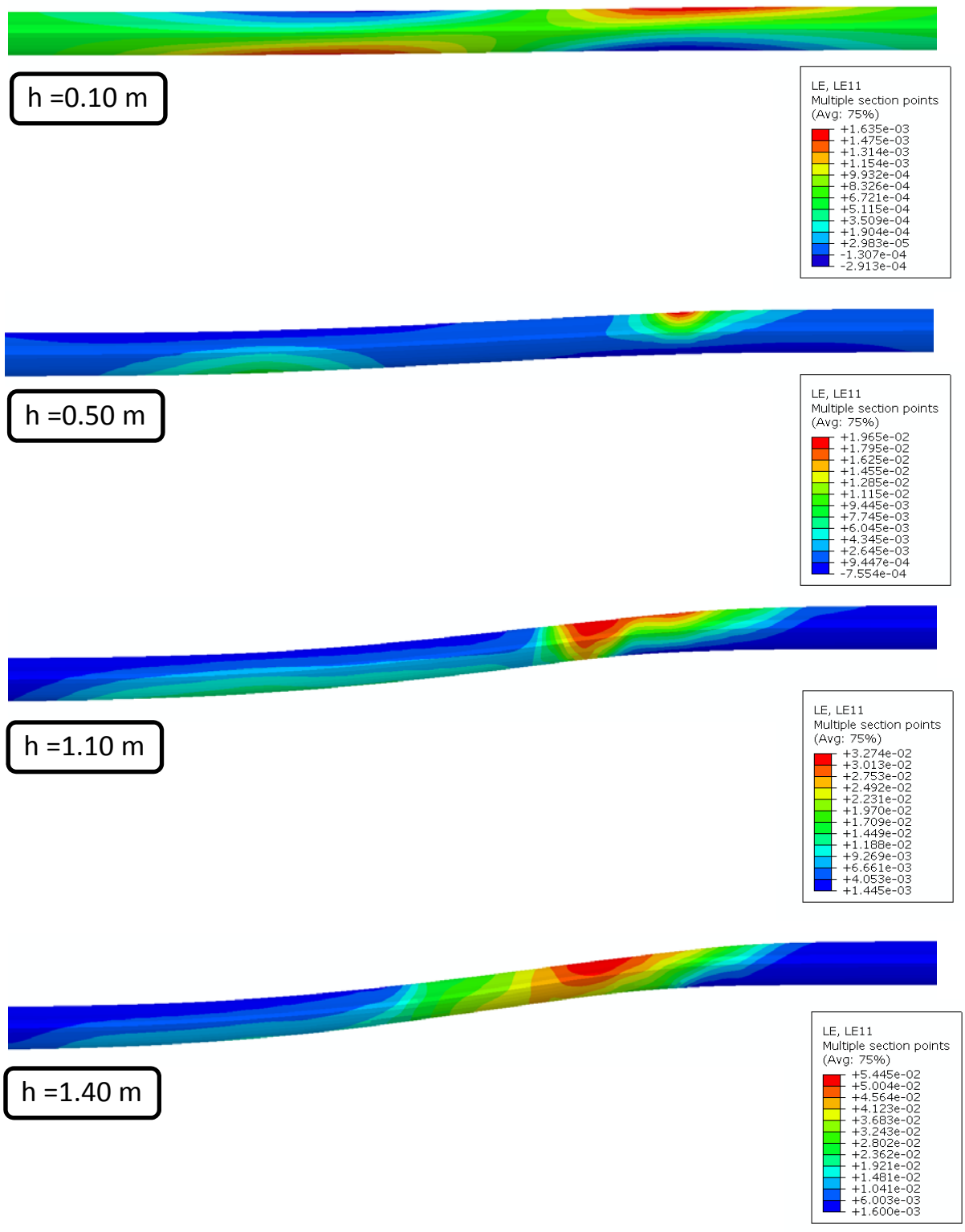

Figure 6.1.2. The axial strain distribution along the critical pipe area (X=20-40 m) for four vertical fault displacements h. (D/t = 72).

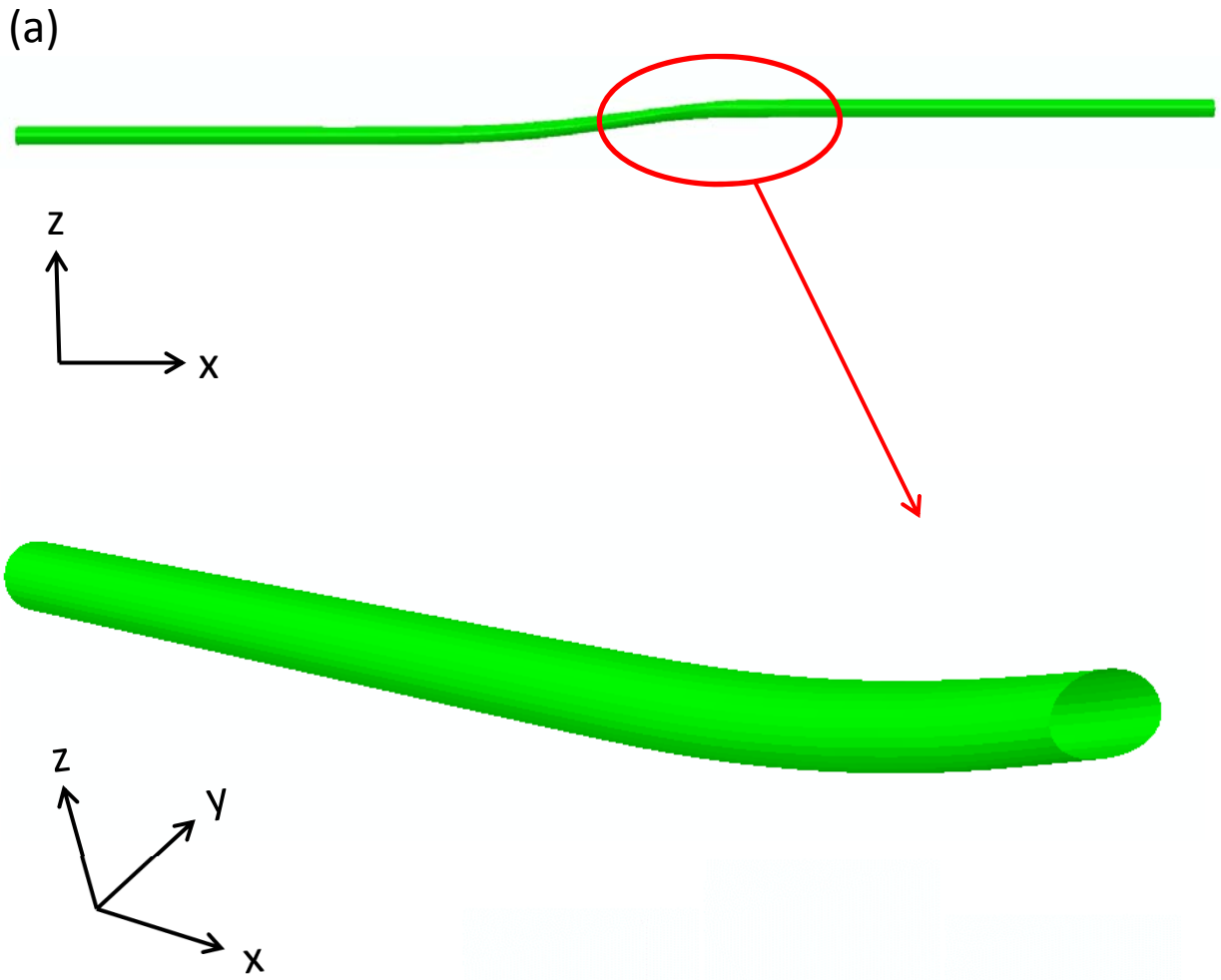

(b)

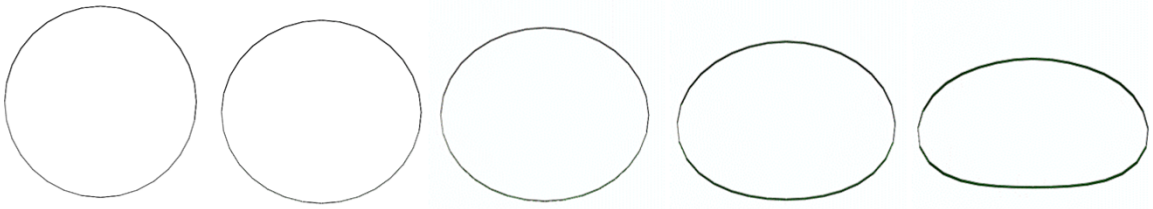

h=0 h=0.2m h=0.5m **h=1m** h=1.45m

$$f = \frac{D_o - D'}{D_o} \leq 0.15$$

Figure 6.1.3. (a) Excessive cross-sectional pipe distortion (ovalization, flattening). b) The evolution of the ovalization with respect to the vertical fault displacement. (D/t = 120)

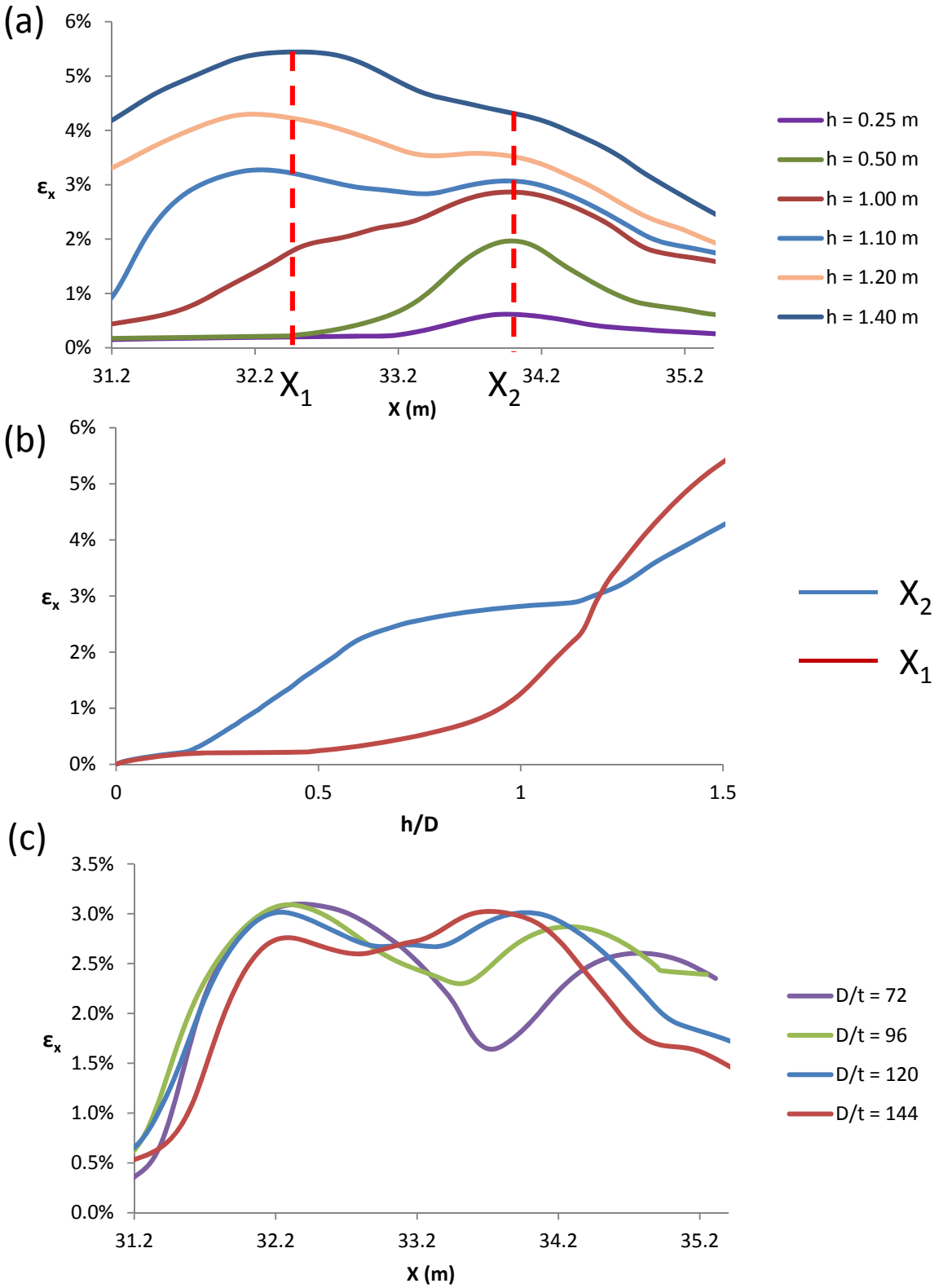

Figure 6.1.4. (a) The axial strain distribution along the critical area. We observe that the point of critical strain is transposed from the X_1 position to the X_2 (D/t = 120). (b) The axial strain development at points X_1 and X_2. (c) The axial strain distribution at the point when the 3% strain limit is reached, for four D/t ratios.

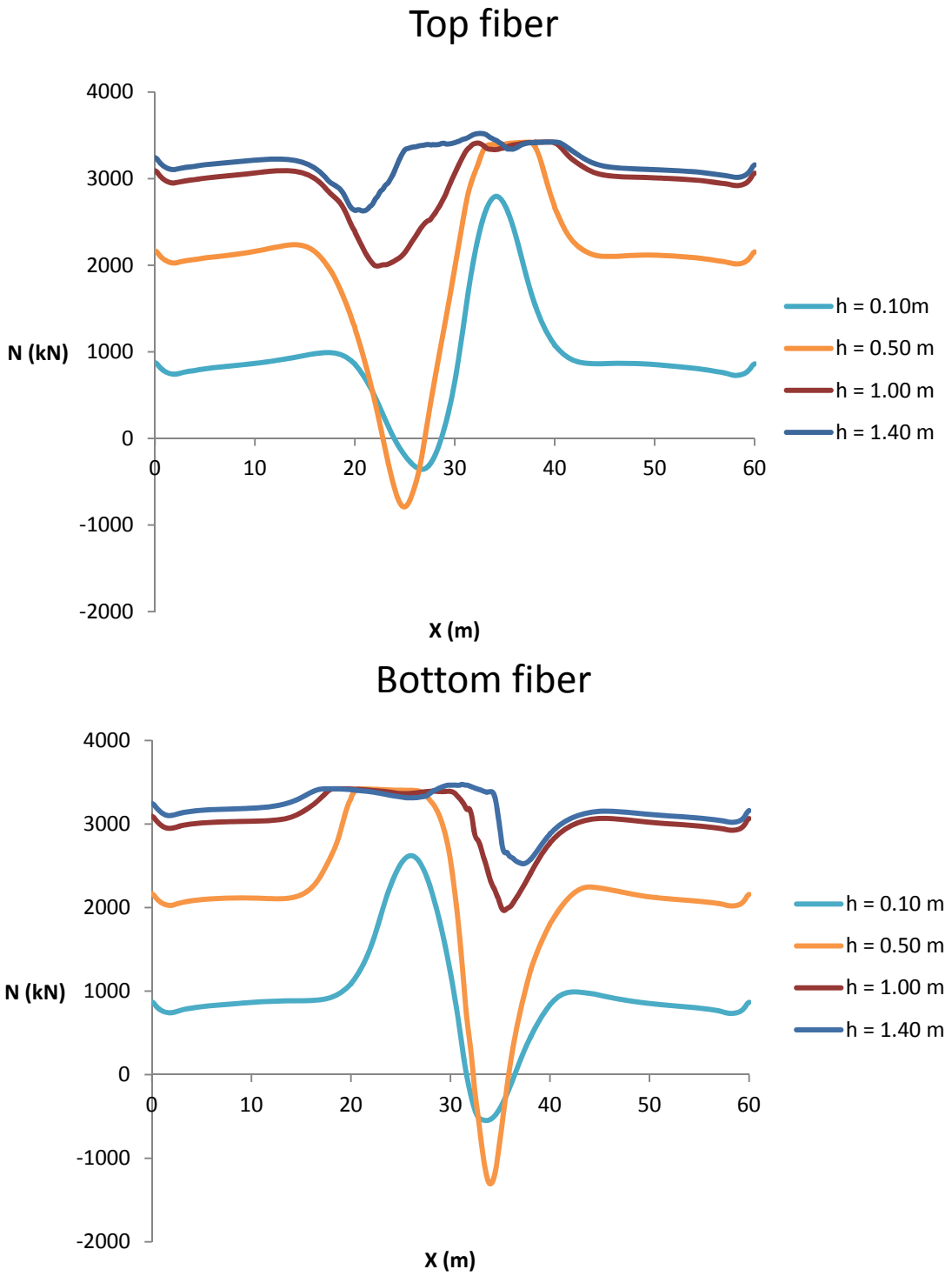

Figure 6.1.5. The axial force distribution along the top and bottom fiber of the pipe. (D/t = 120)

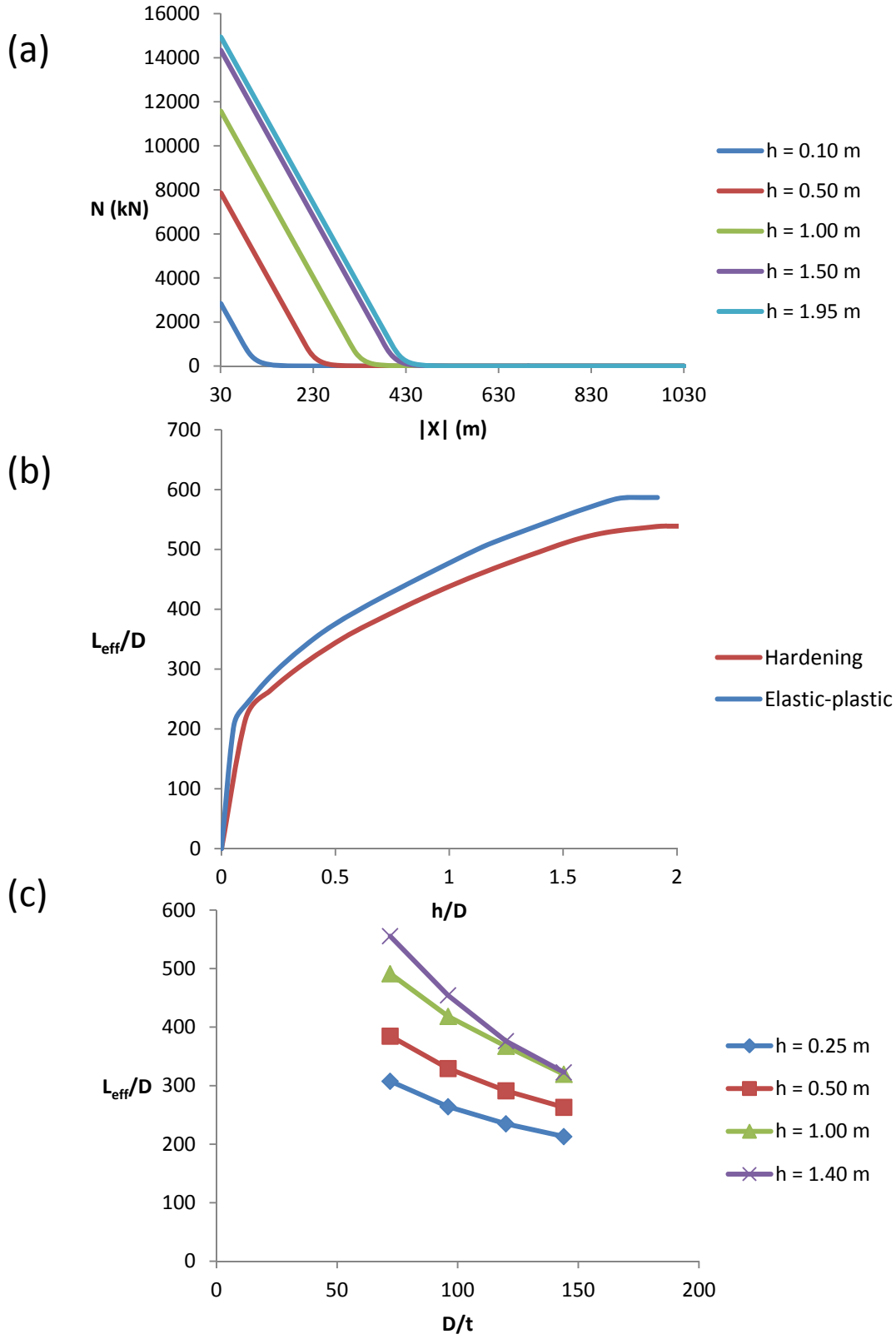

Figure 6.1.6. (a) The axial beam force development in the footwall. (D/t = 72). (b) The effective length of the pipe with respect to the h/D ratio, compared to the Elastic-Perfectly Plastic case. (c) The effective length to diameter ratio with respect to the D/t ratio for four vertical fault displacements.

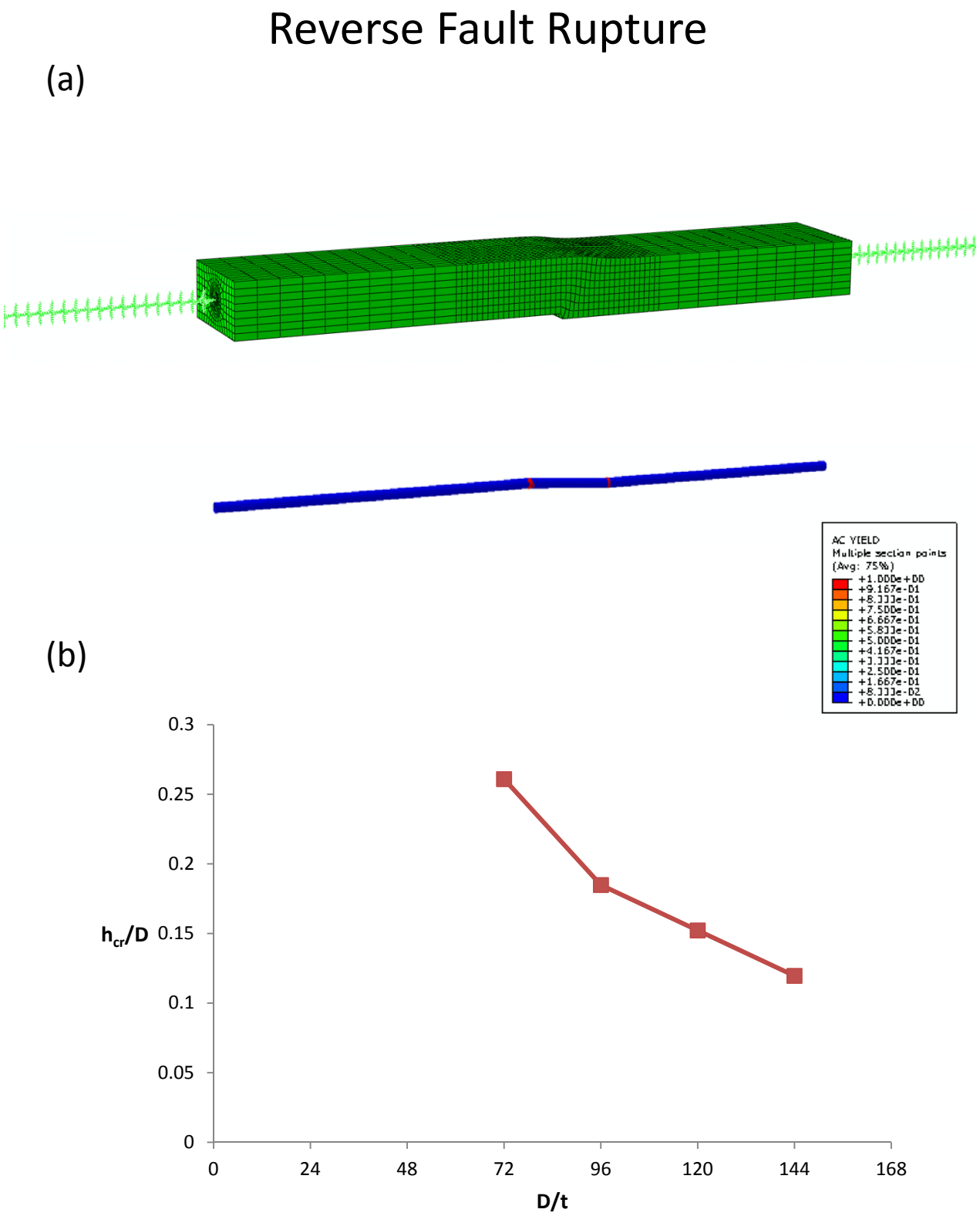

Figure 6.2.1. (a) The deformed model due to reverse fault rupture, with hardening pipe steel. (b) The summarized dimensionless results that demonstrate the critical vertical fault displacement, at which buckling occurs, with respect to the D/t ratio.

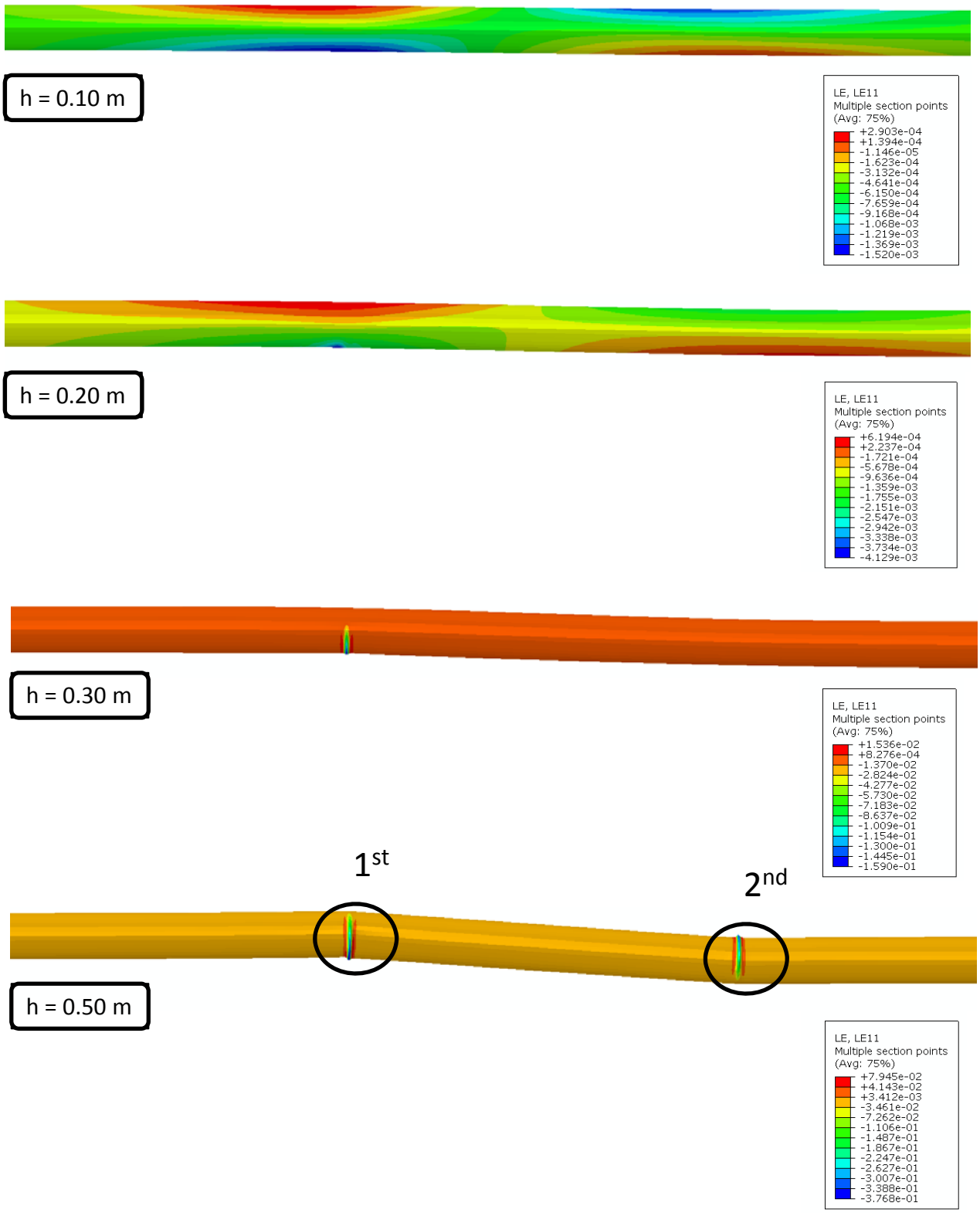

Figure 6.2.2. The axial strains along the critical area for several fault displacement values. The buckling occurs firstly in the hanging wall and afterwards in the footwall.(D/t = 72)

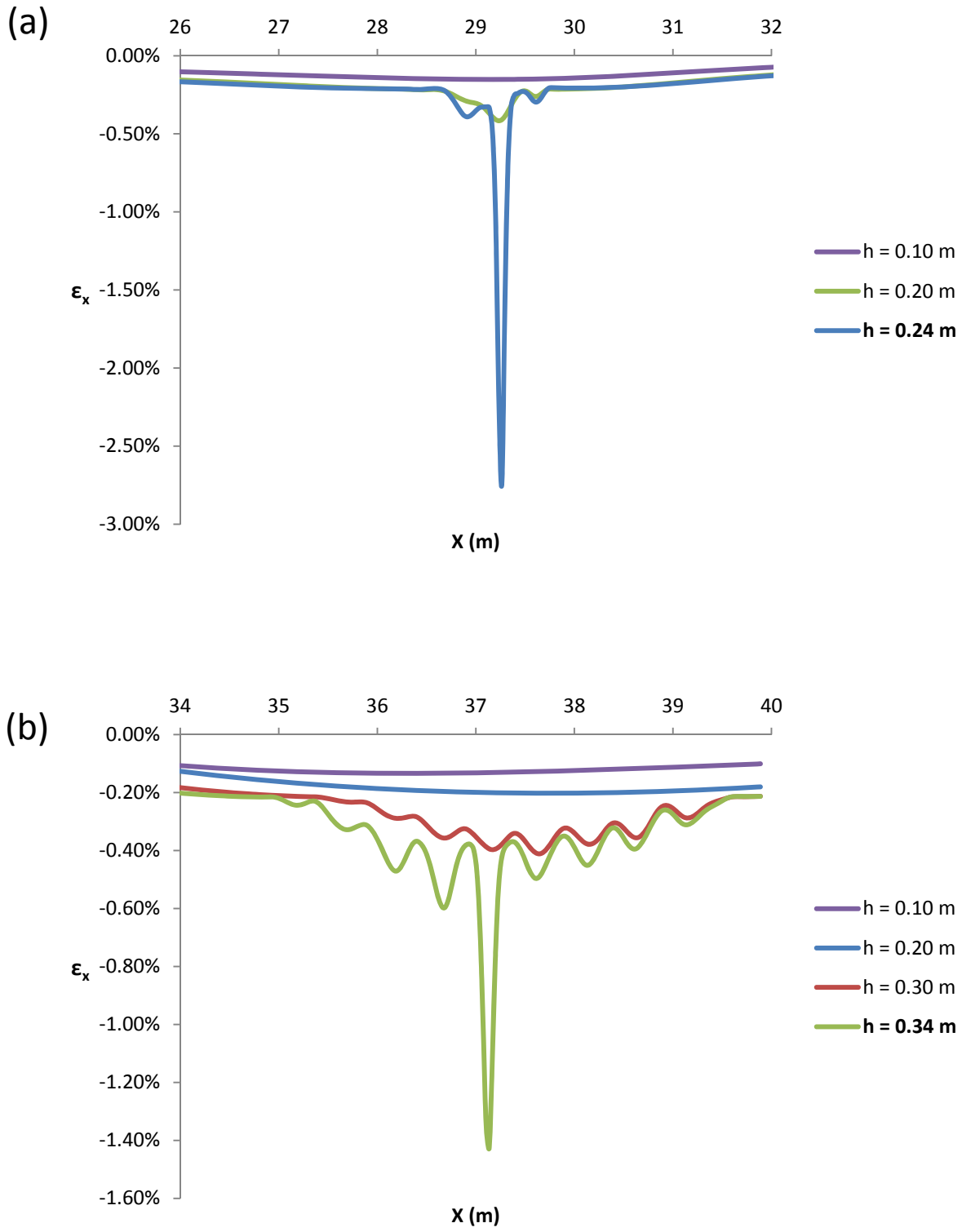

Figure 6.2.3. The axial strains until the occurrence of (a) the first buckling, that occurs at the bottom pipe fiber, in the hanging wall and (b) the second buckling at the top pipe fiber, located in the footwall, (D/t = 72).

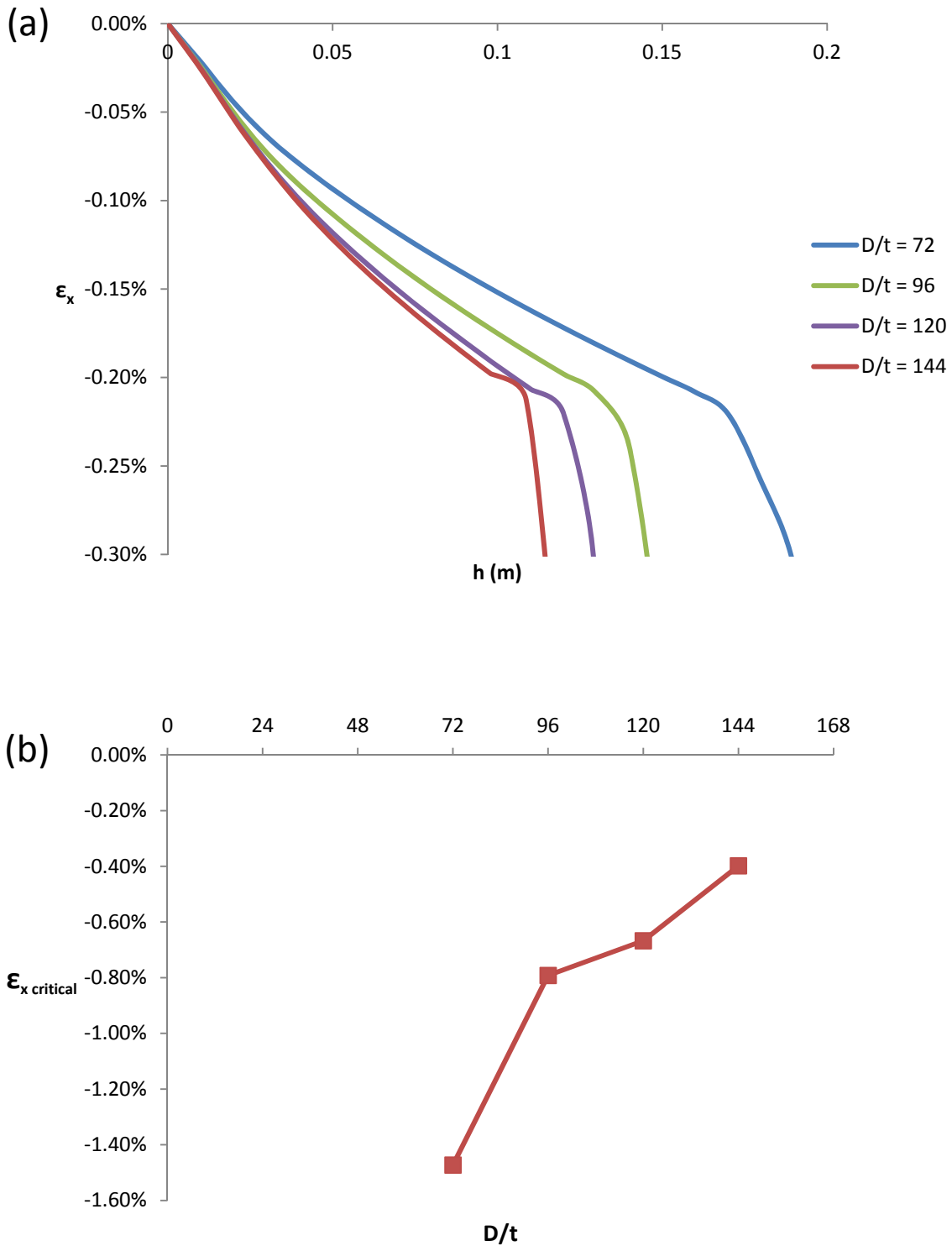

Figure 6.2.4. (a) The axial strain development at the critical pipe where buckling initiates, with respect to the vertical fault displacement for four D/t ratios. (b) The critical axial strain right before the occurrence of buckling with respect to the D/t ratio.

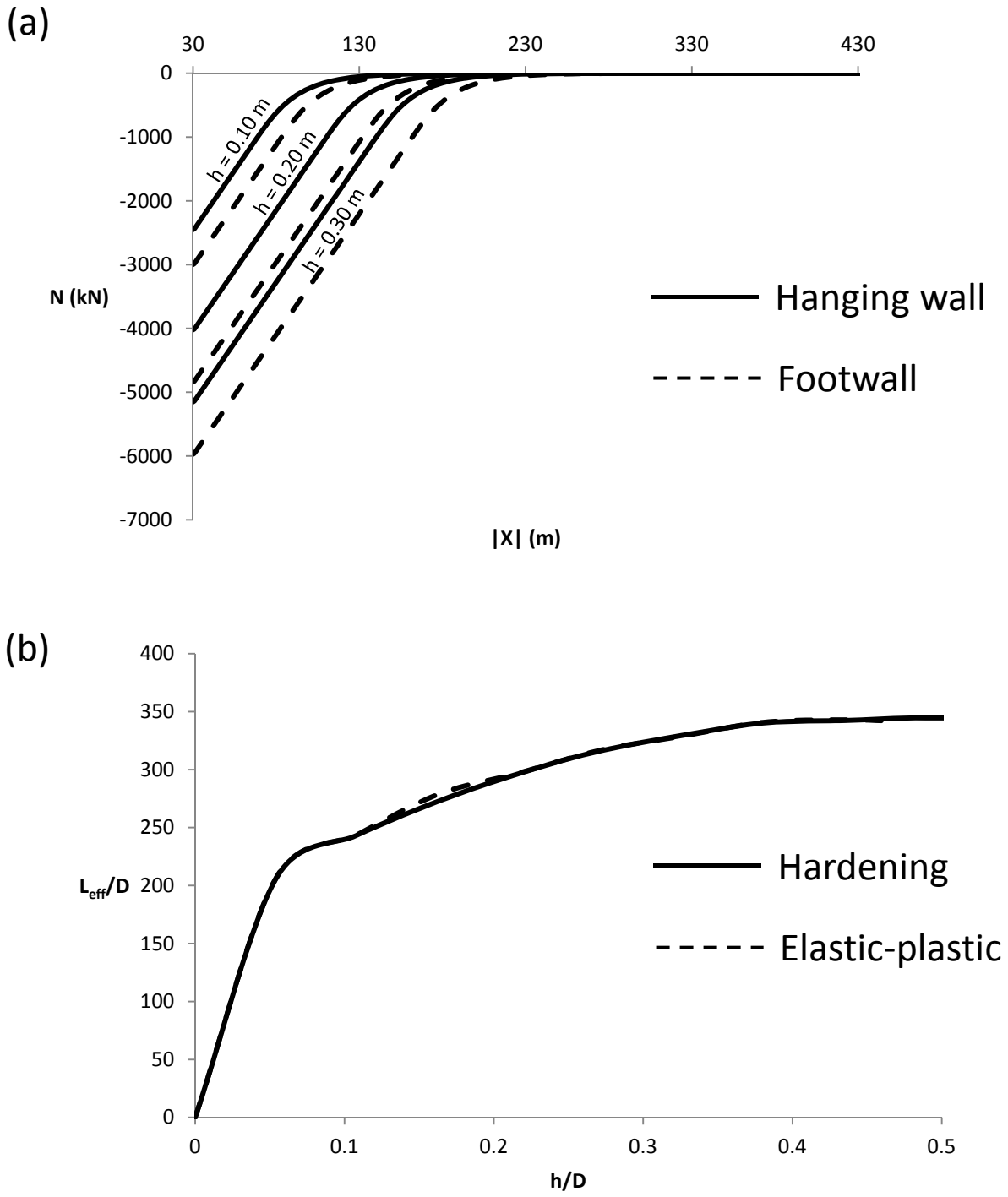

Figure 6.2.5. (a) The axial strain development at the critical pipe where buckling initiates, with respect to the vertical fault displacement for the four D/t ratios. (b) The critical axial strain right before the occurrence of buckling with respect to the D/t ratio.

Summary

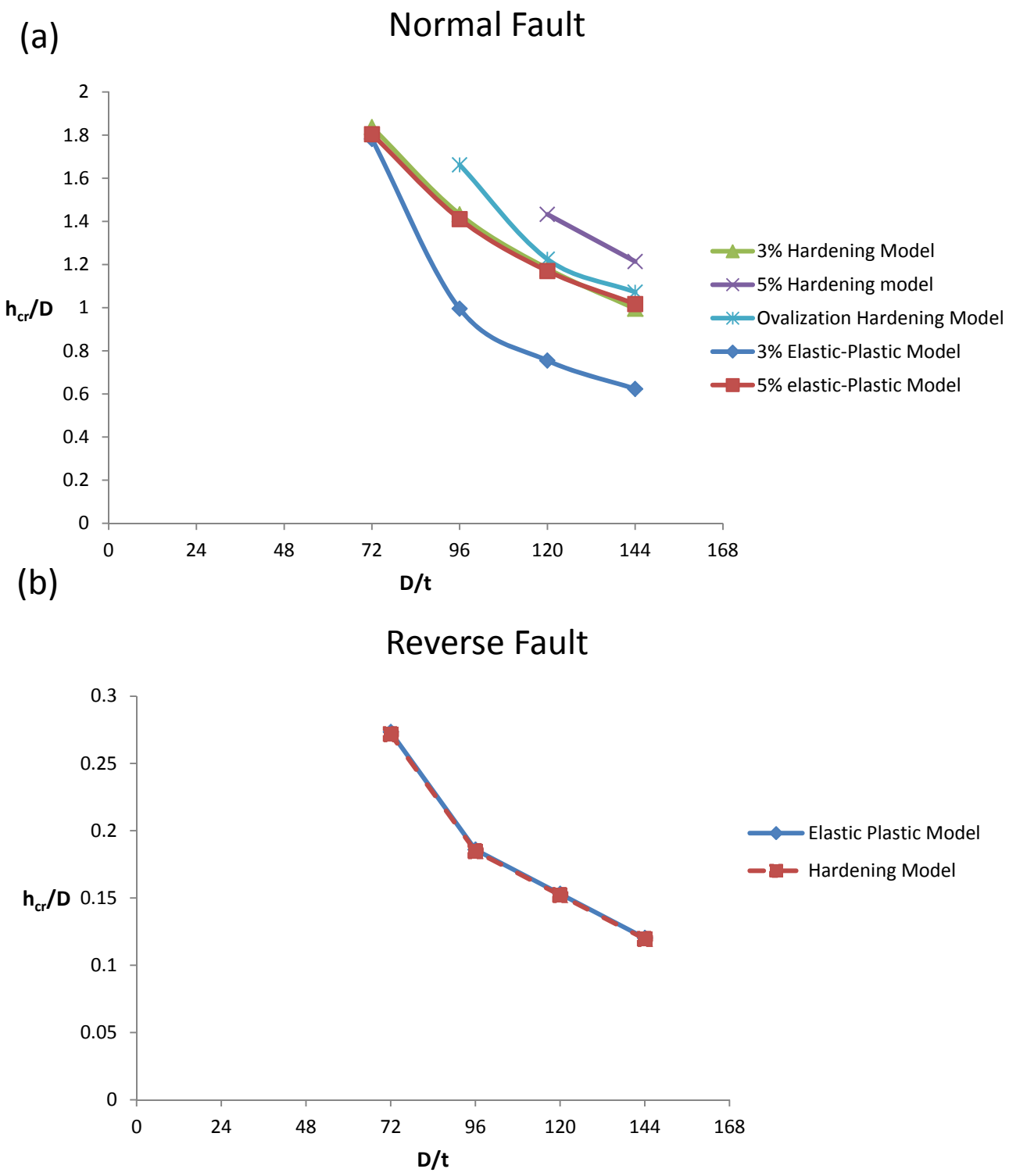

Figure 6.2.6. a) Comparison of the critical fault displacements between the Elastic-Perfectly Plastic model of the previous chapters and the Hardening model of this chapter, concerning the normal fault rupture. Significant differences are spotted, both in terms of h_{cr} and in terms of failure mode. b) The same comparison for the reverse fault case. As demonstrated, the effect of the hardening behavior of the pipe material has no significant effects.

Chapter 7
Internal pipe pressure

Introduction

In the following chapter, the effect of internal pipe pressure is examined. As mentioned in the first chapters, the pipelines we examine are commonly used in oil and gas transportation. Obviously, gas and oil have to be under pressure in order to move along vast distances and variable topographies. This means that the pipe, during its operational period, is subjected to a continuous internal pressure. The aim of this chapter is to investigate what are the effects caused by the internal pressure application and especially, to clarify, whether or not, the internal pressure increases the pipe capacity (in terms of fault displacement magnitude) and as result, whether or not, it should be taken into consideration when studying the pipe resistance to dip-slip fault ruptures.

Internal Pressure

The maximum internal pressure value is given by the following equation, which, considering a factor of safety equal to 0.72, as proposed by the ASME code for pressure piping, is given as:

$$p_{\max} = 0.72 \cdot \left(2 \cdot \sigma_y \cdot \frac{t}{D} \right)$$

However, similarly to the common, real operational pressure values, we applied only a percentage of the maximum pressure allowed, equal to approximately 40% P_{max}. Since, the maximum pressure depends on the D/t ratio the pressure applied for each one of the D/t cases is given by the following table:

D/t	144	120	96	72
$P_{applied}$ (kPa)	1700	2040	2550	3400

7.1 Normal Fault Rupture

Once again, we make use of the Hybrid-Beam model. The material of the pipe is, initially, chosen to be elastic-perfectly plastic, whereas in one of the following paragraphs, the combination of internal pressure and hardening material behavior is examined.

The results obtained are quite different compared to the case of absence of internal pressure. **Figure 7.1.1** demonstrates the pipe capacity in terms of critical fault displacement and indicates that the presence of internal pressure has an adverse effect concerning the pipe resistance to fault movement. Specifically, for the 5% axial tensile strain limit, the pipe resistance is reduced approximately by 35% (**Figure 7.2.6**). This can be simply explained by the fact that the internal pressure causes radial hoop dilation which then provokes additional axial tensile stress and strain, thus, the tensile strain limit is reached earlier.

In **Figure 7.1.2**, the axial strain distribution along the critical area is displayed for several fault movement magnitudes. Combining this image with the information of **Figure 7.1.3**, we observe that the concentration of axial tensile strains is now spotted in several points along the critical area. Especially as the pipe thickness increases, hence the pipe is subjected to bigger fault movement before failure, the critical point is displaced to another, adjacent cross-section. However, dissimilar to the model of Chapter 3, we do not observe the aforementioned transition from prevailing bending to prevailing shearing loading mode.

Regarding the effective pipe length, similarly to the previous chapters, we firstly examine which side is more intensively stressed, the one in the footwall ore in the hanging wall. Once again, no significant difference is observed, as shown in **Figure 7.1.5**. In the same figure, the effect of D/t ratio is also demonstrated and proves, that higher moment of inertia signifies longer active pipe length. Finally, it is proved that the evolution of L_{eff} is absolutely similar to the case without internal pressure, with the exception that now the L_{eff} does not seem to reach a maximum value. In

general, most of the analyses stop after the occurrence of failure, due to excessive distortion and inability of numerical convergence. Thus, it is logical for the model with internal pressure to stop earlier. However, we would expect that since failure is reached, the L_{eff} should stabilize after a few additional steps of fault displacement. The reason that this does not happen is the aforementioned difference, that, now, bending remains the prevailing loading mechanism and there is not such a great strain concentration and strain increase according to a shear-like mode of deformation, as in the case of Chapter 3.

7.2 Reverse Fault Rupture

The effect of internal pressure is also investigated for a reverse fault rupture.

The differences are not as significant as in the normal fault case. The summarized outcome of the analysis is demonstrated in Figure 7.2.6, where the pipe resistance to fault movement is depicted in terms of critical fault displacement with respect to the D/t ratio, both with and without the internal pressure application. It is proven that internal pipe pressure leads to an earlier failure, even though the capacity decrease is only about 17%. This is attributed to the development of additional stresses and strains in the pipeline wall that cause early yielding and premature local buckling formation. **Figures 7.2.2** and **7.2.3** describe the axial strain development and distribution and show no significant alterations with the case of absence of pressure.

Finally, concerning the L_{eff}, things are almost identical. The pipe in the footwall is, again, more stressed than in the hanging wall and compared to the case without pipe pressure, nothing but a slight increase of L_{eff} is depicted (**Figure 7.2.5**).

7.3 Internal Pipe Pressure with Hardening Pipe Steel Behavior

In this paragraph, we investigate the results of a model that combines the application of internal pressure with elastic-hardening plastic stress-strain relation for the pipe material.

Normal fault rupture

The results are presented in **Figures 7.3.1** and **7.3.2.** As demonstrated, the use of hardening plasticity intensifies the strain distribution behavior that was observed with the application of internal pressure. This strain distribution behavior is defined, in the previous paragraphs, as the redistribution of stress and strains in several adjacent cross-sections and thus, the decrease of excessive strain concentration at a single point. It is clearly demonstrated in **Figure 7.3.2** that, as the fault displacement augments and the strains increase, strains concentrate in several positions and hinder the maximum strain value from reaching bigger magnitudes.

In the same figure, the (b) diagram compares the axial strain development at the critical points, for all the four examined combinations:

1) Elastic-Perfectly Plastic / Absence of Internal Pipe Pressure
2) Elastic-Hardening Plasticity / Absence of Internal Pipe Pressure
3) Elastic-Perfectly Plastic with Internal Pipe Pressure
4) Elastic-Hardening Plasticity with Internal Pipe Pressure

In general the effects of hardening appear, logically, after the occurrence of certain axial strain. Hardening prevents the almost vertical increase of axial strains that is observed in the cases of elastic-perfectly plastic material after the plastification.

The effect of internal pressure is clearly amplified when combined with hardening material and leads to a constant redistribution of strains that retain the maximum strain magnitude to relative low values.

Reverse fault rupture

The results are demonstrated in **Figures 7.3.3** and **7.3.4.** The differences between the four cases are not great. However, it is clear that, in general, the presence of internal pressure reduces the pipe strength, whereas the effect of hardening is slightly beneficial but can be practically spotted only when combined with the application of internal pressure.

Conclusions of Chapter 7

- The application of internal pressure has a significant effect, in the case of a buried steel pipeline subjected to normal fault rupture, since it causes premature failure (about 35% less capacity in terms of fault movement when 0.40% P_{max} is applied) compared to the case without pipe pressure. The strain distribution is also altered and is described by strain redistributions and strain concentrations in several points.

- For the reverse fault rupture case, the presence of pipe pressure reduces once again the pipe capacity, although by a smaller percentage of approximately 17%. The strain distribution is not significantly changed.

- The L_{eff} does not seem to be practically affected by the action of internal pressure both in the normal and in the reverse case.

- The combination of hardening with internal pressure has as a result the intensification of internal pressure effects, concerning the axial strain distribution in the case of normal rupture, whereas, in the reverse case, the application of internal pipe pressure is necessary for the effect of hardening to appear.

- Based on the above conclusions, a model that takes into consideration the internal pipe pressure is proposed.

Figures of Chapter 7

(a)

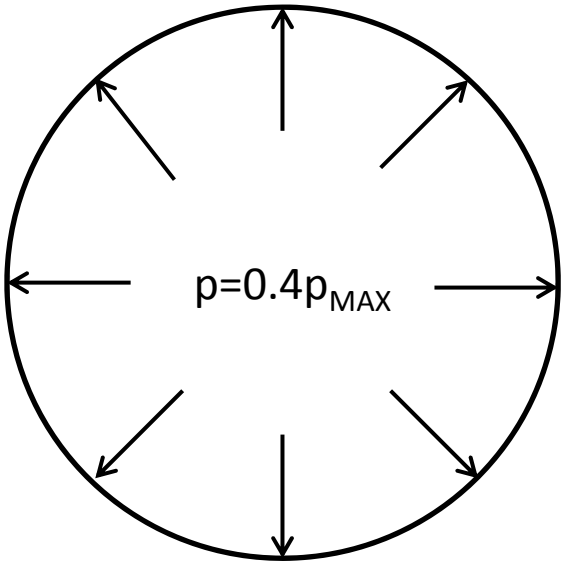

$$p_{\max} = 0.72 \times \left(2\sigma_y \frac{t}{D} \right)$$

(b)

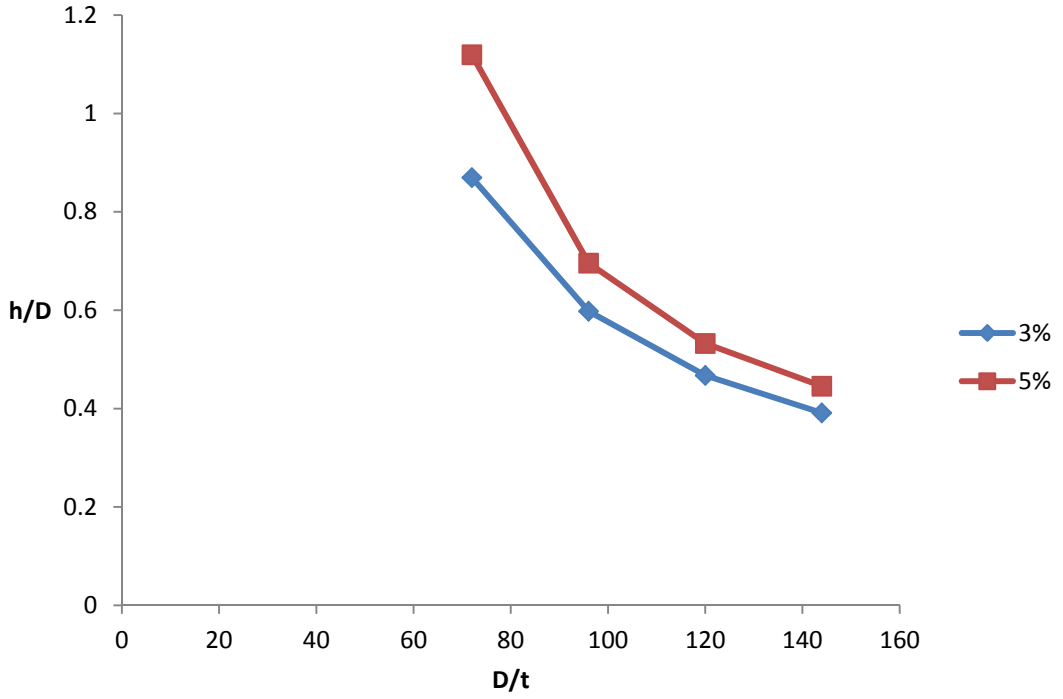

Figure 7.1.1. (a) Internal pipe pressure was applied equal to 40% of the value of p_{max}. P_{max} is different for every D/t ratio. (b) The capacity of the pipes for the normal fault case, in terms of maximum fault displacement, with respect to the D/t ratio.

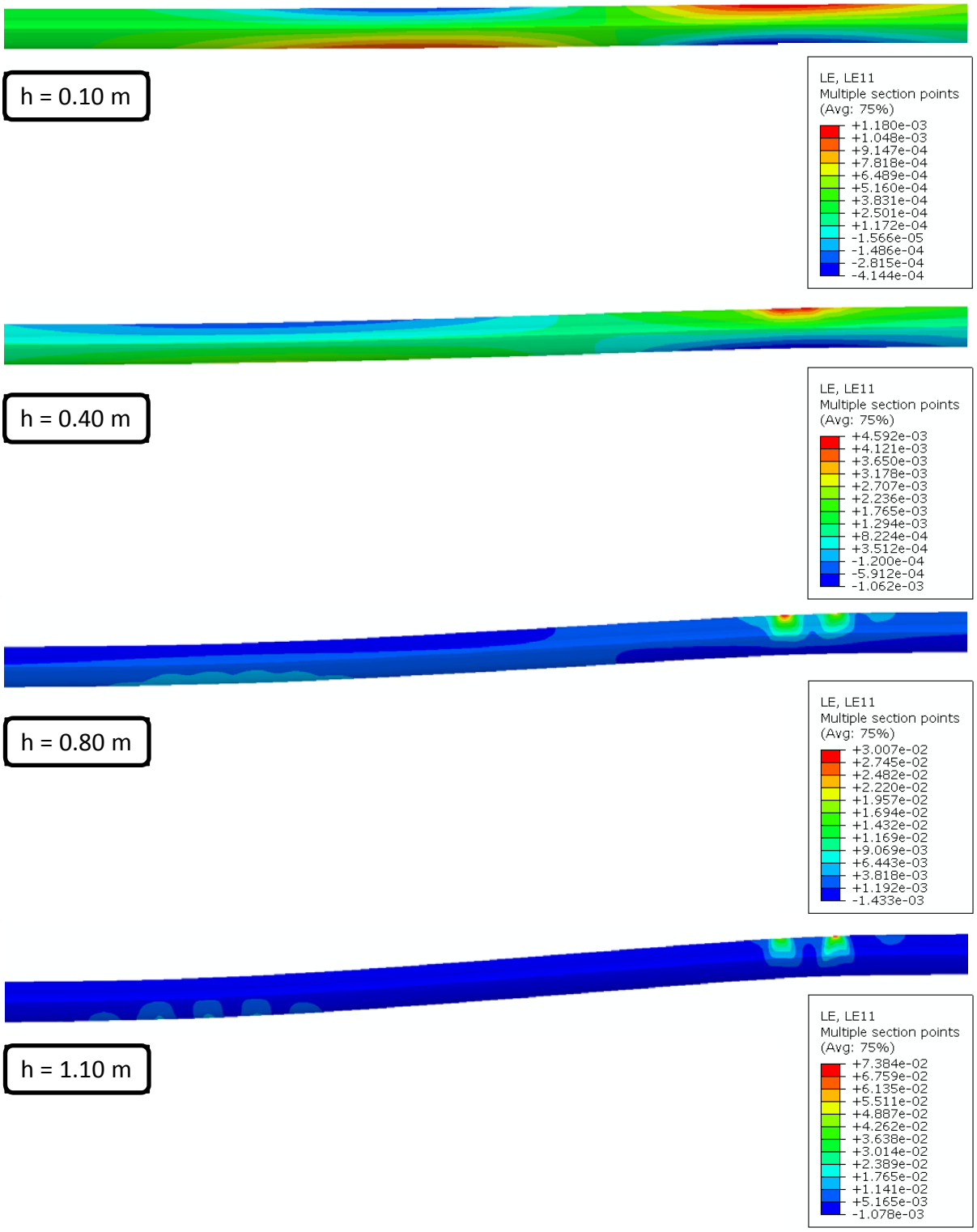

Figure 7.1.2. The axial strain distribution along the critical area (X=16-38 m) for different fault displacements.(D/t = 72)

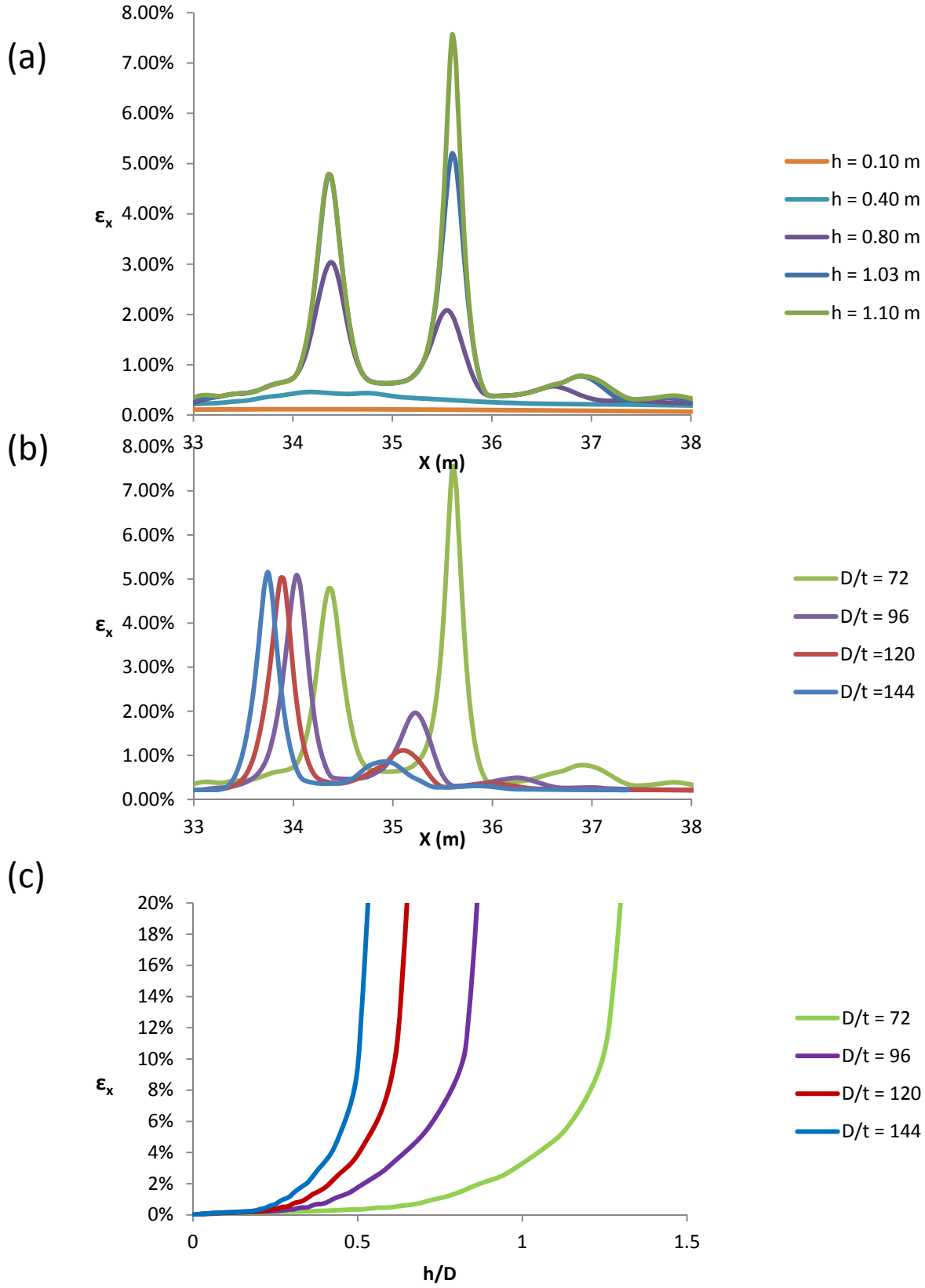

Figure 7.1.3. (a) The distribution development of the axial strains along the critical area, (D/t = 72). (b) The shape of axial strains distribution, at the point where the 5% limit is reached, for four D/t ratios. (c) The evolution of axial strain at the critical pipe points with respect to the vertical fault displacement to diameter ratio, for four D/r ratios.

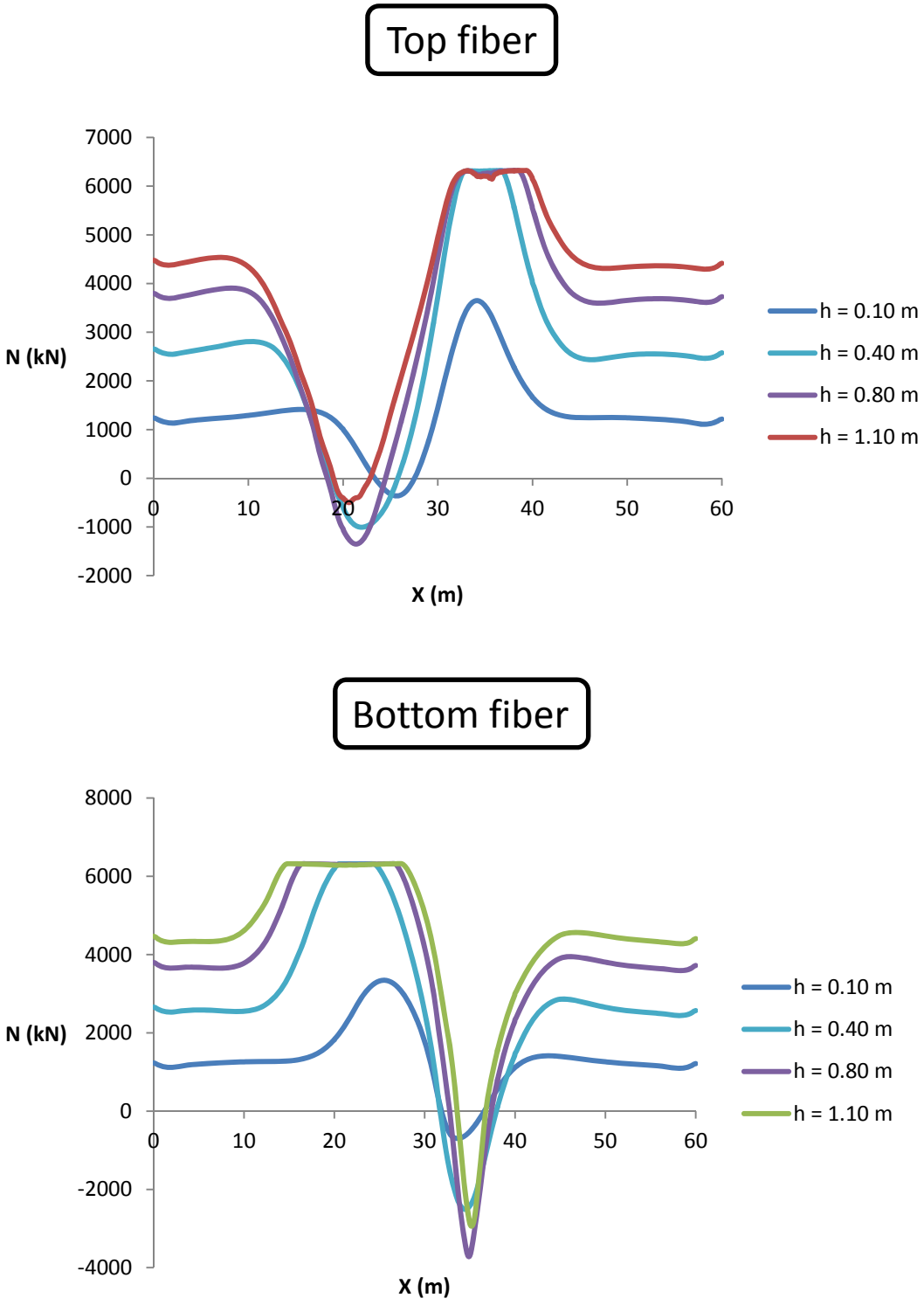

Figure 7.1.4. The axial force distribution along the top and bottom pipe fiber, for different vertical fault displacements.(D/t = 72)

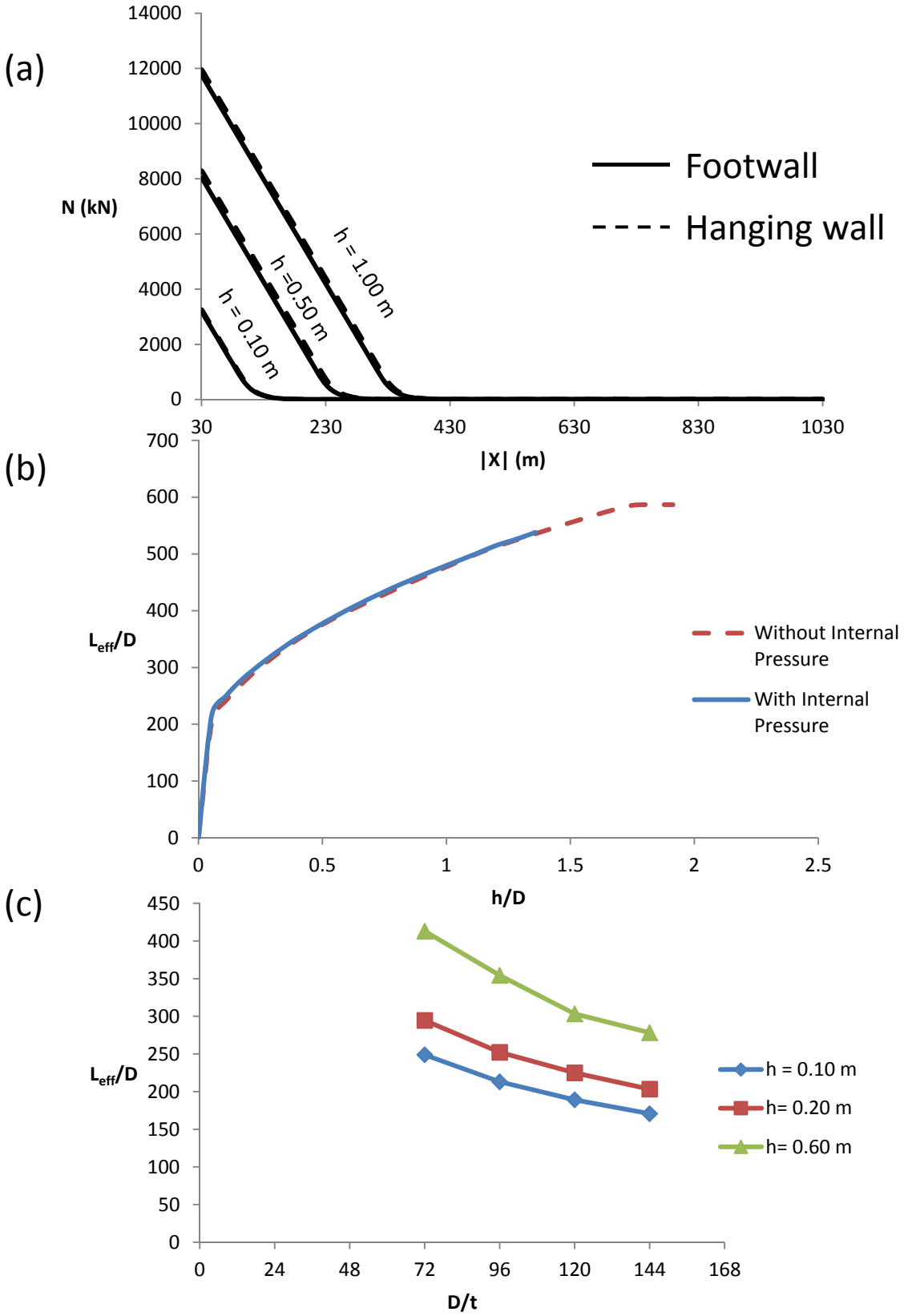

Figure 7.1.5. (a) Comparison of the axial forces, for three fault displacements, along the beam parts of the model, in the footwall and the hanging wall. (b) Comparison of the L_{eff} between the case without internal pressure and the case where internal pipe pressure is applied. (D/t = 72) (c) L_{eff} to Diameter ratio with respect to the D/t ratio for three fault displacements.

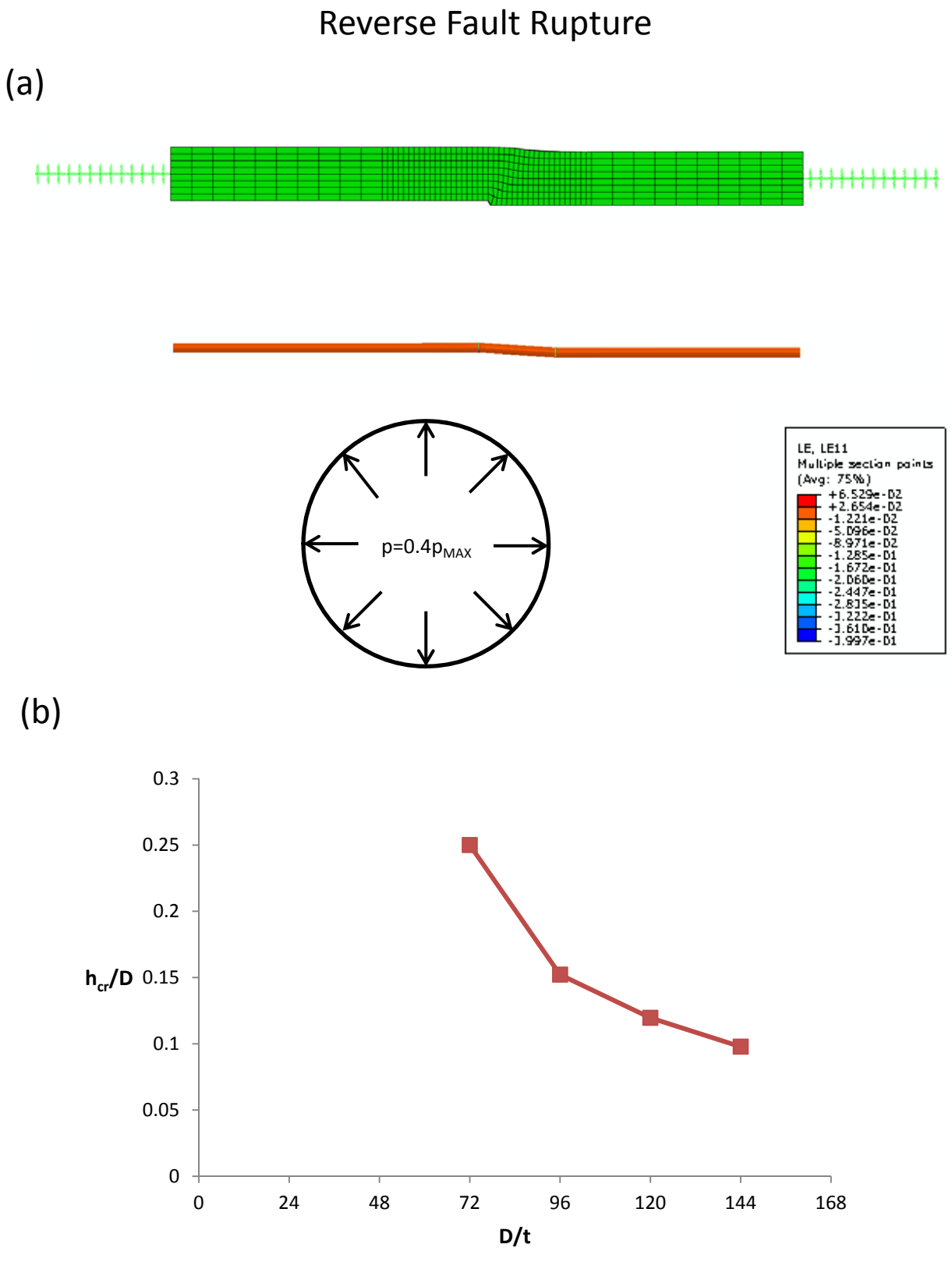

Figure 7.2.1. (a) The internal pipe pressure effect was examined for the reverse fault case as well. (b) The capacity of pipes of different thicknesses (D=1m) in terms of critical fault displacement.

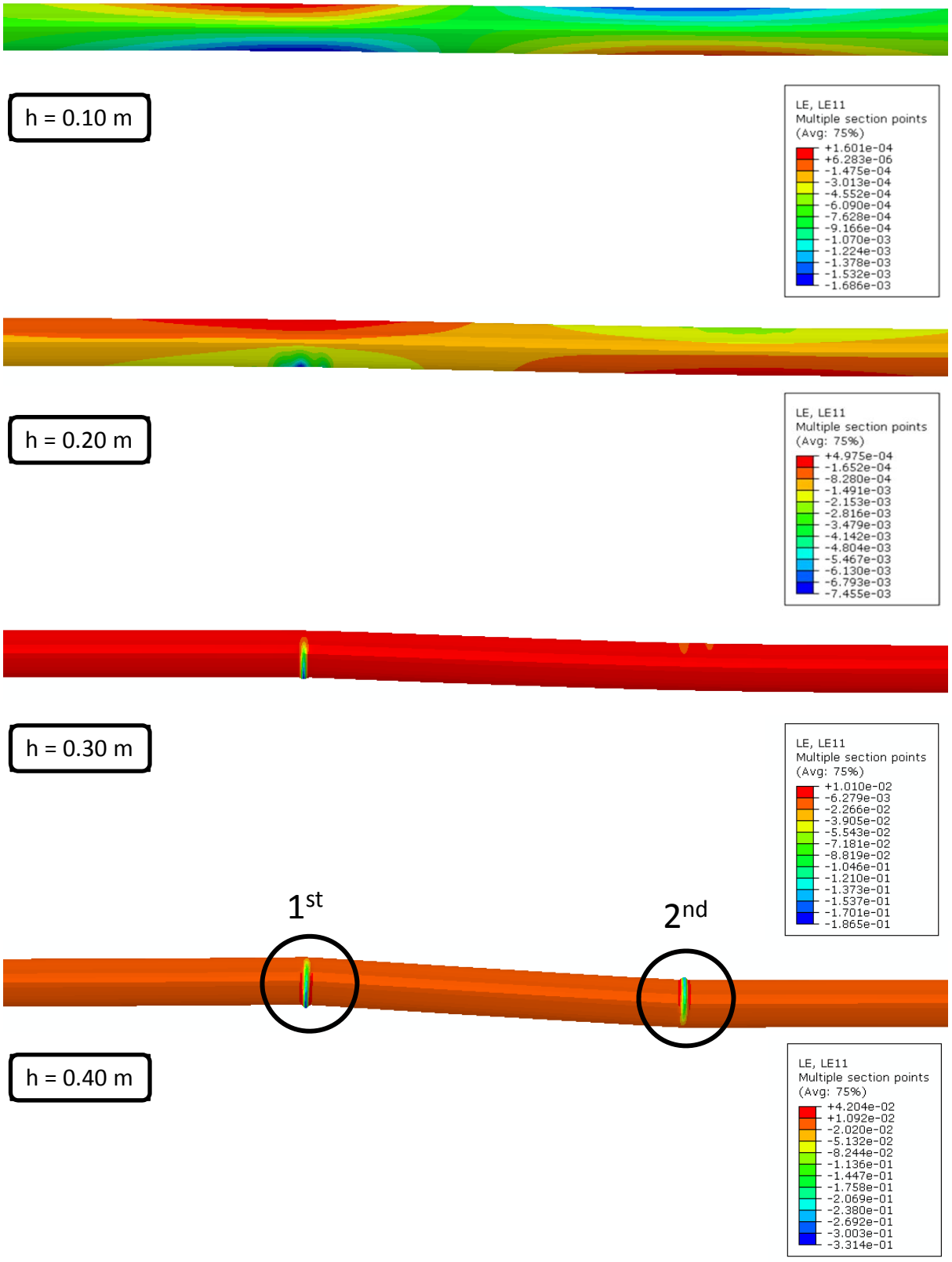

Figure 7.2.2. The axial strain distribution along the critical area (X=23-42 m) for different fault displacements. The buckling areas and the sequence of buckling appearance. (D/t = 72)

(a)

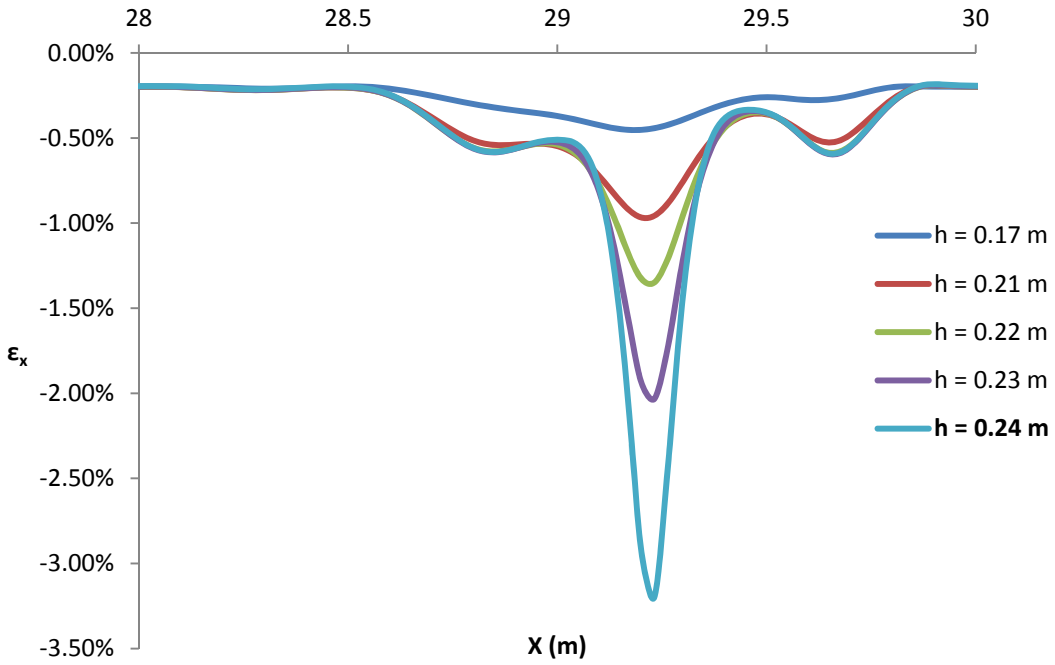

(b)

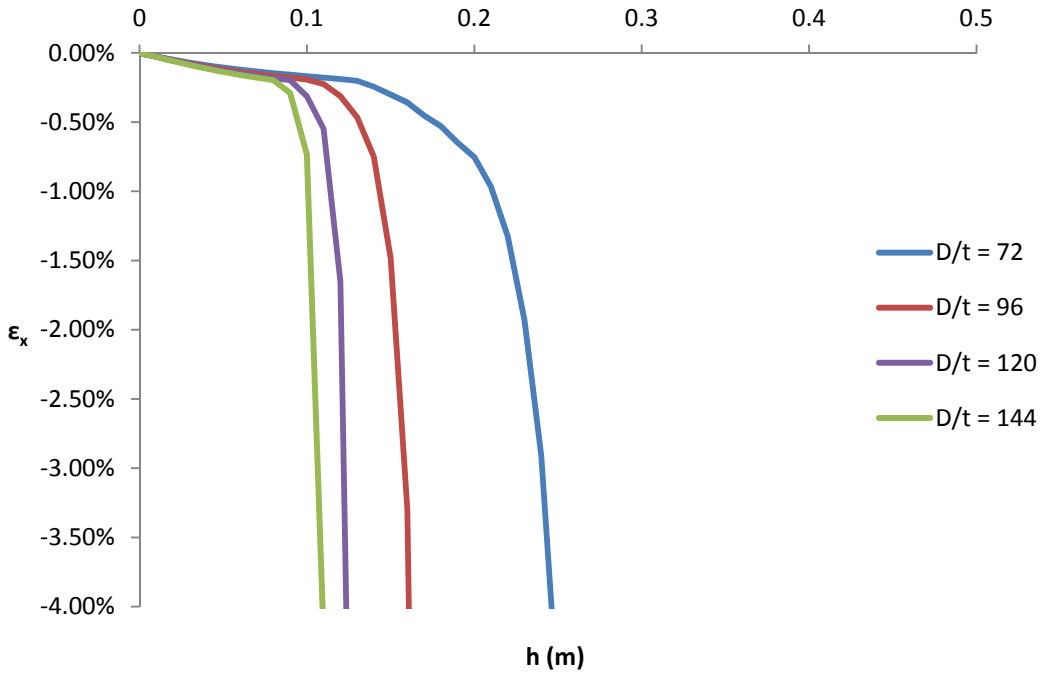

Figure 7.2.3. (a) The distribution of axial compressive strains along the critical buckling area until the appearance of buckling.(D/t = 72). (b) The evolution of axial strains at the critical buckling points for the four D/t ratios.

(a)

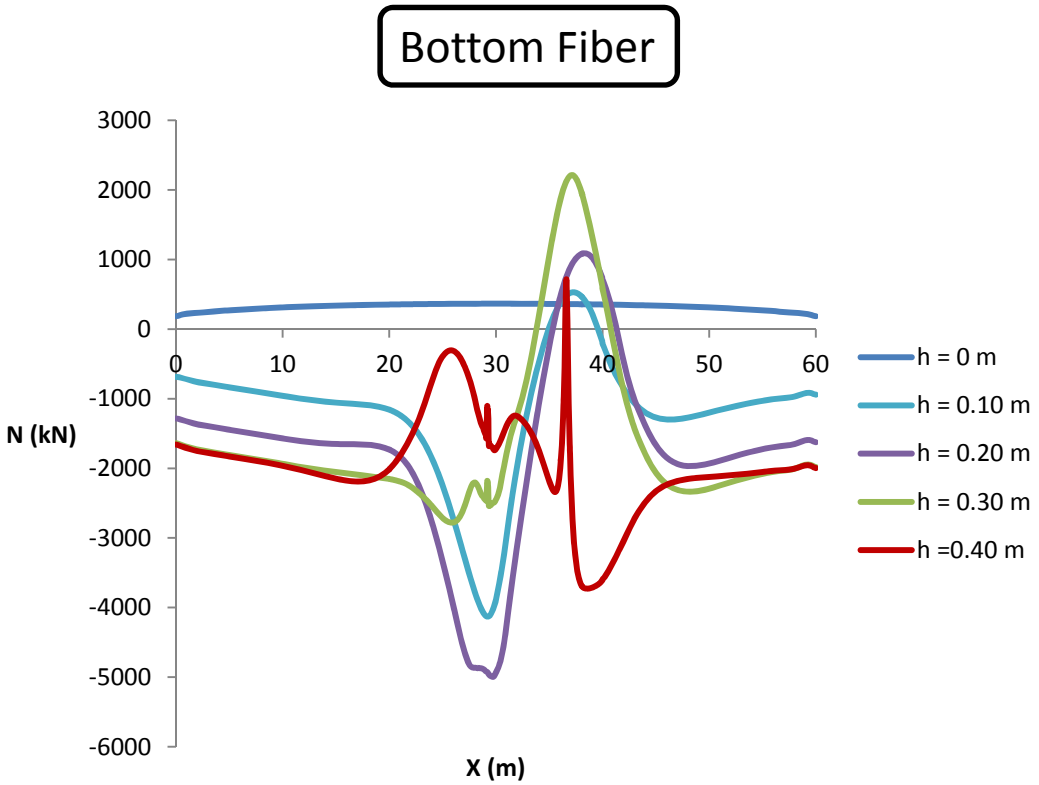

(b)

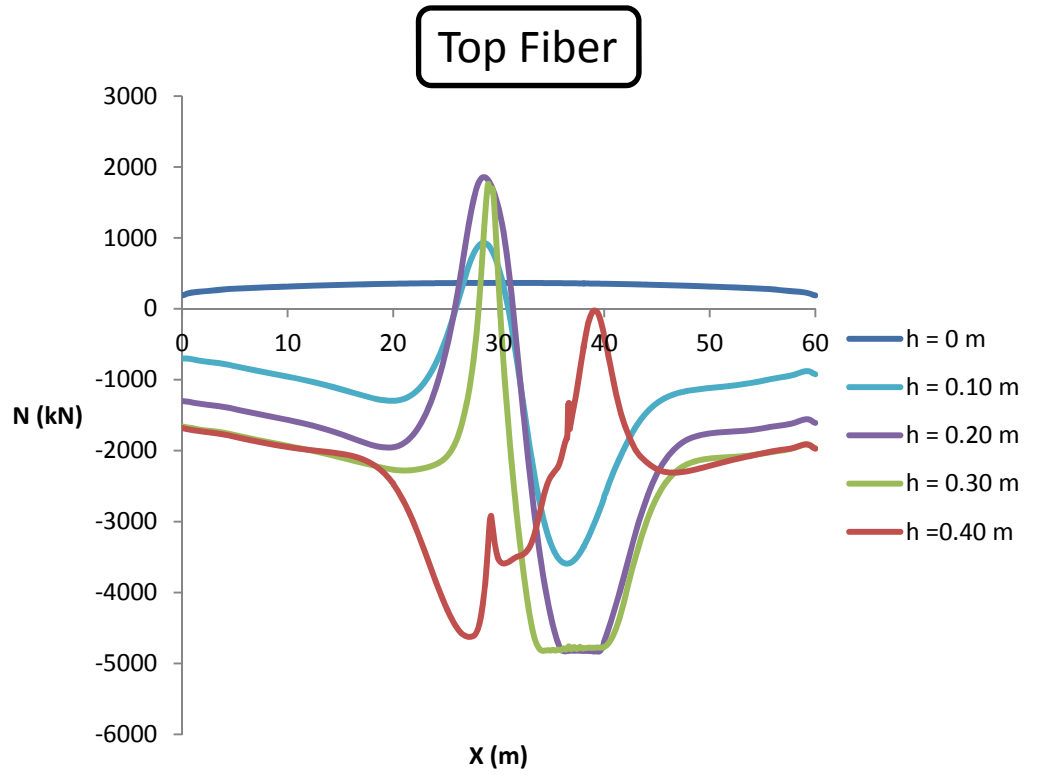

Figure 7.2.4. The axial force distribution along (a) the bottom pipe fiber and (b) the top pipe fiber. Before the initiation of fault movement (h = 0m), the application of internal pressure subjects the pipe to tensile stress.

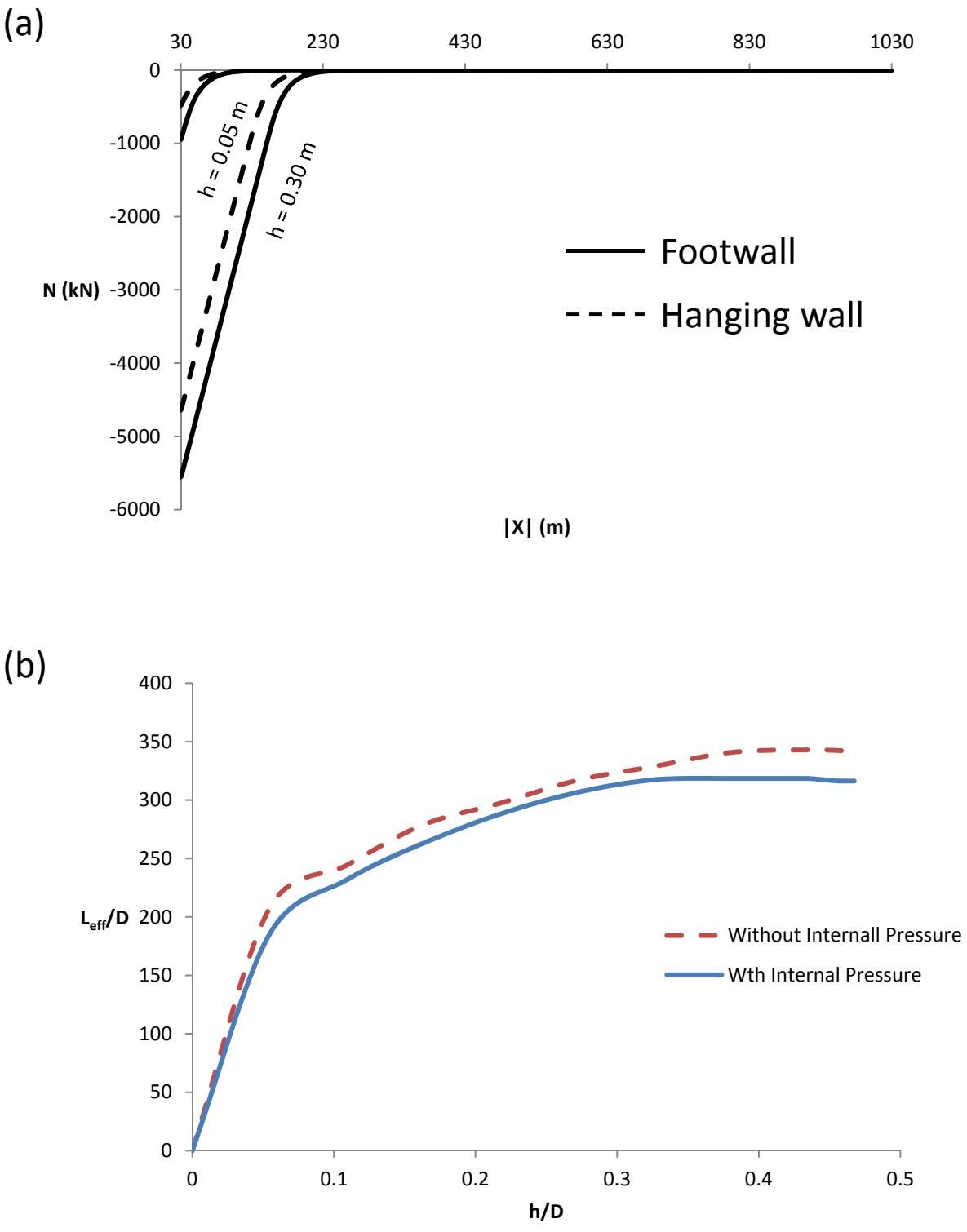

Figure 7.2.5. (a) Comparison of the axial beam forces, for two fault displacements, in the footwall and in the hanging wall . (b) Comparison of the L_{eff} with respect to the fault displacement for the case with and without internal pipe pressure.

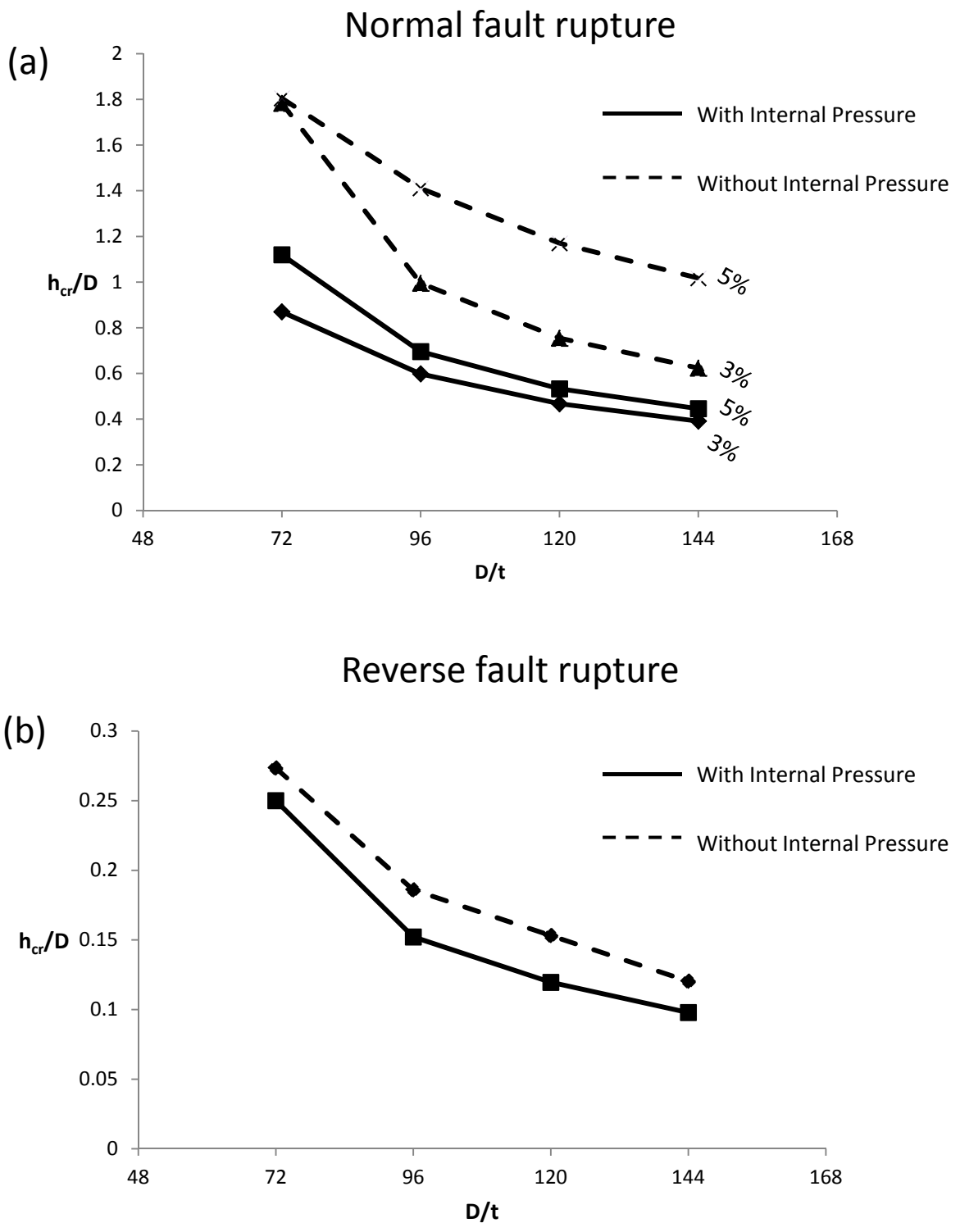

Figure 7.2.6. (a) Comparison of the pipe capacity, in terms of critical fault displacement, with respect to the Diameter to thickness ratio, between the case with and without internal pipe pressure, for normal fault rupture. (b) Comparison of the pipe capacity, in terms of critical fault displacement, with respect to the Diameter to thickness ratio, between the case with and without internal pipe pressure, for reverse fault rupture.

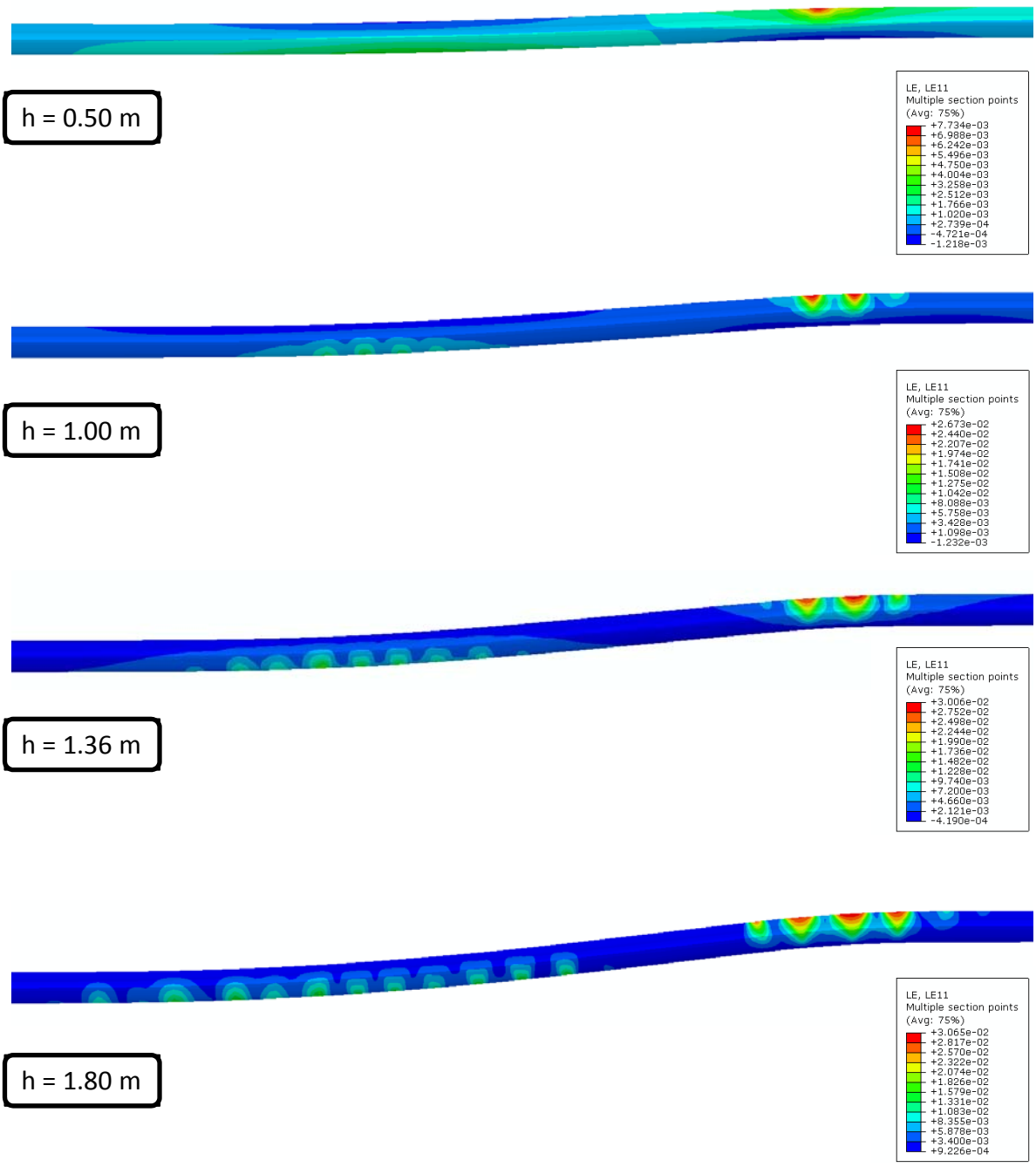

Figure 7.3.1. The axial strain distribution along the central model area (X=10-40 m) for different fault displacements.(D/t = 72)

(a)

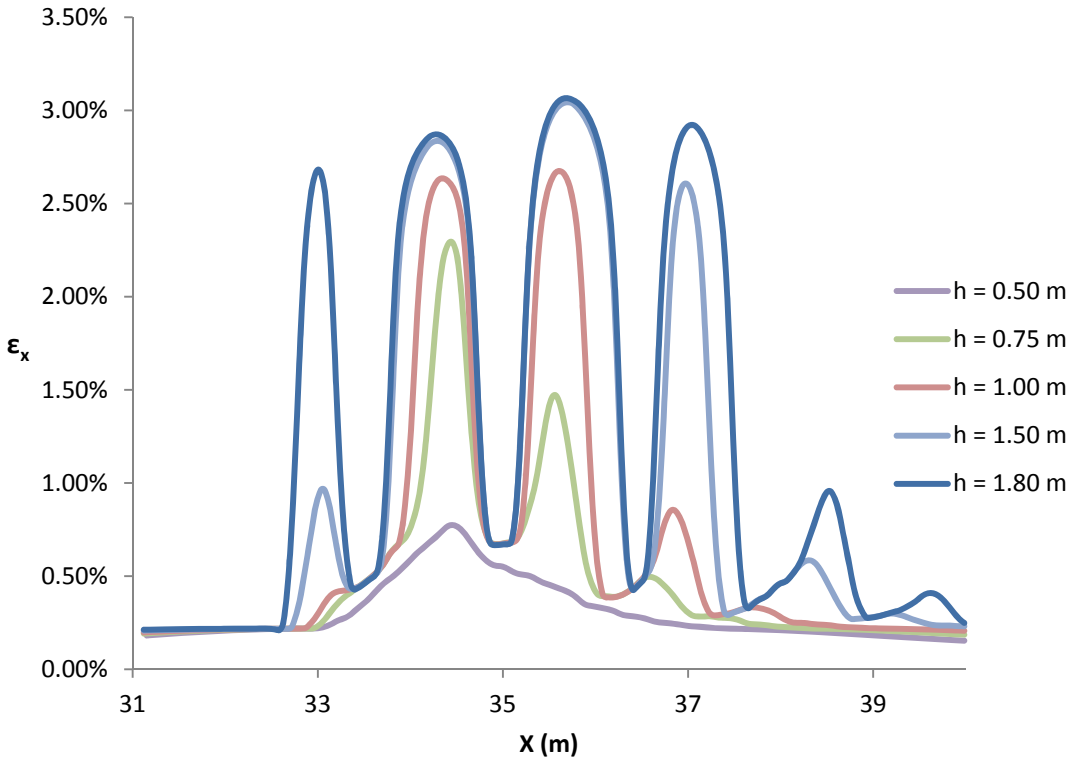

(b)

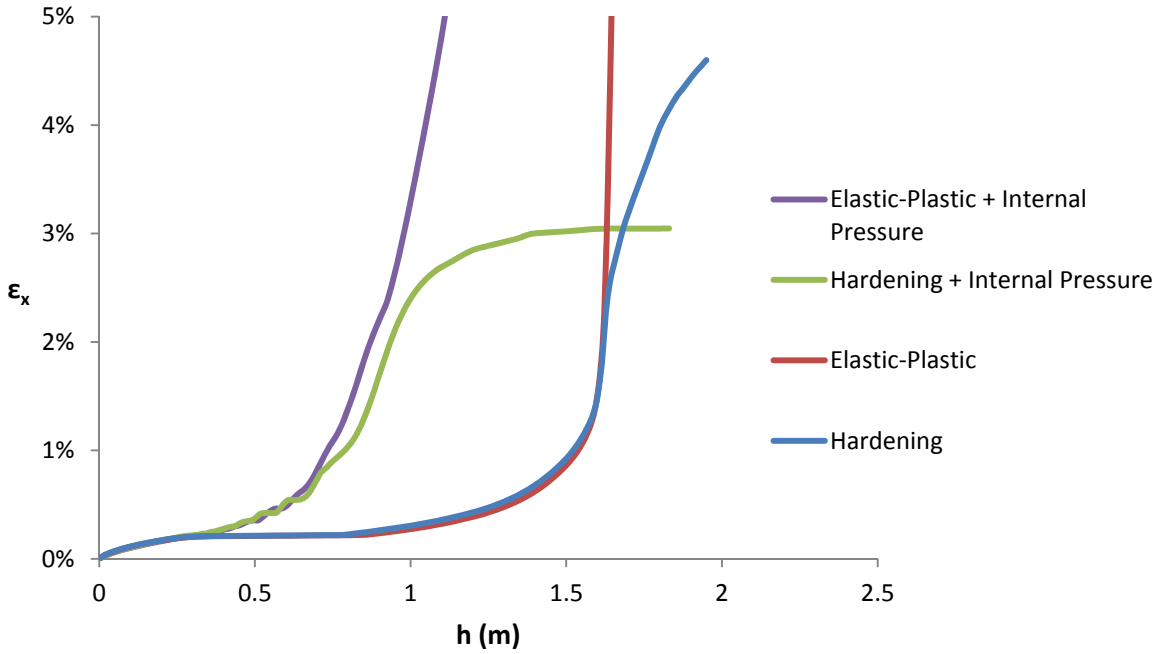

Figure 7.3.2. (a) The distribution of axial compressive strains along the critical buckling area, until the 3% limit of tensile strain is reached.(D/t = 72). (b) The evolution of axial strains at the critical points for the 4 models.(D/t = 72)

Hardening with Internal Pressure – Reverse Fault

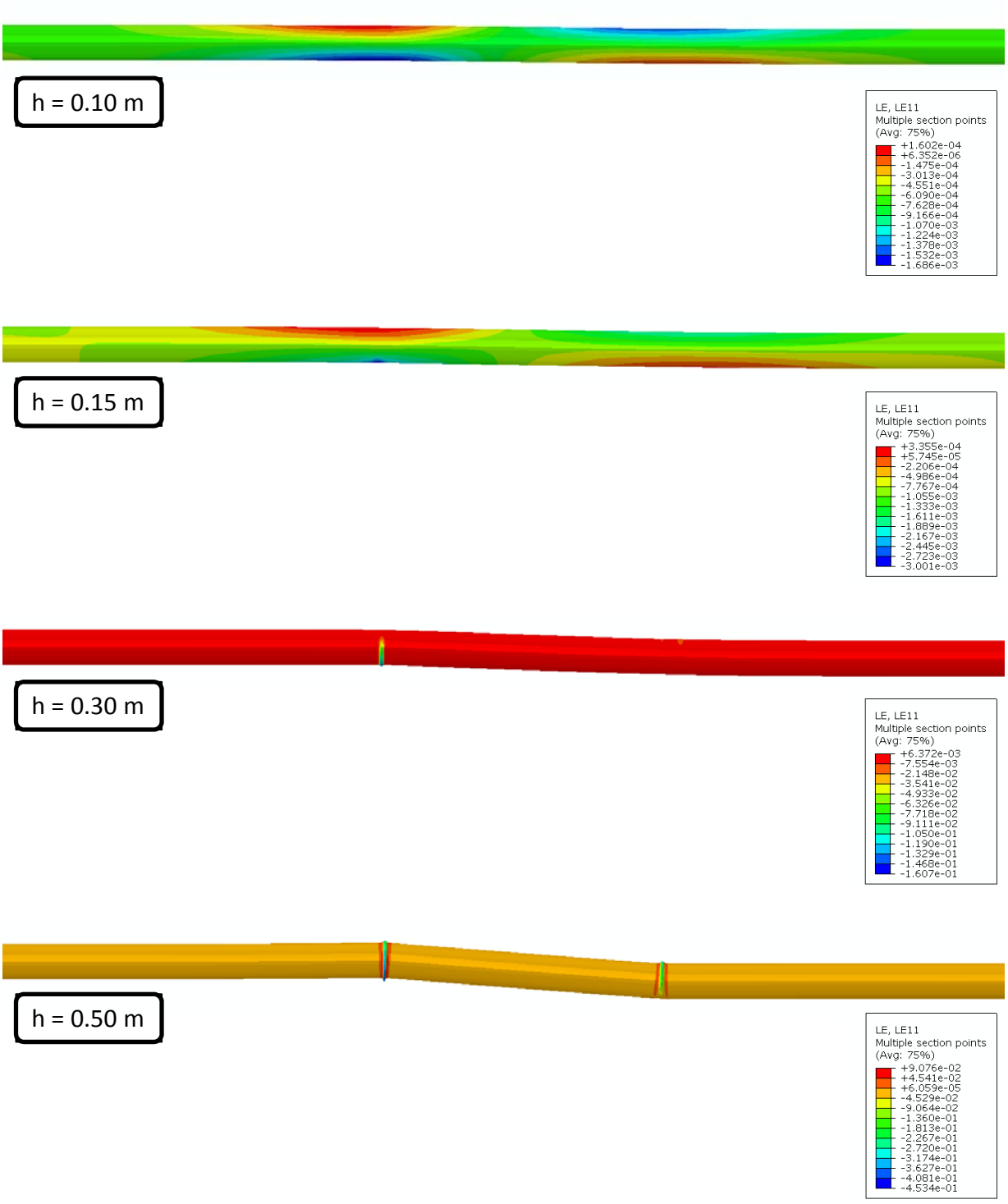

Figure 7.3.3. The axial strain distribution along the central model area (X=20-45 m) for different fault displacements.(D/t = 72)

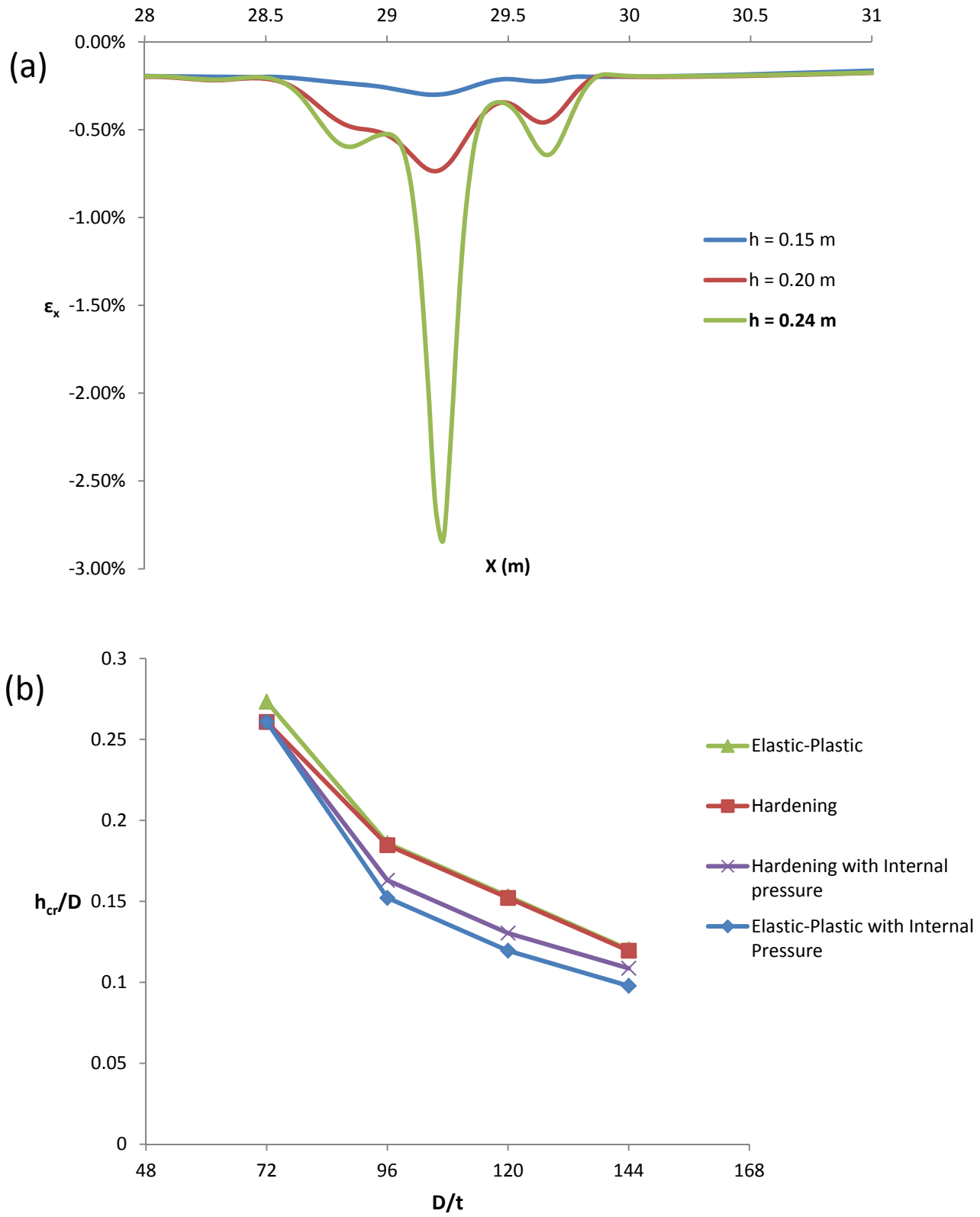

Figure 7.3.4. (a) The distribution of axial compressive strains along the critical buckling area until the appearance of buckling.(D/t = 72). (b) Comparison of the pipe capacity, in terms of critical fault displacement, with respect to to the D/r ratio, between the four models.

Chapter 8

Conclusions and proposals for further research

8.1 Conclusions

The study's purpose was, mainly, to propose a finite element model that properly addresses to the problem of a pipe crossing an active Dip-Slip fault and by using this model, to examine the effect of various parameters such as the type of fault (Normal or Reverse), the diameter to thickness pipe ratio, the depth of the soil layer, the stress-strain relation of the pipe material and the internal pipe pressure.

The model we used is a 3-D F.E. model that simulates the pipe with shell elements and the surrounding soil with continuum "brick" elements. In order to confront the problem that arises from the contradiction of the continuity of the pipeline and the limited dimensions of the model, we expanded the pipe by one kilometer from each pipe end using linear beam elements. The soil around the expansion parts was substituted by axial, vertical and horizontal soil springs, whose properties had been taken by the results of a numerical pushover analysis. The use of the beam elements and soil springs allows the increase of our models dimensions without significant increase of computational effort and time. Comparing the results of this model with models of free and fixed pipe ends, both for normal and reverse fault case, we conclude that the behavior of the pipe is heavily affected by the pipe boundaries and we recommend the proposed model as the most reliable and realistic one. Its expanded dimensions also allow the computation of the effective pipe length that denotes the length of the pipe that is affected by the rupture.

The examination of both normal and reverse fault rupture proved that, because of their tensile and compressive nature respectively, the mode of failure for the normal case is the excessive tensile strain whereas for the reverse case is the local buckling.

In all of the cases examined in this essay, it is demonstrated that the decrease of D/t ratio (or the increase of pipe thickness, since we keep the diameter unchanged) increases the pipe endurance in terms of fault displacement.

The investigation of the soil layer's depth effect concludes that the pipe can resist significantly more bedrock displacement before it reaches the failure state, because of the wider distribution of soil displacements.

All the aforementioned investigations were initially conducted for elastic-perfectly plastic pipe steel and were repeated for an elastic-hardening plastic pipe material. The results of the analyses indicate that for the normal fault case, hardening plays a significant role since firstly, it augments the pipe resistance to fault movement and secondly it is proven necessary for the model to be able to capture another mode of failure knows as ovalization or flattening, related to excessive cross-sectional distortion and operational failure. However, the role of hardening is not that significant for the reverse fault case where local buckling is the failure mode.

Regarding the internal pipe pressure, it has been proven that it has a negative result to the pipe resistance since it causes additional stresses and strains, leading to premature yielding and failure. Finally, it provokes a different strain distribution with multiple critical areas in the case of normal fault and is proven necessary for the beneficial effects of the hardening to appear in the reverse fault case.

8.2 Proposals for further Research

This essay is a preliminary investigation of the behavior of a pipe subjected to Dip-Slip fault rupture. Apart from the aspects that we examined there are lots of other parameters that could be investigated in a future research such as:

- The type of soil. We have conducted analyses for different types of soil (Dense/Loose Sand and Clay). However, we focused only in the Dense Sand case in order to be able to compare the effects of the other parameters. Furthermore, it is proved that the behavior of the system depends on the relative stiffness of the system, in other words, on the ratio of soil stiffness to pipe stiffness, which we do change by adjusting the thickness of the pipe.

- The presence of aquifer of a level close to the surface.

- The backfill material. We have made the assumption that the backfill material has the same properties as the rest of the soil, something that is in contrast to the reality since the soil that is used to cover the pipe is of less density because of the excavation procedure. An interesting idea would be to examine different backfill materials, apart from the excavated soil.

- The type of fault. Apart from our study, which concentrates on Dip-Slip fault ruptures and apart from the Strike-Slip rupture, which is widely examined by various researchers, the case of an Oblique fault rupture could be investigated. Different pipe behavior is expected in that case, because both of the Dip and Strike components of the fault are measurable and significant. The oblique effect can be also examined by changing the pipe-fault plane intersection angle.

References

ABAQUS (2011): Users' Manual, Simulia, Providence, RI, USA.

Abdoun T. H., Ha, D., O'Rourke, M. J., Symans, M. D., O'Rourke, T. D., Palmer, M. C., and Stewart, H. E. (2009), "Factors influencing the behavior of buried pipelines subjected to earthquake faulting.", Soil Dynamics and Earthquake Engineering, Vol. 29, pp. 415– 427.

American Society of Civil Engineers (2009). Buried flexible steel pipe; design and structural analysis. In: Whidden WR, editor. ASCE Manual of Practice, MOP. p. 119.

American Society of Mechanical Engineers (2006), Pipeline Transportation Systems for Liquid Hydrocarbons and Other Liquids, ANSI/ASME B31.4.

American Society of Mechanical Engineers (2007), Gas Transmission and Distribution Piping Systems, ANSI/ASME B31.8.

Anastasopoulos I., Gazetas G., M. ASCE, Bransby M. F., Davies M. C. R., Nahas A. El, (2007), "Fault Rupture Propagation through Sand: Finite-Element Analysis and Vaidation through Centrifuge Experiments", Journal of Geotechnical and Geoenvironmental Engineering, ASCE, p. 943-958

Anastasopoulos I., Callerio A., Bransby M. F., Davies M. C., Nahas A. El, Faccioli E., Gazetas G., Masella A., Paolucci R., Pecker A., Rossigniol E. (2008), "Numerical analyses of fault foundation interaction.", Bulletin of Earthquake Engineering, Sprin\ger, 6(4), 645-675.

Arifin R. B., Shafrizal W. M., Wan B., Yusof M., Zhao P., and Bai Y. (2010), "Seismic analysis for the subsea pipeline system.", Proceedings of the ASME 2010 29th International Conference on Ocean, Offshore and Arctic Engineering, OMAE2010-20671, Shanghai, China.

ANSI/API Spec 5L, "Specification for Line Pipe", 44th edition, American Petroleum Institute, October 2007.

Bray, J. D. (1990). "The effects of tectonic movements on stresses and deformations in earth embankments." Ph.D. dissertation, Univ. of California at Berkeley, Berkeley, Calif.

Bray, J. D., Seed, R. B., Cluff, L. S., and Seed, H. B. (1994a). "Earthquake fault rupture propagation through soil." J. Geotech. Engrg., 120(3), 543–561.

Canadian Standard Association (2007), Oil and Gas Pipeline Systems, CSA-Z662, Mississauga, Ontario, Canada.

Chiou YJ, Chi SY, Chang HY. “A study on buried pipeline response to fault movement”. Pressure Vessel Technology, ASME 1994; Vol: 116, 36-41.

Comité Européen de Normalisation (2006), Eurocode 8, Part 4: Silos, tanks and pipelines, CEN EN1998-4, Brussels, Belgium.

Dama E., Karamanos, S. A., and Gresnigt, A. M. (2007), "Failure of Locally Buckled Pipelines.", Journal of Pressure Vessel Technology, ASME, Vol. 129, No. 2, pp. 272-279.

Douglas G. Honegger et al. (2004), “Trans-Alaska Pipeline System Performance in the 2002 Denali Fault, Alaska, Earthquake.”, Earthquake Spectra, Volume 20, No. 3, pages 707-738, August 2004.

Erickson, S. G., Staryer, L. M., and Suppe, J. (2001). “Initiation and reactivation of faults during movement over a thrust-fault ramp: Numerical mechanical models.” J. Struct. Geol., 23, 11–23.

Gazetas. G., Anastasopoulos I. and Apostolou. M. (2007), “Shallow and deep foundation under fault rapture or strong seismic shaking.”, K. Pitilakis (ed.), Earthquake Geotechnical Engineering, Springer, 185-215.

ICF International, Interstate Natural gas Association of America Report: “Natural gas pipeline and storage infrastructure, Projections through 2030”, October 2009

Karamitros D.K., Bouckovalas G.D., Kouretzis G.P., (2006),”Stress analysis of buried steel pipelines at strike-slip fault corssings”, Soil Dynamics and Earthquake Engineering 27 (2007), p. 200-211.

Karamitros D.K., Bouckovalas G.D., Kouretzis G.P., Gkesouli V.,”An analytical method for strength verification of buried steel pipeline at normal fault crossings”, Soil Dynamics and Earthquake Engineering 31 (2011), p. 1452-1464.

Kennedy, R.P., Chow, A. W. and Williamson, R. A. (1977), “Fault movement effects on buried oil pipeline”, Journal of Transportation Engineering, ASCE, Vol. 103, pp. 617-633.

Kennedy R. P., Kincaid R. H. (1983). “Fault crossing design for buried gas oil pipelines”. ASME,PVP conference; 77:1–9.

Liu, X. and O'Rourke, M. J. (1997), Behaviour of continuous pipeline subject to transverse PGD. Earthquake Engng. Struct. Dyn., 26: 989–1003.

Loukidis, D. (1999). "Active fault propagation through soil." Thesis, School of Civil Engineering, National Technical Univ., Athens, Greece.

MaCaffrey MA, O'Rourke TD (1983). Buried pipeline response to reverse faulting during the 1971 San Fernando Earthquake. ASME, PVP conference 1983; 77:151–159.

Nakai, T., Muir Wood, D., and Stone, K. J. L. (1995). "Numerical calculations of soil response over a displacing basement." Soils Found., 35(2), 25–35.

"NEESR-SG Final Report", Cornell University, Rensselaer Polytechnic Institute, The Sciencenter Discovery Center, June 25, 2008.

Newmark, N.M., Hall W.J. (1975), "Pipeline design to resist large fault displacement". Proceedings of U.S. National Conference on Earthquake Engineering; 416–425.

Odina, L. and Tan, R. (2009), "Seismic Fault Displacement of Buried Pipelines Using Continuum Finite Element Methods.", Proceedings of the ASME 2009 28th International Conference on Ocean, Offshore and Arctic Engineering, OMAE2009-79739, Honolulu, Hawaii.

Odina, L. and Conder, R. J. (2010), "Significance of Lüder's Plateau on Pipeline Fault Crossing Assessment", Proceedings of the ASME 2010 29th International Conference on Ocean, Offshore and Arctic Engineering, OMAE2010-20715, Shanghai, China.

O'Rourke T.D., "Geohazards and large, geographically distributed systems.", (2010), Geptechnique 60, No. 7,507-543

Papazachos B., Papaioannou Ch., Papazachos C., Savvaidis A., (1997), "Atlas of Isoseismal Maps for Strong Shallow Earthquakes in Greece and Surrounding Area (426BC–1995)." Ziti Publication Co, Thessaloniki (1997).

Peter J. Haeussler et al., (2004), "Surface Rupture of the 2002 Denali Fault, Alaska, Earthquake and Comparison with other Strike-Slip Ruptures.", Earthquake Spectra, Volume 20, No. 3, pages 565-578, August 2004.

Potts, D. M., Kovacevic, N., and Vaughan, P. R. (1997). “Delayed collapse of cut slopes in stiff clay.” *Geotechnique*, 47(5), 953–982.

Roth, W. H., Sweet, J., and Goodman, R. E. (1982). “Numerical and physical modeling of flexural slip phenomena and potential for fault movement.” Rock Mech., 12, 27–46.

Scott, R. F., and Schoustra, J. J. (1974). “Nuclear power plant sitting on deep alluvium.” J. Geotech. Engrg. Div., 100(4), 449–459.

Sim W.W., Towhata I., Yamada S., Moinet G.J.-M., (2012), “Shaking table tests modeling small diameter pipes crossing a vertical fault.”, Soil Dynamics and Earthquake Engineering**,** Volume 35, p.59-71, April 2012, Elsevier.

Takada, S., Hassani, N.and Fukuda, K. (2001), “A new proposal for simplified design of buried steel pipes crossing active faults”, Earthquake Engineering and Structural Dynamics, 2001; Vol.30: pp.1243–1257.

Trifonov, O. V. and Cherniy, V. P. (2010), “A semi-analytical approach to a nonlinear stress–strain analysis of buried steel pipelines crossing active faults.”, Soil Dynamics & Earthquake Engineering, Vol. 30, pp. 1298-1308.

Trifonov, O. V. and Cherniy, V. P. (2012), “Elastoplastic stress-strain analysis of buried steel pipelines subjected to fault displacements with account for service loads.”, Soil Dynamics & Earthquake Engineering, Vol. 33, No. 1, pp. 54-62.

U.S. Energy Information Administration, Office of Oil and Gas, Report: “Natural gas compressor stations on the Interstate pipeline network: Developments since 1996”, November 2007

Vougioukas E. A., Theodossis, C., Carydis P. G. (1979), “Seismic analysis of buried pipelines subjected to vertical fault movement.”, Journal of Technical Councils, ASCE, Vol. 105(TCI), pp. 432–441.

Vazouras P., Karamanos S. A., Dakoulas P., (2010),”Finite element analysis of buried steel pipelines under strike-slip fault displacements.”, Soil Dynamics and Earthquake Engineering (2010), doi: 10.1016/j.soildyn.2010.06.011

Vazouras P., Karamanos S. A., Dakoulas P., (2012), “Mechanical behavior of buried steel pipes crossing active strike-slip faults”, Soil Dynamics and Earthquake Engineering, Volume 41, October 2012, Pages 164-180

Walters, J. V., and Thomas, J. N. (1982). “Shear zone development in granular materials.” Proc., 4th Int. Conf. on Numerical Methods in Geomechanics, Vol. I, Edmonton, Canada, 263–274.

Wang, L. R. L. and Yeh, Y. A. (1985), “A refined seismic analysis and design of buried pipeline for fault movement”, Earthquake Engineering & Structural Dynamics, Vol. 13, pp. 75-96.

Wang, Y. Y., Horsley, D. and Liu, M., (2007), “Strain Based Design of Pipelines.”, 16th Joint Technical Meeting, Australian Pipeline Association, Canberra, Australia.

White, R. J., Stone, K. J. L., and Jewel, R. J. (1994). “Effect of particle size on localization development in model tests on sand.” Proc., Inst. Centrifuge Conf., C. F. Leung, F. H. Lee, and T. S. Tan, eds., Balkema, Rotterdam, The Netherlands, 817–822.

Yoshizaki K., O’Rourke T.D., Hamada M., (2003), “Large scale experiments of buried steel pipelines with elbows subjected to permanent ground deformation”, Structural Eng/Earthquake Eng., JSCE, Vol. 20, No. 1, 1-11.

Πιτιλάκης Δ.Κ., “ΓΕΩΤΕΧΝΙΚΗ ΣΕΙΣΜΙΚΗ ΜΗΧΑΝΙΚΗ”, Εκδόσεις ΖΗΤΗ

Internet References

- American Oil and Gas Historical Society, www.aoghs.com
- American Petroleum Institute, www.api.org
- United States Geological Survey, www.USGS.org
- Διαχειριστής Εθνικού Συστήματος Φυσικού Αερίου Α.Ε., www.desfa.gr
- International Gas Union, www.inu.org
- Interconnector Turkey-Greece-Italy Pipeline, www.edison.it/en/company/gas-infrastractures/itgi.shtml
- Trans Adriatic Pipeline, www.trans-adriatic-pipeline.com